Search for Seesaw type III Signals in 2011 LHC CMS Data

Sara Vanini

born in Bergamo, Italy

Physics Department *Galielo Galieli*

University of Padua, Italy

A thesis submitted for the degree of

PhilosophiæDoctor - Field of Physics

Padua, Italy - January 2012

1. Reviewer: prof. Paolo Checchia

2. Reviewer: prof. Gianni Zumerle

Day of the defense: March 2012

Signature from head of PhD committee: Andrea Vitturi

Abstract

In 2010 the Compact Muon Solenoid (CMS) detector at the CERN Large Hadron Collider (LHC) started collecting proton collision data at a center of mass energy $\sqrt{s} = 7$TeV with a target integrated luminosity for the first run of 1 fb^{-1}. Collisions continued during 2011 and on 30th October 2011 the LHC dumped the last proton beams for the year. During 2011 the LHC delivered 5.74 fb^{-1} of proton collisions and CMS experiment has recorded 5.21 fb^{-1}.

The analysis expounded in this thesis performs a search for new physics signals in CMS detector 2011 data in multileptons channels. The analysis uses the data sample corresponding to the overall certified integrated luminosity of 2011, i.e. 4.6 fb^{-1}.

Among several models of Physics Beyond the Standard Model the Seesaw type-III was probed. Seesaw models predict the addition of massive particles in Standard Model; type-III seesaw model specify these particles to be fermion triplets. According to this model, the p-p collisons produce Seesaw triplet which decay in standard model bosons and leptons. Final states contain SM leptons, jets and missing energy. The 3-leptons final states provide the cleanest signature. The signal from this signature, with muons and electrons, was searched, for five values of Seesaw triplet mass.

Detailed Monte Carlo simulation of the physics interactions and detector performance is been compared with 2011 data. A simple and robust event selection, was developed to discriminate Seesaw signature from instrumental and Standard Model backgrounds, as well as methods to control backgrounds estimates from data.

Event yields for tri-leptons channels were computed for predicted Seesaw signal and backgrounds, and were compared to observed data.

No significant excess of events with respect to the standard model expectations was found. The 95% confidence level limits on Seesaw cross section was computed.

Results show that Seesaw mass is excluded below 180 GeV (185 GeV at NLO) for equal lepton mixings. If the Seesaw triplet couples with one leptonic flavor only, the limit on the mass is 200 GeV. The limit on Seesaw cross section is 20 fb for the equal mixings scenario.

To Andrea

...and Niccolò, Pietro, Tommaso, Clara.

Contents

List of Figures

List of Tables

1 Introduction

1.1 Motivations

The Standard Model of particle physics (extended to include right-handed neutrinos) continues to successfully describe all existing data with good approximation. Nevertheless there are both theoretical and experimental reasons to believe that there is physics beyond the Standard Model.

From a theoretical point of view: in the Standard Model the masses and mixings of all the fermions are simply parameters (the Yukawa couplings) that need to be measured, but are not theoretically founded. When going beyond the Standard Model those fermion masses and mixings can arise through underlying mechanisms such as the seesaw mechanism, that generate fermion masses through higher dimension operators involving heavier particles.

From an experimental point of view the data from neutrino oscillations compounds the puzzle of the fermion masses and mixings. The data indicates that the leptonic mixing angles are large - in stark contrast with the small mixing angles of the quark sector. Moreover, the data indicates that neutrinos do have mass, in contrast with Standard Model assumptions.

Therefore several particle physics theories Beyond the Standard Model have been developed in the last decades and their predictions are going to be probed with early LHC data. Among these, we Analise a promising signature from Seesaw type-III mechanism hypothesis and we infer discovery potential and exclusion limits with the CMS detector data.

1.2 Analysis Strategy

The profusion of new physics scenarios to be tested at the LHC will require inclusive searches and model-independent analysis, in order to be sensitive to different types of new physics contributing to a given channel. Therefore in our analysis we will not set fine-tuned kinematic cuts on many variables to enhance the signals, but our criteria for variable selection and background suppression will be rather general, and in most cases valid for seesaw I, II and III signals. In this way, our results and procedures will be adequate for model-independent searches in the multi-lepton final states. Of course, if some hint of new physics is found the analysis can be refined and adapted to some particular scenario, in order to reconstruct the resonance masses and/or enhance the sensitivity. In conclusion, we will focus on the final state signature without fine-tuned cuts to select particular seesaw model, to be as much inclusive as possible.

1.2.1 Blind Analysis

The method used in this analysis is the so-called *blind analysis* method. Its main objective is to avoid biased decisions involving the data selection. This goal is achieved by avoiding looking at the data sample until the signal signature and the total Standard Model backgrounds are evaluated.

1.2.2 Outline

Chapter 1 is the present introduction. The Chapter 2 is dedicated to a brief introduction to the theoretical framework: I give a short summary of the Standard Model and I briefly review the current status of fermion masses and mixings knowledge, and of neutrino oscillations observation results. I present and briefly discuss the recent model of the seesaw mechanism.

The experimental apparatus: the LHC collider and the CMS detector is described in Chapter 3.

The Chapter 4 is dedicated to the feasibility to study the signals from Seesaw models in LHC data.

Furthermore, the complete analysis procedure is sorted out in the next Chapters. The complete procedure is described as follows:

- Use Monte Carlo to generate the Seesaw signal events, Analise the generated signal, then pass through the CMS detector simulation (Chapter 5).
- Identify physics objects in the CMS detector, and reconstruction criteria (Chapter 6).
- Select data sample containing two same-sign leptons passing certain criteria (Chapter 7).
- Identify the Standard Model backgrounds that can yield a similar signature to the Seesaw signal, and generate and pass through the CMS detector simulation and reconstruction the Standard Model backgrounds not present in official production (Chapter 8).
- Study the reconstructed events and develop selection criteria to enhance the Seesaw signal through suppressing the Standard Model backgrounds. The event selection criteria are chosen according to the kinematic distribution of decay products to reject background with a minimal loss of signal acceptance, and optimization process is carried out for the final cuts to improve the results. We then apply the selection criteria to the data sample (Chapter 9).
- Estimate the systematic, statistical and theoretical uncertainties on the number of expected signal and background events (Chapter 10).
- Obtain a 95% confidence level upper limit on the Seesaw cross section from the number of observed data events, then translate it into an upper limit of Seesaw triplet mass. (Chapter 11).

Finally an overview of the full work is presented in the conclusions, Chapter 12.

1.3 Definitions

1.3.1 Coordinate system

When discussing the physical dimensions of the detector, Cartesian coordinates are used, where x points inwards to the center of the accelerator, y is positive in the upwards vertical direction and z is aligned along the beampipe (pointing towards the

Jura mountains). The kinematics of physical events and certain aspects of the detector are discussed in terms of the coordinate system (η; ϕ; z). In this system, z is defined as in the Cartesian system and the azimuthal angle, ϕ, is given by:

$$\phi = arctan\frac{y}{x}.$$

The pseudorapidity, η, is defined as

$$\eta = -ln(tan\frac{\theta}{2}),$$

where the polar angle, θ, is given by

$$\theta = artan\frac{\sqrt{x^2+y^2}}{z}$$

The quantity ΔR is often used, which describes a separation in η and ϕ

$$\Delta R(\vec{v}1;\vec{v}2) = \sqrt{\Delta\eta^2(\vec{v}1;\vec{v}2) + \Delta\phi^2(\vec{v}1;\vec{v}2)},$$

where $\vec{v}_{1,2}$ are vectors in the (η; ϕ; z) basis.

1.3.2 Units

All calculations are expressed in terms of natural units, where energy is measured in eV, and it is defined that

$$\hbar = \frac{h}{2\pi} = c = 1$$

In this system, the units of mass, momentum and time are eV, eV and eV^{-1} respectively. When discussing units of data, powers of 2 are indicated as kiB (1024B), whereas powers of 10 are indicated as kB (1000B).

1.3.3 Other Definitions

Matrices are indicated by bold face (**T**), and three-vectors by an over-arrow ($\vec{x}$). Four vectors are indicated by Greek indices (x^μ), with summation over repeated indices assumed. The Minkowski metric $g^{\mu\nu} = g_{\mu\nu} = diag(+,-,-,-)$ is used throughout. Missing energy is denoted by $E_{\mathrm{T}}^{\mathrm{miss}}$.

1.4 Machine Energy

During the time this thesis was written, the LHC beam energy was $\sqrt{s} = 7$ TeV and therefore the analysis contained within assume $\sqrt{s} = 7$ TeV.

1.4.1 LHC Delivered Luminosity and 2011 Run Summary

2011 proton-proton collisions at $\sqrt{s}$ =7 TeV beam energy started in March. At 17:00 on Sunday 30th October the LHC dumped the last proton beams for the year to start the machine development period and to prepare for heavy ion running. Thus the proton operation for 2011 ended. In 2011 the LHC delivered 5.74 fb-1 of proton collisions and CMS has recorded 5.21 fb-1, as shown in Figure 1.1. The overall data taking efficiency is 91%, and the average fraction of operational channels per subsystem is > 98.5%. Results shown in this thesis use a large fraction of the full data-set. Certied data for physics: Golden 4745pb^{-1} (91.2%), Muon 4965pb^{-1} (96%). The Uncertainty on the luminosity determination is 4.5%.

A few highlights from the 2011 run summary (cfr: (1)) follows.

Peak Instantaneous Luminosity: $3.55 \cdot 10^{33}$ Hz/cm ^{2} in fill 2256 2011.10.26.

Delivered luminosity in one Fill: 123 pb $^{-1}$ in fill 2219 2011.10.16

Maximum Luminosity in one Day: 136 pb^{-1} on 2011.10.13

Maximum Luminosity Delivered in one Week: 538 pb^{-1} in week 41

Maximum Luminosity Delivered in one Month: 1614 pb^{-1} in October 2011.

LHC declared stable beams for 1364 hours in this year.

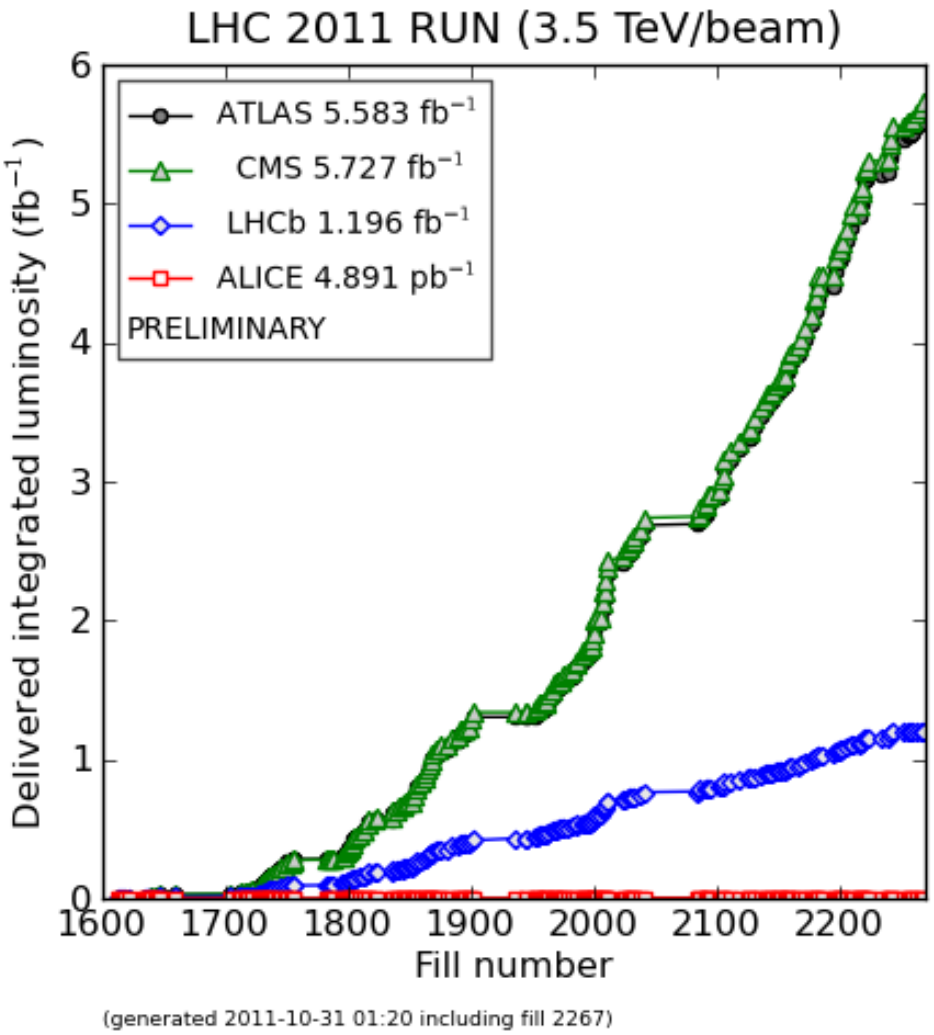

Figure 1.1: LHC delivered luminosity - The plot shows the LHC delivered luminosity for the different experiments, taken from http://cms.web.cern.ch/news/summary-2011-p-p-running.

2

Seesaw theory Beyond the Standard Model

2.1 Standard Model

The Standard Model is regarded as one of the biggest achievements in physics of the last century because it is the current best description of the physics of fundamental particles and their interactions: electromagnetic, weak, and strong interactions. It describes them with high accuracy and stands numerous experimental tests. It has been tested to high precision by the Large Electron Positron (LEP) collider at CERN, the Tevatron at Fermi National Laboratory, and by the Stanford Linear Collider (SLC) at Stanford National Laboratory.(i.e. LEP electroweak measurements).

The Standard Model is a particular quantum field theory. Quantum field theory combines the two great achievements of 20^{th}-century physics, quantum mechanics and relativity.

We'll review in Appendix A the most important features of the Standard Model, stressing the aspects relevant for the theory underling this thesis. For a complete description see References (3) and (2). The evidences for physics beyond the Standard Model are descried in Section 2.2, and a closer examination of the Seesaw model, analyzed in this thesis, is given in Section 2.3.

2.2 Beyond the Standard Model

The Standard Model is a simple, elegant, and successful theory. It successfully describes the majority of current experimental data. Nevertheless, there are *anomalies* and both direct and indirect evidence for it physics beyond the standard model. We'll summarize them in this section.

2.2.1 Direct evidence

2.2.1.1 Neutrinos

The existence of neutrino particle was first postulated in 1930 by Wolfgang Pauli to preserve the conservation of energy, conservation of momentum, and conservation of angular momentum in beta decay: $n \rightarrow p+e+\bar{\nu_e}$. This undetected particle should carry away the observed difference between the energy, momentum, and angular momentum of the initial and final particles.

The experiment for direct detection, the so called β-capture, was proposed in 1942 by Kan-Chang Wang. In 1956 Clyde Cowan, Frederick Reines, F. B. Harrison, H. W. Kruse, and A. D. McGuire detected the neutrino through this process, and were rewarded with the 1995 Nobel Prize. In this experiment neutrinos created in a nuclear reactor by beta decay were shot into protons producing neutrons and positrons both of which could be detected.

In 1962 Leon M. Lederman, Melvin Schwartz and Jack Steinberger showed that more than one type of neutrino exists by detecting interactions of the muon neutrino. When the third type of lepton, the tauon, was discovered in 1975 at the Stanford Linear Accelerator Center, it too was expected to have an associated neutrino, and the evidence for this third neutrino type came from the observation of missing energy and momentum in tauon decays analogous to the beta decay leading to the discovery of the neutrino. The first detection of tauon neutrino interactions was announced in summer of 2000 at the Fermi National Laboratory, making it the latest particle of the Standard Model to have been directly observed. The current best measurement of the number of neutrino types comes from observing the decay of the Z boson. This particle can decay into any light neutrino and its antineutrino, and the more types of light neutrinos available, the shorter the lifetime of the Z boson. Measurements of the Z lifetime have shown that the number of light neutrino types is 3. The Standard Model of particle physics (SM) assumes that neutrinos are 3, they are massless and cannot change flavor.

The neutrino flavor oscillations. Starting in the late 1960s, several experiments found that the number of electron neutrinos arriving from the sun was between one third and one half the number predicted by the Standard Solar Model (SSM), a discrepancy which became known as the solar neutrino problem and remained unresolved for some

thirty years. The idea of neutrino flavor oscillations was first suggested by Bruno Pontecorvo in 1957, and developed in 1967. According to this theory neutrinos are able to oscillate between the three available flavors while they propagate through space.

The observation of neutrino flavor oscillations indicates that neutrinos have mass, which is not explained by the Standard Model. Moreover, the existence of neutrino masses leads to leptonic mixing. The observation of neutrino oscillations is thus unambiguous evidence of physics beyond the standard model.

Neutrino oscillations arise from a straightforward quantum mechanical phenomenon that occurs during the propagation of the neutrinos, causing them to change flavor. This is possible due to the existence of lepton mixing, which is entirely analogous to quark mixing (although the values of the mixing angles are quite different). Instead of the Cabibbo-Kobayashi-Maskawa (CKM) matrix of the quark sector, the respective mixing matrix is sometimes denoted as the Pontecorvo-Maki-Nakagawa-Sakata (PMNS, or often only MNS) matrix. In the basis where the charged lepton mass matrix is diagonal:

$$\nu_i = \sum_\alpha U_{\alpha i} \nu_\alpha \tag{2.1}$$

ν_i are the mass eigenstates, ν_α the flavor eigenstates. The unitary matrix U expressing the linear combination in eq.(2.1) is the PMNS matrix (here we use Greek letters to clearly distinguish the flavor indices α, β from the mass indices i, j). With this in mind it is easy to understand how a specific flavor eigenstate can oscillate to a different one as it propagates: it is composed of a linear combination of mass eigenstates with masses m_i.

The neutrino mass eigenstates propagation could be described by plane wave solutions of the form:

$$|\nu_i(t = L)\rangle = e^{-i(E_i t - \vec{p}_i \cdot \vec{x})} |\nu_i(0)\rangle \approx e^{-i m_i^2 L/2E} |\nu_i(0)\rangle \tag{2.2}$$

with t is the time from the start of the propagation, $\vec{x}$ is the current position of the particle, $\vec{p}_i$ is the 3-dimensional momentum. The neutrinos are very light, with $m_i \ll p_i$, so one can take $t \simeq L$ (natural units), so $c = 1$ $t = L =$ traveled distance. The proportion of mass eigenstates will change during the propagation due to the phase factors $e^{-i m_i \tau}$ in the ν_i rest frame. In the laboratory frame, the phase factor becomes

$e^{-i(E_i t - p_i L)}$ (E_i and p_i being the energy and momentum of ν_i, t and L the time and position, all quantities in the laboratory frame). Since neutrino masses are less than 1 eV and their energies are at least 1 MeV, we could consider the ultra-relativistic limit, therefore the energy could be approximated as: $E_i = \sqrt{p_i^2 + m_i^2} \simeq p_i + \frac{m_i^2}{2p_i}$.

Eigenstates with different masses propagate at different speeds. Since the mass eigenstates are combinations of flavor eigenstates, this difference in speed causes interference between the corresponding flavor components of each mass eigenstate.

The phase factor becomes (approximately) $e^{-i(m_i^2/2p)L}$, and considering the average energy of the various mass eigenstates $E \simeq p$, we can obtain the formula for probability of flavor change from flavor state α into flavor state β after propagation for a distance L in the vacuum:

$$P_{\alpha\to\beta} = \left| \sum_i U^*_{\alpha i} U_{\beta i} e^{-i\frac{m_i^2 L}{2E}} \right|^2 \tag{2.3}$$

Eq.(2.3) may be conveniently expressed as $P_{\alpha\to\beta} = \delta_{\alpha\beta} + Q_{\alpha\to\beta}$, with $Q_{\alpha\to\beta}$ being:

$$Q_{\alpha\to\beta} = -4\sum_{i>j} \mathrm{Re}\left(U^*_{\alpha i} U_{\beta i} U_{\alpha j} U^*_{\beta j}\right) \sin^2\left(\frac{\Delta m^2_{ij} L}{4E}\right) + 2\mathrm{Im}\left(U^*_{\alpha i} U_{\beta i} U_{\alpha j} U^*_{\beta j}\right) \sin\left(\frac{\Delta m^2_{ij} L}{2E}\right) \tag{2.4}$$

The terms in eq.(2.4) clearly show that the squared mass differences $\Delta m^2_{ij} \equiv m_i^2 - m_j^2$ are measurable from oscillation (although the overall mass scale isn't).

The phase that is responsible for oscillation is often written as:

$$\frac{\Delta m^2\, c^3\, L}{4\hbar E} = \frac{\mathrm{GeV\,fm}}{4\hbar c} \times \frac{\Delta m^2}{\mathrm{eV}^2} \frac{L}{\mathrm{km}} \frac{\mathrm{GeV}}{E} \approx 1.267 \times \frac{\Delta m^2}{\mathrm{eV}^2} \frac{L}{\mathrm{km}} \frac{\mathrm{GeV}}{E} \tag{2.5}$$

All neutrino experiments observing oscillations measure the squared mass difference and not absolute mass, therefore it could be hypothesized that the lightest neutrino mass is exactly zero, but it is regarded as unlikely by theorists.

A convenient summary of the neutrino oscillation data is given in (16). For reference, we reproduce in Table 2.2.1.1 the relevant table with the values (updated in June 2006 (16)).

It is important to note that the large angles of table 2.2.1.1 contrast with the small angles of the CKM matrix (the largest of which, the Cabibbo angle, has $\sin(\theta_C) < 0.23$).

parameter	best fit	2σ	3σ	4σ
$\Delta m^2_{21}[10^{-5}\text{eV}]$	7.9	7.3–8.5	7.1–8.9	6.8–9.3
$\Delta m^2_{31}[10^{-3}\text{eV}]$	2.6	2.2–3.0	2.0–3.2	1.8–3.5
$\sin^2\theta_{12}$	0.30	0.26–0.36	0.24–0.40	0.22–0.44
$\sin^2\theta_{23}$	0.50	0.38–0.63	0.34–0.68	0.31–0.71
$\sin^2\theta_{13}$	0.000	≤ 0.025	≤ 0.040	≤ 0.058

Table 2.1: Neutrino data: best-fit values, 2σ, 3σ, and 4σ intervals (from (16)).

The experimental data is conveniently displayed in a graphical manner by use of colored or shaded bars, taken from (17). Figure 2.1 features the two possible mass hierarchies (due to the ambiguity in the sign of the atmospheric squared mass difference), and shows the peculiar situation described by tri-bi-maximal mixing quite clearly: one neutrino mass eigenstate (ν_3) is approximately comprised of equal parts ν_μ and ν_τ, and another (ν_2) is approximately equal parts of all three flavor eigenstates.

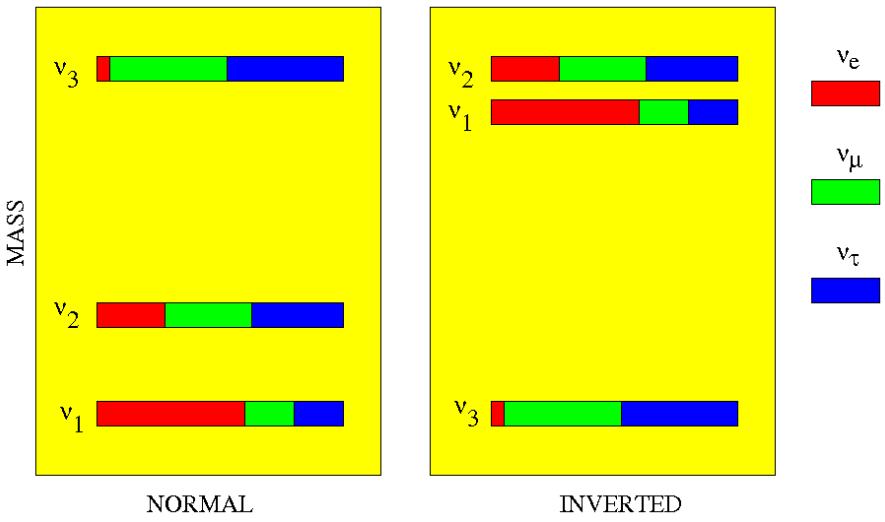

Figure 2.1: Neutrino mixing summary from (27).

Neutrino masses and mixings in the Standard Model could be explained with a conservative hypothesis, i.e.: the Standard Model restricts to the simplest possible interactions, additional interactions are present, but they are suppressed. To add these

additional interactions, we need to add more terms to the Lagrangian in Eq. A.1, with coefficients with dimensions of an inverse power of mass (3):

$$\mathcal{L} = \mathcal{L}_{SM} + \frac{1}{M}\mathcal{L}_5 + \frac{1}{M^2}\mathcal{L}_6 + \cdots \quad (2.6)$$

where M is a mass scale greater than the Higgs-field vacuum-expectation value, v. At energies much less than M, the least-suppressed interactions come from the Lagrangian labeled $\mathcal{L}_5$. There is only one possible term in this Lagrangian (assuming the standard-model particle content and gauge symmetries) (3, 6),

$$\mathcal{L}_5 = c^{ij}(L_L^{iT}\epsilon\phi)C(\phi^T\epsilon L_L^j) + h.c.\ . \quad (2.7)$$

where L_L and ϕ are the lepton and Higgs-doublet fields (see Table A.1) and C is the charge-conjugation matrix. When the Higgs field acquires a vacuum-expectation value, this term gives rise to a Majorana [1]

[1]For the Dirac particle we have to put in the Feynmann rule: $\gamma_\mu(1-\gamma_5)$. If the neutrino is a Majorana particle The Lagrangian looks the same but in the Feynamann rule we have to include instead the term: $\gamma_\mu\gamma_5$. To understand it we need to go back to the field expression:

$$\Phi_{Dirac} = \int (fe^{-ip} + \hat{f}^\dagger e^{ip})$$
$$\Phi_{Majorana} = \int (fe^{-ip} + f^\dagger e^{ip})$$

where f is the fermion annihilation operator, and $\hat{f}$ is the anti-fermion annihilation operator. So the creation in the Dirac case is:

$$< \overline{\nu}\nu|(f^\dagger + \hat{f})\gamma_\mu(1-\gamma_5)(f+\hat{f}^\dagger)|Z>$$
$$=< 0|\hat{f}f[(f^\dagger + \hat{f})\gamma_\mu(1-\gamma_5)(f+\hat{f}^\dagger)]|Z>$$

where $< \overline{\nu}\nu =< 0|\hat{f}f$ and the contractions in the Dirac case are $\hat{f}\hat{f}^\dagger$ and $ff^\dagger$.
In the Majorana case we have:

$$< 0|ff[(f^\dagger + f)\gamma_\mu(-1-\gamma_5)(f+f^\dagger)]|Z> \quad (2.8)$$

in this case we have two contractions: $ff^\dagger$ for each field f, so we obtain: $\gamma_\mu(1-\gamma_5) - \gamma_\mu(1-\gamma_5)$.
Therefore we could write:

$$\begin{aligned}
&\overline{\nu}\gamma_\mu(1-\gamma_5)\nu \\
&\quad = \frac{1}{2}\overline{\nu}\gamma_\mu(1-\gamma_5)\nu + \frac{1}{2}(\overline{\nu}\gamma_\mu(1-\gamma_5)\nu)^t \\
&\quad = \frac{1}{2}\overline{\nu}\gamma_\mu(1-\gamma_5)\nu + \frac{1}{2}(-\nu^t(1-\gamma_5)\gamma_\mu^t\overline{\nu}^t) \\
&\quad = \frac{1}{2}\overline{\nu}\gamma_\mu(1-\gamma_5)\nu + \frac{1}{2}(-\overline{\nu}_c\gamma_\mu(1+\gamma_5)\nu_c
\end{aligned}$$

mass matrix for the neutrinos,

$$M_\nu^{ij} = c^{ij}\frac{v^2}{M}. \tag{2.10}$$

Given this addition lagrangian term, we expect neutrino masses and mixing, with masses much less than v (for $M \gg v$). We will describe neutrino masses and mixings in the following paragraph. For a exhaustive derivation the most indicated reference is the original treatment in (13). It is useful the neutrino mixing review in (15) too, which includes extensive references. The following clear brief summary is taken mostly from (14).

2.2.1.2 Gravity

Gravity is not explained by the Standard Model, thus is another direct evidence of physics beyond the standard model. If a graviton field is added to the theory, $g_{\mu\nu}$, the least-suppressed additional interactions (using dimensional analysis) are

$$\mathcal{L}_{gravity} = \frac{M_P^2}{16\pi}\sqrt{-g}(-2\Lambda + R + \cdots) \tag{2.11}$$

where M_P is the Planck scale, $g \equiv \det g^{\mu\nu}$, R is the Ricci scalar, and Λ is the cosmological constant. The Ricci-scalar term accounts for all of classical gravity. The cosmological constant, long thought to be exactly zero, is able to account for the mysterious *dark energy* needed to accommodate cosmological observations.

2.2.1.3 Astrophysics and Cosmology

Along with the dark energy mentioned above there is also *dark matter*, whose nature is unknown, which accounts for about 35% of the mass-energy. Observations of fluctuations in the spectrum of the microwave background, remnant from the Big Bang, have established the existence of cold dark matter. In particular, recent measurements from the Wilkinson Microwave Anisotropy Probe (WMAP) satellite show that dark matter composes 23.3% of the Universe, while ordinary baryonic matter makes up only 4.6%

Since in the Majorana case: $\nu_c = \nu$ we obtain:

$$\overline{\nu}\gamma_\mu(1-\gamma_5)\nu = \frac{1}{2}\overline{\nu}\gamma_\mu(1-\gamma_5)\nu - \frac{1}{2}(\overline{\nu}\gamma_\mu(1+\gamma_5)\nu = \overline{\nu}\gamma_\mu\gamma_5\nu \tag{2.9}$$

of it. Moreover, observation of large red shifts in the spectrum of the oldest Type Ia supernovas confirms the theory that 70% of the Universe is made up of dark energy. This measurement has also been supported by the WMAP satellite measurements, which established the dark matter content at 72.1%. Whatever this matter is, it is certainly beyond the standard model.

The observed baryon asymmetry of the universe also cannot be explained by the standard model, because it requires a source of CP violation beyond that contained in the CKM matrix. The inflationary model of the universe, so successful in explaining many of the features of our universe, also requires physics beyond the standard model.

2.2.2 Indirect evidence

2.2.2.1 Masses and mixing angles

The standard model accommodates generic masses and mixing angles, but the observed values are far from generic. The fermion masses and mixing angles strongly suggest that there is a deeper structure underlying the Yukawa sector of the standard model. Since the standard model can accommodate any masses and mixing angles, we must seek an explanation from physics beyond the standard model.

The introduction of the scalar field to explain the breaking of the electroweak symmetry is done "by hand" and the Higgs particle has to be still confirmed by the experiments. [1]

Moreover, the natural scale of charged fermion masses is of order v, but all charged fermions (except the top quark) are much lighter than this, and display a hierarchical pattern. The CKM mixing angles are also not generic; they are small, and are also hierarchical. These facts suggest that there is physics beyond the standard model

[1] Discovering and studying the Higgs boson (or bosons) is central to understanding physics beyond the standard model because almost all of these anomalies and hints of physics beyond the standard model involve the Higgs field in one way or another. Neutrino masses involve the Higgs field, via Eq. (2.7); the vacuum-expectation value of the Higgs field contributes to the cosmological constant; the axion (a type of Higgs field) is a dark-matter candidate; there could be additional CP violation in the Higgs sector that generates the baryon asymmetry; the inflaton (a scalar field) could drive inflation; precision electroweak data constrain the Higgs sector; fermion masses and mixing angles result from the coupling of the Higgs field to fermions, Eq. (A.8); SUSY SU(5) grand unification requires two Higgs doublets; and the hierarchy problems involve the Higgs-field vacuum-expectation value.

that explains the pattern of charged fermion masses and mixing. Unfortunately, the standard model does not indicate at what energy scale this new physics resides (8).

2.2.2.2 Dimensional Analysis of the Lagrangian

The Standard Model lagrangian written in Eq. A.1 includes only the simplest terms because these are the renormalizable terms. Renormalizability or dimensional analysis is a stronger constraint than is really necessary (7).

The action has units of $\hbar = 1$:

$$S = \int d^4x \, \mathcal{L} \, . \tag{2.12}$$

so the Lagrangian must have units of mass^4. From the kinetic energy terms in the Lagrangian for a generic scalar (ϕ), fermion (ψ), and gauge boson (A^μ),

$$\mathcal{L}_{KE} = \partial^\mu \phi^* \partial_\mu \phi + i\bar{\psi} \, \partial\!\!\!/ \psi - \frac{1}{2}(\partial^\mu A^\nu \partial_\mu A_\nu + \partial^\mu A^\nu \partial_\nu A_\mu) \tag{2.13}$$

we can deduce the dimensionality of the various fields:

$$\begin{aligned} \dim \phi &= \text{mass} \\ \dim \psi &= \text{mass}^{3/2} \\ \dim A^\mu &= \text{mass} \end{aligned}$$

All operators (products of fields) in the Lagrangian of the Standard Model are of dimension four, except the operator $\phi^\dagger \phi$ in the Higgs potential, which is of dimension two. The coefficient of this term, μ^2, is the only dimensionful parameter in the standard model; it (or, equivalently, $v \equiv \mu/\sqrt{\lambda}$) sets the scale of all particle masses.

Imagine that the Lagrangian at the weak scale is an expansion in some large mass scale M,

$$\mathcal{L} = \mathcal{L}_{SM} + \frac{1}{M}\dim 5 + \frac{1}{M^2}\dim 6 + \cdots \, , \tag{2.14}$$

where dim n represents all operators of dimension n. By dimensional analysis, the coefficient of an operator of dimension n has dimension mass^{4-n}, since the Lagrangian has dimension mass^4. At energies much less than M, the dominant terms in this Lagrangian will be those of $\mathcal{L}_{SM}$; the other terms are suppressed by an inverse power of M. This is the modern reason why we believe the "simplest" terms in the Lagrangian

are the dominant ones. When searching for deviations from the standard model, we need to look for the effects of higher-dimension operators. The least suppressed terms in the Lagrangian beyond the standard model are of dimension five. We should therefore expect our first observation of physics beyond the standard model to come from these terms. Although there is only one operator of dimension five, there are dozens of operators of dimension six.

Thus far, none of the effects of any of these operators have been observed. The best we can do is set lower bounds on M (assuming some dimensionless coefficient). These lower bounds range from 1 TeV to 10^{16} GeV, depending on the operator. As we explore nature at higher energy and with higher accuracy, we hope to begin to see the effects of some of these dimension-six operators.

The mass scale M corresponds to the mass of a particle that is too heavy to observe directly. At energies greater than M, the expansion of Eq. (2.14) is no longer useful, as each successive term is larger than the previous. Instead, one must explicitly add the new field of mass M to the model. For example, if nature is supersymmetric at the weak scale, one must add the superpartners of the standard-model fields to the theory and include their interactions in the Lagrangian. If we raise the mass scale of the superpartners to be much greater than the weak scale, then we can no longer directly observe the superpartners, and we return to a description in terms of standard-model fields, with an expansion of the Lagrangian in inverse powers of the mass scale of the superpartners, M.

2.2.2.3 Grand Unification

$SU(5)$ grand unification it has been a smart idea (9), but now the gauge couplings it is known with good accuracy, and they do not unify at high energies. It is remarkable that by imposing weak-scale supersymmetry on the theory, the relative evolution of the couplings is nudged just enough to successfully unify the couplings at the scale $M_{GUT} \approx 10^{16}$ GeV. This suggests that the supersymmetric partners of the known particles await us as we probe the weak scale.

2.2.2.4 Hierarchy problems

The standard model has only one energy scale, i.e. the Higgs-field vacuum-expectation value, v. The questions why there is a strong hierarchy is still unresolved. In other

words, it appears that physics beyond the standard model is associated with scales wildly different from v, but the questions is unanswered. Perhaps the explanation for this requires yet more physics beyond the standard model, such as supersymmetry or large extra dimensions.

2.3 The Seesaw Model for Mass Generation Mechanisms

An appealing possibility to include the neutrino masses and accounting for their smallness is the seesaw mechanism. With this model new heavy particles having a Yukawa interaction with the lepton and the Higgs doublets generate a small Majorana mass for the neutrinos, generically suppressed, with respect to charged fermion masses, by a factor v/M, where M the mass of the heavy particle. If one requires $\mathcal{O}(1)$ Yukawa couplings, M should be of the order of the grand unification scale in order to account for neutrino masses smaller than the eV. However, in principle nothing prevents the scale to be as low as hundreds of GeV. In this case the heavy field responsible for neutrino masses could be discovered at the LHC.

Detailed description of seesaw mechanism theory is contained in references: (18), (19), (20) and (24). Here we will give only a brief summary.

2.3.1 Seesaw Models

Depending on the nature of the heavy state, seesaw models are called type I (18), type II (19) or type III (20), corresponding to heavy fermionic singlet, scalar triplet or fermionic triplet, respectively.

The three types of seesaw mechanism generate new lagrangian terms with dimension greater then four. They generate dimension five operator which gives light neutrino masses, but also additional lepton number conserving (LNC) dimension six operators, which are different in each seesaw scenario(References (70),(24)). Therefore, seesaw models may in principle be discriminated, albeit indirectly, with precise low-energy measurements sensitive to these dimension six operators.

The only five-dimensional operator allowed by the $\mathrm{SU}(3) \times \mathrm{SU}(2)_L \times \mathrm{U}(1)_Y$ gauge symmetry is the lepton number violating (LNV) dimension five operator (5):

$$(O_5)_{ij} = \overline{L^c_{iL}} \tilde{\phi}^* \tilde{\phi}^\dagger L_{jL} \tag{2.15}$$

where

$$L_{iL} = \begin{pmatrix} \nu_{iL} \\ l_{iL} \end{pmatrix}, \quad i = 1, 2, 3 \tag{2.16}$$

are the SM left-handed lepton doublets, ϕ the SM Higgs and $\tilde{\phi} = i\tau_2\phi^*$, with τ_i the Pauli matrices. This operator yields Majorana masses for the neutrinos after spontaneous symmetry breaking.

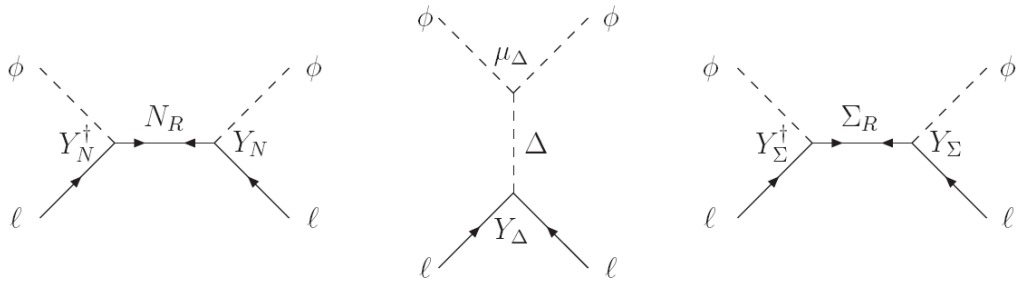

Figure 2.2: The three generic realizations of the Seesaw mechanism, depending on the nature of the heavy fields exchanged: SM singlet fermions (type I Seesaw) on the left, SM triplet scalars (type II Seesaw) and SM triplet fermions (type III Seesaw) on the right.

2.3.2 Seesaw I

Type-I seesaw is usually implemented by adding three right-handed current eigenstates N'_{iR}, $i = 1, 2, 3$, transforming as singlets under the SM gauge group. This allows to write a Yukawa interaction for neutrinos analogous to the one for charged leptons,

$$\mathcal{L}_{\mathrm{Y}} = -Y_{ij}\,\overline{L'_{iL}} N'_{jR}\,\tilde{\phi} + \mathrm{H.c.}\,, \tag{2.17}$$

where Y is a 3×3 matrix of couplings and L'_{iL} the SM lepton doublets (in the weak eigenstate basis). This interaction generates a mass term upon spontaneous symmetry breaking

$$\phi = \begin{pmatrix} \phi^+ \\ \phi^0 \end{pmatrix} \to \frac{1}{\sqrt{2}} \begin{pmatrix} 0 \\ v \end{pmatrix}, \quad \tilde{\phi} \equiv i\tau_2\phi^* \to \frac{1}{\sqrt{2}} \begin{pmatrix} v \\ 0 \end{pmatrix}, \tag{2.18}$$

with $v = 246$ GeV. Since N'_{iR} are SM singlets, gauge symmetry allows a Majorana mass term

$$\mathcal{L}_{\mathrm{M}} = -\frac{1}{2} M_{ij} \overline{N'_{iL}} N'_{jR} + \mathrm{H.c.}\,, \tag{2.19}$$

with M a 3×3 symmetric matrix and $N'_{iL} \equiv N'^{c}_{iR}$.[1] Defining $\nu'_{iR} \equiv \nu'^{c}_{iL}$, where ν'_{iL} are the SM neutrino eigenstates, the full neutrino mass term reads

$$\mathcal{L}_{\rm mass} \;=\; -\frac{1}{2}\,(\bar{\nu}'_L\;\bar{N}'_L)\begin{pmatrix} 0 & \frac{v}{\sqrt{2}}Y \\ \frac{v}{\sqrt{2}}Y^T & M \end{pmatrix}\begin{pmatrix} \nu'_R \\ N'_R \end{pmatrix} + \text{H.c.}\,. \qquad (2.20)$$

The neutrino gauge interactions are the same as in the SM. Then, the relevant interaction terms for the heavy neutrino mass eigenstates $N_i \simeq N'_{iR}$ can be obtained by diagonalizing the mass matrix in Eq. (2.20) and rewriting the interactions in the mass eigenstate basis.

In the absence of any particular symmetry in the Yukawa couplings, light neutrino masses m_ν are of the order $Y^2v^2/2m_N$, and the heavy neutrino mixings are $V_{lN} \sim \sqrt{m_\nu/m_N}$. Hence, for a heavy neutrino within LHC reach, say with a mass $m_N \sim 100$ GeV, its seesaw-type contribution to light neutrino masses is of the order of $300\,Y^2$ GeV, requiring very small Yukawas $Y \sim 10^{-6}$ to reproduce light neutrino masses $m_\nu \sim 0.1$ eV. Moreover, the natural order of magnitude of the mixings is $O(10^{-6})$, too small to give observable signals.

Even if we put aside the connection between heavy neutrino mixing and light neutrino masses, the former must be small due to present experimental constraints. Electroweak precision data set limits on mixings involving a single charged lepton, and using the latest experimental data, the constraints at 90% confidence level (CL) are (25)

$$\sum_{i=1}^{3}|V_{eN_i}|^2 \leq 0.0030\,, \quad \sum_{i=1}^{3}|V_{\mu N_i}|^2 \leq 0.0032\,, \quad \sum_{i=1}^{3}|V_{\tau N_i}|^2 \leq 0.0062\,, \qquad (2.21)$$

which in particular imply constraints on the individual mixings V_{lN} of a heavy neutrino N. These constraints are particularly important since they determine the heavy neutrino production cross sections at LHC. Figure 2.3 is a typical type I seesaw diagram (with the "$\times$" in the ν^c propagator denoting the Majorana mass insertion).

2.3.3 Seesaw II

In type II seesaw light neutrinos acquire masses from a gauge-invariant Yukawa interaction of the left-handed lepton doublets with a scalar triplet Δ of hypercharge $Y = 1$

[1] We avoid writing parentheses in charge conjugate fields to simplify the notation, and write $\psi^c_L \equiv (\psi_L)^c$, $\psi^c_R \equiv (\psi_R)^c$.

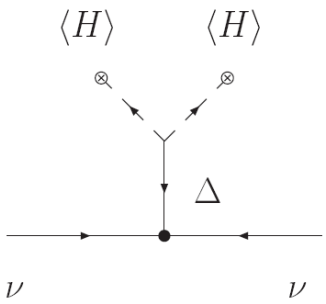

Figure 2.3: Type I seesaw diagram.

(with $Q = T_3 + Y$). Writing the triplet in Cartesian components $\vec{\Delta} = (\Delta^1, \Delta^2, \Delta^3)$, the Yukawa interaction reads

$$\mathcal{L}_{\rm Y} = \frac{1}{\sqrt{2}} Y_{ij}\, \overline{\tilde{L}_{iL}}\, (\vec{\tau}\cdot\vec{\Delta})\, L_{jL} + \text{H.c.}\,, \tag{2.22}$$

with

$$\tilde{L}_{jL} = i\tau_2 \begin{pmatrix} \nu^c_{jL} \\ l^c_{jL} \end{pmatrix} \tag{2.23}$$

and Y a symmetric matrix of Yukawa couplings. We assume without loss of generality that the charged lepton mass matrix is diagonal, and drop primes on the neutrino fields, which are taken in the flavor basis ν_e, ν_μ, ν_τ. The triplet charge eigenstates are related to the Cartesian components by

$$\Delta^{++} = \frac{1}{\sqrt{2}}(\Delta^1 - i\Delta^2)\,, \quad \Delta^{+} = \Delta^3\,, \quad \Delta^0 = \frac{1}{\sqrt{2}}(\Delta^1 + i\Delta^2)\,. \tag{2.24}$$

When the neutral triplet component acquires a vacuum expectation value (vev) $\langle\Delta^0\rangle = v_\Delta$, the Yukawa interaction in Eq. (2.22) induces a neutrino mass term

$$\begin{aligned} \mathcal{L}_{\rm mass} &= -Y^*_{ij} v_\Delta\, \bar{\nu}_{iL}\, \nu_{jR} + \text{H.c.} \\ &\equiv -\frac{1}{2} M_{ij}\, \bar{\nu}_{iL}\, \nu_{jR} + \text{H.c.}\,, \end{aligned} \tag{2.25}$$

where we have again introduced the notation $\nu_{iR} \equiv \nu^c_{iL}$, and

$$M_{ij} = 2 Y^*_{ij} v_\Delta \tag{2.26}$$

are the matrix elements of the light neutrino Majorana mass matrix.

The triplet Yukawa interaction in Eq. (2.22) also generates triplet couplings to the charged leptons.

The gauge interactions of the triplet components are obtained from the kinetic term

$$\mathcal{L}_{\rm K} = (D^\mu \vec{\Delta})^\dagger \cdot (D_\mu \vec{\Delta})\,, \tag{2.27}$$

For a detailed derivation of gauge interactions mediating scalar triplet pair production processes see ref. (24).

Constraints on the triplet parameters are much less important than for heavy neutrino singlets, because the new scalars can be produced at LHC by unsuppressed gauge interactions. Electroweak precision data set an upper limit on the triplet vev v_Δ. The most recent bound obtained from a global fit is (26)

$$v_\Delta < 2 \text{ GeV}\,, \tag{2.28}$$

which is much less stringent than the one derived from neutrino masses, Eq. (2.26), if Y_{ij} are of the order of the charged lepton Yukawa couplings. The type II seesaw mechanism typical diagram is shown in figure 2.4.

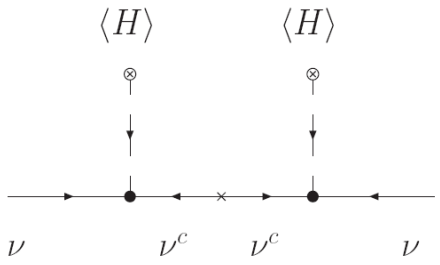

Figure 2.4: Type II seesaw diagram.

2.3.4 Seesaw III

In type III seesaw the SM is usually enlarged with three leptonic triplets Σ_j, each composed by three Weyl spinors of zero hypercharge. Writing the triplets in Cartesian components $\vec{\Sigma}_j = (\Sigma_j^1, \Sigma_j^2, \Sigma_j^3)$ and using standard four-component notation, the triplet Yukawa interaction with the lepton doublets takes the form

$$\mathcal{L}_{\rm Y} = -Y_{ij}\, \bar{L}'_{iL} (\vec{\Sigma}_j \cdot \vec{\tau})\, \tilde{\phi} + \text{H.c.}\,, \tag{2.29}$$

with Y a 3×3 matrix of Yukawa couplings. The triplet Majorana mass term mediating the seesaw is

$$\mathcal{L}_{\rm M} = -\frac{1}{2}\, M_{ij}\, \overline{\vec{\Sigma}_i^c}\cdot\vec{\Sigma}_j + {\rm H.c.}\,, \tag{2.30}$$

with M a 3×3 symmetric matrix. Notice that all the members Σ_j^1, Σ_j^2, Σ_j^3 of the triplet Σ_j have the same mass term. For each triplet Σ_j, the charge eigenstates are related to the Cartesian components by

$$\Sigma_j^+ = \frac{1}{\sqrt{2}}(\Sigma_j^1 - i\Sigma_j^2)\,, \quad \Sigma_j^0 = \Sigma_j^3\,, \quad \Sigma_j^- = \frac{1}{\sqrt{2}}(\Sigma_j^1 + i\Sigma_j^2)\,. \tag{2.31}$$

The physical particles are charged Dirac fermions E'_j and neutral Majorana fermions N'_j (as before, we use primes for the weak interaction eigenstates),

$$E'_j = \Sigma_j^- + \Sigma_j^{+c}\,, \quad N'_j = \Sigma_j^0 + \Sigma_j^{0c}\,. \tag{2.32}$$

Then, for our choice of right-handed chirality for the triplets we have

$$E'_{jL} = \Sigma_j^{+c}\,, \quad E'_{jR} = \Sigma_j^-\,, \quad N'_{jL} = \Sigma_j^{0c}\,, \quad N'_{jR} = \Sigma_j^0\,. \tag{2.33}$$

After spontaneous symmetry breaking the terms in Eqs. (2.29), (2.30) lead to the neutrino mass matrix

$$\mathcal{L}_{\nu,{\rm mass}} \;=\; -\frac{1}{2}\,\left(\bar{\nu}'_L\;\bar{N}'_L\right)\begin{pmatrix} 0 & \frac{v}{\sqrt{2}}Y \\ \frac{v}{\sqrt{2}}Y^T & M \end{pmatrix}\begin{pmatrix} \nu'_R \\ N'_R \end{pmatrix} + {\rm H.c.}\,, \tag{2.34}$$

similar to the one for type-I seesaw in Eq. (2.20). The mass matrix for charged leptons, also including the 3×3 SM Yukawa matrix Y^l, reads

$$\mathcal{L}_{l,{\rm mass}} \;=\; -\left(\bar{l}'_L\;\bar{E}'_L\right)\begin{pmatrix} \frac{v}{\sqrt{2}}Y^l & vY \\ 0 & M \end{pmatrix}\begin{pmatrix} l'_R \\ E'_R \end{pmatrix} + {\rm H.c.} \tag{2.35}$$

The gauge interactions of the new triplets can be obtained from the kinetic term

$$\mathcal{L}_{\rm K} = i\,\overline{\vec{\Sigma}_j}\cdot\gamma^\mu D_\mu\,\vec{\Sigma}_j\,, \tag{2.36}$$

where a sum over $j=1,2,3$ is understood. The covariant derivative is

$$D_\mu = \partial_\mu + ig\vec{T}\cdot\vec{W}_\mu\,, \tag{2.37}$$

The B_μ term is absent because the triplets have zero hypercharge. With the definitions in Eqs. (2.31) and (2.32), the gauge interactions in the weak eigenstate basis could be derived.

As in the case of heavy neutrino singlets, limits on the mixing of new fermion triplets arise from electroweak precision data. The most recent constraints are (25)

$$\sum_{i=1}^{3} |V_{eN_i}|^2 \leq 0.00036\,, \quad \sum_{i=1}^{3} |V_{\mu N_i}|^2 \leq 0.00029\,, \quad \sum_{i=1}^{3} |V_{\tau N_i}|^2 \leq 0.00073 \tag{2.38}$$

at 90% CL.

2.3.5 Seesaw type-III simplified model

The model considered in this thesis is the seesaw type III simplified model derived in Ref. (30), which is based on the full model presented in Ref. (28).

The Complete Lagrangian is written with the addition to the standard model of SU(2) triplets of fermions with zero hypercharge, Σ. In this model at least two such triplets are necessary in order to have two non-vanishing neutrino masses. The beyond the standard model interactions are described by the following lagrangian (with implicit flavor summation):

$$\mathcal{L} = Tr[\overline{\Sigma} i \not{D} \Sigma] - \frac{1}{2} Tr[\overline{\Sigma} M_\Sigma \Sigma^c + \overline{\Sigma^c} M_\Sigma^* \Sigma] - \tilde{\phi}^\dagger \overline{\Sigma} \sqrt{2} Y_\Sigma L - \overline{L} \sqrt{2} Y_\Sigma{}^\dagger \Sigma \tilde{\phi}\,, \tag{2.39}$$

with $L \equiv (\nu, l)^T$, $\phi \equiv (\phi^+, \phi^0)^T \equiv (\phi^+, (v + H + i\eta)/\sqrt{2})^T$, $\tilde{\phi} = i\tau_2 \phi^*$, $\Sigma^c \equiv C\overline{\Sigma}^T$ and with, for each fermionic triplet,

$$\begin{aligned} \Sigma &= \begin{pmatrix} \Sigma^0/\sqrt{2} & \Sigma^+ \\ \Sigma^- & -\Sigma^0/\sqrt{2} \end{pmatrix}, \quad \Sigma^c = \begin{pmatrix} \Sigma^{0c}/\sqrt{2} & \Sigma^{-c} \\ \Sigma^{+c} & -\Sigma^{0c}/\sqrt{2} \end{pmatrix}, \\ D_\mu &= \not{\partial}_\mu - i\sqrt{2} g \begin{pmatrix} W_\mu^3/\sqrt{2} & W_\mu^+ \\ W_\mu^- & -W_\mu^3/\sqrt{2} \end{pmatrix}. \end{aligned} \tag{2.40}$$

Without loss of generality, we can assume that we start from the basis where M_Σ is real and diagonal, as well as the charged lepton Yukawa coupling, not explicitly written above. In order to consider the mixing of the triplets with the charged leptons, it is convenient to express the four degrees of freedom of each charged triplet in terms of a single Dirac spinor:

$$\Psi \equiv \Sigma_R^{+c} + \Sigma_R^-\,. \tag{2.41}$$

The neutral fermionic triplet components on the other hand can be left in two-component notation, since they have only two degrees of freedom and mix with neutrinos, which

are also described by two-component fields. This leads to the Lagrangian

$$\begin{aligned}\mathcal{L} &= \overline{\Psi} i\partial\!\!\!/ \Psi + \overline{\Sigma_R^0} i\partial\!\!\!/ \Sigma_R^0 - \overline{\Psi} M_\Sigma \Psi - \left(\overline{\Sigma_R^0} \frac{M_\Sigma}{2} \Sigma_R^{0c} + \text{h.c.} \right) \\ &+ g \left(W_\mu^+ \overline{\Sigma_R^0} \gamma_\mu P_R \Psi + W_\mu^+ \overline{\Sigma_R^{0c}} \gamma_\mu P_L \Psi + \text{h.c.} \right) - g W_\mu^3 \overline{\Psi} \gamma_\mu \Psi \\ &- \left(\phi^0 \overline{\Sigma_R^0} Y_\Sigma \nu_L + \sqrt{2} \phi^0 \overline{\Psi} Y_\Sigma l_L + \phi^+ \overline{\Sigma_R^0} Y_\Sigma l_L - \sqrt{2} \phi^+ \overline{\nu_L{}^c} Y_\Sigma^T \Psi + \text{h.c.} \right) . \end{aligned} \quad (2.42)$$

The mass matrices of the charged and the neutral sectors need to be diagonalized as they possess off-diagonal terms. Following the diagonalization procedure described in Ref. (28), we obtain the Lagrangian in the mass basis written in Appendix B.1, see ref. (30) from the detailed derivation of the lagrangian terms.

First assumption: one Triplet Restriction: the lagrangian derived is written for a generic number of triplets. Nevertheless, in the presence of more triplets, it will be the lightest the one that will be more easily discovered. Therefore, since we are interested in LHC physics, we can safely restrict the model to the case of only one triplet.

Under this assumption, the new Yukawa couplings matrix reduces to a

1×3 vector:

$$Y_\Sigma = \begin{pmatrix} Y_{\Sigma_e} & Y_{\Sigma_\mu} & Y_{\Sigma_\tau} \end{pmatrix} , \quad (2.43)$$

and the mass matrix M_Σ is now a scalar.

Second assumption: real parameters will be taken, i.e. we do not take into account the phases of the Yukawa couplings nor the ones of the PMNS matrix. Barring cancellations, they should not play a role in the discovery process.

As a consequence ϵ is a 3×3 matrix whose elements are

$$\epsilon_{\alpha\beta} = \frac{v^2}{2} M_\Sigma^{-2} Y_{\Sigma_\alpha} Y_{\Sigma_\beta} , \quad (2.44)$$

and ϵ' is now a scalar:

$$\epsilon' = \frac{v^2}{2} M_\Sigma^{-2} \left(Y_{\Sigma_e}^2 + Y_{\Sigma_\mu}^2 + Y_{\Sigma_\tau}^2 \right) . \quad (2.45)$$

Finally, we express all the couplings in terms of the mixing parameters, $V_\alpha = \frac{v}{\sqrt{2}} M_\Sigma^{-1} Y_{\Sigma_\alpha}$, since they are the parameters which are truly constrained by the electroweak precision tests and the lepton flavor violating processes. Then $\epsilon' = V \cdot V^T$ while $\epsilon = V^T \wedge V$.

By applying these simplifications and redefinitions, the couplings of Eqs. (B.10)-(B.24) in terms of M_Σ and V_α are obtained; they are shown in Appendix B.2.

3

Experimental Apparatus

3.1 Accelerators in Particle Physics

The high energy particle accelerators are like microscopes which have allowed physicist to peer at the 'heart of matter'. A particle accelerator uses electromagnetic fields to propel charged particles to high speeds and to contain them in well-defined beams. Machines make particle beams to collide, either to fixed target or between each others. Main features about colliders are given in Section 3.1.1. A description of LHC collider is given in 3.2, and CMS experiment is presented in Section 3.3.

3.1.1 Colliders main Features

From the point of view of energetics the collider mode is superior for new particle production than the fixed target mode because the energy available is higher[1].

The higher the available energy in the center-of-mass ($\sqrt{s}$), the higher the energy of new particles produced in collisions. Therefore $\sqrt{s}$ is one of the most important aspect of the collider.

The next important aspect of the collider is the rate, and therefore the total number of collisions. Even if $\sqrt{s}$ is high, the production of new particles may never take place if

[1] High energy particle beams are used to collide in two different ways:

- Fixed Target Machines: beams are incident on a stationary target which consists of light or heavy nuclei. In this case for a beam of energy E_b incident on a target of mass M_T, total energy available for new particle production is $E_{cm} = \sqrt{M_T E_b} c$.
- Colliders: beams of accelerated particles collide against each other. In the collider environment, specializing to the case where both the beams have particles with same mass and energy, the energy available for particle production is $2E_b$.

the production cross section of the signal process is considerably small at the design $\sqrt{s}$ with low collision rate. Maximizing the number of collisions per beam fill it is necessary to take data efficiently too, as preparation of beams take time O(1 hour) and beam intensities decrease as the time goes by. The expected event rate depends on the cross section and the luminosity delivered by the accelerator:

$$\frac{N_{\text{events}}}{t} = L\sigma \tag{3.1}$$

where L is the luminosity expressed in units of inverse barn, and σ is the cross section expressed in units of barn. The number and types of possible interactions for a given combination of two partons i and j determine the partonic cross section σ_{ij}. The sum of these partonic cross sections, weighted by the probability to find each combination, is the total cross section. This probability can be described by Parton Density Functions (PDFs) which are equal to the probability to find a given parton i with momentum fraction x_i at an energy scale Q.

Particle beams in colliders could be made of protons or electrons. Hadronic and leptonic colliders have played very complementary roles in particle physics fundamental research. Their main characteristics are listed briefly below, for a complete review see (33).

- **Leptonic Colliders** (e^+e^-) are precision measurement machines, since the initial beam energy is very accurately known as the colliding particles are the same ones which are being accelerated.

- **Hadronic Colliders** (pp or $p\bar{p}$ machines) are 'discovery' machines. The colliding particles are composites and at high energies the colliding fundamental particles are partons (quarks, anti-quarks, gluons). It is known that, on the average, only 1/6 of the energy of the proton is available to the colliding partons. Thus for the same energy of the beams, $E_{cm}(e^+e^-) \sim 6E_{cm}(pp)$. Nevertheless, it is easier to accelerate the $p/\bar{p}$ to much higher energies, and the hadronic machines can provide a broad range of energies at which collisions between partons can happen, so a broad sweep of different energies processes can be analyzed.

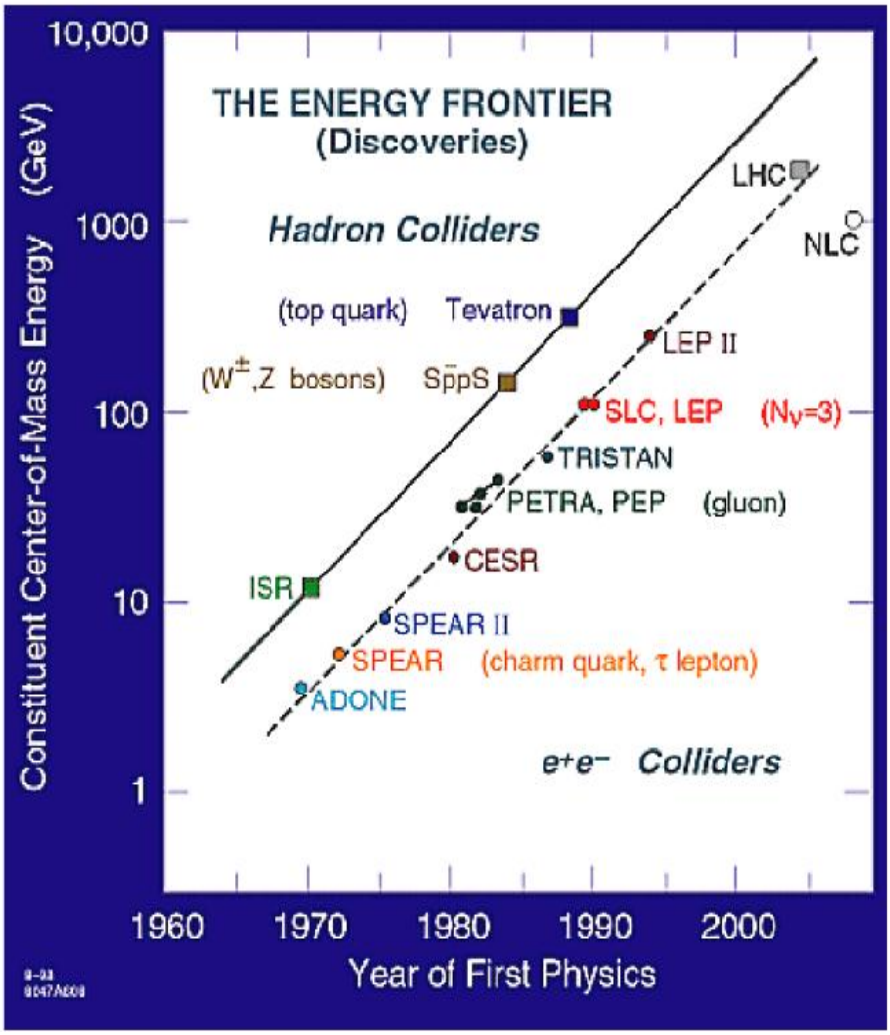

Figure 3.1: A summary of particle physics discoveries made with different machines.

3.1.2 Particle Physics Discoveries

The physics flow and the experimental evidence of the main physics discoveries made at different colliders have been summarized in Fig. 3.1 from (33). Missing from this figure is the fixed target experiment at SLAC, with electron beams of energy up to 50 GeV which made the discovery of light quarks (u,d) inside proton in 1968 and the fixed target machines which followed it at Fermilab and CERN, with μ, ν beams up to energy 800 GeV, which helped confirm the existence of the strange quark (s).

Experimental measurements from the accelerators and colliders have confirmed with a very high level of precision the Standard Model theoretical predictions. In Table 3.1 (Reference (15)), details of some of the most crucial parameters of the unified theory of electromagnetic and weak (EW) interactions is presented. The level of precision of the EW theory predictions as well as the experimental measurements and the agreement between the two is impressive. Theoretical predictions for various EW observables depend on the mass of the Higgs Boson, M_H. The Higgs is expected from the theory but it is still undiscovered. The range of M_H allowed in the SM by the experiments up to now, at 95% CL, is $115 < M_H c^2 < 150$ GeV (34). Physicist are currently analyzing LHC - the Large Hadron Collider - data for discovering Higgs signals. At the moment, the most updated combined Higgs limit, from LHC CMS and ATLAS experiments, is: $M_H c^2 < 141$ GeV.

Observable	Experimentally measured value	SM fit
Width of the Z boson: Γ_Z	2.4952 ± 0.0023 GeV	2.4959 GeV
Mass of the W boson: M_W	80.404 ± 0.030 GeV/c^2	80.376 GeV/c^2
Mass of the t quark M_t	172.5 ± 2.3 GeV/c^2	172.9 GeV/c^2

Table 3.1: Precision testing of the SM.

3.2 The Large Hadron Collider

3.2.1 Introduction

The Large Hadron Collider (LHC), located at CERN, the European Laboratory for Particle Physics, outside Geneva, Switzerland, is a unprecedented tool for fundamental physics research for many years to come. LHC provides two proton beams, circulating in opposite directions, at their design energy of 7 TeV each, corresponding to a center-of-mass energy of $\sqrt{s} = 14$ TeV, and at a design luminosity of 10^{34} cm^{-2}s^{-1}.

Among the particle accelerators LHC is going to be a watershed for the subject of fundamental particle physics. The main purpose of LHC project is to find the last missing piece of the standard model, the Higgs boson. Also, to point the way ahead and help understanding new physics beyond the Standard Model. Important LHC parameters are listed in Figure 3.2.

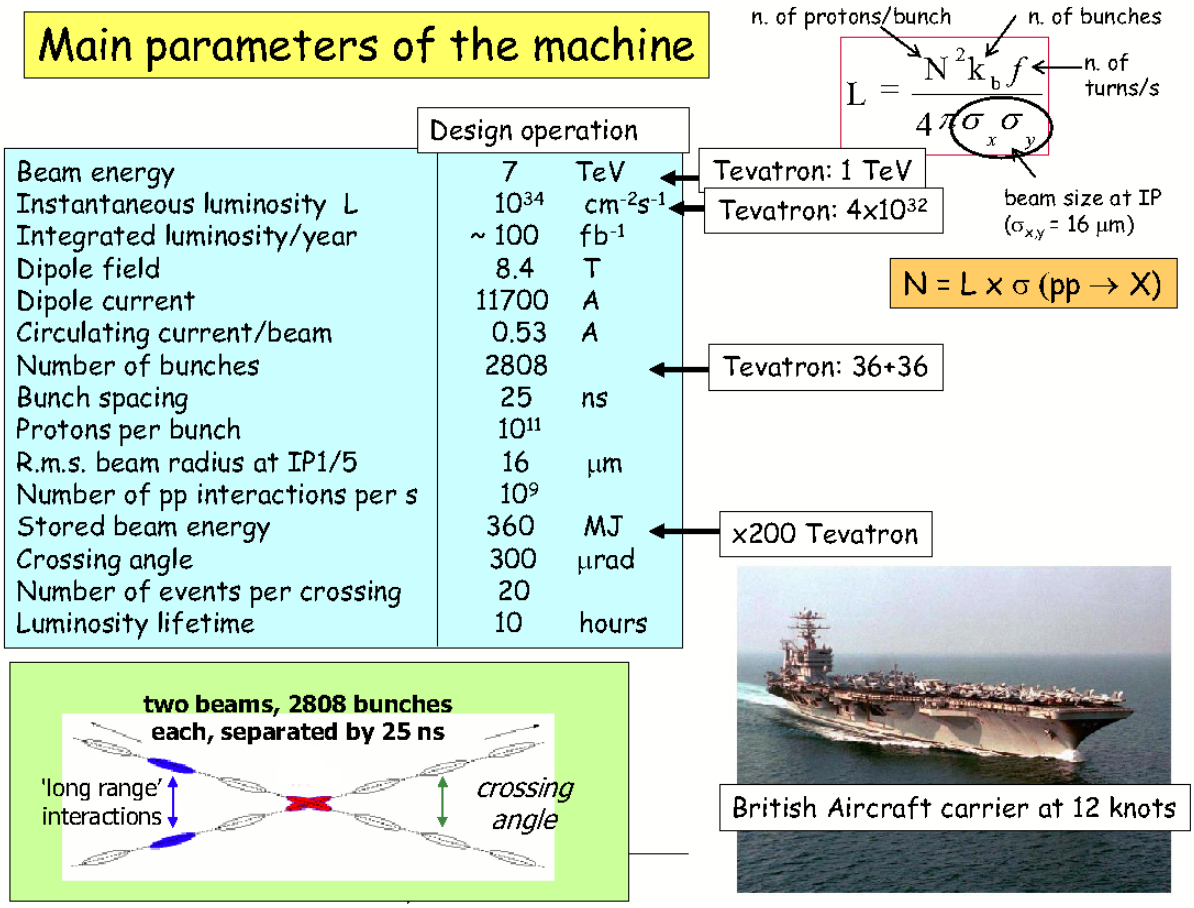

Figure 3.2: Main parameters of LHC machine.

3.2.2 Energy and Luminosity Design

The LHC collides proton on protons [1]. The theoretical knowledge about the SM, has set the bar for the new machine energy and intensity. (33). The choice of the design energy of 7 TeV each proton beam could be easily understood with the following argument. Keeping in mind the Higgs discovery benchmark, consider the scattering process in Figure 3.3 with a Higgs production. For the two W's to have a total energy of 1 TeV, each of them must have energy of 0.5 TeV and hence each of the parent quark in

[1]The physics potential of the machine would be independent of whether one has a pp machine or a $p\bar{p}$ machine. The decision to make pp machine was taken because cheaper and simpler respect to a $p\bar{p}$ machine, with the same physics potential

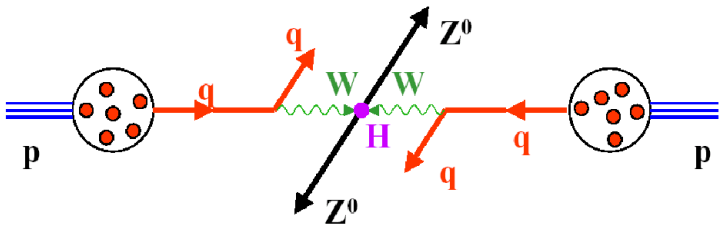

Figure 3.3: How LHC parameters were decided, from (33)

the figure must have energy of 1 TeV (as the collisions at LHC are among quarks and gluons contained in protons). The quarks carry about 1/6 the energy of the proton. This means that the protons must have an energy of 6 TeV. Hence one planned on a *pp* collision energy of 7 TeV on 7 TeV beam.

The total number of *pp* collisions were decided by using the theoretical estimate for the rate of production of the events $pp \rightarrow WW \rightarrow ZZ$ and demanding that at least 10 events per year be produced.

3.2.3 The Global Design

The LHC represents the next major step in the high-energy frontier beyond the Fermilab Tevatron, which is a proton-antiproton collider with a center-of-mass energy of ~ 2 TeV that operated for almost 30 years, until September 20^{th} 2010.

As inferred from Table 3.2, the LHC will be a Z factory, a W factory, a b quark factory, a top quark factory and furthermore a Higgs or SUSY sparticle factory if these new particles have TeV scale masses. In this table the expected rates of some of the most abundantly produced physics processes at $\sqrt{s} = 14$ TeV for an integrated luminosity of 1 fb^{-1} per experiment are listed.

The cross-sections and expected event rates for processes such as leading Standard Model (SM) processes, Higgs-boson production, supersymmetry, etc., are shown in figure 3.4 as a function of $\sqrt{s}$. A very high design luminosity is required because of the small cross-sections expected for many of the benchmark processes to be studied.

To achieve such luminosities and minimize the impact of inelastic collisions occurring simultaneously in the detectors the LHC beam crossings are 25 ns apart in time, resulting in 23 inelastic interactions on average per crossing at design luminosity.

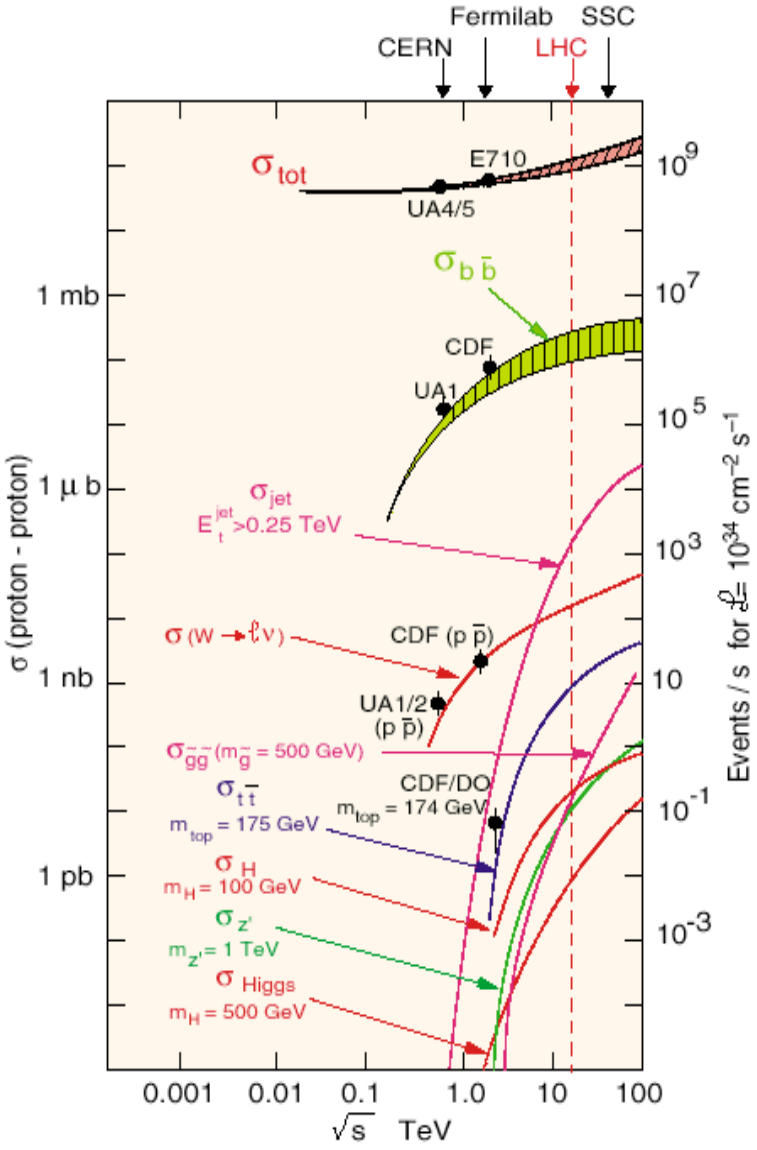

Figure 3.4: Cross sections and event rates at design LHC luminosity for hard scattering processes as a function of the center-of-mass energy $\sqrt{s}$ (32).

In order to cope with the potentially overwhelming SM processes, high rejection power is needed with optimal efficiency for rare channels such as many of the Higgs-boson decays. In the most extreme case, a selection power of $10^{-14} - 10^{-15}$ is required for Higgs-boson discovery when small signal rates are compared to the total interaction rate. This represents an increase of many orders of magnitude over the selection rates

Table 3.2: Some of the most abundantly produced physics processes at the LHC at design luminosity. Expected numbers of events recorded by ATLAS and CMS for an integrated luminosity of 1 fb^{-1} per experiment are listed. From Reference (32).

Physics processes	Number of events per fb^{-1}
QCD jets with $E_{\text{T}} > 150$ GeV	10^6 (for 10% of trigger bandwidth)
$\text{W} \to \mu\nu$	7×10^6
$\text{Z} \to \mu\mu$	1.1×10^6
$\text{t}\bar{\text{t}} \to \text{e}/\mu + X$	1.6×10^5
$\tilde{\text{g}}\tilde{\text{g}}$ production ($m_{\tilde{\text{g}}} \approx 1$ TeV)	10^2 to 10^3

achieved at the Tevatron.

The QCD jet production cross-section is overwhelmingly dominant over all electroweak processes: this means that lepton signatures are most often essential in extracting rare processes from the background at the LHC. It is for this very reason that both excellent measurements and superb identification capabilities of both electrons and muons have been among the primordial requirements of detectors. Additional signatures have also driven the global design to a large extent, e.g. missing transverse energy, $E_{\text{T}}^{\text{miss}}$, typically indicating the presence of high-p_{T} non-interacting particles such as neutrinos, or secondary vertexes, typically indicating the presence of heavy-flavor hadrons usually embedded in high-p_{T} b/c-jets. As already mentioned, excellent lepton identification should be achieved with high efficiency to extract rare signals from the huge QCD backgrounds. For instance, the electron-to-jet ratio at the LHC is $\sim 10^{-5}$ at $p_{\text{T}} \sim 20$ GeV, a factor ~ 100 times worse than at the Tevatron. The online rejection to be achieved in real time is $\sim 10^7$ and huge data volumes have to be recorded to permanent storage, typically $\sim 10^9$ events of 1 Mbyte size per year. For further details see References (32) and (33).

3.2.4 Technical details

LHC (Fig. 3.5) is located at the French-Swiss border west of Lac Leman and in the former LEP tunnel. The tunnel has a circumstance of 27 km and lies between 45 and 170 m below the surface. The energetic beams circulate in vacuum pipes there and are kept on track by a magnetic field provided by dipole magnets. Superconducting Radio

Frequency (RF, usually referred as resonator) cavities are used to accelerate beams to the desired energy. The LHC is capable of operating with either proton or heavy ion beams. At design conditions, it will run at a luminosity of $10^{34} cm^2 s^{-1}$ for pp beams at $\sqrt{s} = 14TeV$, supplying the high luminosity experiments CMS and ATLAS with collisions every 25 ns corresponding to the nominal bunch spacing. During 2010 and 2011 runs, the center-of-mass energy was set to 7 TeV and the highest instantaneous luminosity achieved was about $2 \cdot 10^{32} cm^2 s^1$ in 2010 and $3.55 \cdot 10^{33} cm^2 s^1$. In order to reach the design luminosity 2808 proton bunches are filled in the LHC, separated by 25 ns. These luminosities are high enough to provide a sufficient rate of hard interactions in which the physics processes interesting for most of experiments take place. At the same time the probability for soft interactions is orders of magnitude higher than for hard interactions, thus around 20 significant soft interactions are expected per bunch crossing. As these soft interactions are considered unwanted background by the experiments, the detectors must be able to separate these pile-up events from hard interactions. The number of protons per bunch is limited by the non-linear beam-beam interactions that each proton experiences each bunch crossing. In combination with the constraints from the mechanical aperture the nominal peak beam size is 1.2mm the maximum bunch intensity is thus $N_B = 1.15 \times 10^{11}$. At a pp collider both beams need different magnetic field polarities in the dipoles. Thus the beams run in separated vacuum pipes with separated dipole fields. 1232 dipoles are used to hold beams on track. Only in the $\approx$ 130m long sections at the interaction regions do both beams share one beam pipe. Sustained fields of this strength can only be generated by superconducting magnets, and thus all dipoles are cooled down to 1.9K using superfluid helium. Using state-of-the-art technologies a maximum magnetic field strength of 8.4 Tesla is obtained, providing the possibility of operating with 7 TeV beams.

3.2.5 LHC Operation History

A brief review of LHC operatin history was presented in (31). A brief summary follows. After the formal construction approval of the Large Hadron Collider (LHC) by the CERN Council on December 16 (1994) it took more than 13 years to build the LHC and the four large experiments ALICE, ATLAS, CMS, LHCb as well as the smaller experiments LHCf and TOTEM.

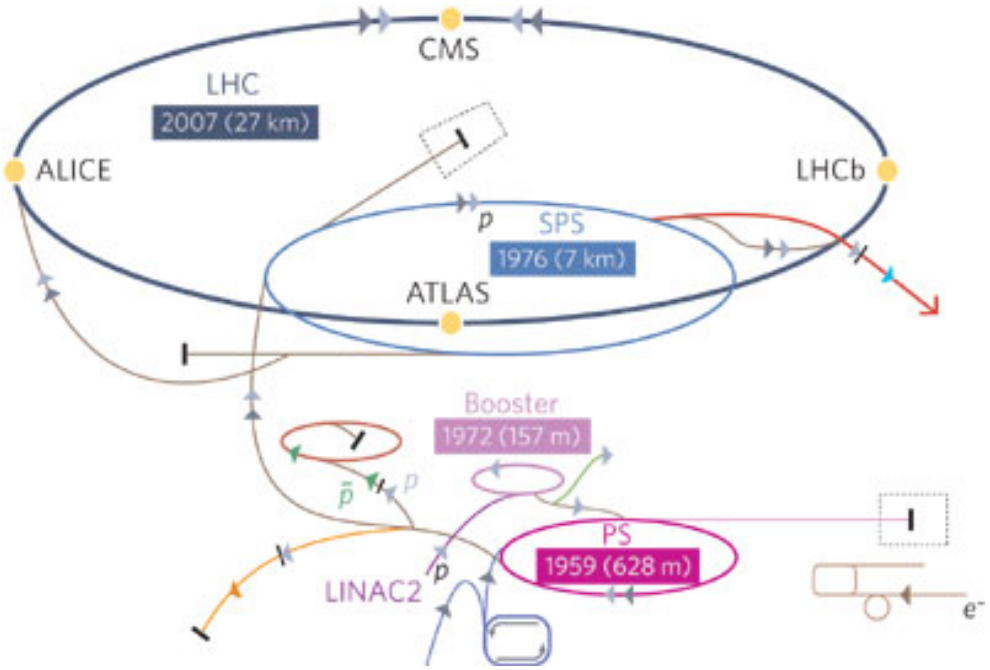

Figure 3.5: The LHC. The injector chain and the CMS experiment are shown with other experiments.

3.5

The injection of the first proton beams into the LHC was scheduled on September 10, 2008. The LHC staff managed to inject and circulate single proton beams in both directions within a few hours. A few days later, on September 19, in an attempt to test super conducting LHC magnets at high currents, a quench occurred in sector 3-4, most likely due to a faulty electrical contact between two magnets. As a consequence, an electrical arc developed and punctured the helium enclosure, leading to release of helium into the insulation vacuum of the cryostat causing substantial damage to the magnets and to the beam pipe.

A subsequent investigation of the possible cause of this accident identified several critical areas, which needed repair and improvements before another attempt for proton-proton collisions could be started. The CERN management decided to replace some of the magnets and to repair only the electrical contacts with the highest resistivity (leaving the others for the first technical stop in 2012), and to operate the LHC for two years at a reduced beam energy of 3.5 TeV for the first two years.

On November 20, 2009, a new attempt to inject proton beams started. Single beams circulated in both directions within a few hours and the first collisions at injection energy (450 GeV) were recorded by the LHC experiments already after four days. Before the Christmas break, collision data sets were recorded at center-of-mass (cms) energies of 900 GeV and 2.36 TeV. The main data taking period in 2010 started with the first collisions at a c.m.-energy of 7 TeV on March 30. The aim of the machine operators in 2010 was to increase the number of protons per bunch, and successively throughout the year the number of bunches and the total stored energy. Each increase of the stored energy was taken with great care to protect the experiments and machine components from beam loss. The specific luminosity increased from $10^{28} cm^{-2} s^{-1}$ in April to $2 \times 10^{32} cm^{-2} s^{-1}$ at the end of the proton run on November 4, exceeding the goal by a factor of two. The experiments recorded data during all 2011, with a total integrated luminosity of about $5 fb^{1}$ up to now. These data, collected till November 2011 have been used for the analysis presented in this thesis.

3.3 The Compact Muon Solenoid Detector

The Compact Muon Solenoid (CMS) Experiment is a general purpose particle detector experiment located at the LHC. The detector goal is to explore physics at an unprecedented physics energy scale. As already mentioned, it is expected that the data produced at the LHC will elucidate the electroweak symmetry breaking mechanism (EWSB) and provide evidence of physics beyond the standard model. CMS will also be an instrument to perform precision measurements of parameters of the Standard Model.

3.3.1 Physics Benchmarks

Detector requirements result from specific physics benchmarks. We will list the most important in this section.

Search for the Higgs Boson. In the design phase of CMS the detection of the SM Higgs boson was an important benchmark. The signatures and the detector requirements depend on the hypothesized range of the mass of the Higgs boson, as described in the following paragraph.

- In the vicinity of 114.4 GeV/c^2 limit (the current lower limit on the mass of the Higgs boson from LEP), the branching fractions of the Higgs boson are dominated by hadronic decays, which are difficult to use to discover the Higgs boson at the LHC due to the large QCD backgrounds and the relatively poor mass resolution that is obtainable with jets. Hence, the search is preferentially conducted using final states that contain isolated leptons and photons, despite the smaller branching ratios.

- In the mass interval 114-130 GeV/c^2, the two-photon decay is one of the principal channels likely to yield a significant signal.

- The Higgs boson should be detectable via its decay into 2 Z bosons if its mass is larger than about 130 GeV/c^2.

- For $2m_Z < m_H < 600$ GeV/c^2 the ZZ decay, with its four-lepton final states, is the mode of choice.

- In the region $600 < m_H < 1000$ GeV/c^2, the cross section decreases so that higher branching fraction modes involving jets or $E_{\mathrm{T}}^{\mathrm{miss}}$ from W or Z decays have to be used.

- The dominant Higgs-boson production mechanism, for masses up to about 700 GeV/c^2, is gluon-gluon fusion via a t-quark loop.

- The WW or ZZ fusion mechanism becomes important for the production of higher-mass Higgs bosons.

Search for Supersymmetric Particles. The decays of supersymmetric particles, such as squarks and gluinos, involve cascades that, if R-parity is conserved, always contain the lightest SUSY particle (LSP). The latter is expected to interact very weakly, thus leading to significant $E_{\mathrm{T}}^{\mathrm{miss}}$ in the final state. The rest of the cascade results in an abundance of leptons and jets. In GMSB schemes with the LSP decaying into a photon and gravitino, an increased number of hard isolated photons is expected.

Search for new massive Vector Bosons. The detector requirements for high momenta can be determined by considering decays of high-mass objects such as $Z' \rightarrow e^+e^-$ and $\mu^+\mu$. Ways of distinguishing between different models involve the measurement of the natural width and the forward-backward asymmetry, both of which require sufficiently good momentum resolution at high p_T to determine the sign of the leptons and a pseudorapidity coverage up to $\eta = 2.4$.

Extra dimensions. The existence of extra dimensions can lead to a characteristic energy scale of quantum gravity, MD, which is the analogue of the Planck mass in a D-dimensional theory, and which could lie just beyond the electroweak scale.

Standard Model. The LHC will also allow studies of QCD, electroweak, and flavor physics. Precision studies can give indications for physics beyond the SM, providing complementary information with respect to direct searches. As an example, extensive tests of QCD will be possible through the measurement of the production of jets and direct photons with transverse energies up to 3-4 TeV and from cross-section measurements which fall by 11 orders of magnitude. Top quarks will be produced at the LHC with a rate measured in Hz, thus the opportunity to test the SM couplings and spin of the top quark is available provided good identification of b-jets in the decays is possible. Searches for flavor changing neutral currents, lepton flavor violation, measurements of B_s^0 decays, measurements of triple and quartic gauge couplings, etc. can open a window onto new physics. Finally, in association with TOTEM, CMS will be able to cover the full range of diffractive physics as well.

Heavy-ion physics. The recent results from RHIC indicate that very strongly interacting nuclear matter is produced in high energy heavy-ion collisions. The most striking experimental signatures of the produced matter are the suppression of high p_T particles (jet quenching) and the strong elliptical flow approaching the hydrodynamic limit. The increase in collision energy at LHC will allow the extension of studies of jet quenching to much higher p_T and the identification of fully formed jets. The measurements of energy flow at LHC will stringently test the liquid-like behavior of the hot nuclear matter. The studies of jet quenching, energy flow, and quarkonium production

will require large-acceptance, high-resolution calorimeters and tracking devices, as well as a flexible trigger.

3.3.2 Detector Requirements

The design of CMS meets the requirements to achieve the goals of the LHC physics program. These requirements can be summarized as follows:

- Good radiation-hard detectors and front-end electronics, to be able to stand the high radiation levels due to the large flux of particles coming from the interaction region.

- High granularity detectors with good time resolution (and thus low occupancy): large number of detector channels with very good synchronization. This requirement is necessary to reduce the effect of pile-up. At the design luminosity, a mean of about 20 inelastic (hard-core scattering) collisions will be superimposed on the event of interest, and so ≈ 1000 charged particles will emerge from the interaction region every 25 ns, and may be confused with the products of an interaction under study in the same bunch crossing.

- High efficiency trigger system. Since the total proton-proton cross-section at $\sqrt{s} = 14$ TeV is roughly 100 mb, the online event selection process must reduce the approximately 10^9 inelastic events/s to no more than about 100 events/s for storage and subsequent analysis.

- Good muon identification and momentum resolution over a wide range of momenta in the region $|\eta| < 2.5$, good dimuon mass resolution (1% at 100 GeV/c^2), and the ability to determine unambiguously the charge of muons with $p_T <$ 1TeV/c.

- Good charged particle momentum resolution and reconstruction efficiency in the inner tracker. Efficient triggering and offline tagging of τs and b-jets, requiring pixel detectors close to the interaction region.

- Good electromagnetic energy resolution, good diphoton and dielectron mass resolution (1% at 100 GeV/c^2), wide geometric coverage ($|\eta| < 2.5$), measurement

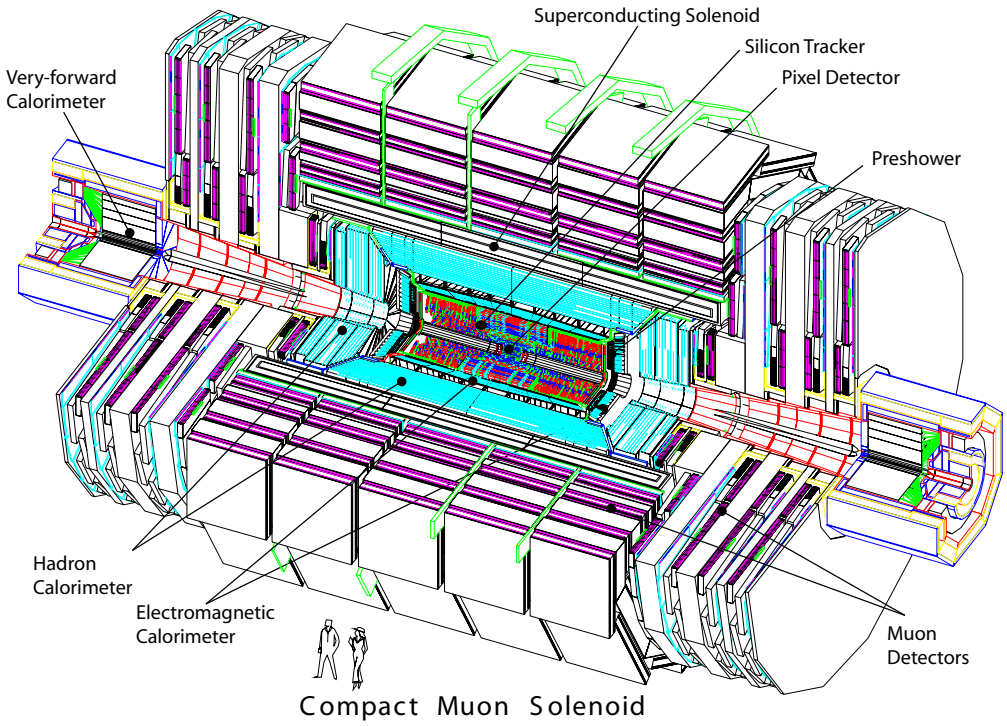

Figure 3.6: Sketch of the Compact Muon Solenoid detector.

of the direction of photons and/or correct localization of the primary interaction vertex, π_0 rejection and efficient photon and lepton isolation at high luminosities.

- Good $E_{\mathrm{T}}^{\mathrm{miss}}$and dijet mass resolution, requiring hadron calorimeters with a large hermetic geometric coverage ($|\eta| < 5$) and with fine lateral segmentation.

3.3.3 CMS Layout

Figure 3.6 shows the overall layout of the CMS Detector. The overall dimensions of the CMS detector are a length of 21.6 m, a diameter of 14.6 m and a total weight of 12500 tons. The thickness of the detector in radiation lengths is greater than $25 \cdot X_0$ for the ECAL, and the thickness in interaction lengths varies from 7-11 λI for HCAL depending on $|\eta|$.

A modular detector design was chosen to allow for construction, installation, and

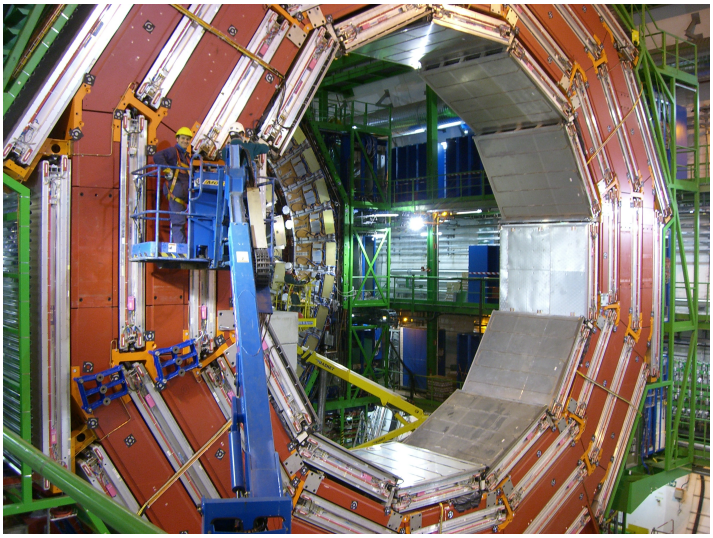

Figure 3.7: The CMS detector during installation of the muon wheels.

testing before lowering underground. Figure 3.7 shows a photo of the CMS detector during installation of the muons detector. The construction phase of the CMS detector is now complete, and the detector has been fully installed and commissioned in the underground cavern at LHC Point 5. Since May 2007, CMS has undergone frequent "global runs" devoted to global commissioning, exercising all of the installed detector subsystems together. In addition, to test the global readout, global runs have also helped exercise event selection and reconstruction, data analysis, alignment and calibration, data quality monitoring, computing operations and data transfer. The global runs culminated in data taking for over a week with first LHC beam in September 2008, and a two week Cosmic Run at Full Tesla (CRAFT) in October-November 2008. See Reference (35) for details about first run performances. From September 2009 to November 2011 CMS has taken data from LHC collisions. See Section 3.2.5 for a brief LHC run-history.

CMS structure and subdetectors are graphically sketched in Figure 3.8. A brief description will be given in the next sections. Main material is taken from CMS TDRs (36), where many other details could be found.

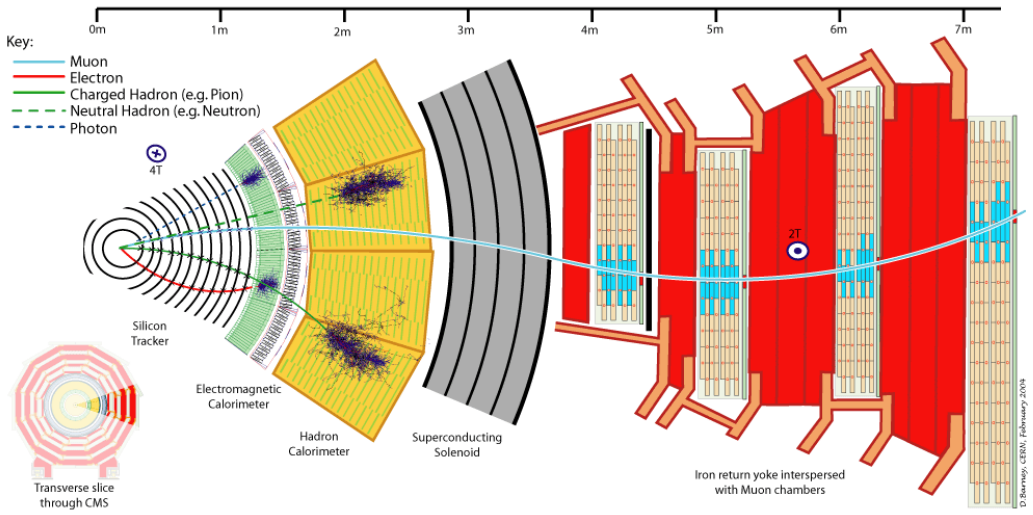

Figure 3.8: Layout of the longitudinal view of CMS experiment.

Magnet. The 4 T iron-core superconducting solenoid is 13-m-long, with a 5.9 m inner diameter. In order to achieve good momentum resolution within a compact spectrometer without making stringent demands on muon-chamber resolution and alignment, a high magnetic field was chosen, as the bending starts at the primary vertex. The return field is large enough to saturate 1.5 m of iron.

Muon system. The iron yoke of the magnet system is instrumented with a muon spectrometer, composed of three types of gaseous detectors used to identify and measure muons: drift tubes (DT) in the central region and cathode strip chambers (CSC) in the endcaps, both complemented by resistive plate chambers (RPC). The choice of the detector technologies has been driven by the very large surface to be covered and by the different radiation environments. In the barrel region ($|\eta| < 1.2$), where the neutron induced background is small, the muon rate is low and the residual magnetic field in the chambers is low, drift tube (DT) chambers are used. In the 2 endcaps, where the muon rate as well as the neutron induced background rate is high, and the magnetic field is also high, cathode strip chambers (CSC) are deployed and cover the region up to $|\eta| < 2.4$. In addition to this, resistive plate chambers (RPC) are used in both the barrel and the endcap regions. These RPCs are operated in avalanche mode to ensure

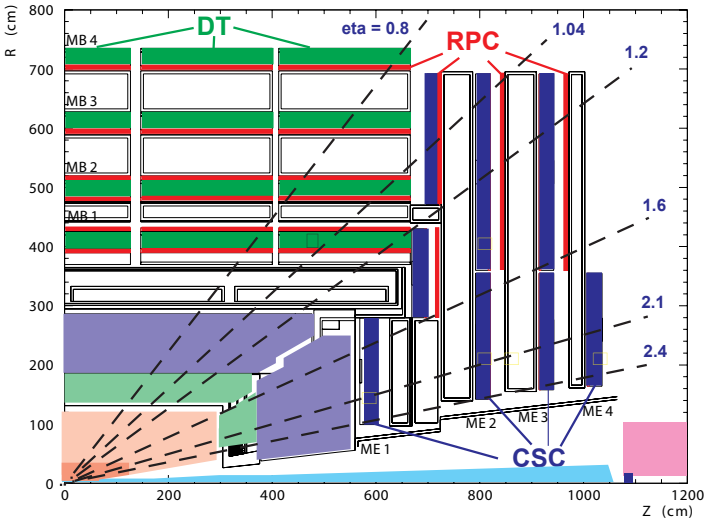

Figure 3.9: Layout of one quarter of the CMS muon system for initial low luminosity running. The RPC system is limited to $|\eta| < 1.6$ in the endcap, and for the CSC system only the inner ring of the ME4 chambers have been deployed.

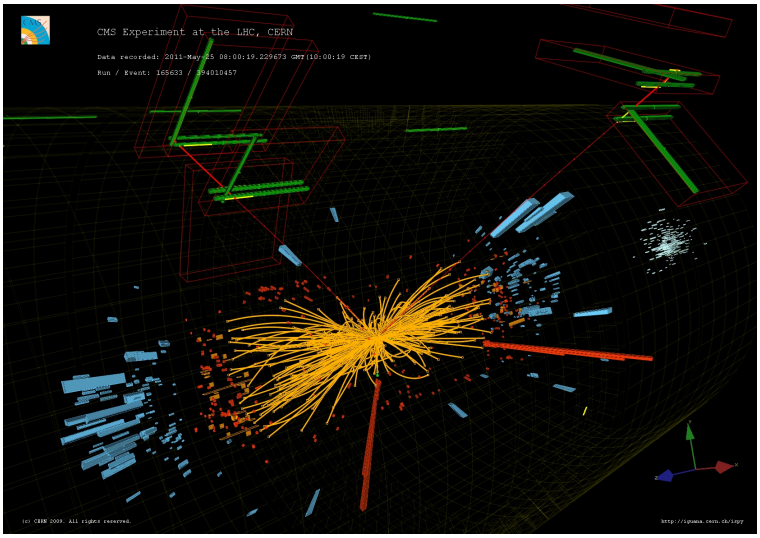

Figure 3.10: Event display of a candidate ZZ event, in which one Z decays to two electrons (red towers) the other to two muons (red lines).

good operation at high rates (up to 10 kHz/cm^2) and have double gaps with a gas gap of $2mm$. RPCs provide a fast response with good time resolution but with a coarser

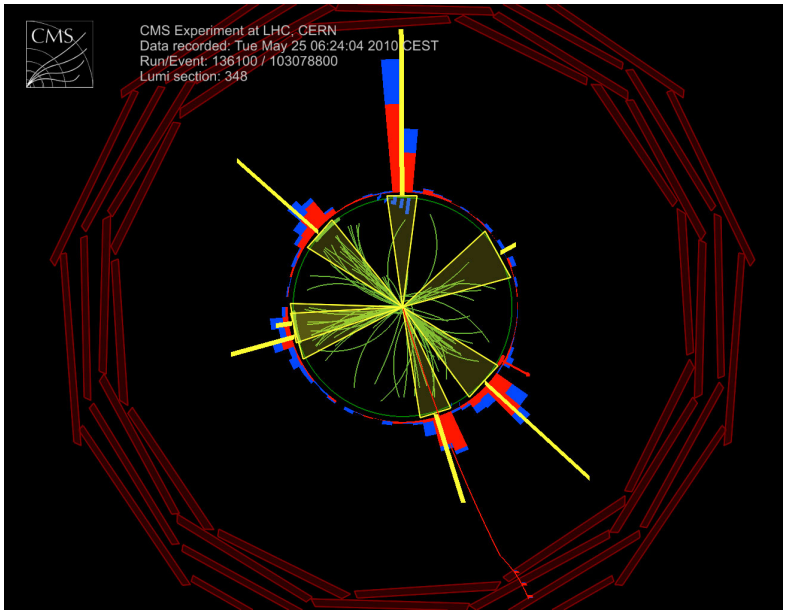

Figure 3.11: CMS collision events: multi-jet event at 7 TeV.

position resolution than the DTs or CSCs. RPCs can therefore identify unambiguously the correct bunch crossing. The DTs or CSCs and the RPCs operate within the first level trigger system, providing 2 independent and complementary sources of information. The complete system results in a robust, precise and flexible trigger device. The layout of one quarter of the CMS muon system is shown in Figure 3.9.

In the Muon Barrel (MB) region, 4 stations of detectors are arranged in cylinders interleaved with the iron yoke. The segmentation along the beam direction follows the 5 wheels of the yoke (labeled YB2 for the farthest wheel in z, and YB+2 for the farthest is +z). In each of the endcaps, the CSCs and RPCs are arranged in 4 disks perpendicular to the beam, and in concentric rings, 3 rings in the innermost station, and 2 in the others. In total, the muon system contains of order 25000 m^2 of active detection planes, and nearly 1 million electronic channels.

The required performance of the muon system, and hence the bending power, is defined by the narrow states decaying into muons and by the unambiguous determination of the sign for muons with a momentum of ≈ 1 TeV/c. This requires a momentum resolution of $\Delta p/p \approx 10\%$ at $p = 1$ TeV/c.

Picture 3.10 shows a real CMS collision event detected in calorimeters and muon chambers.

Electromagnetic calorimeter. Calorimetry is performed by a high-resolution, high-granularity electromagnetic calorimeter (ECAL), comprised of more than 70k lead-tungstate crystals, and a brass-scintillator hadronic calorimeter (HCAL). The EM calorimeter (ECAL) uses lead tungstate (PbWO4) crystals with coverage in pseudo-rapidity up to $|\eta| < 3.0$. 61200 lead tungstate (PbWO4) crystals are mounted in the central barrel part, closed by 7324 crystals in each of the 2 endcaps. The use of PbWO4 crystals has thus allowed the design of a compact calorimeter inside the solenoid that is fast, has fine granularity, and is radiation resistant. These crystals have short radiation ($X_0 = 0.89$ cm) and Moliere (2.2 cm) lengths, are fast (80% of the light is emitted within 25 ns) and radiation hard (up to 10 Mrad). However, the relatively low light yield (30γ/MeV) requires use of photodetectors with intrinsic gain that can operate in a magnetic field. Silicon avalanche photodiodes (APDs) are used as photodetectors in the barrel and vacuum phototriodes (VPTs) in the endcaps. In addition, the sensitivity of both the crystals and the APD response to temperature changes requires a temperature stability (the goal is 0.1^0C). A preshower system is installed in front of the endcap ECAL for π_0 rejection.

Picture 3.10 shows a real CMS collision event detected in calorimeters and muon chambers.

Hadron calorimeter. The ECAL is surrounded by a brass/scintillator sampling hadron calorimeter with coverage up to $|\eta| < 3.0$. The design of the hadron calorimeter (HCAL) is strongly influenced by the choice of magnet parameters since most of the CMS calorimetry is located inside the magnet coil and surrounds the ECAL system. An important requirement of HCAL is to minimize the non-Gaussian tails in the energy resolution and to provide good containment and hermeticity for the $E_{\mathrm{T}}^{\mathrm{miss}}$ measurement. Hence, the HCAL design maximizes material inside the magnet coil in terms of interaction lengths. This is complemented by an additional layer of scintillators, referred to as the hadron outer (HO) detector, lining the outside of the coil. Brass has been chosen as absorber material as it has a reasonably short interaction length, is easy

to machine and is non-magnetic. Maximizing the amount of absorber before the magnet requires keeping to a minimum the amount of space devoted to the active medium. The tile/fiber technology makes for an ideal choice. It consists of plastic scintillator tiles read out with embedded wavelength-shifting (WLS) fibers. The photodetection readout is based on multi-channel hybrid photodiodes (HPDs). The overall assembly enables the HCAL to be built with essentially no uninstrumented cracks or dead areas in ϕ. The gap between the barrel and the endcap HCAL, through which the services of the ECAL and the inner tracker pass, is inclined at 53^0 and points away from the center of the detector. Just outside the solenoid is a scintillator-based tail-catching hadronic outer calorimeter (HO). In addition, a steel and quartz fiber forward hadronic calorimeter system (HF) is placed on both sides of the detector endcaps to ensure hermiticity. See Picture 3.11 for a real CMS collision multi-jet event.

Inner tracking system The bore of the magnet coil is large enough to accommodate the inner tracker and the calorimetry inside. The tracking volume is given by a cylinder of length 5.8 m and diameter 2.6 m. By considering the charged particle flux at various radii at high luminosity 3 regions can be delineated:

- Closest to the interaction vertex where the particle flux is the highest ($\approx 10^7$/s at r $\approx$ 10 cm), pixel detectors are placed. The size of a pixel is $\approx 100 \times 150\mu$ m^2, giving an occupancy of about 10^4 per pixel per LHC crossing. Pixel detectors are placed close to the interaction region to improve the measurement of the impact parameter of charged-particle tracks, as well as the position of secondary vertexes.

- In the intermediate region (20 $<$ r $<$ 55 cm), the particle flux is low enough to enable use of silicon microstrip detectors with a minimum cell size of 10 cm $\times 80\mu$m, leading to an occupancy of $\approx$ 2-3%/LHC crossing. Overall the silicon tracker consist of 66M pixel.

- In the outermost region (r $>$ 55 cm) of the inner tracker, the particle flux has dropped sufficiently to allow use of larger-pitch silicon microstrips with a maximum cell size of 25 cm $\times 180\mu$m, whilst keeping the occupancy to $\approx$ 1%. There are 10M strip detectors.

Even in heavy-ion (Pb-Pb) running, the occupancy is expected to be at the level of 1% in the pixel detectors and less than 20% in the outer silicon strip detectors, permitting track reconstruction in the high density environment. The outer radius of the CMS tracker extends to nearly 110 cm, and its total length is approximately 540 cm.

Trigger and data acquisition The LHC bunch crossing rate of 40 MHz leads to $\approx 10^9$ interactions/sec at design luminosity. Data from only about 10^2 crossings/sec can be written to archival media; hence, the trigger system has to achieve a rejection factor of nearly 10^6. The CMS trigger and data acquisition system consists of 4 parts:

- The detector electronics.
- The Level-1 trigger processors (calorimeter, muon, and global). Custom hardware processors form the Level-1 decision. The Level-1 triggers involve the calorimetry and muon systems, as well as some correlation of information between these systems. The Level-1 decision is based on the presence of trigger primitive objects such as photons, electrons, muons, and jets above set E_T or p_T thresholds. It also employs global sums of E_T and $E_{\mathrm{T}}^{\mathrm{miss}}$. The total time allocated for the transit and for reaching a decision to keep or discard data from a particular beam crossing is 3.2μs. During this time, the detector data must be held in buffers while trigger data is collected from the front-end electronics and decisions reached that discard a large fraction of events while retaining the small fraction of interactions of interest (nearly 1 crossing in 1000). Of the total latency, the time allocated to Level-1 trigger calculations is less than 1μ s. The Level-1 rate is estimated 16 kHz. The design value of 100 kHz is set by the average time to transfer full detector information through the readout system.
- The readout network.
- The online event filter system (processor farm) that executes the software for the High-Level Triggers (HLT). Upon receipt of a Level-1 trigger the data from the pipelines are transferred to front-end readout buffers, and placed in dual-port memories for access by the DAQ system. Through the event building switch, data from a given event are transferred to a processor. Each processor runs the

same high-level trigger (HLT) software code to reduce the Level-1 output rate of 100 kHz to 100 Hz for mass storage. Various strategies guide the development of the HLT code: whenever possible only those objects and regions of the detector that are actually needed are reconstructed. Moreover, events are to be discarded as soon as possible.

4

Seesaw @ LHC

4.1 Introduction

Even with the first year of data-taking at LHC (few fb^{-1} of luminosity of collected data), a remarkable opportunity to explore physics beyond the electroweak scale is offered. In particular, physics at higher scales can be explored in the lepton sector, where the only evidence of physics beyond the Standard Model (SM) has been found up to now, namely massive neutrinos (see Section 2.2.1.1). Many theories have been proposed to enlarge the SM incorporating tiny neutrino masses, as required by experimental data (4).

Among them, seesaw models explain their smallness by introducing extra matter at a high scale, as pointed out in section 2.3. LHC gives a unique chance to uncover the mechanism of neutrino mass generation if these heavy states are directly observed, cfr. Reference (24). In the seesaw models, the introduction of five-dimensional operator allowed by gauge symmetry yields light Majorana masses for the neutrinos after spontaneous symmetry breaking. Moreover, the three types of seesaw mechanism generate additional lepton number conserving (LNC) dimension six operators, which are different in each seesaw scenario (Ref. (23), (70)). Therefore, seesaw models may in principle be probed and discriminated with LHC precise low-energy measurements sensitive to these dimension six operators. The seesaw typeI production is drastically suppressed if the Yukawa couplings are small; on the other hand the seesaws of type II and III can be produced via gauge interactions and can be observed at the LHC if their mass is sufficiently small, independently of the size of the Yukawa couplings or mixing angles.

Previous studies have been performed on the possibility of discovering seesaw signals at LHC. In particular, in the literature papers (24, 29, 68) discussing the possibility of

discovering the type III seesaw at the LHC at 14 TeV are present. According to (28) for scalar triplets of 100 GeV mass, 5σ discovery would be possible with only 3.6 fb^{-1} of luminosity for normal neutrino mass hierarchy and 0.9 fb^{-1} for inverted hierarchy. For fermionic triplets the luminosity needed is 2.5 fb^{-1}, while for heavy neutrino singlets it is much larger, around 180 fb^{-1}. A clean model discrimination would be possible within the first LHC year with 10 fb^{-1}.

The purpose of this thesis is to investigate the LHC potential to discover heavy fermion triplet predicted by the seesaw type III simplified model, and to analyze 2011 LHC data to find hints of seesaw signal or put a limit on the production cross section [1].

In this Chapter the Seesaw type III signal characteristics at LHC are investigated. The Seesaw type III simplified model presented in Chapter 2, was implemented and published in Reference (30). In collaboration with the authors, and cross-checking results with them, we have computed the Seesaw triplet production and final state cross-sections. Many validations and cross checks have been performed, we will present the relevant results in this Chapter. Results about production cross section are presented in Section 4.3. Decays are described in Section 4.4. Mixing angles values and bounds issues are discussed in Section 4.5. Intermediate and final state cross sections of the relevant channels at the LHC running at 7 TeV center-of-mass collision energy results are presented in Section 4.7. Details about the signal simulation will be described in Chapter 5.

The main conclusion of this preliminary signal analysis is that several events are expected for a luminosity of few fb^{-1} in many final states; therefore a discovery is already possible if the mass of the triplet is low enough and the background rejection is good. Otherwise, in case of non-discovery, an upgrade of the bounds on the triplet mass can be set.

[1] The Lagrangian we are considering is a phenomenological one. On the other hand, the parameters are build in a realistic model in which heavy Majorana neutrinos appear with non-negligible mixings

4.2 Σ Production

At the LHC Seesaw triplets are mainly produced in pair. The production of $\Sigma^{\pm}\Sigma^{0}$ and $\Sigma^{+}\Sigma^{-}$ is given by the process:

$$\begin{aligned} q\bar{q} &\rightarrow Z^{*} \,/\, \gamma^{*} \rightarrow \Sigma^{+}\Sigma^{-} \\ q\bar{q}' &\rightarrow W^{*} \rightarrow \Sigma^{\pm}\Sigma^{0}. \end{aligned} \tag{4.1}$$

The neutral lepton pairs are not produced because Σ^{0} has quantum numbers $T_3 = 0$, $Y = 0$ and thus they do not couple to the Z boson.

Some kinematics distribution of Σ, produced at 7 TeV pp collision energy, are given in Figure 4.1.

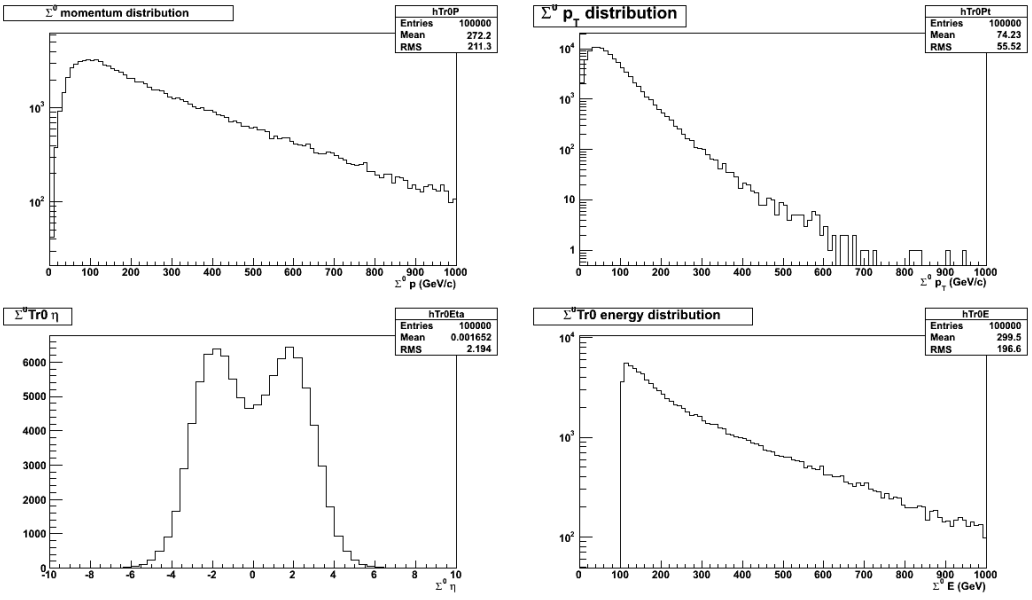

Figure 4.1: Σ^{0} kinematics distributions at 7 TeV

4.3 Production Cross Section

The production cross section only depends on the $\Sigma^{\pm}$, Σ^{0} masses, i.e. do not depend on the mixing parameters, since the triplet are produced via gauge interactions (i.e. fixed by the gauge symmetry).

Σ Mass. Since our main interest is focused in early discoveries, we have concentrated our study on seesaw messengers with masses close to the electroweak scale, since this is the condition for quick discovery at LHC. To be as optimistic as possible in order to have the highest possible cross sections, we decided to take the first mass point of the neutral component of the triplet at the lower bound $M_{\Sigma^0} = 100.8GeV$ (from Reference (15)) and the mass of the charged one $M_{\Sigma^\pm} = 101GeV$. See ref.(29) for details on this mass splitting.

It is possible that having such a small mass for the triplet enhances the cross sections but reduces the efficiency of the cuts, since the produced particle would be softer and much difficult to detect, making more difficult the discovery. Therefore for further analysis we have considered four other mass-points, namely: 120, 130, 140 and 180 GeV, as will be explained in Chapter 9

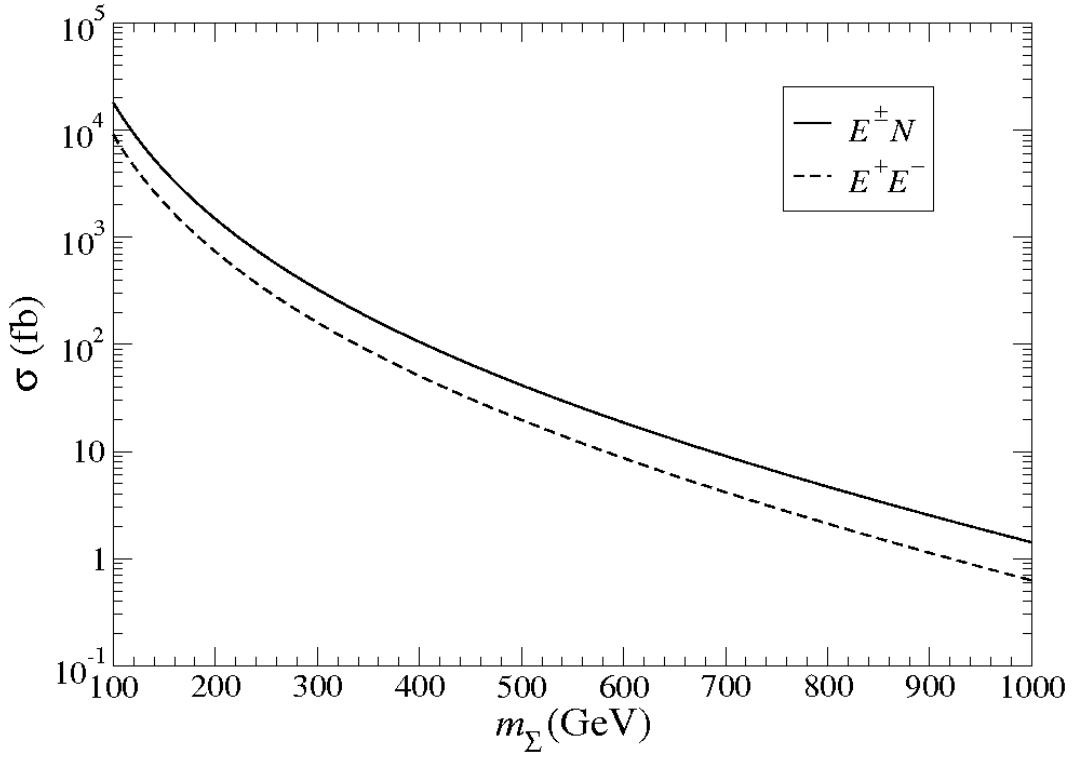

Figure 4.2: Cross section for production of heavy lepton pairs $\Sigma^\pm\Sigma^0$, $\Sigma^+\Sigma^-$ at LHC at 14 TeV Reference (24).

The production cross section of heavy lepton pairs at 14 TeV. It was estimated in previous studies, and have been published in Reference (24), from which Fig. 4.2 is taken. The expected cross sections for production of heavy lepton pairs of mass 100 GeV, are approximately: $\sigma_{\Sigma^{\pm}\Sigma^0} = 2 \cdot 10^4$ fb and $\sigma_{\Sigma^+\Sigma^-} = 10^4$ fb.

In order to test our implementation of the model, we decided to generate signals for a center of mass energy of 14 TeV, to be able to compare the values with previous studies. We have computed the production cross section at 14 TeV for two values of triplet mass, and we have compared our output with the one reported in Reference (24) The values we obtained are the following (cfr. Figure 4.3)

$$\begin{aligned}
m_{\Sigma^0} = 100.8: \quad & pp \to \Sigma^+\Sigma^0 \quad 11.18\text{pb} \\
& pp \to \Sigma^+\Sigma^- \quad 9.19\text{pb} \\
& pp \to \Sigma^-\Sigma^0 \quad 6.95\text{pb} \\
m_{\Sigma^0} = 400: \quad & pp \to \Sigma^+\Sigma^0 \quad 70.5\text{fb} \\
& pp \to \Sigma^+\Sigma^- \quad 49.5\text{fb} \\
& pp \to \Sigma^-\Sigma^0 \quad 30.8\text{fb}
\end{aligned}$$

which agree with the values from Fig. 4.2 if $\Sigma^+\Sigma^0$ and $\Sigma^-\Sigma^0$ cross sections are summed.

The production cross section at 7 TeV. As mentioned before, LHC data we analyze in the thesis were produced with a center-of-mass energy of collisions of 7 TeV. Therefore, we started the generation of Seesaw signals at this collider energy. The results are collected in Table 4.1, were production cross section is listed for different Σ masses. A first important observation from the results shown in the Table, is that the cross sections of $\Sigma^+\Sigma^0$ production have higher values. Therefore, we will concentrate the analysis on this Seesaw production.

4.4 Triplet Decays

To study the feasibility of discover the signal in LHC 2011 data, the decays of Seesaw fermions inside the detector must be studied.

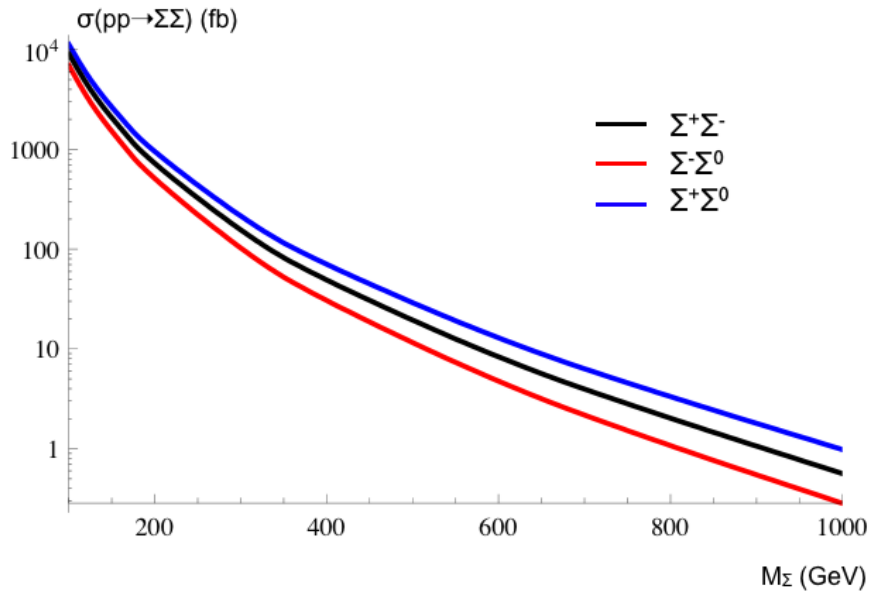

Figure 4.3: Production of a pair of triplets at 14 TeV at the LHC. The mixing parameters as been set to $V_\mu = 0.063$ and $V_e = V_\tau = 0$.

M_Σ	$\sigma(pp \to \Sigma^+\Sigma^0)(fb)$	$\sigma(pp \to \Sigma^+\Sigma^-)(fb)$	$\sigma(pp \to \Sigma^-\Sigma^0)(fb)$
100	4.329×10^3	3.339×10^3	2.325×10^3
120	2.157×10^3	1.629×10^3	1.106×10^3
140	1.200×10^3	8.882×10^2	5.894×10^2
160	7.215×10^2	5.229e+3	3.387×10^2
180	4.555×10^2	3.249×10^2	2.059×10^2
200	3.006×10^2	2.109×10^2	1.311×10^2
300	5.488×10^1	3.580×10^1	2.027×10^1
400	1.434×10^1	8.777	4.632
600	1.527	8.576×10^{-1}	4.118×10^{-1}
800	2.097×10^{-1}	1.132×10^{-1}	5.139×10^{-2}
1000	3.133×10^{-2}	1.774×10^{-2}	7.401×10^{-2}

Table 4.1: Production cross sections at 7 TeV.

It is shown in Reference (24) that except for very tiny mixings $V_{l\Sigma} \sim 10^{-8}$, the new heavy leptons decay almost exclusively to SM leptons plus a gauge or Higgs boson.

The decay width analytic expressions are displayed in Eqs. (4.2)-(4.8) (29). It is worth to notice from the equations that the width depend quadratically on the mixing angle values.

As a cross check of the implementation of the model, the width was computed numerically by a MonteCarlo program and the results were found correctly match the theoretical prediction listed in Eqs. (4.2)-(4.8).

$$\Gamma(\Sigma^0 \to l_\alpha^- W^+) = \frac{g^2}{64\pi}|V_\alpha|^2 \frac{M_\Sigma^3}{M_W^2}\left(1-\frac{M_W^2}{M_\Sigma^2}\right)^2\left(1+2\frac{M_W^2}{M_\Sigma^2}\right), \quad (4.2)$$

$$\Gamma(\Sigma^0 \to l_\alpha^+ W^-) = \Gamma(\Sigma^0 \to l_\alpha^- W^+), \quad (4.3)$$

$$\sum_l \Gamma(\Sigma^0 \to \nu_l Z) = \frac{g^2}{64\pi c_W^2}\sum_\alpha |V_\alpha|^2 \frac{M_\Sigma^3}{M_Z^2}\left(1-\frac{M_Z^2}{M_\Sigma^2}\right)^2\left(1+2\frac{M_Z^2}{M_\Sigma^2}\right), \quad (4.4)$$

$$\sum_l \Gamma(\Sigma^0 \to \nu_l H) = \frac{g^2}{64\pi}\sum_\alpha |V_\alpha|^2 \frac{M_\Sigma^3}{M_W^2}\left(1-\frac{M_H^2}{M_\Sigma^2}\right)^2, \quad (4.5)$$

$$\sum_l \Gamma(\Sigma^+ \to \nu_l W^+) = \frac{g^2}{32\pi}\sum_\alpha |V_\alpha|^2 \frac{M_\Sigma^3}{M_W^2}\left(1-\frac{M_W^2}{M_\Sigma^2}\right)^2\left(1+2\frac{M_W^2}{M_\Sigma^2}\right), \quad (4.6)$$

$$\Gamma(\Sigma^+ \to l_\alpha^+ Z) = \frac{g^2}{64\pi c_W^2}|V_\alpha|^2 \frac{M_\Sigma^3}{M_Z^2}\left(1-\frac{M_Z^2}{M_\Sigma^2}\right)^2\left(1+2\frac{M_Z^2}{M_\Sigma^2}\right), \quad (4.7)$$

$$\Gamma(\Sigma^+ \to l_\alpha^+ H) = \frac{g^2}{64\pi}|V_\alpha|^2 \frac{M_\Sigma^3}{M_W^2}\left(1-\frac{M_H^2}{M_\Sigma^2}\right)^2. \quad (4.8)$$

4.5 Bounds on the Mixing Angles

Since the widths depend on the mixing angle values, care must be taken in the choice of a mixing scenario to be studied. In particular, the bounds on the mixing values, and the repercussion of mixing scenario on experimental observables (e.g. Σ decay length), have to be studied with care.

The mixing angles of the seesaw triplet with light leptons is defined by the following quantity:

$$V_\alpha = \frac{v}{\sqrt{2}}\frac{Y_\alpha}{M}, \quad (4.9)$$

```
In[40]:= Reg = RegionPlot3D[Abs[ve] < 0.055 && Abs[vm] < 0.063 && Abs[vt] < 0.063 &&
             Abs[ve * vm] < 0.00000017 && Abs[ve * vt] < 0.00042 && Abs[vm * vt] < 0.00049,
           {ve, -0.07, 0.07}, {vm, -0.07, 0.07}, {vt, -0.07, 0.07}]
```

Out[40]=

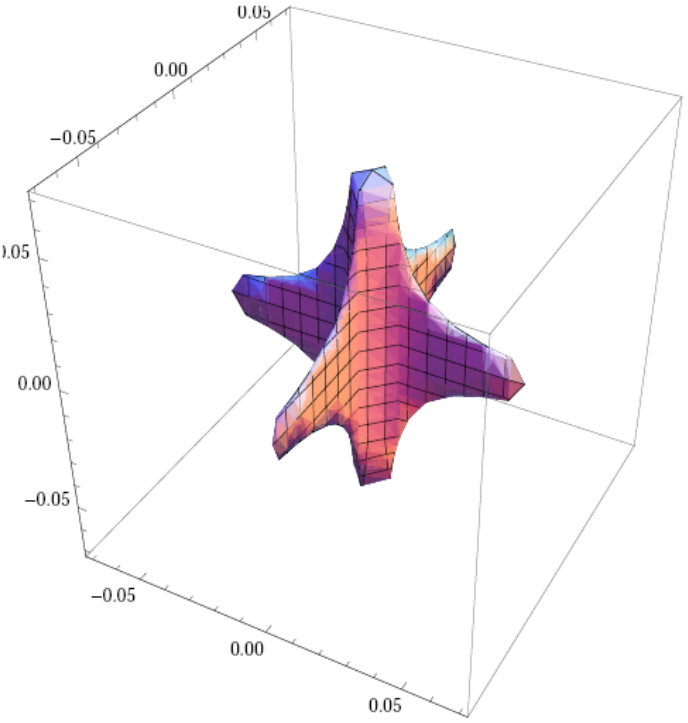

Figure 4.4: Contour plot of the parameter space allowed by equations 4.11-4.16. Mathematica package has been used.

where α is the particular flavor, Y_α is the Yukawa couplings (see 2.3.5) M the triplet mass and v the Higgs vev.

The bounds on the mixing angles are derived from electroweak processes (like W and Z decays) and lepton flavor violating processes. The former set a constrain on the single mixing angle V_α, while the latter on combinations of two of them. The latter are stronger, but can be evaded if we assume that only one mixing angle is different from zero.

Stronger constraint would be set if we consider neutrino masses. In general, when a seesaw mechanism is at work, neutrino mass are given by the expression: $v^2 Y^t M^{-1} Y/2 = m_\nu$. Since $m_\nu \approx 1$ eV and we are searching for signals in LHC data, we require $M \approx$ TeV scale (200 GeV $< M <$1 TeV $= 10^{12}$ eV) This in turn implies $V < 10^{-6}$, which is a stronger bound with respect to the ones discussed above. This goes under the

"naturalness" criteria. Notice however that the combination of parameters which characterizes all the other electroweak processes, such the decays in which we are interested at the LHC, is given by $v^2 Y^\dagger M^{-2} Y/2 = V^\dagger V$. This means that in principle neutrino masses could be small while this combination is large. This happens if cancellation in the expression of neutrino masses occur or if we are in presence of some extension of the seesaw. For example, in the so-called "Inverse Seesaw", a small parameter η in the neutrino mass formula appears: $v^2 Y^t M^{-2} Y \eta/2$, which permits to the Yukawas to be large even with low mass M. In this case only the constraints derived from electroweak processes have to be respected.

In particular, electroweak precision data set limits on mixings involving a single charged lepton, and using the latest experimental data, the constraints at 90% confidence level (CL) are found in Reference (25, 28, 70) and reported in Equations 4.11-4.16.

The bounds apply to the following combination of parameters:

$$\frac{v^2}{2}\left|Y^\dagger M^{-2} Y\right|_{\alpha\beta} = |V_\alpha V_\beta|\,. \tag{4.10}$$

And the constraints are:

$$|V_e| < 5.5\cdot 10^{-2} \tag{4.11}$$
$$|V_\mu| < 6.3\cdot 10^{-2} \tag{4.12}$$
$$|V_\tau| < 6.3\cdot 10^{-2} \tag{4.13}$$
$$|V_e V_\mu| < 1.7\cdot 10^{-7} \tag{4.14}$$
$$|V_e V_\tau| < 4.2\cdot 10^{-4} \tag{4.15}$$
$$|V_\mu V_\tau| < 4.9\cdot 10^{-4}. \tag{4.16}$$

A contour plot of the parameter space allowed by equations 4.11-4.16 is shown in Figure 4.4.

Notice that if only V_e or V_μ is present the stronger constrain of Eq. (4.14) does not apply and $\mathcal{O}(10^{-2})$ mixings are allowed. On the other side, if both are different from zero, then either one of the two is much smaller than the other, effectively reducing this case to the one with only one non-zero V_α, or they are both $\mathcal{O}(10^{-3})$, in order to satisfy the strong bound of Eq. (4.14).

The maximum allowed mixing angle corresponds to the value $V = 0.063$ [1] for muon and electron mixing, while the maximum for tau mixing is $V = 0.05$. The bound on V_μ and V_e is: $V_\mu \cdot V_\mathrm{e} < 1.710^{-7}$; splitting equally between V_μ and V_e, gives the values: $V_\mathrm{e} = V_\mu = 4.1 \times 10^{-4}$. As for V_τ, it can take the maximum allowed mixing angle value, and still satisfy the bounds with V_μ and V_e.

so these bounds have to be taken into account, but the mixing angles are not crucial (the same consideration is not valid for type I seesaw). The only experimental implication is on the Seesaw triplet decay length.

[2]

The observability of the new states $\Sigma^\pm$ and Σ^0 strongly depends on their coupling to the SM leptons. In paper (24) it is suggested that the coupling could be restricted to one generation only (and the observability in case of coupling with the first generation is similar).

Since the cross section values do not depend on mixing parameters (the production of the triplet happens via gauge interactions) we will select a scenarios for the analysis of the signal, presented in this Chapter, in which we assume that $\Sigma^\pm$ and Σ^0 only couple to μ, and all three generations of ν. We are going to report results on this specific case, in order to illustrate how our model works and to show that even with the LHC running at 7 TeV there is the possibility of testing the low scale type III seesaw. We are going to give the cross section of the relevant channels for the case $V_e = V_\tau = 0$, $V_\mu = 0.063$.

Other cases of interest could be considered:

Mixing with taus. Even if the case in which the triplet entirely mixes with muons is somehow considered the one with the highest discovery potential, mixing with electrons and even taus can be studied too. As already discussed in the literature (24), the situation for mixing with electrons is comparable to the one with muons. As for the taus, it is generally believed that the discovery potential is much smaller, since taus are difficult to detect and reconstruct.

[1] If the mixing is so large, then some cancellation or an extended seesaw mechanism like the inverse seesaw must be invoked in order to obtain the correct value for neutrino masses. However, all the discussion we perform in this section applies also in the case of small mixing.

[2] Note that if we consider complex V_α, as we are not doing in this study, cancellations could occur and we could satisfy the strong bound of Eq. (4.14) even with $|V_e|$ and $|V_\mu|$ saturating the bounds of Eqs. (4.11,4.12).

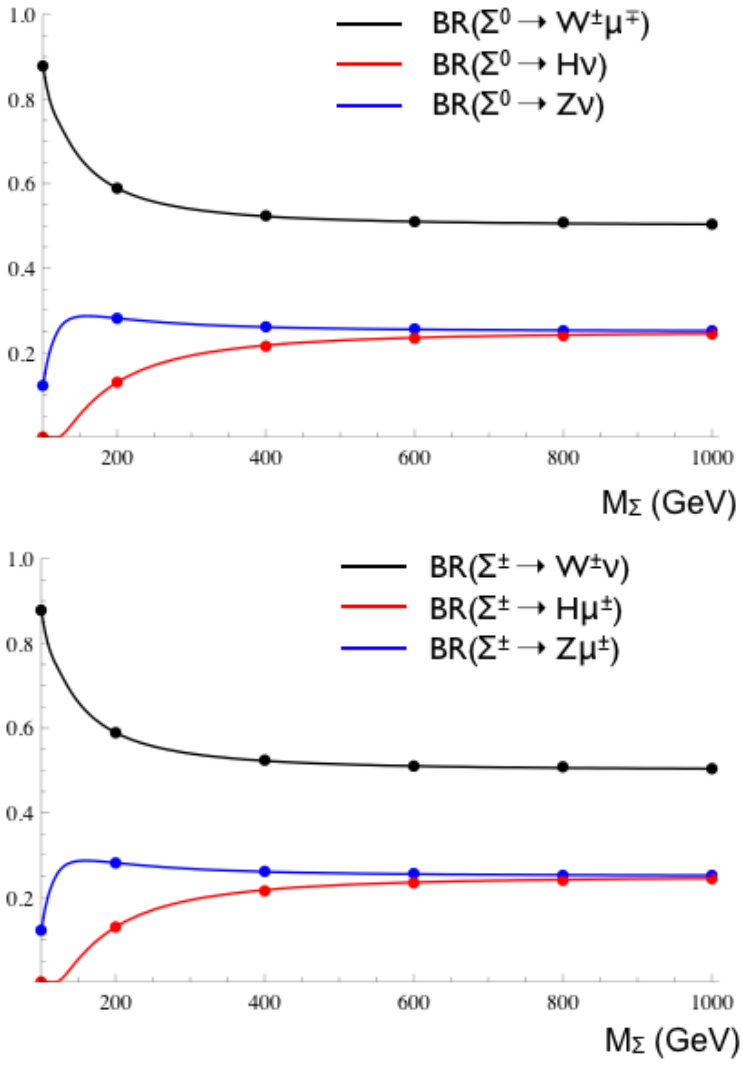

Figure 4.5: Branching ratios of the neutral component (up) and charged component (down) of the fermionic triplet in the case $V_e = V_\tau = 0\,,\ V_\mu = 0.063$. The dots correspond to numerically evaluated values while the lines correspond to the theoretical predictions. Notice that, as expected from Eqs. (4.2)-(4.8) in the case of one non-zero mixing angle, the result is the same for charged and neutral triplet decay.

Mixing with 2 or 3 charged leptons. In such a case the triplet can couple to more than one family. The mixing angles are thus more constrained. As we have already shown (see Figs. 4.5-4.6), the simultaneous presence of two (or three) non

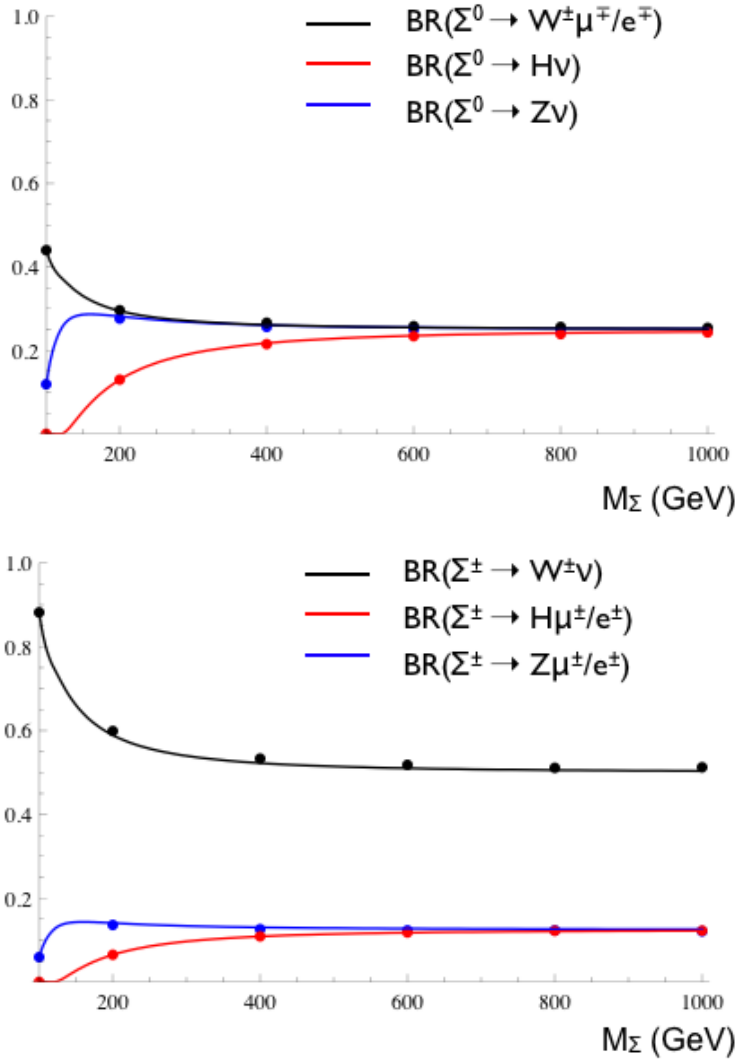

Figure 4.6: Branching ratios of the neutral component (up) and charged component (down) of the fermionic triplet in the case $V_\tau = 0$, $V_e = V_\mu = 4.1 \cdot 10^{-4}$. The dots correspond to numerically evaluated values while the lines correspond to the theoretical predictions while the lines correspond to the theoretical predictions. When both channel with e and μ are open, only one is displayed, since, for this particular choice of the mixing angles, they are overlapped.

zero V_α would reduce the corresponding branching ratio by a small factor: if, for instance, two of them are taken to be equal, then the corresponding branching ratio will be decreased by a factor 2 with respect to the case with only one non-

zero mixing angle (see Figs. 4.5-4.6). However the pair production cross section of triplets is not affected by the mixing values and thus only the branching ratios and the mass of the triplet drive the relevant processes studied here.

Small mixing angles, $\mathcal{O}(10^{-6})$. This case is the "most natural" one, since here small neutrino masses can be accommodated without any cancellation or further source of suppression [1]. Such small mixing angles drastically reduce the value of the triplet decay width, so that displaced vertexes up to few millimeters can be present (see also (29), and the results presented in Section 4.5.2). In case of finding an excess of events in some of the considered channels, the measurement of these displaced vertexes could be a clear signal that we are in presence of this kind of physics. A part from this, in general the cross sections are not affected and the analysis can proceed as in the case of large mixing.

Given these considerations, we performed analysis on LHC data, considering different mixing scenario as the one choose here for cross sections analysis. A discussion about different mixing values scenario will be presented in Chapter 9, the implication on deriving the correct cross sections from the $V_e = V_\tau = 0\,,\ V_\mu = 0.063$ case is briefly discussed in the following Section.

4.5.1 Mixing Angle Scenarios

In the case we consider the mixing angle with all the lepton flavors different from zero, care must be taken in computing the cross section contributions from different processes giving the same final state, from the cross sections we have quoted in this Chapter, namely of the case of coupling with muons alone, and decay in final state with the muon flavor only. A description of the issue is given in this paragraph, were an example for two processes is given. If more other processes are considered, the derived formulas need to take into account all the contributions.

Given

$$b_\alpha = \frac{|V_\alpha|^2}{\Sigma_i |V_i|^2} \tag{4.17}$$

[1] Notice that in this case the approximation of taking zero neutrino masses is no longer consistent and they should be turned on in the numerical simulations; for consistency also non-zero electron and muon masses should be considered, even if the effect of all these masses turns out to be negligible.

with α =e, μ , τ, and considering the two processes of Σ^0, Σ^+ decay

$$P_1^{\alpha\alpha\alpha} : \Sigma^0 \to \alpha^- W^+,\ \Sigma^+ \to W^+\nu,\ W^+ \to \alpha^+\nu \tag{4.18}$$

and the process

$$P_{11}^{\alpha\alpha\alpha} : \Sigma^0 \to \alpha^+ W^-,\ \Sigma^+ \to W^+\nu,\ W^\pm \to \alpha^\pm\nu \tag{4.19}$$

we consider the cross section for the process $P_1^{\alpha\alpha\alpha}$, $P_{11}^{\alpha\alpha\alpha}$: $\sigma_{P_1} = P_1$=$\sigma_{P_{11}} = P_{11} = \sigma_1$. Neglecting the contributions from leptonic τ decays, the cross sections for the positive final states can be expressed in terms of b_α:

$$\sigma_{\mu^-\mathrm{e}^+\mathrm{e}^+} = b_\mu P_1 + b_\mathrm{e} P_{11} = (b_\mu + b_\mathrm{e})\sigma_1 \tag{4.20}$$

$$\sigma_{\mu^-\mathrm{e}^+\mu^+} = 2b_\mu P_1 + b_\mu P_{11} + b_\mathrm{e} P_{11} = (3b_\mu + b_\mathrm{e})\sigma_1 \tag{4.21}$$

$$\sigma_{\mu^-\mu^+\mu^+} = b_\mu P_1 + b_\mu P_{11} = 2b_\mu\sigma_1 \tag{4.22}$$

$$\sigma_{\mathrm{e}^-\mu^+\mu^+} = b_\mathrm{e} P_1 + b_\mu P_{11} = (b_\mu + b_\mathrm{e})\sigma_1 \tag{4.23}$$

$$\sigma_{\mathrm{e}^-\mathrm{e}^+\mu^+} = 2b_\mathrm{e} P_1 + b_\mathrm{e} P_{11} + b_\mu P_{11} = (3b_\mathrm{e} + b_\mu)\sigma_1 \tag{4.24}$$

$$\sigma_{\mathrm{e}^-\mathrm{e}^+\mathrm{e}^+} = b_\mathrm{e} P_1 + b_\mathrm{e} P_{11} = 2b_\mathrm{e}\sigma_1. \tag{4.25}$$

Including τ decay contributions, we have to rewrite eq.(4.20-4.25) as e.g.

$$\sigma_{\mu^-\mu^+\mu^+} = b_\mu(P_1+P_{11})(1+2\epsilon_{W\tau\mu}+\epsilon^2_{W\tau\mu})+b_\tau\epsilon_{\Sigma\tau\mu}(P_1+P_{11})(1+2\epsilon_{W\tau\mu}+\epsilon^2_{W\tau\mu}) \tag{4.26}$$

where $\epsilon_{W\tau\ell}$ ($\epsilon_{\Sigma\tau\ell}$) corresponds to the efficiency (including τ leptonic branching ratio) to select events from $W \to \tau \to \ell$ ($\Sigma \to \tau \to \ell$) decay chain. Since $\epsilon_{X\tau\ell}$ are all expected to be $< 10\%$, second order terms in ϵ can be neglected and then the cross sections (4.20-4.25) have to be multiplied by a factor $\sim (1 + 2\epsilon_{W\tau\ell} + \epsilon_{\Sigma\tau\ell})$.

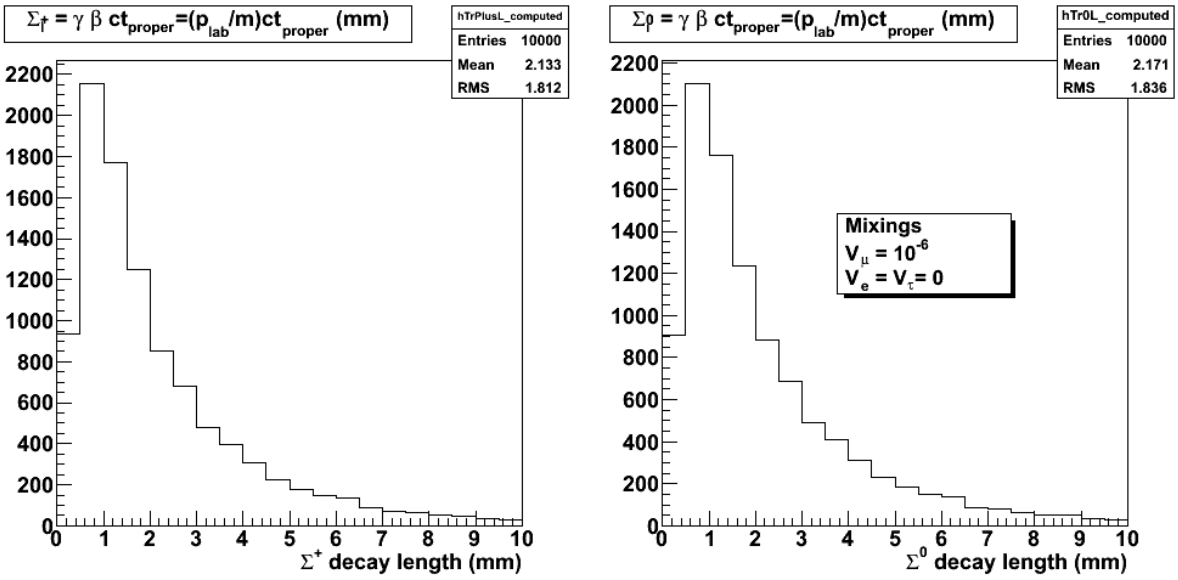

Figure 4.7: Small mixing angle case. Proper decay length of the charged (left) and neutral (right) seesaw triplet.

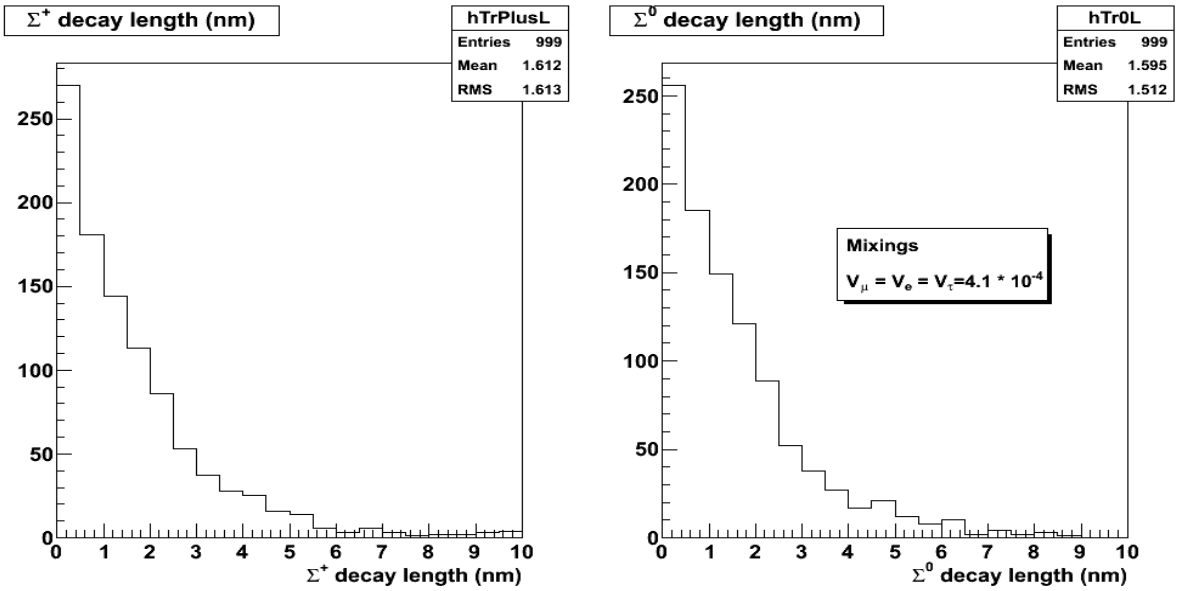

Figure 4.8: Large mixing angle case. Decay length of the charged (left) and neutral (right) seesaw triplet (BRIDGE output).

4.5.2 Mixing Angle and Decay Length

As pinpointed in the previous section, there is a strong relationship between mixing angles values and the triplet decay width, and this relationship is very important to be exploited in order to set up a proper displaced vertexes analysis. For this purpose, we have computed the decay length of the triplet for two values of the mixing angles, and the results are shown in Figures 4.7 and 4.8. Decay length for the large mixing angle case ($V = 4 \times 10^{-4}$) is of the order of nm. In the case of small mixing angles it is of the order of mm. The conclusion is that with the large mixing angle scenario $V = 4.10^{-4}$, it is perfectly safe not to consider displayed vertexes in the analysis.

4.6 Branching Ratios

While the decay width depends strongly on the value of the mixing angles V_α, the branching ratios (Br) dependence is very mild. Since we are always in the narrow width regime, the total cross section is driven only by the mass of the triplet (for the production) and its branching ratios (for the decays). Therefore, a non-discovery at the LHC will permit to constrain the mass of the triplet, after some assumption on the branching ratios have been taken. The choice of the mixing angle values have no influence on the mass limits.

	$\Sigma^+ \to \bar{\nu} W^+$ (0.88)	$\Sigma^+ \to \mu^+ Z$ (0.12)
$\Sigma^- \to \nu W^-$ (0.88)	$\nu\bar{\nu} W^+ W^-$ (0.77)	$\mu^+ \nu Z W^-$ (0.11)
$\Sigma^- \to \mu^- Z$ (0.12)	$\mu^- \bar{\nu} Z W^+$ (0.11)	$\mu^+ \mu^- Z Z$ (0.01)
$\Sigma^0 \to \mu^- W^+$ (0.44)	$\mu^- \bar{\nu} W^+ W^+$ (0.39)	$\mu^+ \mu^- Z W^+$ (0.05)
$\Sigma^0 \to \mu^+ W^-$ (0.44)	$\mu^+ \bar{\nu} W^+ W^-$ (0.39)	$\mu^+ \mu^+ Z W^-$ (0.05)
$\Sigma^0 \to \nu Z$ (0.12)	$\nu\bar{\nu} Z W^+$ (0.11)	$\mu^+ \nu Z Z$ (0.01)

Table 4.2: Intermediate states for $\Sigma^+\Sigma^-$ and $\Sigma^+\Sigma^0$ production, with their approximate branching ratio for $m_{\Sigma^0} = 100.8$ GeV and $m_{\Sigma^+} = 101$ GeV. In this case with light masses the decay channels into the Higgs boson are of course forbidden.

We found Br values for $\Sigma^\pm$ and Σ^0 decays to SM bosons and leptons. We've compared the values we obtained with previous literature, in particular Reference (24). Results are in agreement. The branching ratios for Σ decays are given in Table 4.2,

where the mixing angles have been taken, as stressed in previous section, $V_e = V_\tau = 0$ and $V_\mu = 0.063$.

4.7 Final States

Once the triplets have decayed into leptons and gauge bosons (we call it the intermediate state), further decays take place. In the final state the observable particles will be: charged leptons, quarks[1], and neutrinos, which will manifest themselves as missing energy.

There is a plethora of possible final states resulting from $\Sigma^\pm$ and Σ^0 production and decay possibilities of each heavy lepton. All decays of $\Sigma^\pm$, Σ^0 to light leptons and gauge or Higgs bosons could be in principle calculated. This is a cumbersome task since it involves 289 different final states with 128 different matrix elements for $\Sigma^+\Sigma^-$ and 748 final states with 72 matrix elements for $\Sigma^\pm\Sigma^0$, which have to be generated with their corresponding weights.

Therefore, we classify signals by the signatures actually seen at the experiment. As the number of jets in the final state is not a good discriminant due to radiation and pile-up, signals are classified in terms of the charged lepton multiplicity, and the number of hard jets is considered only in few special cases as an extra information for the kinematic reconstruction. The possible signals from Seesaw triplet decays are classified in terms of the following charged lepton multiplicity, ranging from one to six charged leptons:

- six leptons: $\Sigma^+\Sigma^- \to l^+ Z l^- Z$ and $Z \to l^+ l^-$;
- five leptons: $\Sigma^+\Sigma^0 \to l^+ Z l^\pm W^\mp$ and $Z \to l^+ l^-$; negligible cross section;
- four leptons:

  $l^\pm l^\pm l^\pm l^\mp X$: negligible cross section (only seesaw III);

  $l^\pm l^\pm l^\mp l^\mp X$: negligible cross section (common to scalar i.e. seesaw II);
- three leptons:

  $l^\pm l^\pm l^\pm X$;

  $l^\pm l^\pm l^\mp X$: good channel with small background and high cross section;

[1] quarks will show up as either as jets, or leptons, when heavy quarks decay semileptonically

- two leptons:

  $l^{\pm}l^{\pm}X$

  $l^{\pm}l^{\mp}jjjjX$: very large background;

- $l^{\pm}jjjjX$

Process	Production Cross Sections (fb)			Final State	Final Cross Section (fb)		
	100 GeV	120	140		100 GeV	120	140
Final State ++							
$W^-\mu^+Z\mu^+$	$2.36e+2$	$2.02e+2$	$1.16e+2$	$\mu^+\mu^+jets$	108	92.7	53.4
				$\mu^+\mu^+\nu\nu jets$	32.4	27.8	15.9
$W^-\mu^+h\mu^+$	$1.22e-3$	$1.39e-1$	$1.40e+1$	$\mu^+\mu^+jets$	-	-	8.9
				$\mu^+\mu^+\nu\nu jets$	-	-	-
Final State −−							
$W^+\mu^-Z\mu^-$	$1.27e+2$	$1.04e+2$	$5.67e+1$	$\mu^-\mu^-jets$	58.3	47.7	26.1
				$\mu^-\mu^-\nu\nu jets$	17.4	14.3	7.8
$W^+\mu^-h\mu^-$	$5.87e-6$	$7.13e-2$	6.86	$\mu^-\mu^-jets$	-	-	4.4
				$\mu^-\mu^-\nu\nu jets$	-	-	-

Table 4.3: Final states with two muons of the same sign for $V_e = V_\tau = 0$, $V_\mu = 0.063$. The final cross sections have been computed using the measured branching ratios, except for the Higgs, whose branching ratios have been calculated assuming a mass of 120 GeV. Only channels with a final cross section higher than 0.1 have been reported.

Using a fast detector simulation (see Chapter 5 for details about simulation) of signals and backgrounds, it has been found that the tri-lepton channel $l^{\pm}l^{\pm}l^{\mp}X$ is by far the best one for fermion triplets, as good as the like-sign di-lepton channel $l^{\pm}l^{\pm}$, balancing large signal branching ratios and small backgrounds. Reference (22), (23), (24), (25), (26). It is a good signature even if the cross section is not very high, because for the discovery channel we don't need a very large cross-section. In addition to evaluating the discovery potential, if a positive signal is observed we could make special emphasis on the discrimination among seesaw models since this channel is the same in seesaw model II and III. This could be accomplished, for example, by searching for signals in different final states, and also by reconstructing the mass and determining

Process	Production Cross Sections (fb)			Final State	Final Cross Section (fb)		
	100 GeV	120	140		100 GeV	120	140
Final State $+ + -$							
$W^+\mu^-W^+\nu$	$1.66e+3$	$6.08e+2$	$2.82e+2$	$\mu^+\mu^+\mu^-\nu\nu\nu$	20.9	7.7	3.5
$W^-\mu^+W^+\nu$	$1.66e+3$	$6.06e+2$	$2.82e+2$	$\mu^+\mu^+\mu^-\nu\nu\nu$	20.9	7.7	3.5
$W^+\mu^-Z\mu^+$	$2.36e+2$	$2.03e+2$	$1.16e+2$	$\mu^+\mu^+\mu^-\nu jets$	18.2	15.7	8.9
				$\mu^+\mu^+\mu^-\nu\nu\nu$	5.5	4.7	2.7
$W^-\mu^+Z\mu^+$	$2.36e+2$	$2.02e+2$	$1.16e+2$	$\mu^+\mu^+\mu^-\nu jets$	18.3	15.6	8.9
				$\mu^+\mu^+\mu^-\nu\nu\nu$	5.5	4.6	2.6
$W^+\nu Z\nu$	$4.62e+2$	$4.02e+2$	$2.32e+2$	$\mu^+\mu^+\mu^-\nu\nu\nu$	1.8	1.6	0.9
$Z\mu^+Z\nu$	$6.55e+1$	$1.35e+2$	$9.48e+1$	$\mu^+\mu^+\mu^-\nu jets$	1.6	3.2	2.28
				$\mu^+\mu^+\mu^-\nu\nu\nu$	0.47	0.98	0.68
$Z\mu^+h\nu$	$6.80e-4$	$1.54e-1$	$2.28e+1$	$\mu^+\mu^+\mu^-\nu jets$	-	-	0.76
$W^-\nu Z\mu^+$	$3.61e+2$	$3.08e+2$	$1.71e+2$	$\mu^+\mu^+\mu^-\nu jets$	8.4	7.2	4.0
$W^+\mu^-h\mu^+$	$1.22e-3$	$1.39e-1$	$1.40e+1$	$\mu^+\mu^+\mu^-\nu jets$	-	-	1.5
$W^-\mu^+h\mu^+$	$1.22e-3$	$1.39e-1$	$1.40e+1$	$\mu^+\mu^+\mu^-\nu jets$	-	-	1.5
Total Cross Sections $\mu^+\mu^+\mu^-$ + jets + missing E_T					46.5	41.7	27.8
Total Cross Sections $\mu^+\mu^+\mu^-$ + jets + missing E_T (only via W)					36.5	31.3	20.8
Total Cross Sections $\mu^+\mu^+\mu^-$ + missing E_T					55.1	27.0	13.9
Total Cross Sections $\mu^+\mu^+\mu^-$ + missing E_T (only via W)					52.8	24.7	12.3

Table 4.4: Intermediate and final states with three muons $\mu^+\mu^+\mu^-$ for $V_e = V_\tau = 0$, $V_\mu = 0.063$ cross sections. The final cross sections have been computed using the measured branching ratios, except for the Higgs, whose branching ratios have been calculated assuming a mass of 120 GeV. Only channels with a final cross section higher than 0.1 have been reported.

the charge of the new resonances (seen as a peak in the invariant mass[1] distribution of two opposite charge leptons plus the missing momentum) [2]

[1] $m(l_1, l_2) = \sqrt{(E_{l_1} + E_{l_2})^2 - |\vec{p_{l_1}} + \vec{p_{l_2}}|^2}$.

[2] A first straightforward discrimination of seesaw models results from considering a systematic analysis of all possible final states in which the signals can be seen and their statistical significance, which are not the same for seesaw I, II and III. Moreover, if a positive signal is found in a given channel, the mass reconstruction of the heavy resonance can be often performed and its charge measured, giving clear direct evidence for the production of the new particle, if the peak is present. For high integrated luminosities, the opening angle distribution can also be tested in the cleanest channels, giving evidence

Process	Production Cross Sections (fb)			Final State	Final Cross Section (fb)		
	100 GeV	120	140		100 GeV	120	140
Final State $+--$							
$W^-\mu^+W^-\nu$	$8.94e+2$	$3.13e+2$	$1.39e+2$	$\mu^-\mu^-\mu^+\nu\nu\nu$	11.1	3.9	1.7
$W^-\mu^+W^-\nu$	$8.96e+2$	$3.11e+2$	$1.39e+2$	$\mu^-\mu^-\mu^+\nu\nu\nu$	11.2	3.9	1.7
$W^-\mu^+Z\mu^-$	$1.27e+2$	$1.04e+2$	$5.67e+1$	$\mu^-\mu^-\mu^+\nu jets$	9.8	8.0	4.4
				$\mu^-\mu^-\mu^+\nu\nu\nu$	2.9	2.4	1.3
$W^+\mu^-Z\mu^-$	$1.27e+2$	$1.04e+2$	$5.67e+1$	$\mu^-\mu^-\mu^+\nu jets$	9.8	8.0	4.4
				$\mu^-\mu^-\mu^+\nu\nu\nu$	2.9	2.4	1.3
$W^-\nu Z\nu$	$2.49e+2$	$2.07e+2$	$1.13e+2$	$\mu^-\mu^-\mu^+\nu\nu\nu$	1.0	0.8	0.4
$Z\mu^-Z\nu$	$3.53e+1$	$6.93e+1$	$4.65e+1$	$\mu^-\mu^-\mu^+\nu jets$	0.85	1.7	1.1
				$\mu^-\mu^-\mu^+\nu\nu\nu$	0.25	0.5	0.3
$Z\mu^-h\nu$	$3.27e-4$	$7.87e-1$	$1.12e+1$	$\mu^-\mu^-\mu^+\nu jets$	-	-	0.37
$W^+\nu Z\mu^-$	$3.62e+2$	$3.07e+2$	$1.72e+2$	$\mu^-\mu^-\mu^+\nu jets$	-	-	0.37
$W^-\mu^+h\mu^-$	$5.87e-6$	$7.13e-5$	6.86	$\mu^-\mu^-\mu^+\nu jets$	8.4	7.2	4.0
$W^+\mu^-h\mu^-$				$\mu^-\mu^-\mu^+\nu jets$	-	-	0.7
Total Cross Sections $\mu^+\mu^-\mu^-$ + jets + missing E_T					28.9	24.9	15.7
Total Cross Sections $\mu^+\mu^-\mu^-$ + jets + missing E_T (only via W)					19.6	16.0	8.8
Total Cross Sections $\mu^+\mu^-\mu^-$ + missing E_T					29.4	13.9	6.7
Total Cross Sections $\mu^+\mu^-\mu^-$ + missing E_T (only via W)					28.1	12.6	6.0

Table 4.5: Intermediate and final states with three muons $\mu^+\mu^-\mu^-$ for $V_e = V_\tau = 0$, $V_\mu = 0.063$ cross sections. The final cross sections have been computed using the measured branching ratios, except for the Higgs, whose branching ratios have been calculated assuming a mass of 120 GeV. Only channels with a final cross section higher than 0.1 have been reported.

Given these results, we choose the signature $l^\pm l^\pm l^\mp X$ to be studied in this thesis, and we computed cross sections of the tri-leptons final states. [1]

for the scalar or fermionic nature of the heavy states produced. For high luminosities, further evidence is provided by the analysis of the production angular distributions in the cleanest channels with three or four leptons. Nothing could be said, on the other hand, from the shape of the kinematic distribution. Should be noted that for discriminating among different seesaw models we need a big cross-section, because of high statistic study needs.

[1] However, since the probability of missing a lepton is relatively high for multi-lepton channels, when studying signal in the tri and di-leptons channels, events with 4 leptons should be generated too. The inclusive 4-leptons final state cross section varies between 5-10 fb for triplet masses in the range

Since the $l^{\pm}l^{\pm}l^{\mp}$ final state receives contributions from many processes, we have computed the cross sections of the intermediate and final state for $\Sigma^{+}\Sigma^{0}$ decay processes (similar channels are for $\Sigma^{-}\Sigma^{0}$), and we reported in the Table only the relevant ones. While the intermediate ones are calculated with `MadGraph`, the final ones are obtained by multiplication with the branching ratios from Reference (15)

The branching ratios for the Higgs have been calculated assuming a mass of 120 GeV.

Tables 4.3 and 4.4 and 4.5 display the cross sections for the intermediate and final states with 2 and 3 leptons at different mass energies. [1] Only channels with a final cross section higher than 0.1 have been reported.

Important comments and conclusions could be drawn from these results.

- Even with LHC running at 7 TeV, with the few fb^{-1} of luminosity several events are expected, for low triplet mass.

- In some channels involving a Z boson the cross section increases moving from 100 GeV to 120 GeV. This is simply due to the faster growing of the branching ratio of the triplet decay into Z with respect to the decreasing of the production cross section.

- In the 3-leptons table, in the total cross section we have isolated the channels with leptons not-coming from Z decay. Indeed, the channels with muons generated via Z decay have a very large background and are difficult to analyze. If a Z-veto cut on the invariant mass of the leptons will be applied in order to reduce the background events coming from Z decay, these events will mostly disappear. Then the numbers we quote in blue in Table 4.4 can be considered the effective cross section after the application of this cut.

By looking at these table we see that there are 4 possible final states with 2 and 3 leptons:

100-140 GeV. We didn't generate 4-leptons final states, since we considered negligible the fraction of three-lepton events from four-lepton samples with one missed lepton.

[1] We give numbers for the case of mixing with muons exclusively, however similar results apply when the final states contains electrons as well. On the other hand, they do not apply completely to taus. Indeed, taus are not detected as such, because of their fast decay. Moreover, in a detector like CMS, leptons coming from taus decay are not distinguished from prompt leptons and therefore identified taus are only hadronic taus.

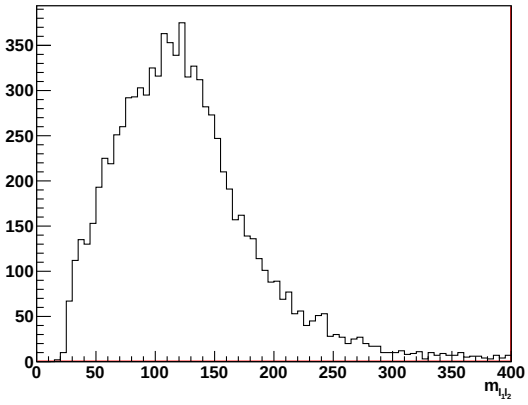

Figure 4.9: Invariant mass of the two μ^+ for a luminosity of 30fb^{-1} and $M_\Sigma = 100$ GeV. Pre-selection cuts selected only the events with 3 charged leptons among which 2 positive muons.

A) 3 leptons + missing transverse energy (MET);

B) 3 leptons + 2 jets + MET;

C) 2 same-sign leptons + 4 jets;

D) 2 same-sign leptons + 2 jets + MET.

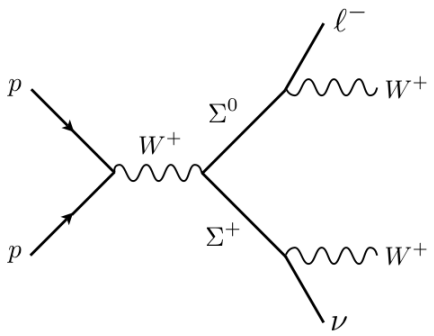

Figure 4.10: Dominant process for the discovery channel for the fermionic triplet at the LHC.

4.7.1 Detector Response

We are going to summarize the main features of the signals described in the previous Section, from the treatment given in Reference (30), were results about CMS simulation via the PGS software (71) are given. (after `MadGraph/MadEvents` event generation and hadronization with `PYTHIA` (47) package).

$pp \to \Sigma^+\Sigma^0 \to \mu^+\mu^+\mu^- + \nu s(+jets)$ with . The CMS detector has been simulated

3 leptons + MET. This is the best discovery channel. One of the two dominant processes generating it is depicted in Fig. 4.10, the other dominant process is the analogues with $\Sigma^0 \to l^+W^-$. Indeed, not only it possesses the highest cross section, but the background is more easily reduced due to the absence of jets in the final state. In an ideal detector where jets are not misidentified with leptons, the only physical irreducible background sources would be WWW, WZ and ZZ when a lepton is missed. The backgrounds will be discussed in detail in Chapter 8.

In this channel, the invariant mass $m_{\mu^+\mu^+}$ of the two same-sign muons presents a long tail in the high energy region that is characteristic of the presence of new physics, see Fig. 4.9, and can be exploited to reduce the background. Moreover, this is typical of this kind of seesaw, permitting thus to distinguish among type I, II and III (24). Other characteristics of the final leptons can be used to reduce the different SM backgrounds. In Fig. 4.11, the three leptons p_T are plot. However, the p_T emitted by the triplet has a softer transverse momentum as shown in Figure 4.12 where the mixing values are $V_\mu = V_e = V_\tau = 4.10^{-4}$ and the simulated mass point is 100 GeV.

3 leptons + 2 jets + MET. This channel is the best one in order to reconstruct the mass of the triplet. Moreover it can be used also to discriminate between type II and type III seesaw (24). It also appears in the type I seesaw with a gauged $U(1)_{B-L}$ (72). In this case the reduction of the background can be more complicated, due to the impossibility of applying a jet veto. A precise estimation of the sensitivity to this new physics would require the complete simulation of the background and a detailed analysis.

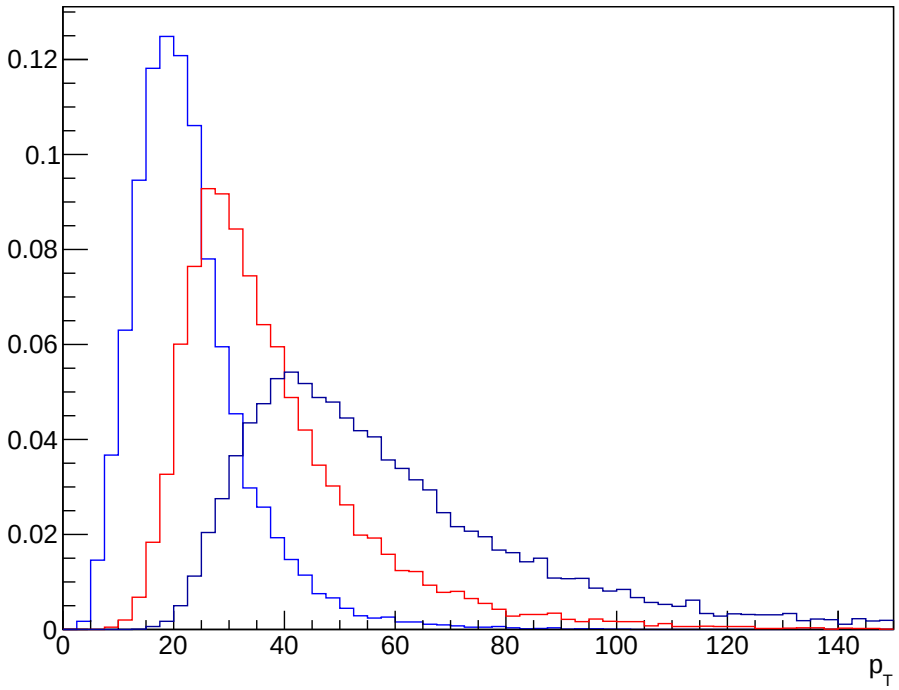

Figure 4.11: p_T distribution of the different leptons for $M_\Sigma = 100$ GeV. The black, red and blue curves represent the lepton with the highest, intermediate and smallest p_T respectively. Pre-selection cuts selected only the events with 3 charged leptons among which 2 positive muons.

Once the triplet has been observed, its mass needs to be measured. To this aim, this channel, emerging from the process $pp \to (\Sigma^\pm \to \ell^\pm Z/H)(\Sigma^0 \to \ell^\pm W^\mp)$ with Z/H decaying into jets, is the best one. Indeed the momentum of the Z/H boson is reconstructed from the jets momenta, while its combination with the momentum of one of the two same-sign leptons gives the mass of the charged triplet. Since there are two possibilities for this combination, the chosen one will be that giving closest invariant mass for the reconstructed charged and neutral triplets, where the latter is given by the combination of the momenta of the two remaining leptons *plus* MET [1].

[1]The neutrino longitudinal momenta should be added as well (24).

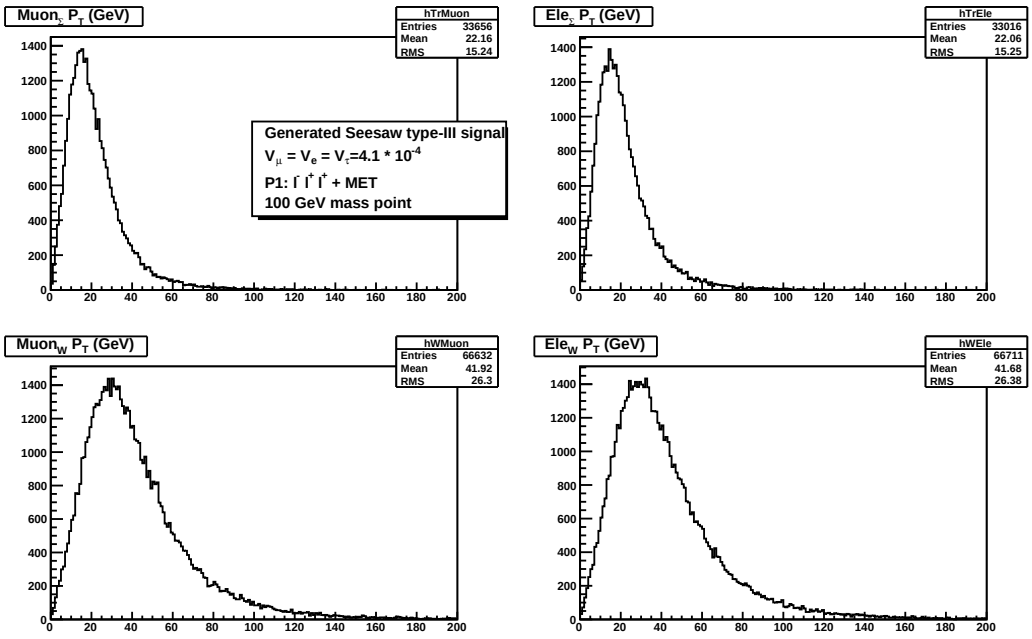

Figure 4.12: p_T distribution of the muons and electrons, for $M_\Sigma = 100$ GeV and mixing values $V_\mu = V_e = V_\tau = 4.10^{-4}$. The muons and electrons are coming from Σ decay (top) and W decays (bottom)

The reconstructed mass of the charged and neutral triplet are shown in Fig. 4.13 where no cuts has been applied. Note that a selection cut on the invariant mass m_{jj} of the jets

$$|m_{jj} - M_{Z/H}| < 10\,\text{GeV} \tag{4.27}$$

will improve the mass reconstruction. Even if the background is added, a clear peak in the reconstructed mass will still be visible, which should also permit to distinguish from type II seesaw (24).

2 same-sign leptons + jets (+MET) As it is clear from Table 4.3, the cross section for these final states is comparable to the one of the previous channels. In this case the backgrounds are essentially the same as in the previous channel and it has been shown (24) that the discovery and the discriminatory potentials are similar too. A realistic study, especially a study on real data, should consider this channel as well.

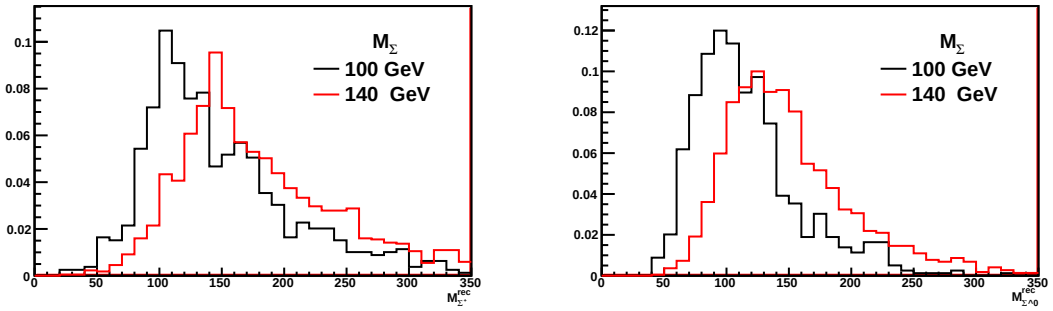

Figure 4.13: Reconstructed mass of the charged triplet (left) and neutral triplet (right), for a luminosity of 30fb^{-1}, in the case $M_\Sigma = 100$ GeV (black curve) and $M_\Sigma = 140$ GeV (red curve). Pre-selection cuts selected only the events with 3 charged leptons and at least 2 jets.

5 Simulation

5.1 Introduction

High energy physics analysis results depends on very accurate comparisons of theoretical expectations with experimental output from the detector. Based on current theoretical models, theoretical expectations are computed with computer simulations. The simulation uses Monte Carlo techniques (named after the city widely known for its gambling casino) to perform simulated experiments using random number generators for evaluating the integrals typically involved in the computation. We have implemented

the minimal seesaw type III model described in Chapter 2 in high energy physics simulation applications, and we have tested the implementation. In the present Chapter we'll present a brief review of the simulation tools, and we'll discuss the model implementation and validation. Section 5.2 reviews the fundamentals of high energy physics collisions, in Section 5.3 the simulation of the collision is described, with a particular emphasis on the software tools we used for simulation in this work.

5.2 Particle Collision Physics

In the following section I'll give some information about the simulation of the physics of high energy particle collision, with particular focus on proton-proton collisions at LHC energy scale. A sketch of two protons collision process is shown in Figure 5.1.

Basic Information. Simulated events in high energy physics collisions are constituted by a sets of outgoing particles produced in the interactions between two incoming particles. All the information about the collision itself must be provided to the

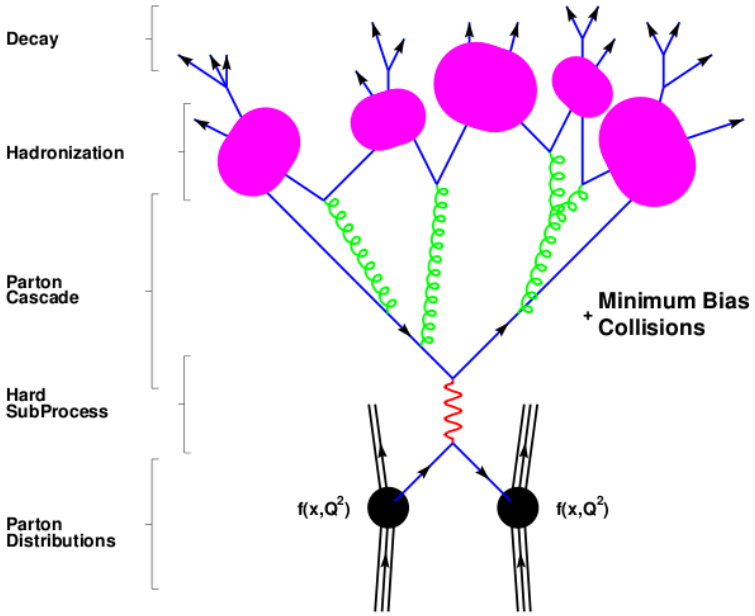

Figure 5.1: Sketch showing the event collision stages.

simulation program: the particles to be collided and the center-of-mass energy of the collision. We consider LHC colliding protons with a center-of-mass energy of 7 TeV.

Colliding Protons Structure. The structure of the colliding protons is modeled with the use of parton distribution functions (PDFs), which define the probability density for finding a parton (a quark or gluon) with a given longitudinal momentum fraction x at a particular value of momentum transfer Q^2 of the collision. PDFs containing this information cannot be calculated perturbatively, and are instead determined by fits to data from processes such as deep inelastic scattering (DIS) and Drell-Yan (DY).

The Hard Process. The collision occurs between individual partons within each proton, and is referred to as *the hard process*, in which the particles of interest for the event are produced (e.g. heavy quarks, vector bosons, hypothetical new particles, etc.). The production of these particles, and their subsequent decays, are described by matrix elements corresponding to each interaction. These are calculated from Feynman

diagrams in quantum field theory, where the square of the matrix element gives the probability density for the process, so that the production cross section can be derived from this matrix element. The programs used to generate the events are tree level (i.e. leading order) generators, and separate programs could be used to calculate the cross sections in order to include higher-order effects.

Hadronization. In addition to the hard scattering process the interaction produces parton showers, hadronizing into collections of hadrons seen as jets. The primary collision includes QCD radiation from both the incoming (ISR initial state radiation) and outgoing partons (FSR final state radiation). This radiation depends primarily on the momentum transfer scale Q^2, rather than the details of the particular process being simulated. This QCD radiation depends on color confinement: partons produced in the hard scatter cannot exist on their own. Their kinetic energy is transferred to the color field, where it produces additional partons from the vacuum. The partons in this shower then hadronize, forming color-neutral combinations. The resulting collinear spray of particles is called a *jet*. The process of hadronization is not well described theoretically, it is modeled phenomenologically with the Lund string model instead ((60)). In this model, the gluons binding two quarks are treated as field lines. Gluons are self-interacting, and hence the color field they produce is compressed into a narrow tube (or string). By contrast, the electromagnetic field tends to spread much more, because the photon has no self-interaction terms. When sufficient energy is stored in the color field to produce new quark-antiquark pairs, the string snaps, and the newly produced particles form bound-state mesons with the original quarks. In hadronization this process happens repeatedly, and the produced bound states model the kinematics of the original parton. Moreover, the remaining partons from the protons cannot be ignored, and represent the underlying event. The proton remnants are left behind after the hard scatter, but due to their strong interactions with the hard process, they must be included when considering hadronization. These interactions are typically soft and the description of the underlying event relies on non-perturbative or semi-perturbative phenomenological models.

Pileup. Additionally, the effect of *pileup* must also be considered, where multiple protons in a single bunch crossing interact. Pileup is simulated in generated events by

superimposing minimum bias events on the events in the nominal samples, according to the distribution of number of pileup collisions observed in the data for 2011.

5.3 Event Simulation Chain

Monte Carlo event generation is used to simulate high-energy-physics events (Ref. (39), (44)), therefore it must "mimic" the physical processes described in Section 5.2. HEP Monte Carlo event generation is typically modular and proceeds in stages. It is usually split into the following steps: Matrix Element calculation, Parton Shower, Underlying Event and Hadronisation. Last stage in event processing is the simulation of the detector response, which reproduces the experimental output. Usually the physics event of interest, as well as the cross-section information is done with the computation of the Matrix Element (PDF evaluation, phase space, amplitudes, spin correlations, etc...) and the remaining steps are used to evolve the parton-level event to its final state, and to simulate the detector response.

Different programs could be used to perform each step of the simulation chain. Figure 5.2 includes a sketch of the programs used to perform the different stages for the signal simulation of the present thesis. Each simulation step, the software used and a reference are listed here and described in the following sections:

1. Feynman rules and couplings computation: FeynRules (63);
2. Matrix Element (ME) calculation, event generation and decay: Madgraph5 (58);
3. Parton showering and hadronization: Pythia6 (47), (46);
4. CMS detector simulation, digitization and reconstruction: CMSSW 4_2_5 (64).

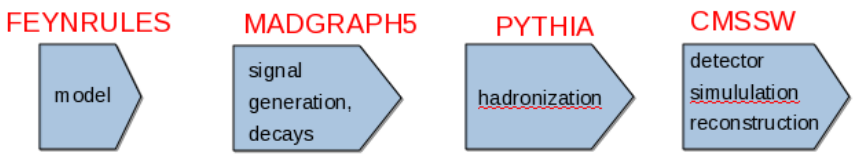

Figure 5.2: Sketch showing the software chain for event simulation.

5.3.1 FeynRules

FeynRules is a Mathematica package that allows the calculation of Feynman rules in momentum space for any QFT physics model. The user needs to provide FeynRules with the minimal information required to describe the new model, contained in the so-called model-file. This information is then used to calculate the set of Feynman rules associated with the Lagrangian. The Feynman rules calculated by the code can then be used to implement the new physics model into other existing tools, such as MC generators. This is done via a set of interfaces which are developed together and maintained by the corresponding MC authors. The seesaw type III model was implemented in FeynRules for the subsequent event generation and analysis for this thesis; the implementation of the model has been published in: (65).

5.3.1.1 Seesaw Model Implementation

In the literature few papers (24, 29, 68) discussing the possibility of discovering the type III seesaw at the LHC are present. However so far no code was publicly available to perform calculations and simulations in this model. Very recently, the minimal Seesaw type-III model was implemented and published (119), (30). In this references, implementation details are given. With the help of the authors we have generated and simulated the seesaw signal to be compared with real data.

5.3.2 Madgraph Generation

5.3.2.1 Generators Introduction

The generators used in High Energy Physics could be classified in:

- Matrix Element (ME) calculators, such as Alpgen, MadGraph, MCatNLO, etc. They deliver an event at the parton level.
- general-purpose generators, such as Herwig, Pythia or Sherpa. They can further be used to develop a fully hadronized event. The objective of general-purpose event generators is to provide as accurate as possible a description of what happens in a particle collision. They contain theory and models for a number of physics aspects, such as hard and soft interactions, parton distributions, initial and final state parton showers, multiple interactions, fragmentation and decay.

Most ME generators output is a standardized text file: the Les Houches Events (LHE) file format is an agreement between Monte Carlo event generators and theorists to define Matrix Element level event listings in a common language. This LHE text files contains some arbitrary headers and comments, information about the run (processes, cross-sections, PDFs, beam type, beam energy) and a per-event parton listing with incoming particles, outgoing particles and optionally decays of those particles (like e.g. top quark and W boson decay including spin correlations).

Matrix Element calculations are to be combined with Parton Showers of any multi-purpose event generator, so a matching procedure has to be performed in order to avoid double-counting of emissions between the ME and the PS. Generators like MadGraph/MadEvent come with their own preferred matching prescription (MLM-style jet matching), which should be used preferably. Also more recent Parton Showers come with an alternative matching procedure called CKKW re weighting which exploits knowledge of the Sukadov form factors during the Parton Shower evolution to re weight the events. [1]

5.3.2.2 Madgraph

MadGraph/MadEvent (MG/ME) is a event generator software that allows to generate amplitudes and events for any process (with up to 9 external particles) in any model. MadEvent is a multi-purpose, tree-level event generator which is powered by the matrix element generator MadGraph. A process-dependent, self-consistent code for a specific

[1] The matching procedure involves jet matching, see for Reference(38). Multi-jet events generation need to be able to simulate physics down to QCD scale (around the GeV) in order to have a simulated interaction between stable particles and a detector. This means that a parton-shower (PS) generator (PYTHIA, HERWIG,...) is mandatory for this work. On the other hand, an issue in the PS method is the algorithm of showering itself, working on a cascade-decay basis, and therefore being very sensitive to the shower parameters/definition. In fact the best way to simulate the kinematics is by using a true matrix-element calculation. This means that if the matrix-element calculation is used, the physical result is less sensitive to the parametrization of the showers.

The main problem comes up when both kind of generation are used together because of the overlapping of the respective phase-spaces of the two regimes. To avoid this, the solution is the jet-parton matching of which the general aims are: avoid overlapping between phase-space descriptions given by matrix-element generators and showering/hadronization software in multi-jets process simulation, avoid dead zones: the region of the phase space between PS and ME cover has to be filled correctly, and obtain a result invariant from the choice of showering parametrization: the matching parameters are not physical observable.

SM process is generated upon the user's request on a web form or using the standalone program see References (58).

Given the process, MadGraph automatically generates the amplitudes for all the relevant subprocesses and produces the mappings for the integration over the phase space. This process-dependent information is packaged into MadEvent, and a standalone code is produced that can be downloaded from the web site and allows the user to calculate cross sections and to obtain unweighted events automatically.

Once the events have been generated - event information (e.g. particle id's, momenta, spin, color connections) is stored in the Les Houches format, and the events may be passed directly to a shower Monte Carlo program.

5.3.2.3 Seesaw Event Generation

To provide seesaw type-III signal data-sets to be analyzed for the study presented in this thesis, we performed event generation as described in this section. We imported the seesaw model computed with FeynRules package and described in Section 5.3.1 into Madgraph application. We generated 100k events for each sample (for each mass point and each process contributing to the final state $\ell^{\pm}\ell^{\pm}\ell^{\mp}$ (described in Chapter 9). Decays of standard model bosons were included in the Madgraph processing.

Madgraph run details are listed in Appendix C.

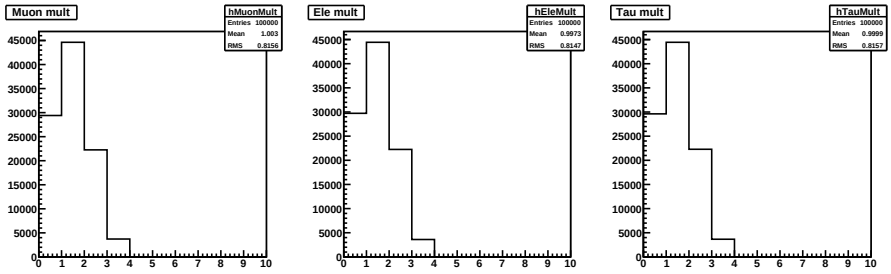

Figure 5.3: Lepton multiplicity in the final state from process: $pp \rightarrow \Sigma^{+}\Sigma^{0} \rightarrow l^{-}W^{+}W^{+}\nu_{l}$, $W^{+} \rightarrow l^{+}\nu_{l}$

5.3.2.4 Validation

Some sanity checks were performed on Madgraph output, to check implementation of the model. The LHE files were dumped on a rootuple and analyzed with a ROOT

program macro. (Reference (81)). The output agrees with expectations fairly well. In Figure 5.3 lepton multiplicity is plot for the lepton flavor. As expected, there is no difference between the three flavor multiplicity because the branching ratio of the W boson into leptons is the same for each flavor, as reported in Section A.7.1. The number of events with three leptons of the same flavor is around ≈ 3700, as expected from the branching ration of seesaw triplet and W boson.

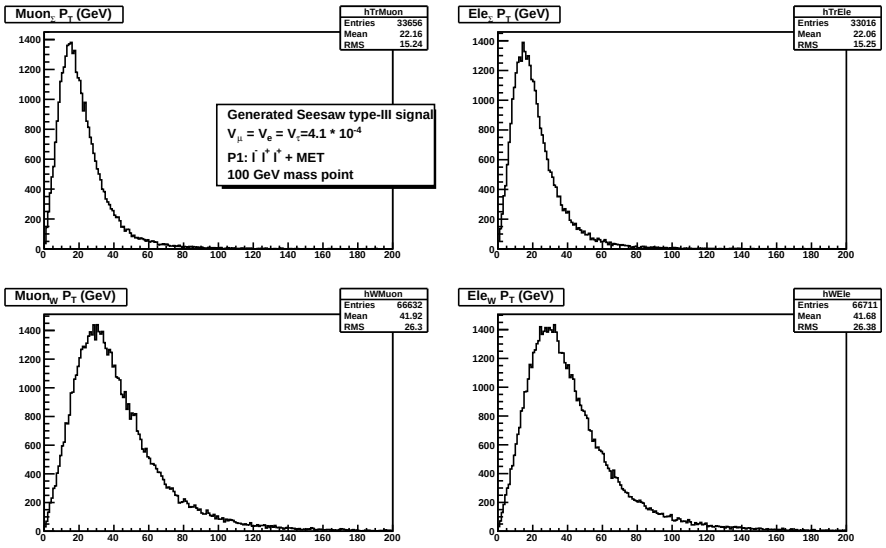

Figure 5.4: Muons and electrons distribution from the final state: $pp \rightarrow \Sigma^+\Sigma^0 \rightarrow l^- w^+ w^+ \nu_l$, $w^+ \rightarrow l^+ \nu_l$. The p_T of the muons and electrons decayed from a heavy seesaw fermion distribution (top) is compared with the p_T distribution of the muons and electrons decayed from standard model W boson.

In Figure 5.4, the p_T of the muons and electrons decayed from a heavy seesaw fermion distribution (top) is compared with the p_T distribution of the muons and electrons decayed from standard model W boson. The mean of the distribution in the former case in smaller, so the leptons in this case are more soft.

5.3.3 Pythia-CMSSW

Running a ME generator requires a subsequent step to deliver fully hadronized event. For the hadronized event step of our event simulation we used the PYTHIA application, fully integrated in the CMS detector response official software named CMSSW.

5.3.3.1 Pythia

PYTHIA is a program for the generation and/or hadronization of high-energy physics events, i.e. for the description of collisions at high energies between elementary particles such as e+, e-, p and $\bar{p}$ in various combinations. It contains theory and models for a number of physics aspects, including hard and soft interactions, parton distributions, initial- and final-state parton showers, multiple interactions, fragmentation and decay. It is largely based on original research, but also borrows many formulas and other knowledge from the literature. Development of JETSET, the first member of the "Lund Monte Carlo" family, was begun by members of the Lund theory group in 1978, and has continued since then, on and off (47). A number of people have contributed to this and other programs based on it. The most extensive of these is PYTHIA. Over the years, these two programs have more and more come to be maintained in common. In 1997 they were therefore merged to one, under the PYTHIA label. Up until recently the current version was PYTHIA 6.4. Many examples of Pythia6 configuration cards can be found in (40).

5.3.3.2 Madgraph-CMSSW interface

MadGraph cannot be directly integrated in parton shower and hadronization programs. To pass the events to Pythia and interface MadGraph to CMSSW, the MadGraphInterface package has been written (45). MadGraphInterface is a CMSSW package in the GeneratorInterface subsystem that allows to read in events in the Les Houches format, perform parton shower and hadronization using Pythia and write CMSSW objects (edm::HepMCProduct) in the event (edm::Event).

As for many other recent parton level generators, events are passed to CMSSW as parton level files in the standard format called Les Houches format. These parton level files are passed to CMSSW through interfaces. PYTHIA, integrated in CMSSW, takes care about the parton showering and the fragmentation part before passing the event to simulation. The matching procedure of matrix elements to parton shower (ME-PS) also happens in the interface . So, producing GEN level events is a two-step procedure which factories the physics contents of the matrix element calculation from the parameters of the parton showering/fragmentation/UE. It is for this reason that the physics content of a process are in the MG cards and not in the CMSSW cfg files.

The only process dependent parameter entering the cfg files for a MG production is the threshold for the matching, which needs to be known by the interface: this significantly simplifies the production of CMSSW cfg files for MG. The generator group of CMS, in collaboration with the MadGraph authors and developers, has set in place a (as much as possible) complete partition of the SM (+BSM) phase space, covering every portion with proper generations. Cuts and input parameter settings have been agreed with the CMS PAGs (Physics Analysis Groups).

In the particular case in which a LHE source is used as input source in CMSSW, it needs to be converted into EDM-compatible form, and become an LHEEventProduct branch (C++ implementation of the Les Houches Accord format) in the edm::Event (via Source). The branch is always kept in the event. Run-specific information for the ME generators is recorded in a form of LHERunInfoProduct. The LHEInterface focuses on integrating the LHE file standard in a general way into CMSSW. The software resides in GeneratorInterface subsystem in CMSSW repository. The data formats are defined in SimDataFormats/GeneratorProducts package. The CMSSW modules to be run in order to read an LHE file and process it through a shower generator are:

- reading the LHE file → LHESource: is a EDM source and behaves similarly as PoolSource in that it provides a stream of events to the EDM main loop. In contrast to other generators it does, however, not provide an edm::HepMCProduct but rather an LHEEventProduct per event that carries such event characteristics as weight(s), scale, PDF, etc and a LHERunInfoProduct for the run.

- processing the ME information through a shower generator → "HadronizerFilter": provides an interface to the shower generators and in turn reads already existing LHE products (as provided by the LHESource) and produces the edm::HepMCProduct in the end. In case ME/PS matching is done, this module also acts as an EDM filter which can veto the event.

- The LHEWriter module: merges different LHE files;

- LHEAnalyzer can do a jet matching analysis.

Details about the Madgraph-Pythia-CMSSW interface configuration used for this thesis are described in Appendix C.2.

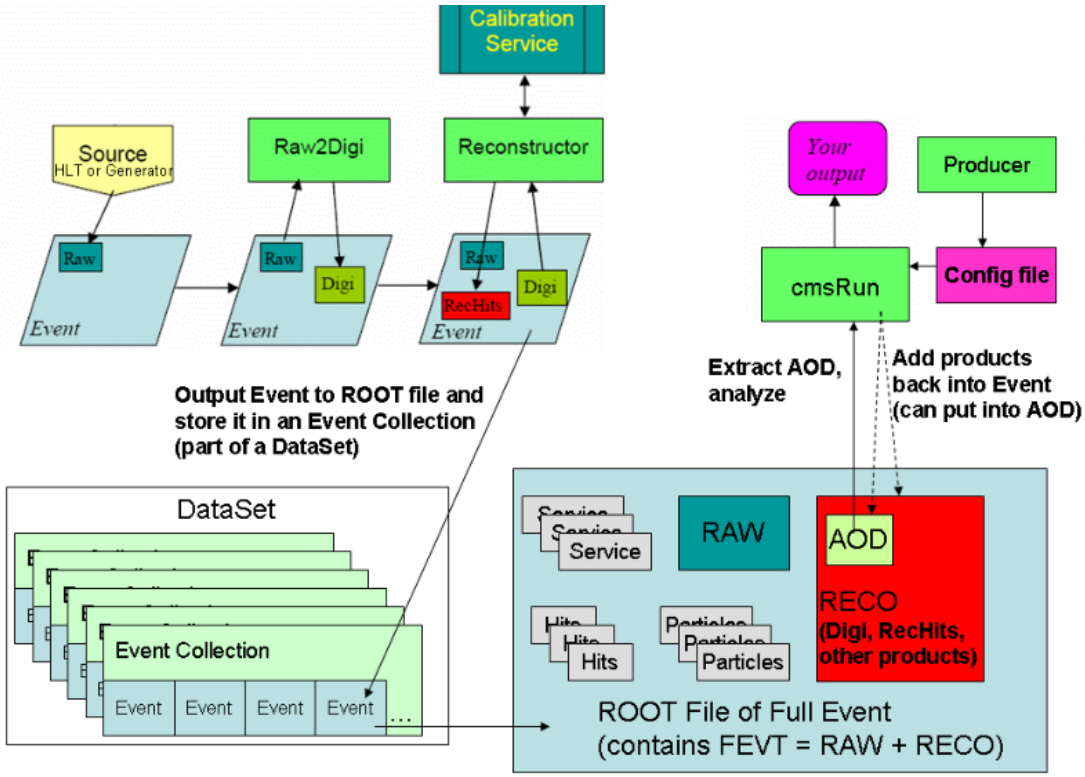

Figure 5.5: Framework diagram illustrating how an Event changes as data processing occurs in CMSSW processing chain.

5.3.4 CMSSW: Detector Response

Physics event generation is the earliest steps in the event processing chain that leads to producing data-sets suitable for physics analysis.

The following steps are:

- Simulation: the newly generated particles are run through a detailed, Geant4-based (62) simulation of the CMS detector, a toolkit used to model: the interactions of particles in the detector, and the detector electronics response. The algorithm incorporates information on the materials, magnetic fields and specific geometry of the CMS detector. In alternative to the full GEANT4-based-Simulation is the Fast Simulation approach. It uses parametric approach to simulate and reconstruct events with the CMS detector; the concept of FastSim is to reduce the CPU time overhead, while still benefiting from an accurate simu-

lation of the detector effects, in view of doing physics analysis, develop and tune reconstruction algorithms, design detector upgrades, etc.

- Digitization: the detector response to the simulated particles is determined.
- Reconstruction: from detector response, physical objects are reconstructed for the analysis. A description of objects reconstruction in for CMS experiment are given in the following Chapter.

The event processing chain is illustrated in Figure 5.5

6

Reconstruction of Physics Objects

6.1 Introduction

The data from an event is collected by the CMS detector in a very low-level form (e.g. hits in the tracker, energy deposits in the calorimeters). The output of the Data Acquisition (DAQ) system consists of signal pulse heights, the time when the signal occurred, and the address of the detector element where it occurred.

This raw data from the detector contains all the information relevant to analyzing interesting physics. Nevertheless, the information must be correlated with the information about the geometry of the detector, the current values of all detector alignment and calibration constants, the beam parameters and other relevant experimental conditions. Furthermore, the DAQ information must be synthesized into the actual objects that are used in the analysis, employing knowledge about the Standard Model and the interactions of particles and with the material of the detector.

This process is called offline reconstruction. In reconstruction all detector information is used and all possibilities of particle trajectories are checked and compared to each another. The resulting physics objects are the particles which were produced in the collision (muons, electrons, taus, jets and missing energy), their energies, momenta, masses, and the coordinates of their origin.

The same reconstruction software is applied to MonteCarlo simulated events.

In this chapter we will describe the general particle flow approach and the particle flow algorithms for the different physical objects.

6.2 The Particle Flow Algorithm

In this analysis we use the particle flow framework to reconstruct the physical objects used, i.e. leptons, jets and missing transverse energy.

The Particle-flow algorithms aim to individually reconstruct and identify all stable particles in the event, (electrons, muons, photons, charged hadrons and neutral hadrons) by comprehensively using all sub-detectors in an optimal way to determine each particle's direction, energy and type. The list of individual reconstructed particles in the event can then be used to reconstruct higher level observables, such as jets, missing transverse energy, isolated electrons and muons, identification of tau and b jets, etc.

The particle flow algorithm consists in the following steps:

- Fundamental ingredients:

  calorimeter clustering

  tracking (with the tracking POG), and extrapolation to the calorimeters

  muon identification (from the muon POG)

  electron pre-identification (with the e/gamma POG)

- Linking topologically connected elements;

- Particle identification and reconstruction.

The key elements of Particle Flow approach are described in the following sections.

6.2.1 Track

One of the most fundamental components of many physics objects is the reconstruction of tracks of charged particles. In CMS experiment, the large magnetic field and high resolution of the tracker make it possible to measure the momentum of charged particles extremely accurately.

Tracks in the CMS detector are reconstructed via the combinatorial track finder (CTF). Initial estimates (or seeds) of tracks are constructed either from triplets of hits or from pairs of hits with additional constraints from the beam spot or a vertex. This seed is then propagated outwards, and as new hits are found in the tracker, they are

added to the seed trajectory and the entire track is updated with the new information. This collection of hits is then fit to obtain the best estimate of the track parameters, including the pT, η and ϕ of the reconstructed track. Multiple iterations of this process are performed, with hits removed from the collection as they become unambiguously assigned to tracks. After each iteration, filtering is applied to remove potential fake tracks. The initial seeding criteria are very tight, to ensure the initial fake rate is negligibly low. The criteria are progressively loosened for subsequent iterations in order to increase the efficiency to match charged hadrons and to find tracks far from the interaction vertex, such as electrons from photon conversion and tracks from b-jets. The successive removal of matched hits ensures that rates of fake tracks are kept low, and tracks with high efficiency and small fake rate can be constructed down to transverse momenta on the order of 100 MeV.

6.2.2 Vertex

In CMS experiment is possible to determine the production vertex of the event with high precision. The primary interaction vertex is reconstructed from the collection of tracks. Prompt tracks, coming directly from the primary interaction, are defined based on multiple variables, including the transverse impact parameter d_0, the number of hits in the track, and its normalized χ^2. These tracks are then clustered along the z axis, and this cluster is fit using an adaptive vertex fit (84). The location of the primary interaction vertex is then determined from this fit.

6.2.3 Calorimeter Energy

The calorimeters first aim is determining the energy of a number of different particles, including electrons and photons (which deposit all their energy in the ECAL) and hadrons (which deposit energy in both the ECAL and the HCAL). Combining information from the two calorimeters to obtain a single energy estimate gives an energy resolution of order 10% for a typically energetic hadron of 100 GeV. This makes it possible to separate neutral hadrons from charged hadrons by identifying an excess of energy beyond that deposited by the charged hadrons. The PF algorithm employs a clustering method in the calorimeters to measure the energy from neutral particles, separate them from charged particles, and reconstruct the energy of electrons, which can undergo significant energy loss on their way to the calorimeter due to the process

of Bremsstrahlung. First, the cluster is seeded by a single calorimeter cell with a local energy maximum above some threshold, defined as a two standard deviation excess above the electronics noise in the calorimeter (80 MeV in the barrel and 300MeV in the endcaps). Next, the algorithm grows the cluster by aggregating cells that share a side with a cell already in the cluster and have an energy greater than the threshold. Each separate seed eventually becomes a particle flow cluster.

6.2.4 Link Algorithm

Particle Flow approach employs a link algorithm whose purpose is to combine information from each detector element in a way that ensures that it is not double-counted, in order to construct final state object. A link is established between two elements, with the distance between them determining the link quality, and blocks are formed from these linked elements. A link between a charged particle track and a calorimeter cluster is established by extrapolating the track from the last measured hit in the tracker to the ECAL and HCAL. If this extrapolated track lies within a cluster boundary defined in the calorimeter, that cluster is then linked to the track. The link distance here is defined as the difference in $\eta - \phi$ space between the position of the extrapolated track and the position of the cluster. Other clusters are linked by taking positions tangent to the track, in order to include the energy lost due to Bremsstrahlung. Links between deposits in the ECAL and HCAL are performed similarly. Here, the cluster position is defined in the ECAL, which has greater granularity, and extrapolated into the HCAL. If the cluster position lies within the envelope defined by the HCAL cluster, then the two are linked.For muons, it is also necessary to link tracks in the tracker to tracks in the muon chambers. This link depends on matching the hits in each detector element to a global fit, and requiring that this fit return an acceptable χ^2. In the case where a given track in the muon chambers is compatible with multiple tracks in the tracker, the fit that returns the smallest χ^2 is used to define the muon.

6.3 Particle Flow Electrons

The electron identication and reconstruction within the particle-ow algorithm is described in detail in References (83) and (85). A short description is given here.

Particle Flow Electrons algorithm consists in two main parts: a tracker-driven seeding for GSF tracks focused on low p_T or non-isolated electrons, complementing the ECAL-driven seeding; and an electron recon- struction and identication included in the core of the particle ow algorithm. The key step of the reconstruction is the Bremsstrahlung recovery. The super-cluster thus obtained allows calorimeter-track matching variables to be easily built. The resulting observables are combined with the electron track properties in a multivariate analysis.

6.4 Particle Flow Muons

The muon reconstruction is done prior to the particle-flow event reconstruction. The reconstructed muons contain in general a significant amount of misidentified (un-decayed) charged hadrons. In order to have a pure sample of muon can- didates, identification requirements must be applied to the original reco muon collection. A standard choice of possible selections is presented in Ref. (54).

The particle-flow algorithm makes use of some of these identification tools and together with the use of the measurement of energy released in the calorimeter, defines an alternative set of selections which are appropriate for and needed by the particle-flow algorithm. These selections have been optimized to identify muons in jets with high efficiency and low fake rate, as missed or fake muons can seriously bias jet and missing E_T measurements. As a consequence, this selection is able to retain non-isolated muons, including hadron decays in flight, usually considered as a background in typical analysis. Additional muon selections can be performed after particle-flow reconstruction without any residual bias.

6.5 Particle Flow Taus

As described in References (88) and (89), tau reconstruction and identification using particle flow with the CMS detector has three major components: a general particle flow reconstruction, a common tau reconstruction using reconstructed particles, and a higher level identication.

The optimization of the tau identification performance in terms of efficiency and the fakerate is achieved by analyzing the constituents of jets in order to identify specific individual tau hadronic decay modes. The majority of tau decays proceeds through

intermediate resonances, therefore the hadronic tau identification can be re framed from a search for collimated hadron jets satisfying the tau mass constraint into an ensemble of searches for production of the differ- ent hadronic tau decay resonances.

CMS developed two main tau reconstruction algorithms : Tau Neural Classifier (TaNC) and Hadron plus Strips (HPS). Both algorithms use Particle Flow (PF) objects. The resulting list of particles computed from PF algorithm is used to construct taus. One of the major tasks in reconstructing the decay mode of the tau is determining the number of π^0 mesons produced in the decay. The TaNC attempts to reconstruct the best π^0 candidate based on the existing PF photon candidates, whereas the HPS combines PF electromagnetic particles in strips, to take into account possible broadening of calorimeter depositions from photon conversions. The neutral objects are then combined with existing charged hadrons to recon- struct the hadronic tau decay products. After the decay mode of the tau candidate has been reconstructed, the TaNC algorithm feeds the tau candidate to an ensemble of neural networks, each corresponding to one of the five dominant hadronic decay modes. By adjusting the thresholds of cuts on the neural network output three working points: loose,medium and tight were defined. In the case of HPS if more than one hypothesis for possible tau decay signatures exists the hypothesis leading to the lowest ET sum of jet constituents not associated to tau decay products is given preference. Finally, reconstructed candidates are required to satisfy isolation criteria which are based on counting the number of charged hadrons and photons above a certain ET threshold, not associated to the tau decay signature within an isolation cone of size $\Delta R = 0.5$. Three sets of ET thresholds dene loose, medium and tight working points. It has been shown in Reference (89) that the performance of the tau algorithm in data is well reproduced by predictions of the MC simulation.

6.6 Particle Flow Missing Energy

The signature we study for the thesis contains neutrinos in the final state. Neutrinos do not register by the detector but create an energy imbalance which can be measured. The energy imbalance is computed in the transverse view only, since the longitudinal momentum of the individual colliding partons is not known (just the longitudinal momentum of the whole proton can be measured) and only the transverse momentum of

the colliding partons can be assumed with a large precision to be zero. Thus we only measure the transverse part of the energy imbalance, which we call the missing transverse energy E^T_{miss}. This is the sum of the transverse momenta of all particles. The particle flow algorithm reconstructs the missing transverse energy along with all the other particle reconstruction. Care must be taken in the evaluation of the calorimeter noise. The noise in calorimeter towers and crystals can be reconstructed as neutral hadrons and photons and included into the calculation of the missing transverse energy. Therefore a simple cleaning algorithm was developed and tuned by the CMS collaboration to identify the noise patterns even if they are in the neighborhood of the real signal, to mask noisy channels so that they are not used in the particle flow reconstruction while insuring that none of the real signal was suppressed. Together with cleaning applied the particle flow missing transverse energy exhibited better resolution when compared to the missing transverse energy calculated using only calorimeter information. Thus it was used in our analysis.

6.7 Particle Flow Jets

For this analysis, Jets are reconstructed following a particle-flow (PF) technique (86, 87). Particle found by the PF algorithm are clustered to jets using the anti-k_T algorithm with the distance parameter of 0.5. Jet energies are corrected for non-uniformity in calorimeter response and for differences found between jets in simulation and data (99).

The process of the hadronization usually results in a number of hadrons in tight cone around the original quark or gluon direction. Hadrons originating from heavy-favor quarks can decay emitting a lepton, that is sometimes isolated from the jet of hadrons in a jet. In other cases, the hadron itself can be confused with an electron by depositing all of its energy in the electromagnetic calorimeter or with a muon by punching through the calorimeter and the magnet and leaving a track segment in the muon chambers. Leptons originating from hadrons are called *fake leptons* as they are not part of the signal.

For this analysis, it is important to understand their rate and how it depends on the properties of the jets in the event. For that reason we need to reconstruct the parameters of the jets.

In particle flow framework, jets are defined as groups of any reconstructed particles that have been clustered (their four-momentum combined to yield the jet's four-momentum) according to some clustering algorithm. In this analysis we used jets clustered by the anti-kT algorithm [7], which is a fast, infrared safe and collinear safe jet clustering algorithm. The criteria for clustering particles into a jet are the following:

$$\begin{aligned} d_{ij} &= min(k_{ti}^{2p}, k_{ti}^{2p})\frac{\Delta_{ij}^2}{R^2} \\ d_i &= k_{ti}^{2p} \end{aligned}$$

where $\Delta_{ij}^2 = (\eta_i - \eta_j)^2 + (\phi_i - \phi_j)^2$, with k_{ti}, η_i and ϕ_i are the transverse momentum, pseudo-rapidity , and azimuthal angle of the particle i, respectively and R is the radius that defines the jet. The algorithm loops over all entities (particles, clusters of particles) and compares d_{ij} and d_i. If $d_{ij} < d_i$, then i and j entities are clustered, if $d_{ij} > d_i$ is smaller, then it is called a jet and removed from the list. The traditional k_t algorithm has $p = 1$, thus the anti-k_t algorithm has $p = -1$. It is easy to demonstrate that with anti-kt condition the clustering algorithm prefers to cluster around hard particles, thus forming nice conical jets with a hard particle center, while the jets of the soft particles in the neighborhood of the hard particles will have deformed cones. The anti-kt jet clustering algorithm with the jet cone size $R = 0.5$ is the default jet clustering algorithm in CMS. Thus it was used in this analysis within a particle flow framework. Except for applying threshold on jet transverse momentum and assuring that a jet was not coinciding with one of the selected leptons no additional jet identification variables were used in this analysis.

7

CMS 2011 data

7.1 Introduction

The data used for this analysis were taken with the CMS Detector at LHC in the year 2011 (RunA and RunB). In 2011 the LHC delivered $5.74 fb^{-1}$ of proton collisions and CMS has recorded $5.21 fb^{-1}$. From recorded data, runs with technical hitches or other kind of issues are removed, and only the so-called 'certified' data are available for analysis. CMS certified data amount to a luminosity of $4745 pb^{-1}$, and this is the total luminosity we used for the data analysis in the thesis. In this Chapter, a brief introduction regarding CMS data flow is given in Section 7.2, the choice of the trigger path is discussed in Section 7.3, the skimming selection is specified in Section 7.5. Finally, a first look at 2011 data with 2 opposite-sign leptons is reported in Section 7.6.

7.2 Data Flow

A brief summary of the data flow is given in this section. Figure 7.1 from Reference (90) shows the schematic flow of the real event data through CMS Computing Centers.

Online System. The CMS online, named High Level Trigger (HLT) farm, processes events from the Data Acquisition System (DAQ) which have successfully passed the L1 trigger criteria. An entire event is distributed to an HLT node which either rejects it forever, or accepts it based on its passing one or more of the HLT selection criteria (according to the HLT trigger table). The raw event data constitutes the output of the HLT farm. The first attribute of an event is its trigger path. Thus events will be clustered into a number of Primary Datasets, as a function of their trigger history. Datasets greatly facilitate prioritization of first-pass reconstruction, the scheduling of

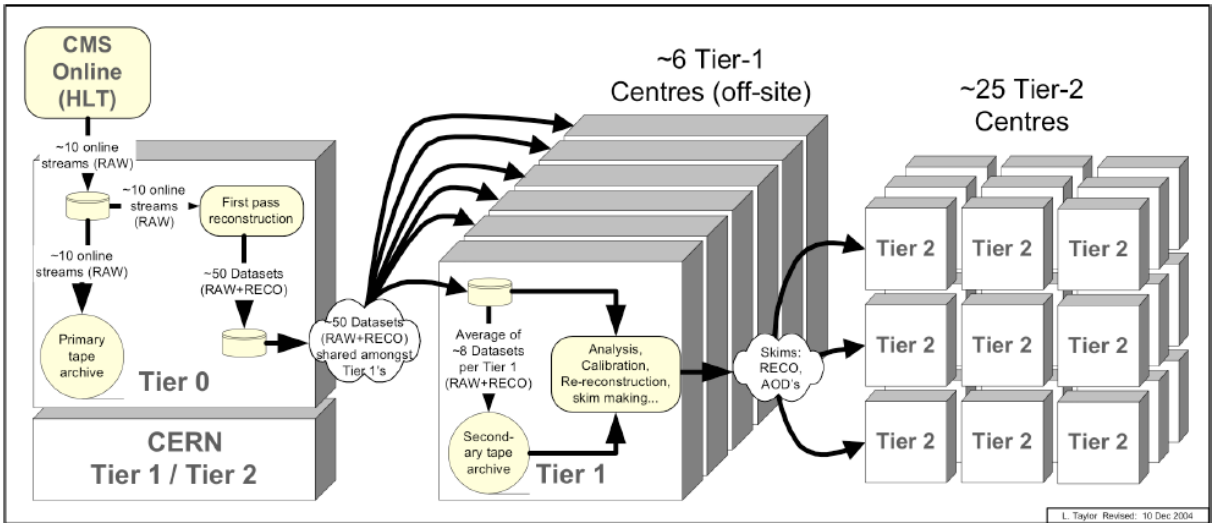

Figure 7.1: Schematic flow of bulk (real) event data in the CMS Computing Model. Not all connections are shown - for example flow of MC data from Tier-2s to Tier-1s or peer-to-peer connections between Tier-1s. Reference (90).

re-calibration and re-reconstruction passes, and the organization of physics analysis. The CMS online system classify RAW events into O(50) Primary Datasets based solely on the trigger path (L1+HLT). Duplication of events between Primary Datasets is up to $\approx 10\%$).

For performance reasons, sets of the O(50) Primary Datasets are grouped into O(10) Online Streams with roughly similar rates. The online streams are data management artifacts, they are not visible as such to end users. The subdivision of events into online streams allows: to prioritize processing of a calibration stream; to delay processing of certain lower-priority online Streams; to simplify handling of production job output. The online system will write one or possibly several Express-Line streams, at a rate of a few % of the total event rate, containing (by definition) any events which require very high priority for the subsequent processing. The express-line is not intended for final physics analysis but rather to allow for very rapid feedback to the online running and for hot and rapidly changing offline analysis. As well as being written to a normal online stream, an event may also be written into an *express line* stream (maybe one or several).

Online-Offline System Link. The offline system holds data storage and further processing. It must be able to keep up with a data rate from the online of about 225 MB/s. Indeed, the HLT farm will write events at the maximum possible data rate, independently of the event size. Trigger thresholds will be adjusted up or down to match the maximum data rate, in order to maintain consistency with the downstream data storage and processing capabilities of the offline systems. No dead-time can be tolerated due to the system transferring events from the online systems to the Tier-0 center; therefore the online-offline link must run at the same rate as the HLT acceptance rate. The trigger threshold are described in the Trigger Tables for each run luminosity, see (93). Trigger rates are described in Reference (94).

Primary Dataset	Trigger Path
Dimuon	HLT_DoubleMu7_v1,2 or
	HLT_Mu13_Mu8_v2,3,4,6,7 or
	HLT_Mu17_Mu8_v10,11
DiElectron	HLT_Ele17_CaloIdL_CaloIsoVL_Ele8_CaloIdL_CaloIsoVL_v1,2,3,4,5,6 or
	HLT_Ele17_CaloIdT_TrkIdVL_CaloIsoVL_TrkIsoVL_Ele8
	_CaloIdT_TrkIdVL_CaloIsoVL_TrkIsoVL_v2,3,4,5 or
	HLT_Ele17_CaloIdT_CaloIsoVL_TrkIdVL_TrkIsoVL_Ele8
	_CaloIdT_CaloIsoVL_TrkIdVL_TrkIsoVL_v5,6,7,8,9,10
E-Mu	HLT_Mu10_Ele10_CaloIdL_v2,3,4 or
	HLT_Mu17_Ele8_CaloIdL_v1,2,3,4,5,6,8 or
	HLT_Mu17_Ele8_CaloIdT_CaloIsoVL_v4,7,8 or
	HLT_Mu8_Ele17_CaloIdL_v1,2,3,4,5,6 or
	HLT_Mu8_Ele17_CaloIdT_CaloIsoVL_v3,4,7,8

Table 7.1: Trigger Paths used in the analysis.

7.3 Trigger Paths

The Primary Datasets considered for this analysis are: Double-Electron, Double-Mu, MuEG. As described in the previous section, the trigger history is a fundamental attribute of the events, therefore the data-sets name include primary data-set and trigger history main information, primarily the HLT version path and the physical objects

p_{T}thresholds set in HLT path. Primary Datasets and Trigger Paths used in this analysis are listed in Table 7.1.

To clarify the meaning of trigger path nomenclature, we will describe the features of few of them, e.g.:

- Di-electron primary data-set:
  - `HLT_Ele17_CaloIdT_CaloIsoVL_TrkIdVL_TrkIsoVL_Ele8_CaloIdT_CaloIsoVL_TrkIdVL_TrkIsoVL_v*`
    This is a double electron trigger which requires one HLT electron with $E_{\mathrm{T}} > 17$ GeV and a second HLT electron with $E_{\mathrm{T}} > 8$ GeV together with some identification and isolation requirements on both legs. At Level-1 this HLT path is seeded by the trigger `L1_SingleEG12` i.e. a trigger which requires one electromagnetic object with $E_{\mathrm{T}} > 12$ GeV.
- Di-muon primary dataset:
  - `HLT_Double_Mu7_v*`
    This is a double muon trigger which is based on L3 (combined muon system and tracker information) muon reconstruction and requires two L3 muons at HLT with $p_{\mathrm{T}} > 7$ GeV. At Level-1 this HLT path is seeded by the trigger `L1_DoubleMu3` i.e. a double muon trigger which requires $p_{\mathrm{T}} > 3$ GeV.
  - `HLT_Mu13_Mu8_v*`
    This is a double muon trigger which is based on L3 (combined muon system and tracker information) muon reconstruction and requires two L3 muons at HLT with $p_{\mathrm{T}} > 8$ and 13 GeV. At Level-1 this HLT path is seeded by the trigger `L1_DoubleMu3` i.e. a double muon trigger which requires $p_{\mathrm{T}} > 3$ GeV.
  - `HLT_Mu17_Mu8_v*`
    This is a double muon trigger which is based on L3 (combined muon system and tracker information) muon reconstruction and requires two L3 muons at HLT with $p_{\mathrm{T}} > 8$ and 17 GeV. At Level-1 this HLT path is seeded by the trigger `L1_DoubleMu3` i.e. a double muon trigger which requires $p_{\mathrm{T}} > 3$ GeV.

The choice of Di-lepton primary datasets and trigger path, instead of single-lepton ones, is motivated by the following argument. Clearly, single lepton (muon or electron)

trigger is more efficient (about 10% larger) than di-lepton trigger. Efficiency wise, it would be convenient to use single lepton trigger. Nevertheless, for full dataset in 2011, single lepton trigger is not an option because it is pre-scaled too tight. Moreover, single lepton triggers have usually high p_T thresholds, whereas we want to keep lepton p_T thresholds as low as possible because the leptons coming from Seesaw triplet are soft (especially for light mass points), as shown in Chapter 4. Therefore, we choose di-lepton triggers for 2011 full dataset, to retain all the available events without cancellations. [1]

Trigger efficiency and event overlapping will be discussed in the following subsections.

7.3.1 Trigger Efficiency

The trigger efficiency estimation is an important issue in order to apply the same efficiency to the MonteCarlo background simulated sample, because the simulation by definition has a 100% efficiency.

We will refer to trigger efficiency estimation performed by CMS Muon HLT analysis group (with the Tag and Probe method), reporting the results from Reference (92).

The trigger path probed in this work is *HLT_Mu13_ Mu18*, one of the path we used in our analysis. The measurements were done on 4 different data taking periods, written in Table 7.2. The Json file (i.e. the certified collection of runs) was:
Cert_160404-177515_7TeV_PromptReco_Collisions11_JSON.txt

The efficiency results for full path HLT_Mu13_Mu18 trigger are shown in Figures 7.3 and7.2, were the trigger efficiency versus p_{T}, η and primary vertex number is shown.

Taking the reported results, we could draw the following conclusion. Di-muon trigger efficiency is greater then 95% in most of the phase space. We could suppose

[1] In particular for our di-muon analysis, we are going to use HLT_Mu13_Mu8 for the data up to 2011A prompt-v4 and HLT_Mu17_Mu8 as a main trigger for the data above 2011A prompt v4 to get the most of data without the prescale. This ensures we loose only about 3% of the data. We can use these triggers only after run 165970 since they are not available before that run. For this initial period (covering $\approx 0.3 fb^{-1}$) DoubleMu7 is available without any prescale, and trigger efficiency should not be different than $Mu13\_Mu8$ trigger efficiency when we are using p_{T}>20 GeV. From run 160410 to 163261, we can use $HLT\_DoubleMu6\_v1$ and $HLT\_DoubleMu7\_v1$ and from run 163270 to 163869 we can use $HLT\_DoubleMu7\_v2$ (Mu6 is prescaled in this second range). And there are no good runs in between 163869 to 165088. Using $Mu13\_Mu8$ or $Mu17\_Mu8$ in the range after 170249, we loose less then 1% of the events in the di muon sample that pass our selections.

Period	Menus ($\cdot 10^{33}$)	Run Range	L (pb^{-1})	Comments
1	1.-1.4	165088-167913	930	L2 Quality cuts applied
2	2.	170249-173198	744	Double Muon L1 seeds (Mu3-Mu3p5)
3	3.	173236-173692	216	Technical Stop
4	3.	175971-177515	659	

Table 7.2: Information about the run period, ran range, luminosity, of the datasets used to compute di-muon HLT_Mu13_Mu18 trigger efficiency. Reference (92).

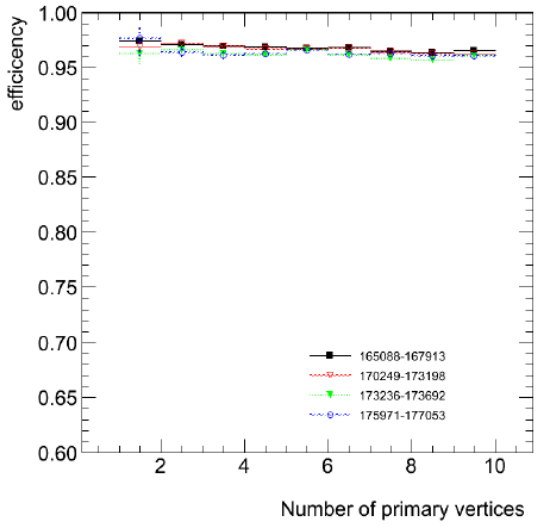

Figure 7.2: Full path HLT_Mu13_Mu18 trigger efficiency versus the number of primary vertexes in the event ($p_T < 20$ and $|\eta| < 2.1$. Reference (92).

pessimistically to loose around 10% of the di-muons events when using di-muon triggers. Since we are looking for 3-leptons events, it is realistic to suppose that the third lepton in our selection could fire the di-lepton trigger with one of the first two leptons. The efficiency would be 90% of 10% equal to 9%. Summing the initial 90% efficiency with the latter 9% a very high efficiency of 99% is reached. For di-electrons and muon-electrons triggers similar reasoning could be follow. The conclusion is that for the analysis of the seesaw signature with three leptons final state the trigger efficiency is reasonable to be around 99%. Thus, we could neglect to apply trigger efficiency to the MonteCarlo samples.

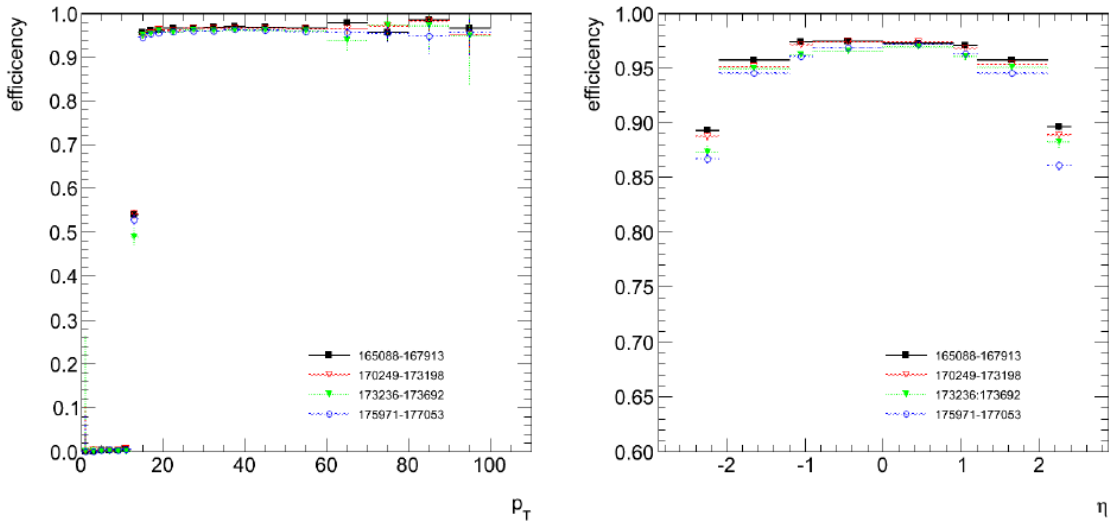

Figure 7.3: Full path HLT_Mu13_Mu18 trigger efficiency versus p_T(left) and η (right). Reference (92).

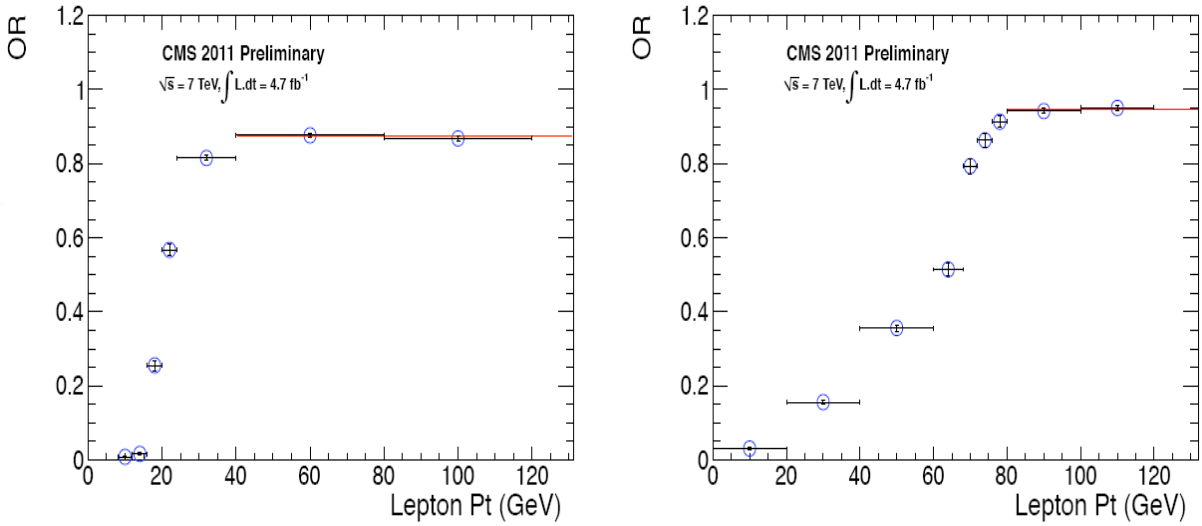

Figure 7.4: Using trigger HLT HT600 v8 , Muon OR Efficiency (left) and Electron OR efficiency (right) by the method described in Reference (97).

To cross check the above conclusion, we studied the reported results in several analysis, which have performed in detail the di-leptons trigger efficiency. We will refer in this section to Reference (97). Double leptons trigger efficiencies are measured directly in Data using an independent triggered data sample (e.g. $E_{\mathrm{T}}^{\mathrm{miss}}$or H_{T}triggered), assuming no correlations between these and the signal triggers. In such samples one searches for events containing the number of tight leptons respecting the trigger threshold and determines for which fraction the signal trigger fired. This fraction represents the trigger efficiency. In order to estimate the trigger efficiencies, Reference (97) analysis use the HT primary data set and select events that have a single isolated lepton that passes selection criteria and that fires a HT600 trigger. The trigger efficiency is estimated by taking the ratio of the number of events that satisfied both the HT and lepton trigger to the number of events that satisfied the HT trigger. This ratio will be equal to $\epsilon_{ij}/\epsilon_i = \epsilon_j$ if the HT and lepton triggers are uncorrelated [1].

The single-lepton trigger efficiency is determined for the OR of all selected single electron and single muon triggers in the run range 162803 to 180252 for the p_{T}range 30 GeV/c to 140 GeV/c, for different triggers path. In Figure 7.4 from Reference (97) the efficiency versus lepton p_T is shown for the HLT_HT600_v8 trigger. Overall, in this note the isolated electron trigger efficiency is quoted to be 94.5%, and the muon trigger efficiency to be 87%. Result for di-electron efficiency is 99% and for di-muons is 92.6%. Using HLT HT500 v8, as tag single non-lepton trigger, the electron trigger efficiency is $93\% \pm 2.8\%$ and the muon trigger efficiency is $89.6\% \pm 2.3\%$. For electron-muon cross trigger they found $96.9\% \pm 2\%$ efficiency [2].

7.3.2 Duplicated Events

In principle, different trigger paths could contain duplicated events, therefore we analyzed the number of duplicated event in our datasets. Priory we select events with

[1] Additionally they require pfMET ¿ 180 or HT ¿ 550 or HT ¿ 300 and pfMET ¿ 70 to try and remove trigger correlations or biases between HT and lepton triggers, especially electron triggers.

[2] The cuts on the leptons for to fire the dilepton triggers are looser than the ones for single lepton triggers, including the L1seeds for the dilepton and single lepton triggers. This is one of the primary reasons why the dilepton trigger efficiencies are larger than, or comparable to single lepton trigger efficiencies . This true especially for electrons. The single electron triggers rely on either L1 SingleEG15 and L1 SingleEG20 where as the dielectron triggers rely on L1 SingleEG12.

at least two-same-sign leptons, then we count the events passing the different trigger path, and their combinations.

Trigger Path	DiMu Events	DiEle Events	Mu-E Events
NONE	269	1195	441
Di-Mu	266		
Di-Ele		1178	
Di-Ele AND !(Di-Mu)		1177	
Mu-Ele			406
!(Di-Mu) AND !(Di-Ele) AND Mu-Ele			204
!(Di-Mu) AND Di-Ele AND Mu-Ele	3	1194	305
!(Di-Mu) AND !(Di-Ele) AND Mu-Ele	1	17	339

Table 7.3: Two-same-sign leptons events yield after the trigger paths combination specified in the first column is applied (path description in 7.1).

Results are summarized in Table 7.3. Di-Muons trigger paths rejects 3 di-muon events. Di-Ele trigger paths rejects 17 di-electron events. Di-Ele trigger combined with Mu-E trigger rejects only one di-electron event. DiMu and DiEle have one event overlap only. As regards the Mu-Ele sample: 441 events are in the Primary Dataset Mu-Ele. If we veto on Di-Mu triggers we loose 136 events. If we veto on Di-Ele events we are going to loose 102 events. Therefore, with the veto on both the Di-Mu and Di-Ele triggers we expect 441-(136+102) = 203 events, this is coherent with the value reported in the table (204) if we consider the 1-event-overlap between DiMu and DiEle.

The conclusion is that for our event pre-selection (i.e. two same-sign leptons) the overlap is really negligible, nevertheless, we removed duplicated events in datasets before analysis.

7.4 Reconstructed Data Samples

The data samples used in this analysis were recorded by the CMS experiment in 2011; the primary datasets and trigger path described above were used. The standard CMS selection of good runs and luminosity sections has been applied.

The samples were reconstructed and analyzed with CMS software version `CMSSW_4_2_5`. The reconstructed datasets are listed in Table 7.4 The official "TLBSM" PAT-uples

(version 9) have been used for the analysis.

Dataset	Run range
/DoubleMuon/Run2011A-May10ReReco-v1/AOD	160329-163869
/DoubleMuon/Run2011A-PromptReco-v4/AOD	165071-168437
/DoubleMuon/Run2011A-05AugReReco-v1/AOD	170053-172619
/DoubleMuon/Run2011A-PromptReco-v6/AOD	172620-175770
/DoubleMuon/Run2011B-PromptReco-v1/AOD	175832-180296
/DoubleElectron/Run2011A-May10ReReco-v1/AOD	160329-163869
/DoubleElectron/Run2011A-PromptReco-v4/AOD	165071-168437
/DoubleElectron/Run2011A-05AugReReco-v1/AOD	170053-172619
/DoubleElectron/Run2011A-PromptReco-v6/AOD	172620-175770
/DoubleElectron/Run2011B-PromptReco-v1/AOD	175832-180296
/MuEG/Run2011A-May10ReReco-v1/AOD	160329-163869
/MuEG/Run2011A-PromptReco-v4/AOD	165071-168437
/MuEG/Run2011A-05AugReReco-v1/AOD	170053-172619
/MuEG/Run2011A-PromptReco-v6/AOD	172620-175770
/MuEG/Run2011B-PromptReco-v1/AOD	175832-180296

Table 7.4: Data samples used for the analysis

7.5 Event Skimming

The immutability of Primary Datasets in no way precludes the possibility to form subsets of these Primary datasets for some specific analysis purposes. For example it is expected that subsets of events that further satisfy some more complex offline selection can be made. These are called *Skims*. Central skims for physics have been run during data processing. The aim of a central skim is to provide a small sized release validation data sample, saving a lot a processing time.

We decided to use the following central skim for our analysis: HWW prompt skim. It was requested by CMS analysis group for $Higgs \rightarrow WW$ analysis. The Primary Datasets used in this skim are: SingleMu, DoubleMu, SingleElectron, DoubleElectron, MuEG. The rate at a luminosity of $1.\cdot 10^{33}$ is: 0.9% (1.8Hz) of SingleMu, 2% (0.7Hz) of DoubleMu, 2% (1Hz) DoubleEle 5% (1.3Hz) MuEG. See Reference (91) for details. As regards Muon selection and isolation, this skim requires the use of global reconstructed

muons (see Chapter 6), adding some additional requirements; the isolation is a combination of several variables in order to be able to go down in p_{T}. The Electron selection and isolation foreseen a re-optimization of electron Id, with the use of new techniques, and the isolation is combination of several variables in order to be able to go down in $p_{\mathrm{T}}$for electrons too.

The HWW request are summarized in Table 7.5.

Particle	Cut
Muon	$pt > 10$ GeV relative isolation < 1.0 GlobalMuon and TrackerMuon
Electron	GsfElectronRefSelector $pt > 10$GeV fully instrumented η coverage
Di-Muons	invariant mass > 5 GeV
Di-Electron	invariant mass > 5 GeV
E-Mu	invariant mass > 1 GeV

Table 7.5: HWW skim selections.

7.6 2011 2-Opposite-Sign Leptons

A very preliminary look at 2011 data has been performed and most important plots are presented in this sections. Data were selected with the trigger path and skimming described in this chapter, plus the physical objects selections described in Chapter 9. Two-opposite-sign leptons were requested in each of the datasets: MuMu, EE, MuE. Plots of the most important kinematic variables are shown for the three datasets, lepton and jets distribution, together with standard model backgrounds and significance plot (i.e. data-MC/MC plot). The relevance of these plots the following. In the opposite-sign leptons control region data and Standard Model background agrees with a considerable precision. At this level of selection no hints of new physics is of course present. This is a important cross check and validation for the algorithms and all data processing we developed for the thesis analysis. Moreover, the plots shows that opposite sign same flavor leptons events are largely dominated by Z backgrounds,

whereas opposite sign different flavor events are dominated by $t\bar{t}$ events. A detailed discussion about standard model backgrounds involved in this analysis will be given in the following Chapter.

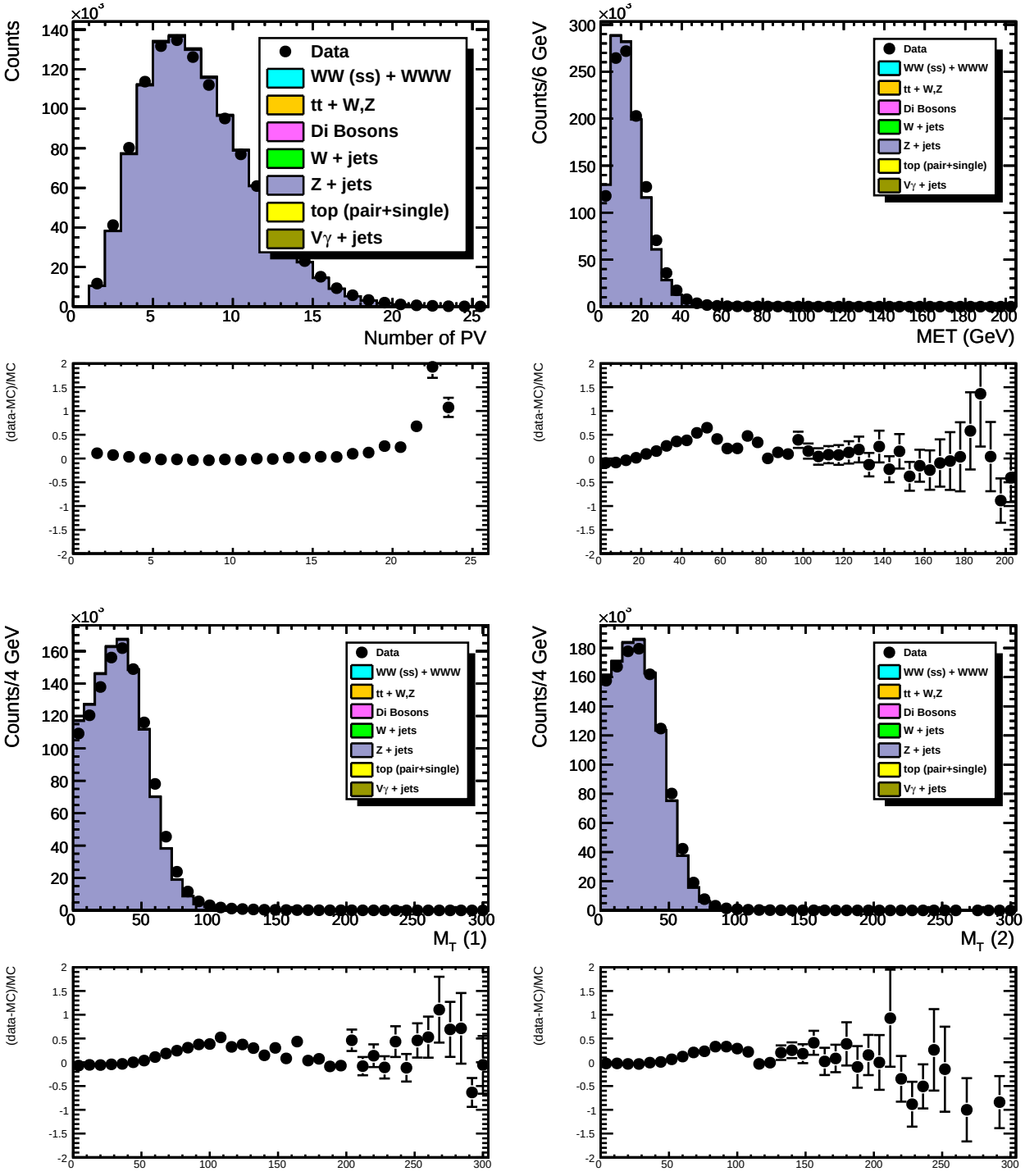

Figure 7.5: Di-muon datasets. Event plots for 2011 two opposite-sign muon events: PV, $E_{\mathrm{T}}^{\mathrm{miss}}$, M_T distributions.

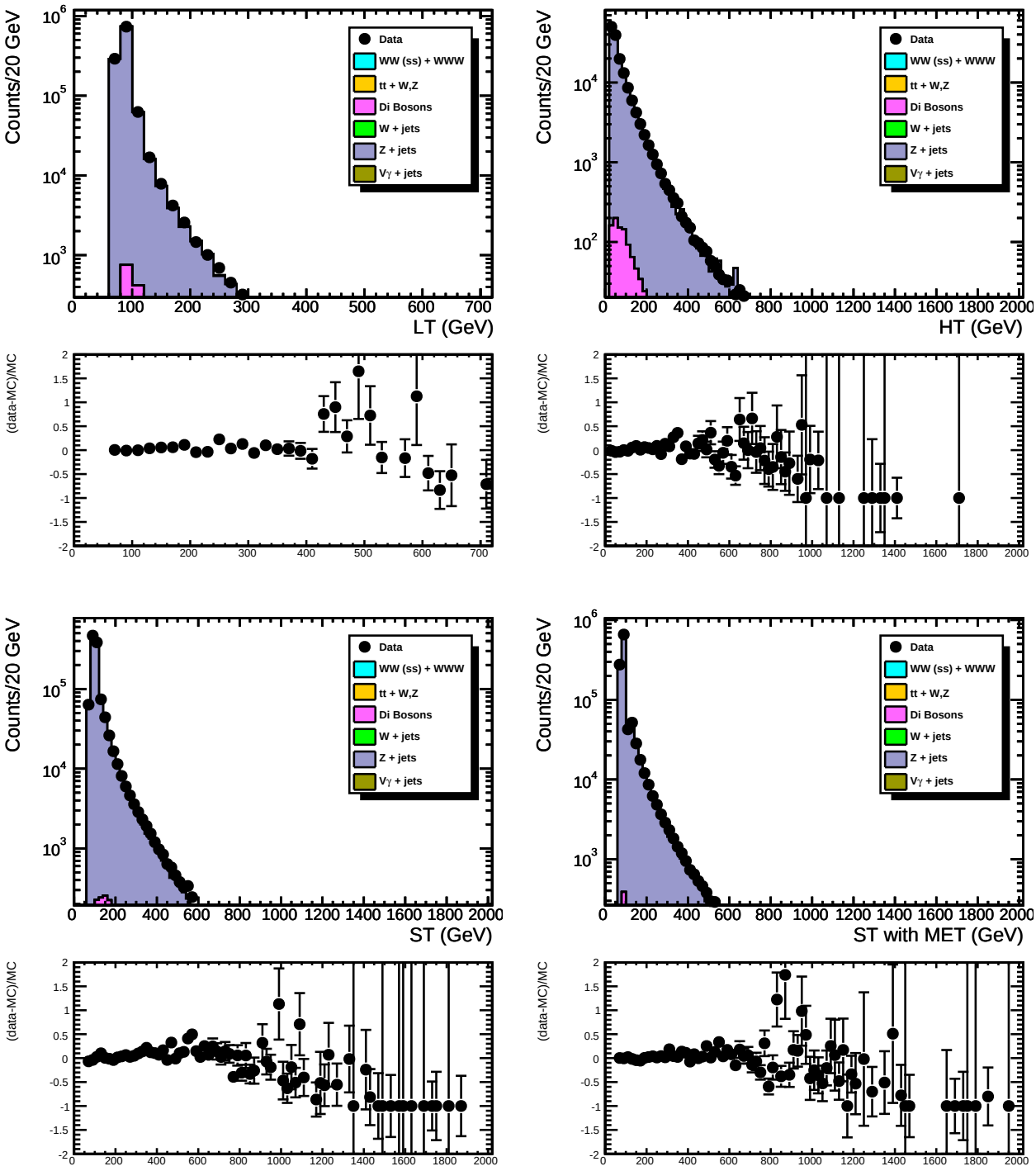

Figure 7.6: Di-muon datasets. Event plots for 2011 two opposite-sign muon events: LT, H_{T}, S_T distributions.

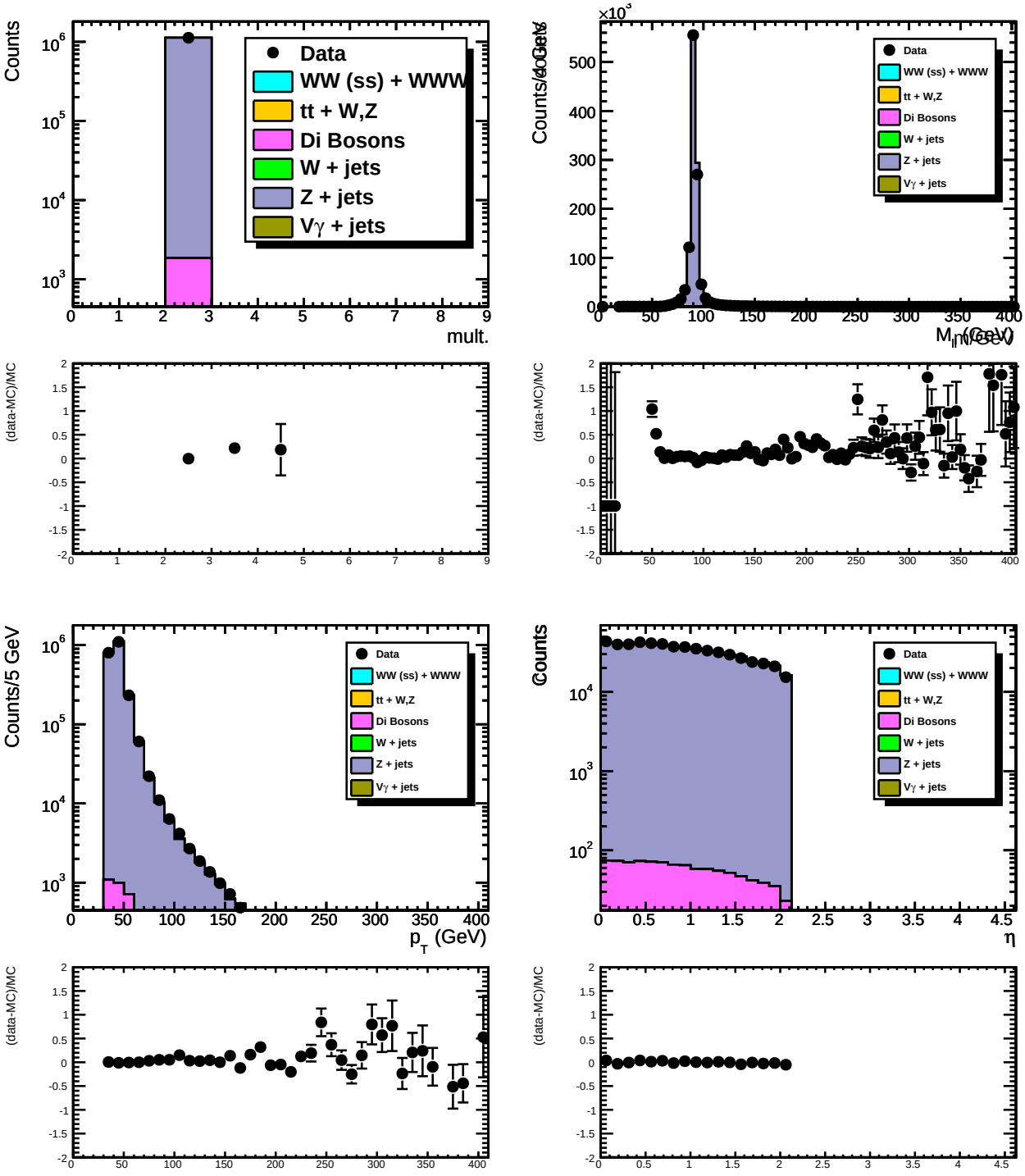

Figure 7.7: Di-muon datasets. Event plots for 2011 two opposite-sign muon events: multiplicity, M_{ll}, p_{T}, η distributions.

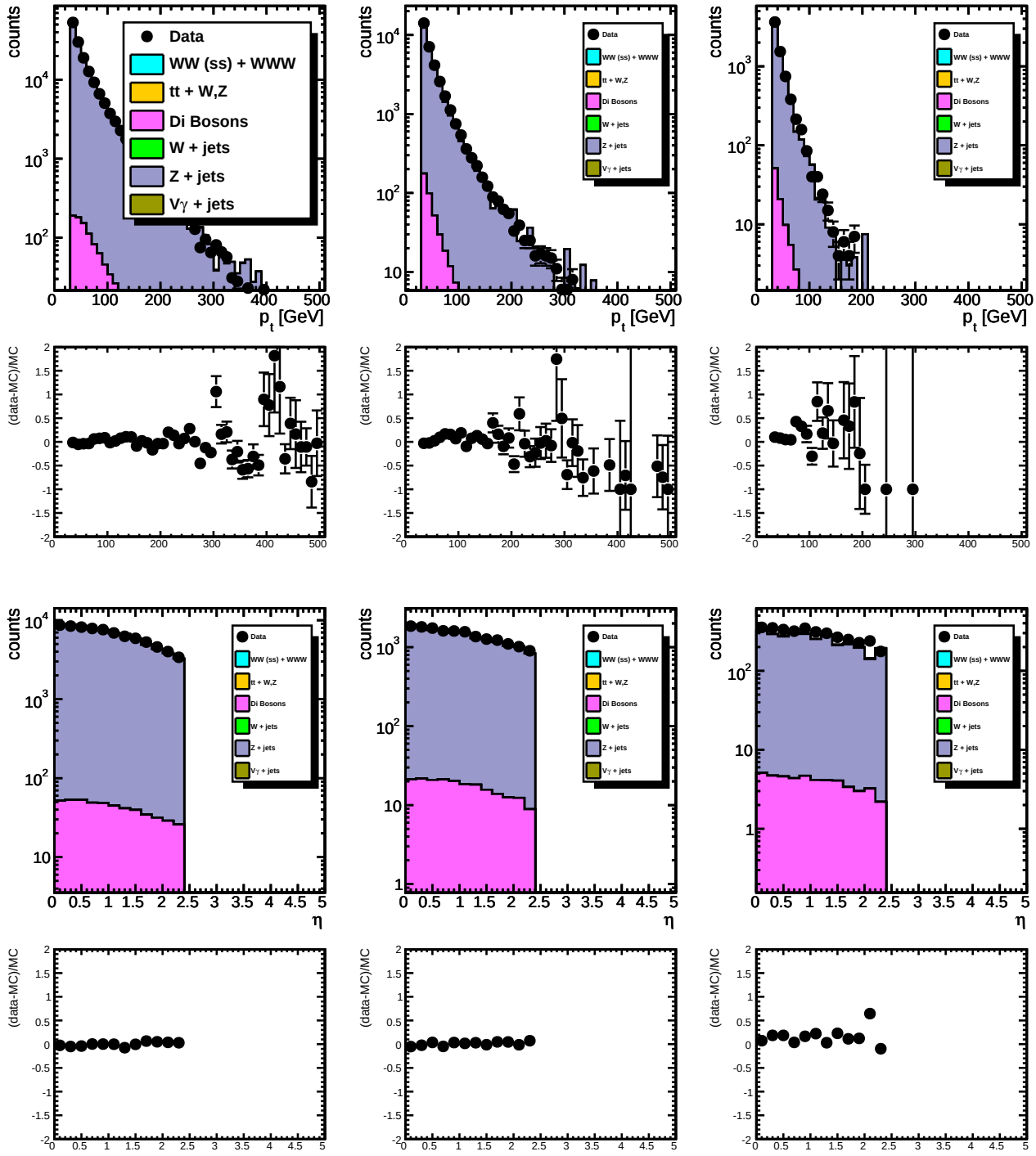

Figure 7.8: Di-muon datasets. Event plots for 2011 two opposite-sign muon events: jet $p_{\mathrm{T}}$and η distributions, from the first (left) to the third (right) jet, in p_{T}descending order.

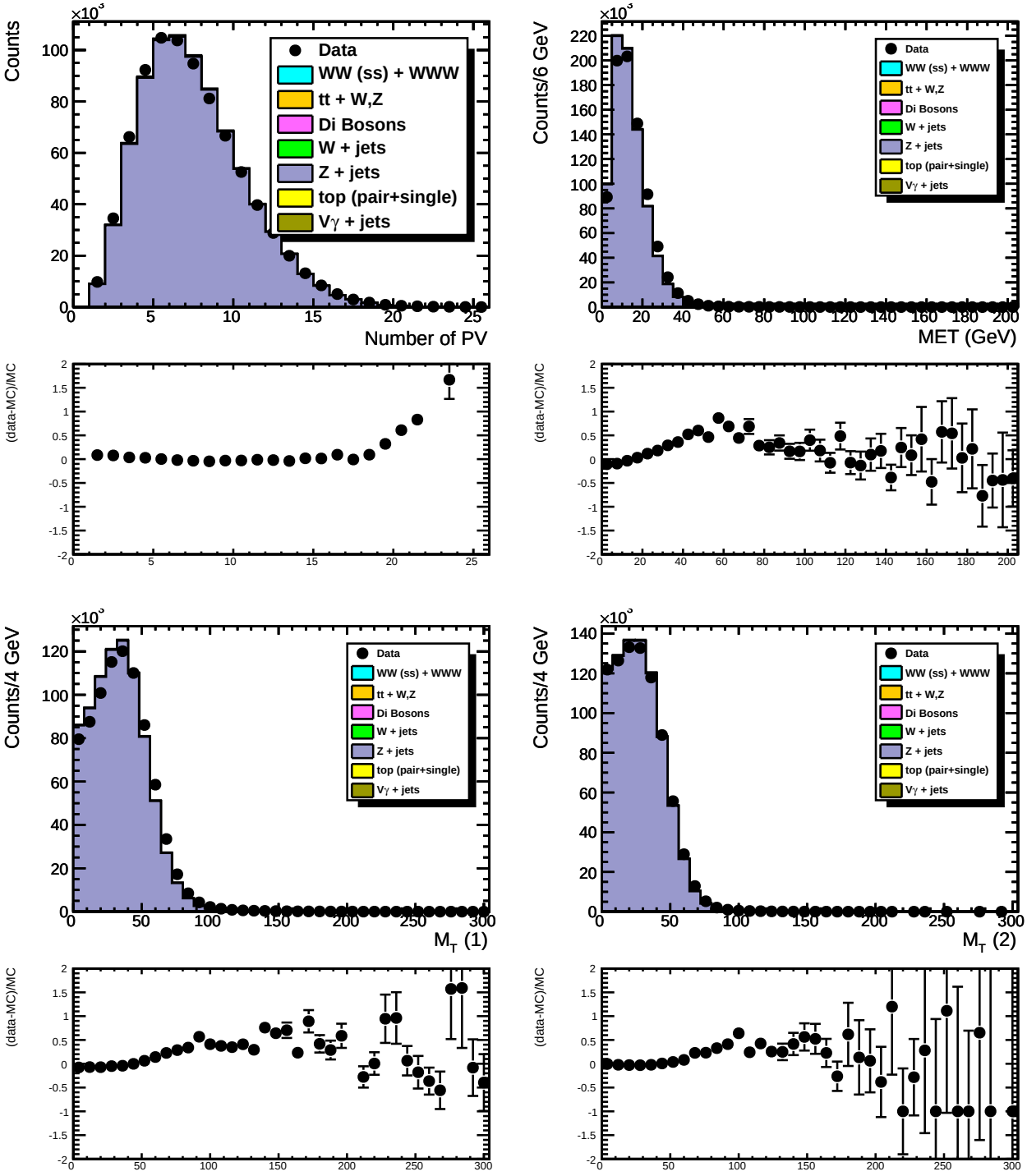

Figure 7.9: Di-electron datasets. Event plots for 2011 two opposite-sign electron events: PV, $E_{\mathrm{T}}^{\mathrm{miss}}$, M_T distributions.

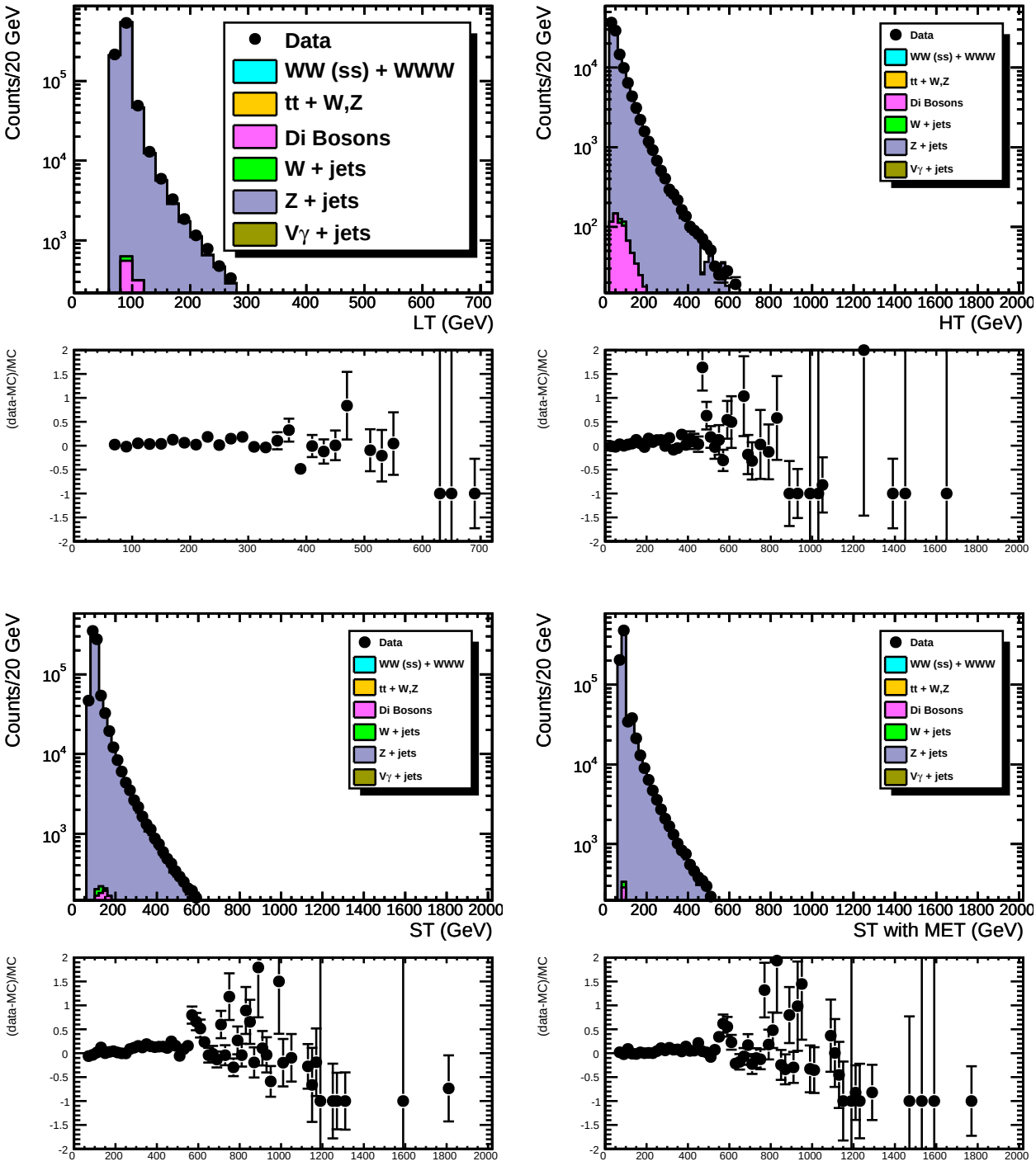

Figure 7.10: Di-electron datasets. Event plots for 2011 two opposite-sign electron events: LT, H_{T}, S_T distributions.

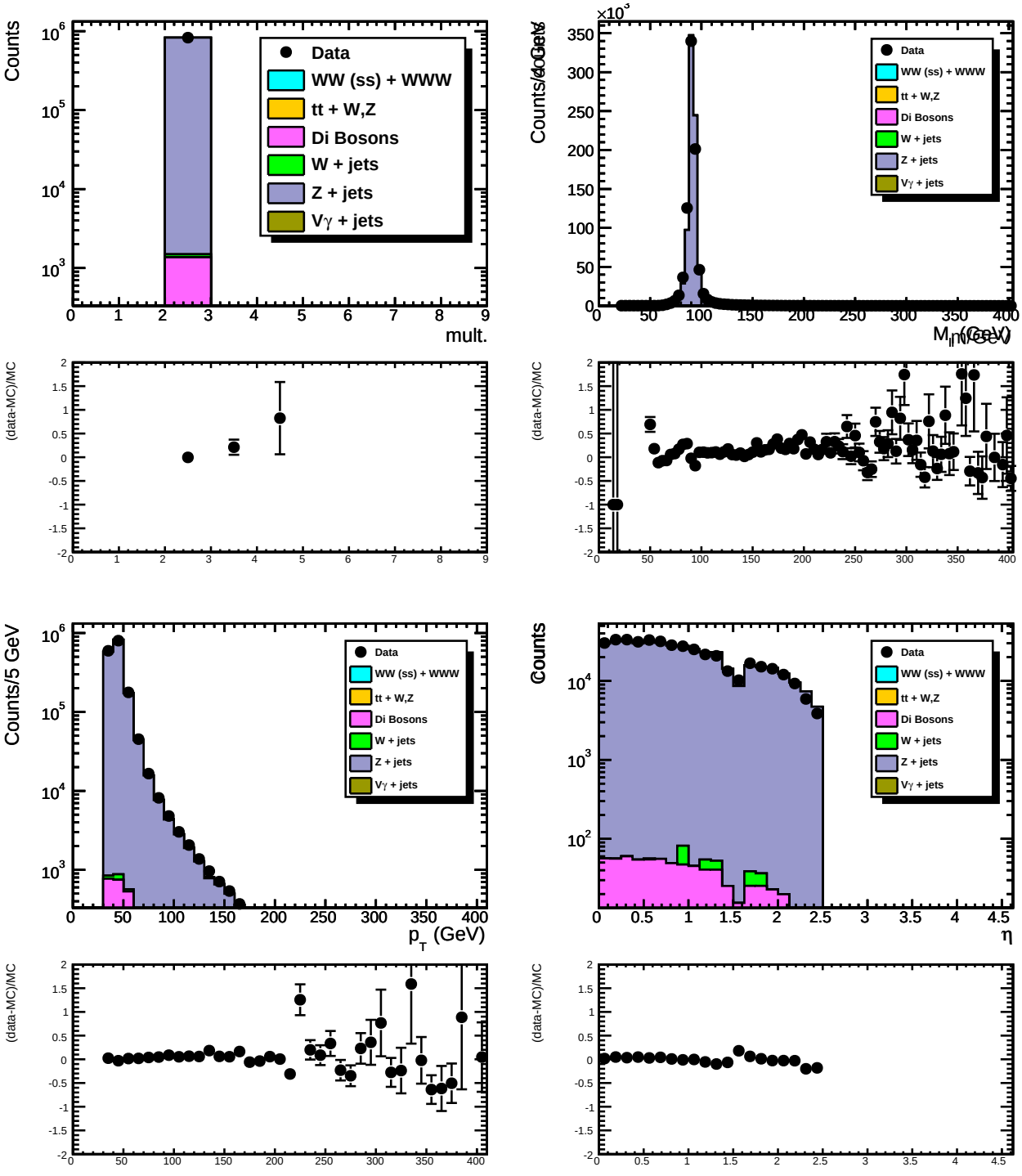

Figure 7.11: Di-electron datasets. Event plots for 2011 two opposite-sign electron events: multiplicity, M_{ll}, p_{T}, η distributions.

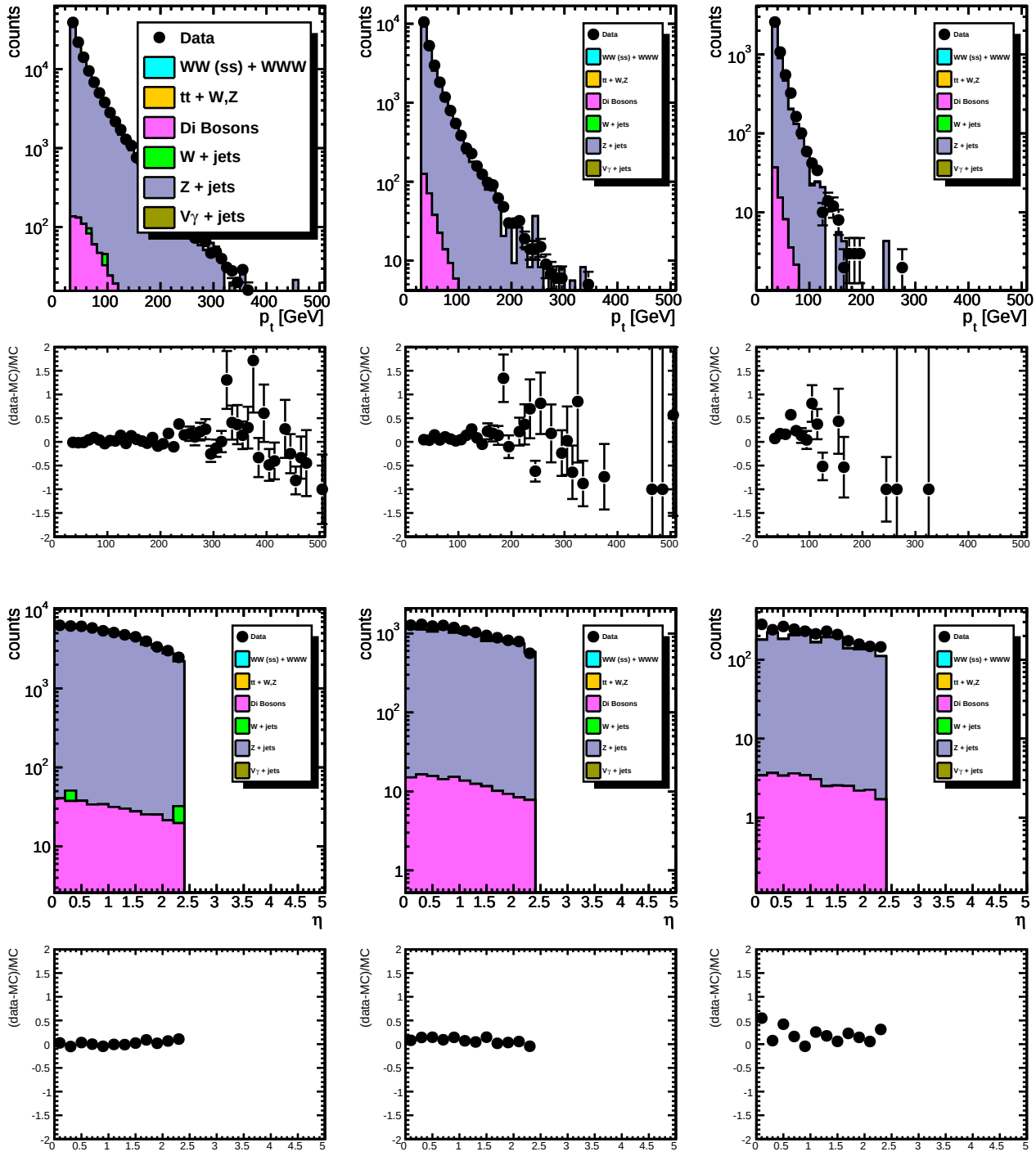

Figure 7.12: Di-electron datasets. Event plots for 2011 two opposite-sign electron events: jet $p_{\mathrm{T}}$and η distributions, from the first (left) to the third (right) jet, in p_{T}descending order.

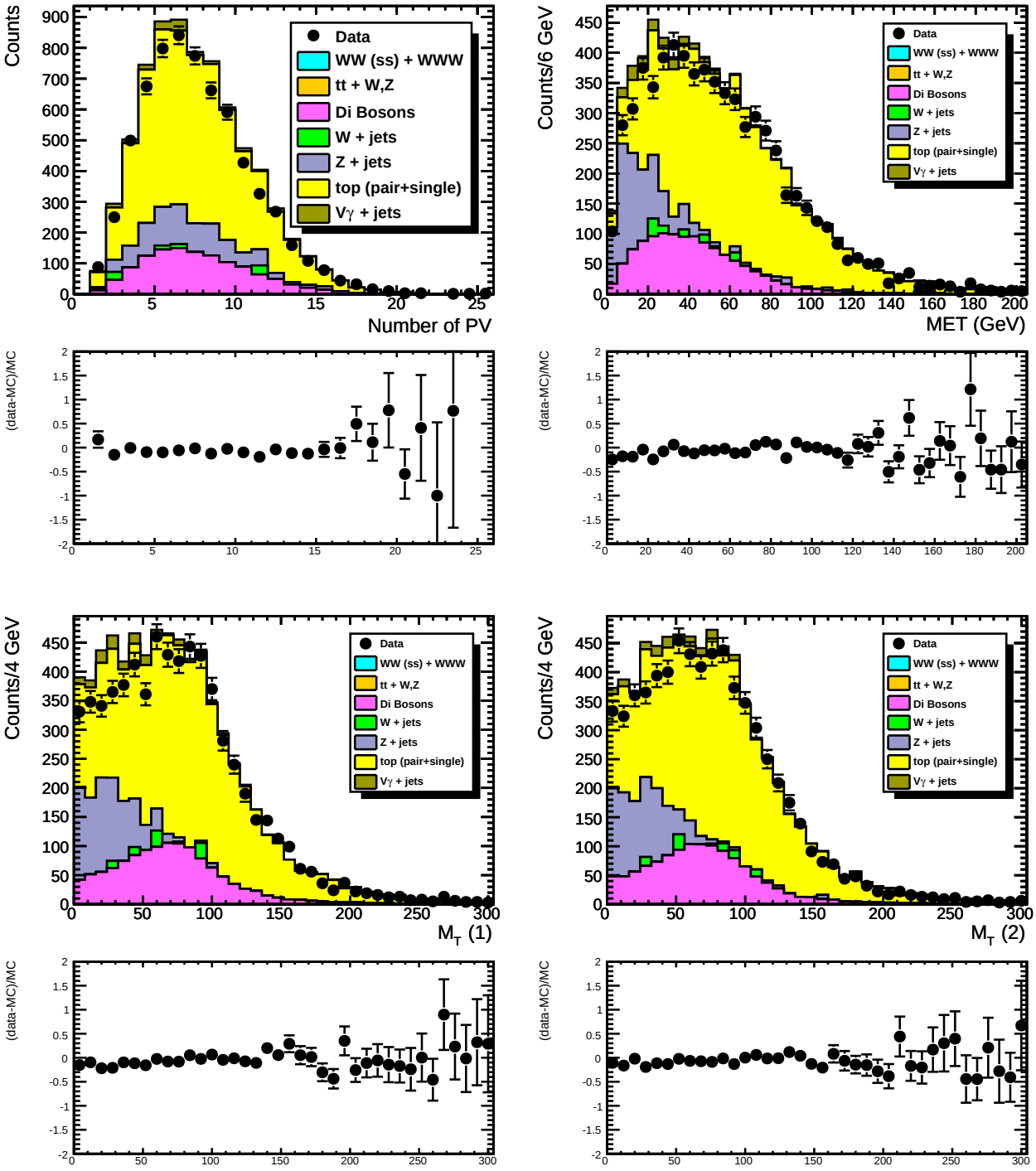

Figure 7.13: Electron plus muon datasets. Event plots for 2011 two opposite-sign electron plus muon events: PV, $E_{\mathrm{T}}^{\mathrm{miss}}$, M_T distributions.

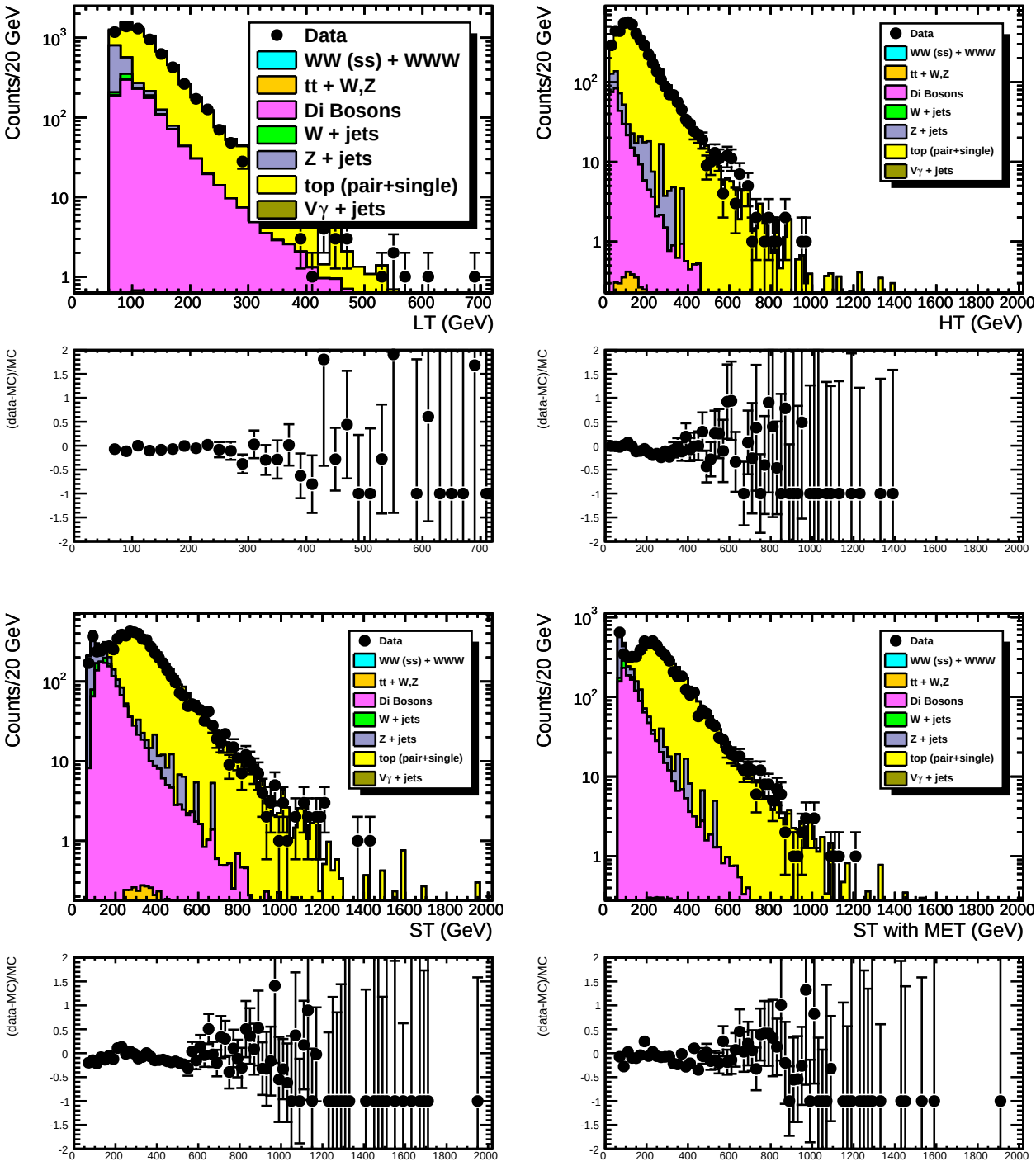

Figure 7.14: Electron plus muon datasets. Event plots for 2011 two opposite-sign electron plus muon events: LT, H_{T}, S_T distributions.

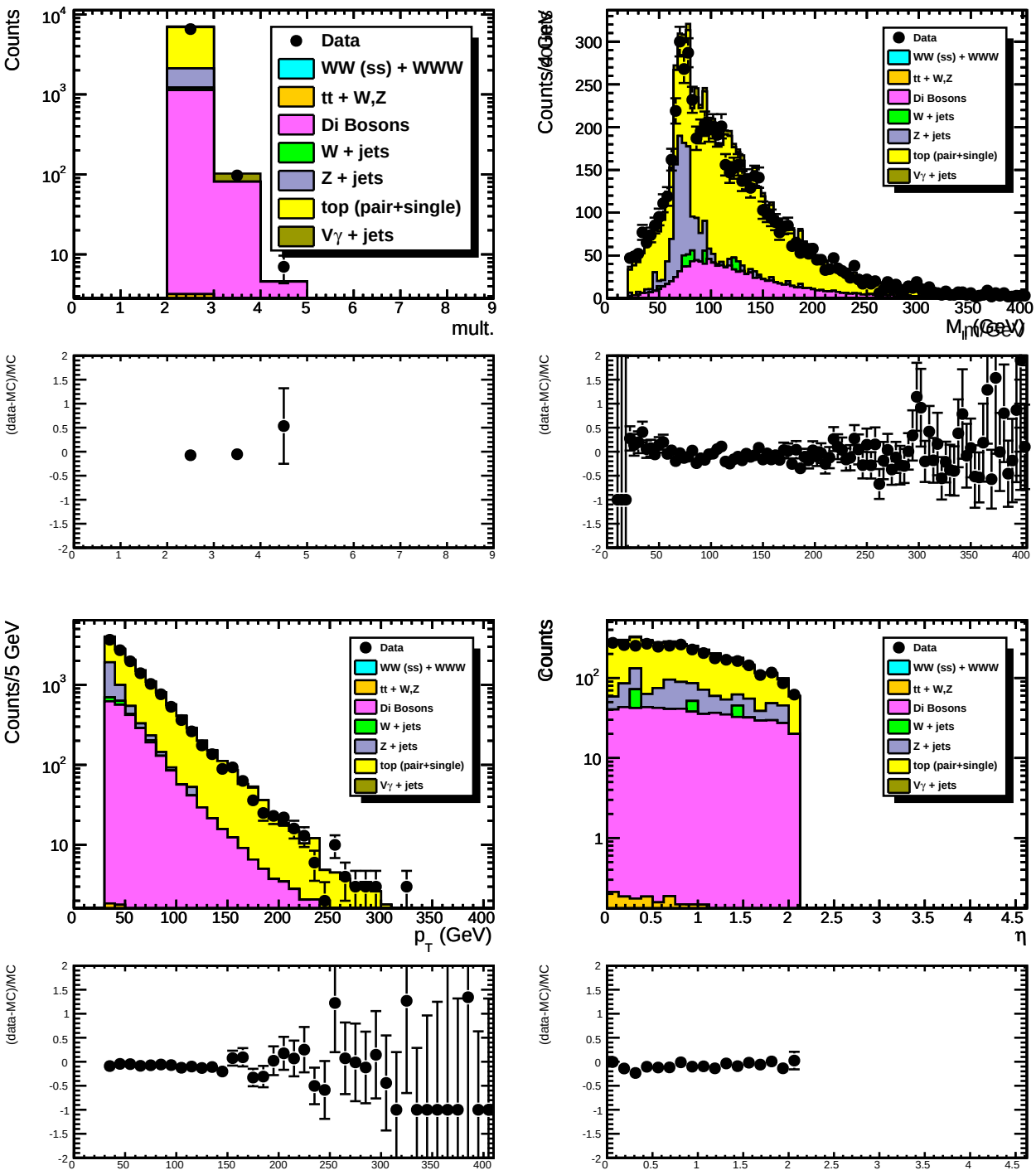

Figure 7.15: Electron plus muon datasets. Event plots for 2011 two opposite-sign electron plus muon events: multiplicity, M_{ll}, p_{T}, η distributions.

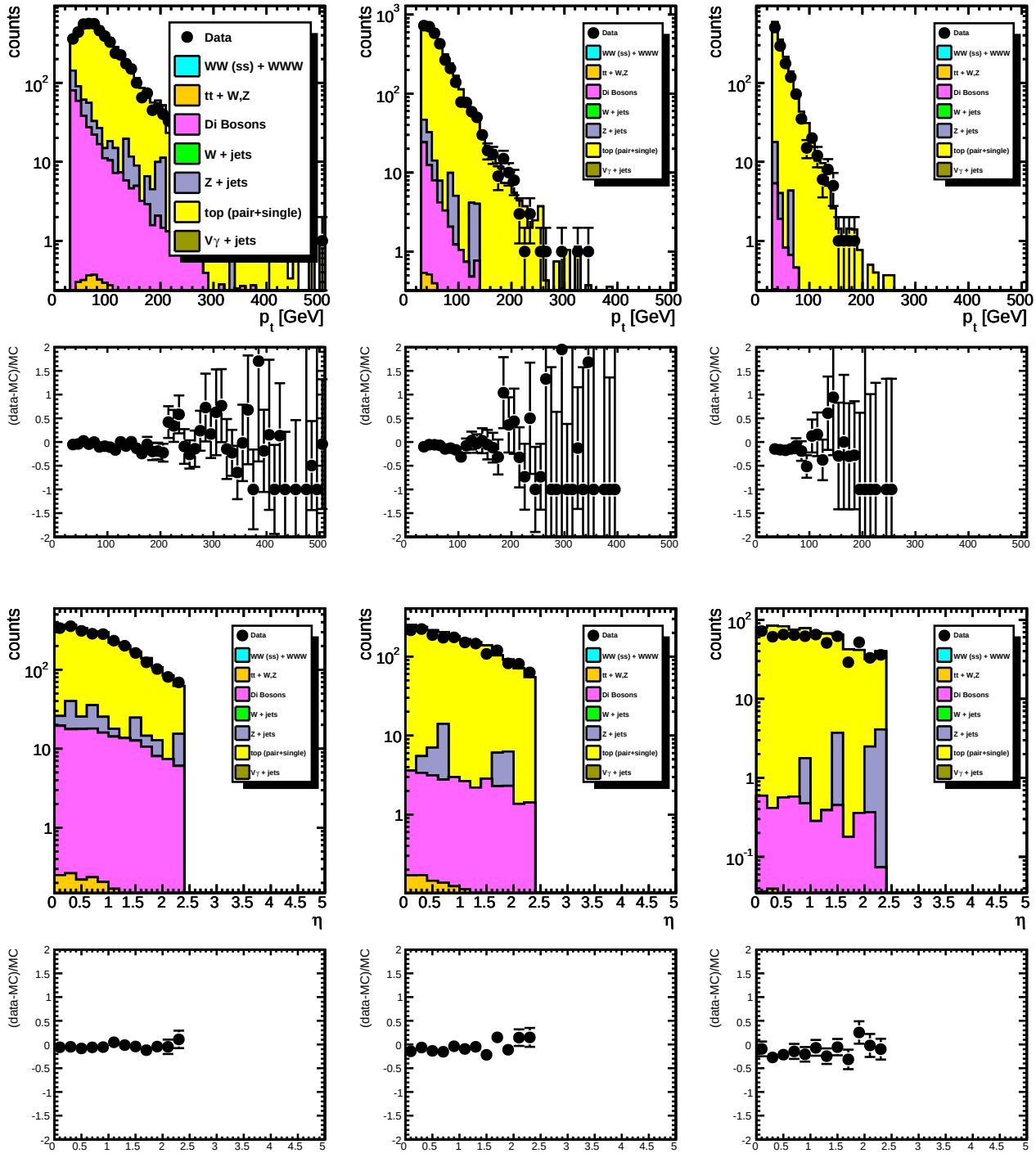

Figure 7.16: Electron plus muon datasets. Event plots for 2011 two opposite-sign electron plus muon events: jet $p_{\mathrm{T}}$and η distributions, from the first (left) to the third (right) jet, in p_{T}descending order.

8

Backgrounds Analysis

8.1 Introduction

The background is defined as a process that can mimic the signature of the signal. Background evaluation is crucial for a correct estimation of the discovery potential of a signal. In evaluating the background sources for a particular analysis, we need to focus carefully on the physical processes which could give the same final state we are looking for, and, in addition, on all other instrumental effects which could mimic the signature as well.

With this in mind, the background contributions are often classified into two categories:

1. **Physical**: i.e. physical processes ending in the same final states, both at generator level and at showering level.

2. **Instrumental or non-physical**: pile-up, mis-calibration of jets, charge mis-identification, mis-identified leptons or *fakes*[1]; charged leptons missed by the detector[2].

In the following sections we will list all possible background sources for the signal channels we are analyzing. In case the background source is relevant, we will describe in detail the contribution and the strategy for removing it.

[1] Fake events are defined as real leptons from the unrelated parts of the event (underlying event), or a hadronic track misidentified as a lepton, or non-prompt leptons coming from decays of heavy particles as t and b quarks and τ

[2] A charged lepton could be missed by the detector, for example if it is located inside a hadronic jet and thus it is not isolated

8.2 Backgrounds for Multi-Lepton Final State

As a preliminary consideration it is important to notice that the request of two hard same-sign leptons (the two coming from the boson decays) nearly removes all SM backgrounds at particle-antiparticle level.

Still, there are standard model processes which can produce a three-lepton final state; following the classification given before, those backgrounds are:

- physical backgrounds: events with three or more real leptons (some of them could be missed by the detector) can be produced by di-boson and tri-boson decays, as explained in Section 8.3;

- non-physical backgrounds: events with one or two real leptons plus fake leptons could be produced by $t\bar{t}$ and $b\bar{b}$, WWj, $c\bar{c}$ and Drell-Yan (γ^* and Z). These will be discussed in Section 8.4.1.

8.3 Real Three-Lepton Backgrounds

The physics backgrounds that can produce three or more real leptons are dominated by SM WZ production, but also include ZZ and tri-bosons production where one of the leptons is either outside the detector acceptance or mis-reconstructed.

8.3.1 Di-bosons

The Standard Model processes can produce 3 or more real, prompt leptons with $E_{\mathrm{T}}^{\mathrm{miss}}$or H_{T} via diboson+jets production where both bosons decay leptonically. The production of dibosons: ZZ and $W^{\pm}Z$ are illustrated in Figure 8.1. ZZ is a source of background when the Z bosons both decay in $l^{+}l^{-}$, but one of the four leptons is missed by the detector.

The measured cross section by the CMS collaboration (79) for these backgrounds are:

- $\sigma(pp \to WZ + X) = 17.0 \pm 2.4(\mathrm{stat.}) \pm 1.1(\mathrm{syst.}) \pm 1.0(\mathrm{lumi.})$ pb. This will give ~ 60 fb for the final state cross section.

- $\sigma(pp \to ZZ + X) = 3.8^{+1.5}_{-1.2}(\mathrm{stat.}) \pm 0.2(\mathrm{syst.}) \pm 0.2(\mathrm{lumi.})$ pb.

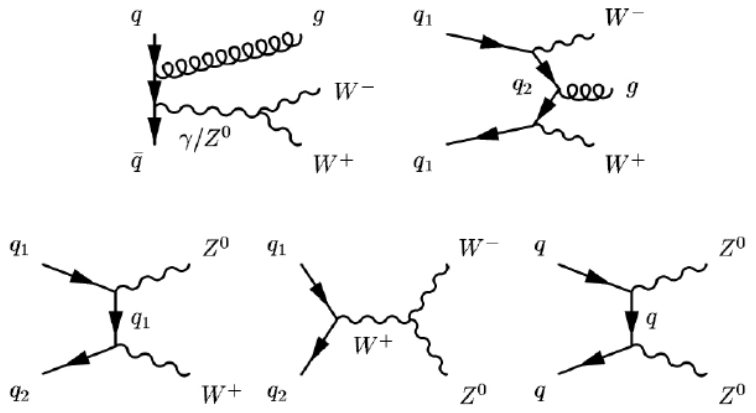

Figure 8.1: The Feynman diagrams of tree-level di-boson production.

Both the production cross section of ZZ and WZ times the branching ratio to three lepton final states are small. However this class of processes is the most important source of background because the characteristics are too similar to the search signature. We will refer to it as *irreducible* background.

Di-boson backgrounds cannot be predicted directly from the data without invoking specific models, therefore they must be obtained from theory and Monte Carlo simulations. Several analysis have checked the simulation against control samples, by comparing it with data samples enriched in WZ-production (the dominant contribution to trilepton signatures from diboson+jets). WZ samples can be selected by requiring three leptons, $E_{\mathrm{T}}^{\mathrm{miss}}$, and an on-shell Z. These analysis show that the simulation describes such a pure sample of WZ events well within the statistical uncertainty of 15%. In this analysis we will use MonteCarlo WZ sample with the cross section measured from data fro normalization.

To reduce the di-boson backgrounds we can use a Z veto to remove them, since A Z is contained in both ZZ and $W^{\pm}Z$ productions. As discussed in Chapter 9, we applied a cut on the invariant mass of two leptons with opposite sign, $|M_Z - m_{ll}| > 10$ GeV to eliminate leptons coming from Z decay. Moreover, it is important to notice that channels without two same-sign-same-flavor leptons, as: $e^-W^+W^+\nu \rightarrow e^-\mu^+\nu\mu^+\nu\nu$

and $\mu^- W^+ W^+ \nu \rightarrow \mu^- e^+ \nu e^+ \nu\nu$ $\mu^- e^+ e^+$, are free from such a background. This will be clarified in Chapter 9 were cuts for the different analysis channels are discussed.

8.3.2 Tri-bosons

Among the 3 gauge bosons backgrounds $3V$ (where V is the generic vector boson), we have considered WWW as the most relevant background source, since it is the one that cannot be removed by Z veto, and it has the highest production cross section[1].

According to Reference (52) the cross section for the background $W^+W^+W^-$ is around $65fb$, and for the opposite sign dataset $W^-W^-W^+$ is around $29fb$.

Anyway, when considering the branching ratio into the final state with leptons, even WWW background is negligible. As a cross check we added this source of background to our analysis and the results are in agreement with the prediction. Since there was no official WWW produced sample, we generated it with Madgraph, and then run the simulation-reconstruction chain. We obtained the computed cross section from Madgraph value to be around $\sigma_{WWW} = 71$ fb for the positive charged sample, which is in agreement with the published values within statical errors.

8.3.3 $V\gamma$

Photon conversions, in presence of W or Z bosons, give rise to isolated leptons forming a source of a background for three-leptons signature searches, very similar to WZ and ZZ.

There are two different types of photon conversions that can give rise to backgrounds in multi-lepton analysis. The first type is an *external conversion* where a photon interacts with the material in the detector and generates an l^+l^- pair. Such conversions primarily produce e^+e^- pairs. The ratio of the rate of external conversions to e^+e^- and the rate of external conversions $\mu^+\mu^-$ is between $6.0 \cdot 10^4$ and $2.0 \cdot 10^5$ (Reference (96)). This is not a dangerous source of background since it could be largely reduced by a requirement on the two opposite-sign-same-flavor leptons invariant mass; as explained in Chapter 9 we put a cut $M(l^+l^-) > 4GeV/c2$.

The second type is asymmetric (internal) photon conversions, and will be discussed in detail in Section 8.3.4.

[1] Considering that Z has a cross section approximately 1/10 respect to the W, then WWZ, WZZ and ZZZ have very small cross sections in comparison

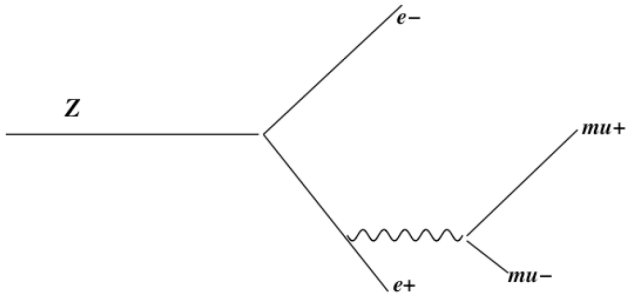

Figure 8.2: A Feynman diagram showing a Z decay to electrons, and an asymmetric FSR decay to muons (indicated by length of the muon legs).

8.3.4 Backgrounds From Asymmetric Photon Conversions (Dalitz Background)

Internal or asymmetric photon conversions involve a virtual photon and one lepton that takes most of the photon energy, and a second lepton very soft and not measured. The internal conversion can produce muons almost as often as electrons.

The most important source of background from internal photon conversion for this analysis involves Z bosons decaying to leptons, and one of the leptons radiating an off-shell photon, γ^* (FSR), and γ^* undergo an asymmetric conversion. The FSR would cause the invariant mass of the leptons from the Z decay to not reconstruct at the Z-pole, and the asymmetric internal conversion would add one more lepton to the event. Figure 8.2 shows a diagram of this process. The Z is shown decaying to electrons, and the e^+ emitting an FSR γ^* which produces a $\mu^+\mu^-$. If one of the muons carries most of the γ^* momentum, this could appear as a 3-lepton event. In such events, the invariant mass of the l^+l^-l shows a peak in correspondence to the Z boson mass.

Both $Z+\gamma$ (ISR) and $Z \rightarrow l^+l^-\gamma$ (FSR) can clearly be seen in the data by plotting the $M(l^+l^-\gamma)$ mass versus $M(l^+l^-)$. The FSR band is seen spread along at the x-axis at 90 GeV on the y-axis. The ISR band is seen spread along the y-axis at 90 GeV on the x-axis. The 3-body z-peak is a clear indication that the photon (or third lepton) involved is produced by FSR. If on-resonance $Z \rightarrow l^+l^-$ has FSR on one of the legs, the dilepton mass will be pushed off the Z peak. However, the 3-body mass of the $l^+l^-\gamma^*$ will still be on the Z peak. We find clean FSR events in CMS 2011 data by searching for a 3-body Z peak as shown in Figure 8.3 for muons and 8.4 for electrons.

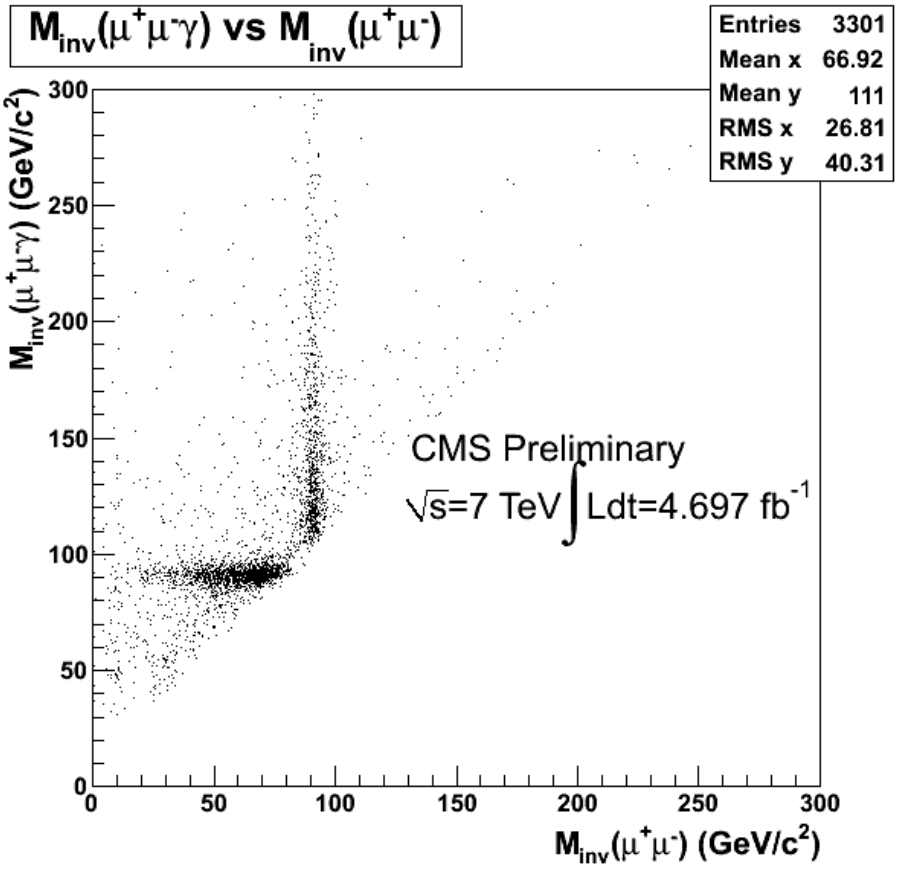

Figure 8.3: $M_{\mu^+\mu^-\gamma}$ versus $M_{\mu^+\mu^-}$.

Internal conversions are an important background to any analysis with leptons and may be underestimated by various MC generators. While MC generators do simulate internal conversion of emitted photons, by necessity they have a cutoff on the conversion lepton momentum. Therefore highly asymmetric conversions, with one of the leptons at $p_T \leq 1GeV/c$ and the other one carrying all the momentum of emission, is not properly accounted for. This is shown in Figure 8.5, were the invariant mass of the three leptons measured in data is compared to those obtained in simulation in events where no OSSF dilepton pair forms an invariant mass of Z boson, after all analysis selections. The disagreements seen in the figure confirms that MC samples do not properly account the internal conversion process, and it motivates the need for a data-based determination of photon conversion factors.

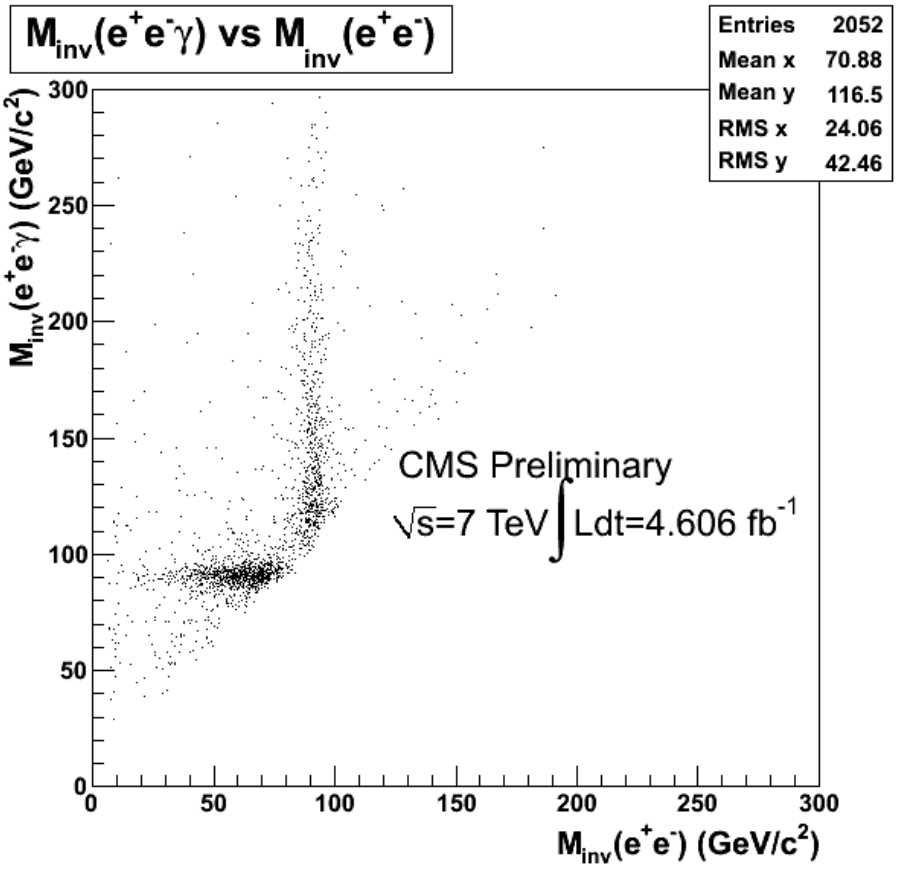

Figure 8.4: $M_{e^+e^-\gamma}$ versus $M_{e^+e^-}$.

For these reasons, we used a data driven method to estimate the background due to asymmetric photon conversions. In this method, we assume that the rate for standard model to produce on-shell photons is proportional to the rate for producing virtual photons that yield asymmetric conversions. The conversion factor is a ratio of the probability for a photon to produce a valid lepton candidate via asymmetric conversion divided by the probability for the photon to be on-shell and pass all photon selection criteria.

Several analysis have computed the conversion factors from final state radiation (FSR) of the Z for both muons and electrons. See References (96) and (97), were the conversion factors is measured in a control region devoid of new physics (e.g. low $E_{\mathrm{T}}^{\mathrm{miss}}$and high H_{T}) . To get the conversion factor the number of $l^+l^-l^\pm$ on the Z peak

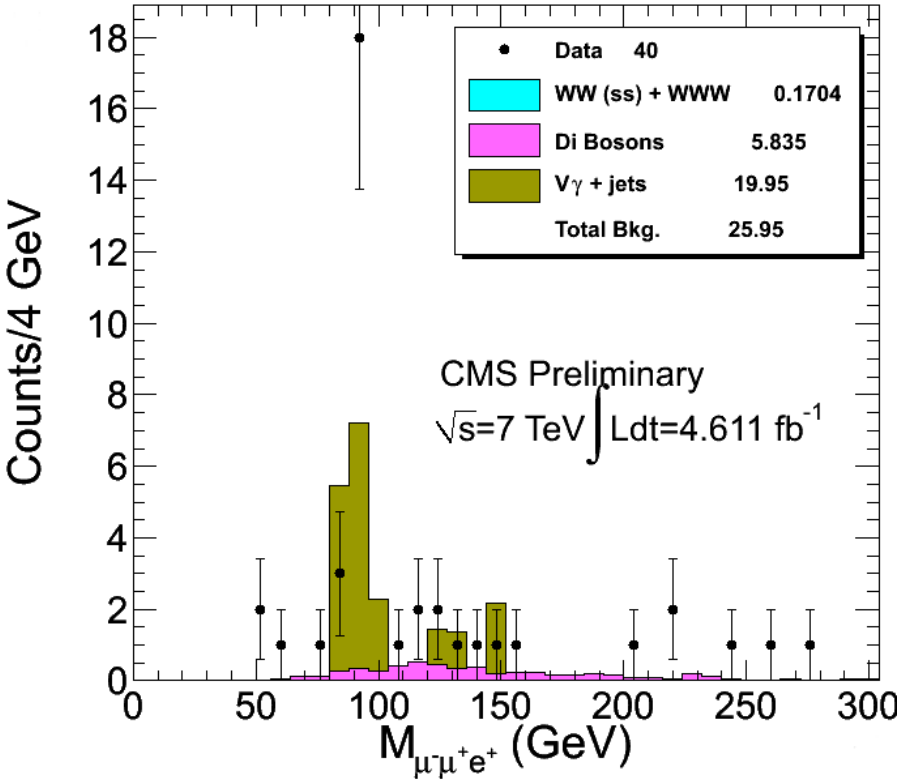

Figure 8.5: Three-lepton invariant mass distributions after Z veto (on OSSF dilepton pairs) and all our analysis selections, in $\mu^+\mu^-e^+$ channel. The disagreement shows that the MC fails to get the conversion background correctly, thus motivating the data-based measurement of photon conversion factors as described in the text.

is divided by the number of $l^+l^-\gamma^*$ on the Z peak. Figure 8.6 on the left from Reference (97) shows the 3-body mass $l^+l^-\gamma^*$ in data where the l^+l^- is not on the Z peak (< 75 GeV and > 105 GeV). Figure 8.6 on the right shows the 3-body $l^+l^-e^\pm$ peak where no opposite sign same flavor (OSSF) pair makes a Z candidate. Reference (97) reports the following values for conversion factors: $C_\mu = 0.35\% \pm 0.10\%$ for muons and for electrons $C_e = 1.1\% \pm 0.2\%$ where uncertainties are statistical only, and systematic uncertainties have been determined to be again 100%.

Reference (96) reports a measured conversion factor for muons $C_\mu = 0.5\% \pm 0.15\%$ and for electrons $C_e = 1.5\% \pm 0.2\%$ where uncertainties are statistical only. Theoretical systematic uncertainties have been determined to be 100% to these conversion factors

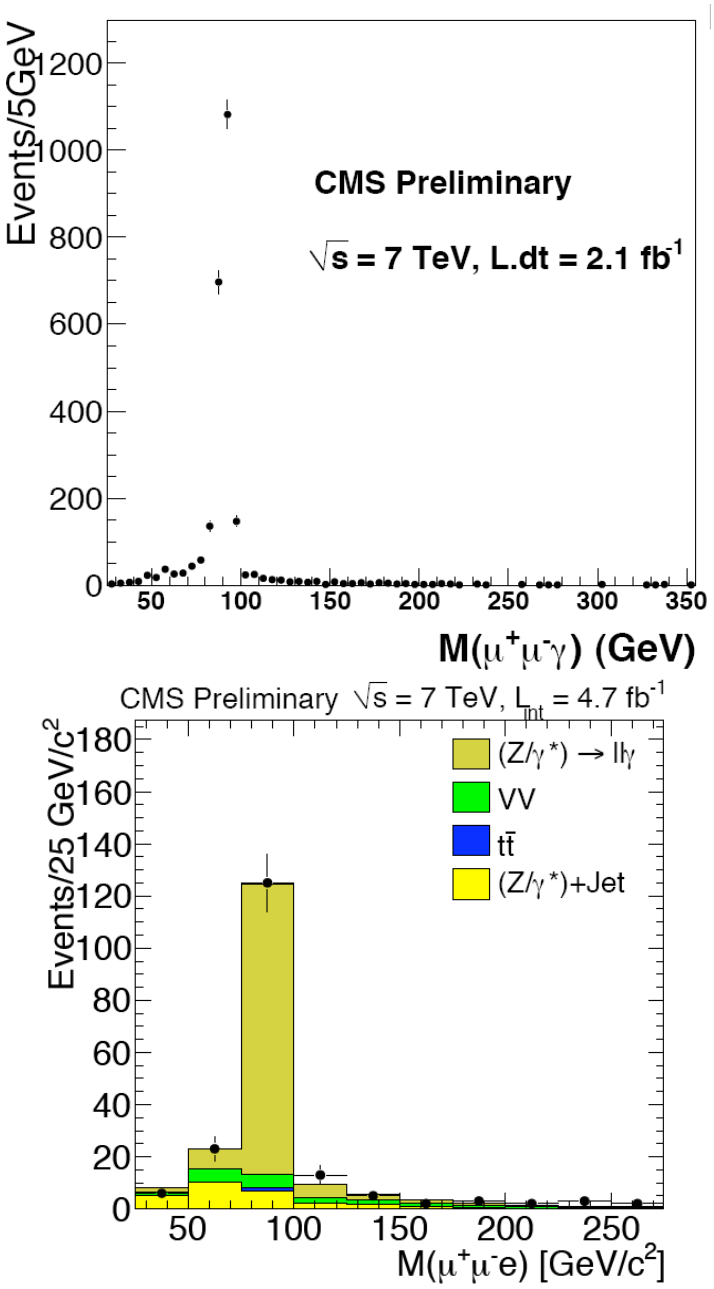

Figure 8.6: $M(l^+l^-\gamma)$ (Left) and $M_{l^+l^-e^\pm}$ (bottom), where $M(l^+l^-)$ is outside the range $[75, 105]$ GeV. Reference (97)

.

from the underlying assumption that the number of isolated photons is proportional to the number of leptons from asymmetric internal and external conversions.

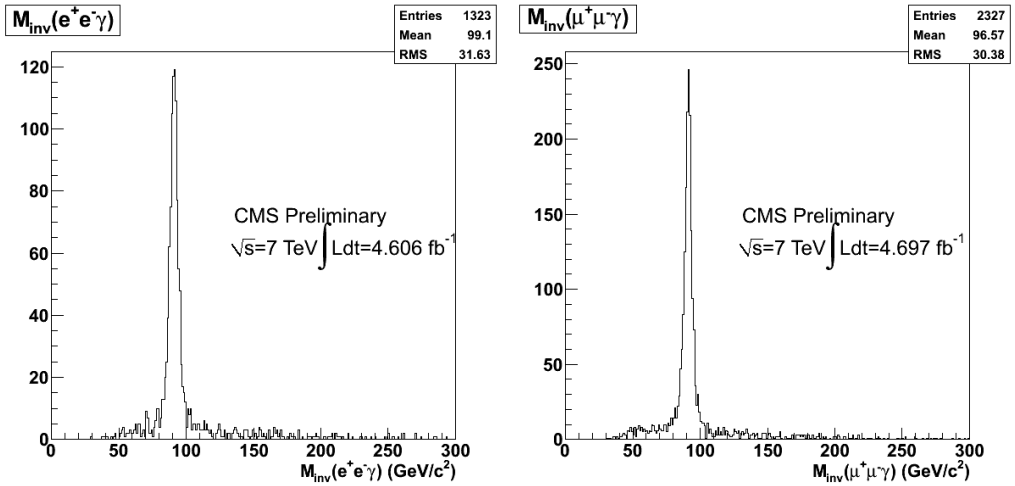

Figure 8.7: On the left: $M(e^+e^-\gamma)$ where $M(e^+e^-)$ is outside the range $[82, 102]$ GeV and all our analysis selections have been applied. On the right: $M(\mu^+\mu^-\gamma)$ where $M(\mu^+\mu^-)$ is outside the range $[82, 102]$ GeV and all our analysis selections have been applied.

Channel	Number of Dalitz Events
$\mu^-e^+e^+$	-
$\mu^-\mu^+e^+$	9.27 ± 1.69
$\mu^-\mu^+\mu^+$	2.95 ± 0.84
$e^-\mu^+\mu^+$	-
$e^-\mu^+e^+$	1.69 ± 0.48
$e^-e^+e^+$	5.31 ± 0.97

Table 8.1: Dalitz Events - Estimation of the number of events from asymmetric gamma internal conversion. Conversion factor values are: $C_\mu = 0.35\% \pm 0.10\%$ and for electrons $C_e = 1.1\% \pm 0.2\%$. Statistical errors are reported. A systematic error of 100% is assumed in the analysis.

We used the values of C_μ and C_e computed in (97) analysis to estimate the background due to FSR in our signal regions. We found clean FSR events by searching for a 3-body Z peak in the signal region, as is evident from Figures 8.7 for electrons (Left) and for muons (Right). Rescaling the plots with the conversion factors above gives the number of events and distribution of asymmetric photon conversion backgrounds.

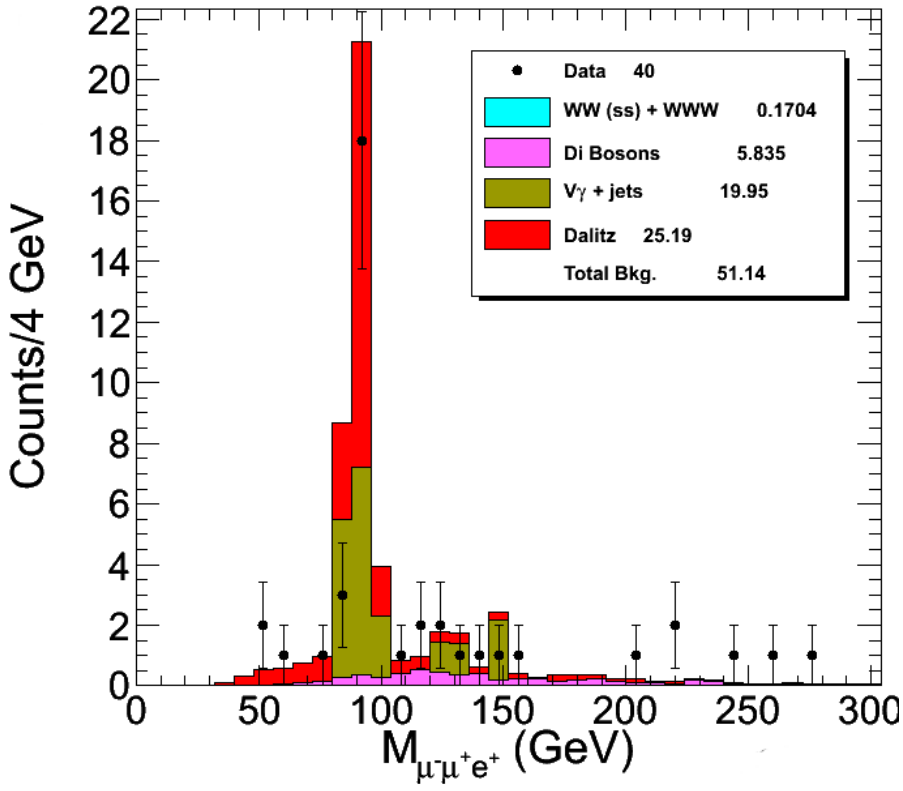

Figure 8.8: $M_{\mu^+\mu^-e^+}$ where $M_{\mu^+\mu^-}$ is outside the range $[82, 102]$ GeV and al other analysis selections are applied.

The error on this background determination is the sum of statistical error plus 100% of systematical error. The results are summarized in Table 8.1.

We compared the data with the data-driven background just described, plus the other source of backgrounds for our signal region, and we find a very nice agreement between data and backgrounds as shown in Figure 8.8 for channel $\mu^+\mu^-e^+$. As will be described in Chapter 9, we decided to remove events within the 3-body Z peak in the range $[82, 102]$ GeV for channels $\mu^+\mu^-e^+$ and $e^+e^-e^+$, since the Dalitz contribution is remarkable. For the other channels we used the data-driven prediction as a source of background since the predicted Dalitz number of events is small and a cut on the 3-body Z peak would reduce the efficiency of the signal.

8.3.5 Opposite sign prompt-prompt Leptons

Prompt leptons could be mis-reconstructed with the wrong charge leading to a same-sign di-lepton final state. Therefore processes with two prompt leptons that have opposite sign can contribute to the Seesaw background if the charge of the negative charged lepton is incorrectly identified, and another negative charged lepton is present in the event.

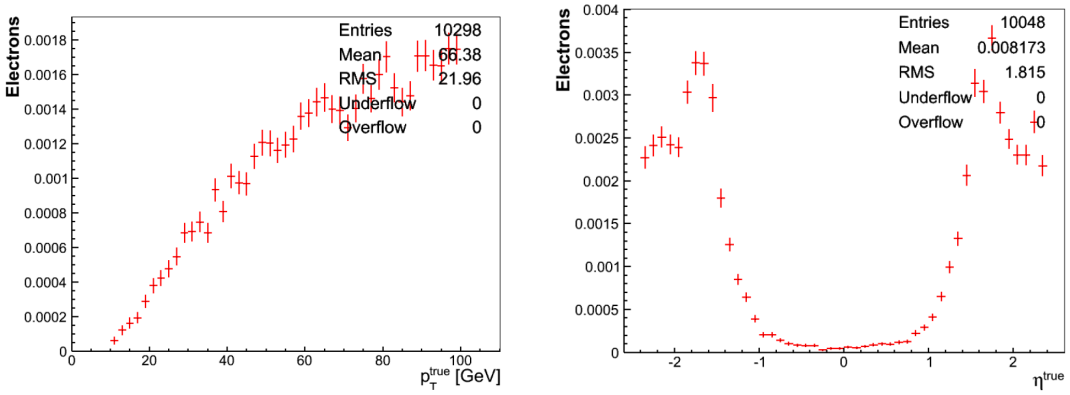

Figure 8.9: Projection of the charge mis-identification rate onto p_T (Left) and η. Reference (103).

The magnitude of this contribution can be derived from the Monte-Carlo backgrounds and for data by using the Z-boson resonance. We have checked the contribution for 2 same-sign events, passing all cleaning, trigger, and lepton quality cut requirements. The fraction of misidentified leptons is obtained by considering events with two leptons of the same flavor in which the invariant mass of the leptons falls inside the Z-mass window: 76 GeV $< M(ll) <$ 106 GeV. As can be seen in the Table 8.2, this sample is expected to be dominated by Z+Jets. For electrons, Z+Jets dominates both the overall sample and the same sign sub-sample whereas for muons, the simulation predicts the rate of charge mis-identification to be negligible.

The results of applying the same method to data are shown in Table 8.3. They are consistent with the prediction taken from Reference (103) and shown in Figure 8.9. The probability of misidentifying the charge of each lepton is computed by assuming that the entirety of the same sign contribution is due to misidentified Z+Jets events.

Electrons								
	Total Bckd	$t\bar{t}$	ZJets	W+Jets	$W^{\pm}W^{\pm}$	WWW	$t\bar{t}W$	$t\bar{t}Z$
In Z-Window	8.69e+05	600	8.68e+05	32.4	0.0929	0.536	0.456	1.48
Same Sign	992	1.01	981	9.38	0.0929	0.343	0.264	0.0717
Muons								
	Total Bckd	$t\bar{t}$	Z+Jets	W+Jets	$W^{\pm}W^{\pm}$	WWW	$t\bar{t}W$	$t\bar{t}Z$
In Z-Window	1.08e+06	723	1.08e+06	0	0.130	0.600	0.500	1.68
Same Sign	2.19	1.37	0	0	0.130	0.332	0.308	0.0474

Table 8.2: Expected events yields within the Z invariant mass window (76 GeV $< M(ll) <$ 106 GeV) for backgrounds.

	In Z-Window	Same Sign	Mis-ID Probability
Electrons	857241	1010	5.89E-4
Muons	1107821	27	1.22E-5

Table 8.3: Events yields within the Z invariant mass window (76 GeV $< M(ll) <$ 106 GeV) for electrons and muons in data and the estimated charge mis-identification probability based on these events.

To confirm that this upper limit is close to the true probability, we consider the di-lepton invariant mass spectrum shown in Figure 8.10. In the case of electrons, both the simulation and the mass spectrum suggest that the upper limit is close to the true probability (within approximately 1% according to the simulation). For muons, the charge misidentification probability is so small that we use the upper limit in its place.

The number of expected same sign events due to charge mis-identification can be estimated from the mis-ID probability in Table 8.3. The contribution for the seesaw final state selections, requiring three leptons with charge ++- can be considered negligible for both electrons and muons.

8.4 Non-Physical Backgrounds

8.4.1 Real Plus Mis-identified Leptons Events

One or two true prompt leptons resulting from SM processes together with isolated tracks or leptons that are mis-identified as prompt leptons gives rise to a multi-lepton background. Isolated tracks can be mis-identified as an electron or muon because of

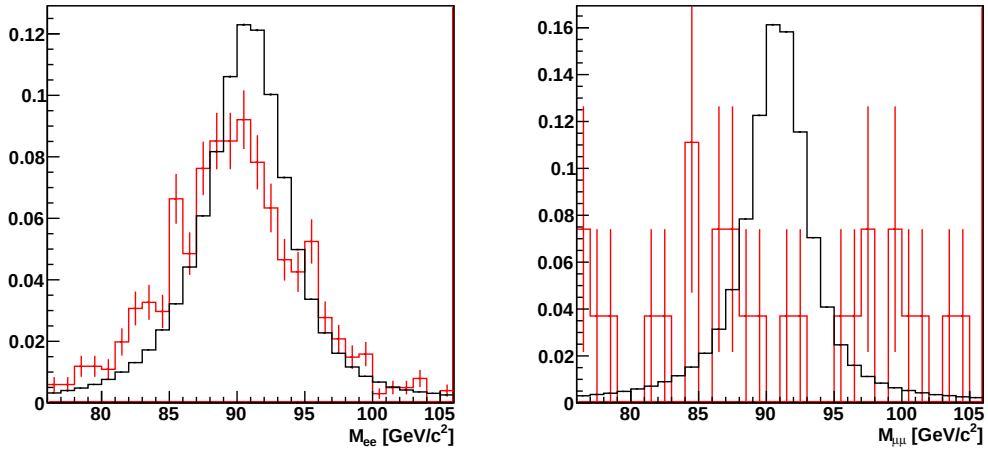

Figure 8.10: Di-lepton invariant mass spectrum in data for electrons (left) and muons (right). The opposite sign distributions are shown in black and the same sign ones are in red. All distributions are normalized to unit area.

the overlap of a hadron with an electromagnetic or an hadronic shower (with a large electromagnetic component) or from a punch through of a hadronic shower. Moreover, leptons that are misidentified as prompt can be real leptons from the decay of mesons which satisfy the isolation and vertex criteria of the prompt leptons, but are not from the physical process of interest, thus the name *fake*.

Throughout this thesis, we refer to as *fake lepton* any lepton that is not a prompt isolated lepton from a W, Z, γ or some beyond the standard model source. In particular, muons from K/π in flight decay, electrons or muons from heavy flavor decay, etc. are all referred to as *fake leptons*.

Processes which can produce two real leptons plus a fake lepton, relevant for our analysis, include Drell-Yan (γ^* and Z) plus jets, and WWj production. Processes which can produce one real leptons plus two fake leptons, as for example Wjets, are less relevant because the probability to have two fake leptons that pass the standard isolation requirements is very low.

8.4.1.1 Drell-Yan (γ^* and Z) + Jets

The largest background remaining after the basic three-lepton reconstruction originates from the Z+jets process (including Drell-Yan production), in which the Z boson decays

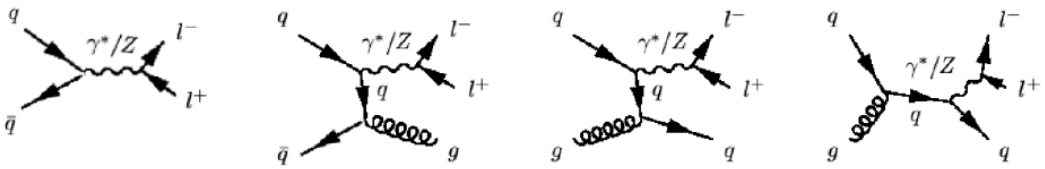

Figure 8.11: The Feynman diagrams for leading and some higher order Drell-Yan production.

leptonically and a third fake lepton is produced from a jet in the event. The Feynman diagrams for leading and some higher order Drell-Yan productions are shown in Figure 8.11.

The Drell-Yan background can be split up into three categories, depending on the energy scale. The list of the processes and the strategy for removing each category of events is the following:

- $q\bar{q} \rightarrow \gamma^* \rightarrow l^+l^-$; events could be removed with an opening angle cut since the virtual photon momentum is low;
- low-pT Z production: $q\bar{q} \rightarrow Z \rightarrow l^+l^-$: leptons are back-to-back on the transverse plain, so they can be removed with an opening angle cut (Z veto would result in efficiency decrease);
- high-pT Z production: $q\bar{q} \rightarrow Z \rightarrow l^+l^-$; leptons will not be back to back so they will be removed with a Z veto.

The Drell-Yan MonteCarlo sample background has been validated by other analysis, in particular: (96).

The conclusion of this analysis is that the MC simulation describes the data well.

Nevertheless, fake rates are very depend upon the particular selections of each analysis, therefore the Drell-Yan process simulation validation performed for a particular analysis cannot be trusted for another analysis. We decided therefore not to consider Drell-Yan process simulation MC datasets, but to estimate it with a data-driven method instead, as described in Section 8.4.5.

8.4.1.2 WW + Jets

Each W can decay semi-leptonically so the WW decay will produce only two real leptons; thus a fake lepton must be present in the event to be accepted by three-lepton selection.

WW process has a large production cross section: at 7 TeV, it has been measured by CMS (77) and ATLAS (78) to be : $\sigma_{WW} = 41.1 \pm 15.3(\text{stat.}) \pm 5.8(\text{syst.}) \pm 4.5\text{lumi.})$ pb and $\sigma_{WW} = 41^{+20}_{-16}(\text{stat.}) \pm 5(\text{syst.}) \pm 1\text{lumi.})$ pb, with an integrated luminosity of 36 and 34 pb^{-1}, respectively. CMS collaboration also found (79) : $\sigma(pp \to WW + X) = 55.3 \pm 3.3(\text{stat.}) \pm 6.9(\text{syst.}) \pm 3.3(\text{lumi.})$ pb.

In spite of a big cross section, our pre-selection cuts (3 charged leptons out of which 2 have the same sign, 2 hard leptons) reduce this background to a negligible level, as will be shown in Chapter 9.

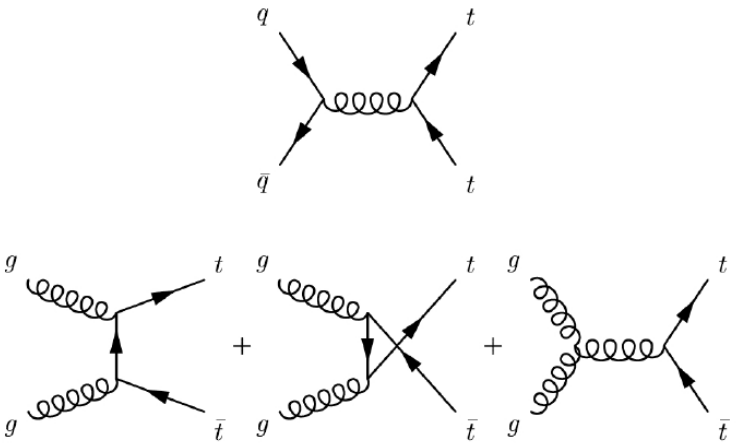

Figure 8.12: The Feynman diagrams of tree-level $t\bar{t}$ production.

8.4.2 $t\bar{t}$

The $t\bar{t}$ production is illustrated in Figure 8.12. A top quark decays via $t \to W^{\pm}b$ (with a branching ratio of 100%). We can get up to two leptons from the $W^{\pm}$ decays [1]. At 7 TeV

[1] One from the t and the other from the $\bar{t}$, and at least a third lepton from the semi-leptonic decay of a b quark.

the production of a top quarks pair has been measured by CMS (75) and ATLAS (76) to be $\sigma_{t\bar{t}} = (173^{+39}_{-32})$ pb and $(171 \pm 20 \pm 14^{+8}_{-6})$ pb, with an integrated luminosity of 36 and 35 pb^{-1}, respectively. Combining the branching ratio $BR(W \to l\nu) = 30\%$ with the 10% of branching ratio for the semileptonic decay of the b, the final cross section for such background should be around $0.15 - 1.5$ pb depending on how many different lepton flavors one expect in the final state.

The simulation of $t\bar{t}$ process has been carefully validated as reported for example in Reference (96).

We have studied the contribution of $t\bar{t}$ background in our signal region and we have found that our isolation criteria nearly kills all this background. From $t\bar{t}$, b and c quarks could decay semi-leptonically and give true leptons indeed, but they should be non-isolated and so are rejected by our isolation requirements discussed in Chapter 6. We have further studied a cut on the number of jets or hadron activity (H_{T}) to reduce this background to negligible levels, and b-tagging have also been considered, as will be discussed in Chapter 9.

Other $t\bar{t}$ background *alterations* could be considered. For example: $t\bar{t}W^{\pm}j$, $t\bar{t}WW$, $t\bar{t}Z$, etc. The presence of one or two bosons in addition to $t\bar{t}$ ensures the presence of three leptons in the final state, if the top decays semi-leptonically. To have an idea of the approximate cross section of these backgrounds, we have computed the production cross section with Madgraph5 package and we have found that the only backgrounds among these that could be relevant are $t\bar{t}$ W, and $t\bar{t}$ Z. We generate 30k events of these processes with Madgraph5, and request the standard simulation and reconstruction processing for Summer 11 CMS production. Anyway, cross section is so low that even these two processes turned out to be irrelevant for our analysis.

8.4.3 $b\bar{b}$

The $b\bar{b}$ production is illustrated in Figure 8.13. A b quark can decay via $b \to Wc \to W(Wd)$. Each W has equal chance of decaying to an electron and a muon, about 11%, thus the probability of both Ws to decay leptonically is about 4%. If either of the W from the $\bar{b}$ also decays leptonically, we will have three real leptons in the event. Charged leptons from b quark decays typically have small transverse momentum, but the cross section for $b\bar{b}$ production at LHC is high, as reported in Appendix D, so the $b\bar{b}$ can be a substantial background. Nevertheless, in our analysis, the same consideration on $t\bar{t}$

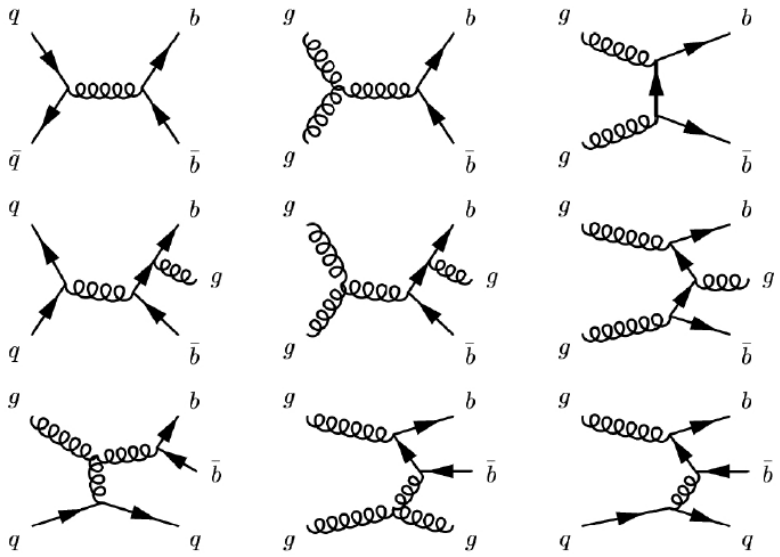

Figure 8.13: The Feynman diagrams for leading and some higher order production of $b\bar{b}$. The production of c is obtained by replacing b with c.

isolation could be applied. Moreover, since the invariant mass of the two leptons coming from the same b hadron is typically below 4 GeV/c^2, we have added this requirement to our selection criteria[1]

8.4.4 QCD

QCD multi-jet events produce all non-isolated fake leptons. The probability for selecting three fake lepton events with the selection requirements of our analysis is deep-low, therefore we neglected this background contribution. We made a quick cross check with QCD simulation [2] and found that at pre-selection level nearly all the QCD events are removed. We decided not to estimate QCD background with a data-driven method because of the considerations above.

[1]Strictly speaking, the two closest leptons between any two of the three lepton candidates (regardless of flavor) must be considered to calculate the invariant mass, i.e. the two that form the smallest spatial angle, because they are most likely to be from the same b quark.

[2]QCD processes are very difficult to simulate, nevertheless several analysis have cross-checked MonteCarlo versus data-driven QCD estimation and no relevant discrepancies have been found.

8.4.5 Data-driven Estimation

As remarked in the previous sections, processes with fake leptons are not properly simulated by the MC, and the samples validations are very sensitive to analysis selections. Therefore, we performed data-driven estimation of all non-physical backgrounds, and add the results to our total background estimation.

The background becomes very small in events with more than one fake lepton: for this reason we have computed the fake contribution both for: one fake lepton plus two real leptons, and two fake leptons plus one real lepton; we have neglected the case with three fake leptons. From now on we will name true-fakes contribution the former, fake-fake contribution the second mentioned.

In general the largest source of the true-fakes contribution is semi-leptonic top or W/Z plus jets events where the second or third lepton comes from a heavy flavor decay. The fake-fake contribution is dominated by pure multi-jet QCD events.

The data driven calculation of the fake contribution is done with the Tight-Loose method described in Ref. (103) and (102).

The following assumptions are made:

- the probability of a lepton to be fake is independent from the presence of another lepton;
- for final states with both μ and electron we consider electron and muon fakes separately, and add them up;
- no correlation is included for the fake-fake lepton case;
- the fake rate as measured in an inclusive QCD sample as described in Ref.(102) is applicable to the case of a QCD object in a lepton plus jet event;
- we assigned a systematic uncertainty of 50% as in Reference (102) to this procedure.

The procedure is in two steps: first the average fake rate is determined using control samples. Secondly the fake rate is applied to the events selected by the analysis. The fake rate is defined as follows: it is the probability for a Loose lepton to pass the Tight identification selection in samples where the presence of prompt isolation leptons is suppressed, and therefore all leptons are candidate fakes. In formula: $FR = N_{TL}/N_L$

Dataset	$FR(A)^{\mu}$	$FR(B)^{\mu}$	$FR(A)^{e}$	$FR(B)^{e}$
/MultiJet/Run2011A-PromptReco-v4	0.27	0.18	0.30	0.19
/MuHad/Run2011A-PromptReco-v4	0.26	0.23	0.20	0.18
/ElectronHad/Run2011A-PromptReco-v4	0.29	0.24	0.28	0.27
/SingleMu/Run2011A-PromptReco-v4	0.40	0.28	0.38	0.19
/SingleElectron/Run2011A0-PromptReco-v4	0.48	0.32	0.41	0.35

Table 8.4: Primary datasets used for the analysis and values of the fake rates obtained for electron and muons with the A and B method.

where N_{TL} = number of Loose leptons passing the Tight criteria, N_L = number of all Loose leptons.

The Tight lepton definition is the one already described in Chapter 9, while the Loose selection is as follows.

For muons:

- χ^2/ndof < 50 (for tight is 10)
- $d0 <$ 2mm (tight $d0 < 0.02$ mm)
- Iso$<$ 0.4 (tight$<$ 0.15)

For Electrons:

- $d0$ cut removed (tight$<$ 0.02 mm)
- Iso$<$ 0.6 (tight $<$ 0.15)

The data samples used to determine the fake rate are samples with suppressed prompt isolated leptons and enriched in non-prompt leptons: QCD-enriched data sample: multi-jets PD (and for cross-check: SingleMu, SingleEle, MuHad, EleHad). All the datasets are listed in Table8.4.

Events are selected with the same kinematics cuts of the analysis and further cuts to reduce prompt leptons from W/Z (away from signal region):

- at least one loose lepton;
- $E_{\mathrm{T}}^{\mathrm{miss}} < 20$ GeV;

Selection:	SS leptons $E_{\mathrm{T}}^{\mathrm{miss}}$> 20 GeV	+ 3 leptons $\geq$ 2 leptons p_T >15 GeV	$+H_T$ <100 GeV b-veto	$+Z_{ll}$ veto Z_{lll} veto
$\mu^-e^+e^+$ channel				
$N_{\bar{n}\bar{n}}$	11	1	1	1
$N_{n\bar{n}}$	57	3	1	1
N_{nn} fakes	20.04 ±3.71	0.99±0.68	0.24± 0.41	0.24 ± 0.41
$\mu^-\mu^+e^+$ channel				
$N_{\bar{n}\bar{n}}$	759	34	25	6
$N_{n\bar{n}}$	1610	114	91	15
N_{nn} fakes	501.49 ±51.64	38.35±5.89	30.92±5.03	4.83±1.59
$\mu^-\mu^+\mu^+$ channel				
$N_{\bar{n}\bar{n}}$	1111	22	17	5
$N_{n\bar{n}}$	758	76	52	17
N_{nn} fakes	124.97±16.50	27.08±5.83	18.21±4.24	6.05±1.99
$e^-\mu^+\mu^+$ channel				
$N_{\bar{n}\bar{n}}$	33	2	0	0
$N_{n\bar{n}}$	62	15	2	2
N_{nn} fakes	18.77 ±3.56	5.4±1.61	0.76±0.54	0.76±0.54
$e^-\mu^+e^+$ channel				
$N_{\bar{n}\bar{n}}$	759	13	7	4
$N_{n\bar{n}}$	1610	52	34	14
N_{nn} fakes	501.49 ±51.64	17.85±3.43	11.89 ±2.63	4.73± 1.54
$e^-e^+e^+$ channel				
$N_{\bar{n}\bar{n}}$	584	13	10	0
$N_{n\bar{n}}$	3972	59	44	7
N_{nn} fakes	1339.78±69.19	19.35±2.92	14.39 ±2.49	2.49±0.95

Table 8.5: Estimation of the number of fake events in the various channels, for the subsequent steps of our analysis selections: from left to right the cuts are applied subsequently. The errors on the fake event values are purely statistic. For a comparison with selected events in the analysis, see Chapter 9.

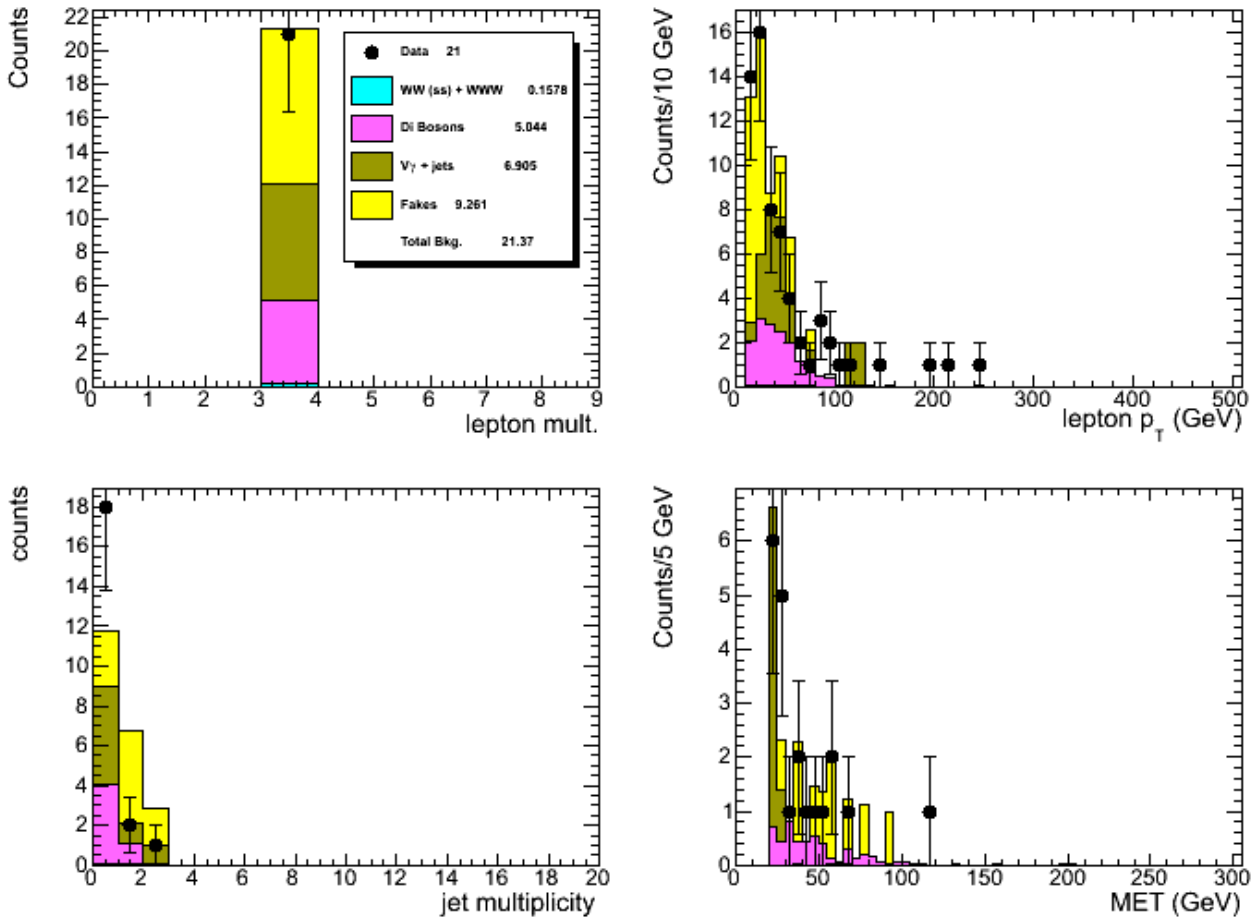

Figure 8.14: Some kinematics distribution of 2011 data, physical background, and fake estimated backgrounds, for the channel $\mu^- e \mu^+$, after all the analysis selections.

- $M_T < 25$ GeV;
- Z veto: reject events if 71 GeV $< M(\ell\ell) <$111 GeV;

This we called method A. We used a second approach, with the further requirement of one additional jet with $p_T > 40\,\text{GeV}$ and $\Delta R(\ell, jet) > 1.0$ (method B). The results of the two approaches are used to evaluate the systematic uncertainty on FR value. The values used for the final calculation are those obtained with the method A in the Multi-Jet sample. The other values are used to determine the systematic uncertainty on the FR itself. The estimated statistical uncertainty is 4% for muons and 1% for

electrons. The systematic uncertainty has been included in the systematic uncertainty on fake event number estimation.

In order to predict the final contribution to the background we use the technique described in Ref. (103) and (102). The procedure is the following:

- select events that pass the full kinematics selections of the analysis, in the signal region, but relax lepton isolation criteria;
- count the events that contain: 1 Tight lepton and 1 lepton passing a looser set of requirements but not tight $N_{n\bar{n}}$;
- count the events that contain: both leptons satisfying the Loose-no-Tight conditions $N_{\bar{n}\bar{n}}$;
- apply the Formulas 8.1-8.4 to find the number of fake events prediction.

Assuming $N_{\bar{n}\bar{n}}$ is dominated by QCD (both leptons are fake), a relatively simple calculation leads to the following, neglecting much smaller terms. The contribution to the signal sample N_{nn}^{ff} is given by (were ff=fake-fake, fp=fake-prompt):

$$N_{nn}^{ff} = \sum_{i,j} \frac{FR_i FR_j}{(1-FR_i)(1-FR_j)} N_{\bar{n}\bar{n}}^{ij} \tag{8.1}$$

where the indices i, j correspond to the binning and flavor of corresponding non-numerator lepton objects. The contribution from one true and one fake lepton (e.g. $t\bar{t}$, single top, Wjets) contribution in the signal sample $N_{nn}^{W,raw}$ is given by:

$$N_{nn}^{fp,raw} = \sum_{i} \frac{FR_i}{(1-FR_i)} N_{n\bar{n}}^{i} \tag{8.2}$$

$$N_{nn}^{fp} = N_{nn}^{fp,raw} - 2N_{nn}^{ff}. \tag{8.3}$$

To account for both single and double fakes, we take as total prediction the quantity:

$$N_{nn}^{total} = N_{nn}^{fp,raw} - N_{nn}^{ff} \tag{8.4}$$

The result about FR estimation are summarized in Table 8.4. The number of predicted fake events for our analysis selection are listed in Table 8.5 [1].

[1] We have neglected the dependency of FR and fake event number on p_{T} and η.

Furthermore, we made an estimation of fake events distributions from data samples, requiring one anti-isolated and one isolated lepton, and applying the analysis selection. Figure 8.14 shows the distribution of physical backgrounds, fake events, and data for the channel $\mu^- e \mu^+$, after all the analysis selections. Data and backgrounds are in good agreement and no hint of new physics is present.

8.5 Background Simulation

In order to determine the contribution of the physical SM processes to the signal we used MonteCarlo samples. We considered WZ and ZZ backgrounds, WWW, Vγ. They are listed in Appendix D, together with all other backgrounds we have studied and examined for the present study.

Pile-up was modeled by re weighting the Monte Carlo simulation to match the number of reconstructed vertexes found in data, using the 3D re weighting method (108), the input data distribution reflects the 73.5 mb minimum bias cross section. The individual event weight is calculated using 3D histograms which take as input the in-time and out-of-time bunch crossing number of interactions. These weight histograms are created using, as the input, the Monte Carlo distribution used in the sample generation process, and the data distribution. MC events were re-scaled to match the data effective luminosity before comparison with data.

Since the detector simulation program does not model trigger efficiencies or isolation efficiencies, and tends to be over-efficient in lepton identification, an evaluation of the efficiencies and corrections to apply to MC samples is important for a correct background evaluation. We will discuss this issue in the following sections. Further details about the efficiency values used in our analysis are contained in Chapter 10 about the analysis systematics.

8.5.0.1 Trigger Efficiencies

The data need to pass various triggers to enter the final data set. In order to compare MC events with data, we need to check each lepton candidate of the MC event to determine which triggers it would have most likely activated. More detailed study could be done on an event-by-event basis, and for each event a weighting factor could be applied in order to take into account the overall trigger efficiency. Trigger efficiency

considerations are described in Section 7.3.1. The conclusion is that we decided to assign a trigger efficiency correction of the order of 1%.

8.5.0.2 Lepton Identification Efficiencies

The MonteCarlo production tends to overestimate the lepton identification efficiency due to not including subtle detector efforts. An overall lepton identification efficiency correction factor must be obtained. We decided to pursue a most conservative approach: review similar analysis were the efficiency have been computed, and combine the correction factors that will give us the largest correction, and apply to both the background and signal MC calculation.

In Reference (97) there is a computation of the lepton identification efficiency for CMS, and we will refer to these results, summarized below. In this analysis, a tag and probe method on $Z \rightarrow e^+e$ and $Z \rightarrow \mu^+\mu$ events is used to measure the efficiency of the identification and isolation requirements for electrons and muons.

For both the electron and muon cases, selection request for tag and probes are described in (97).

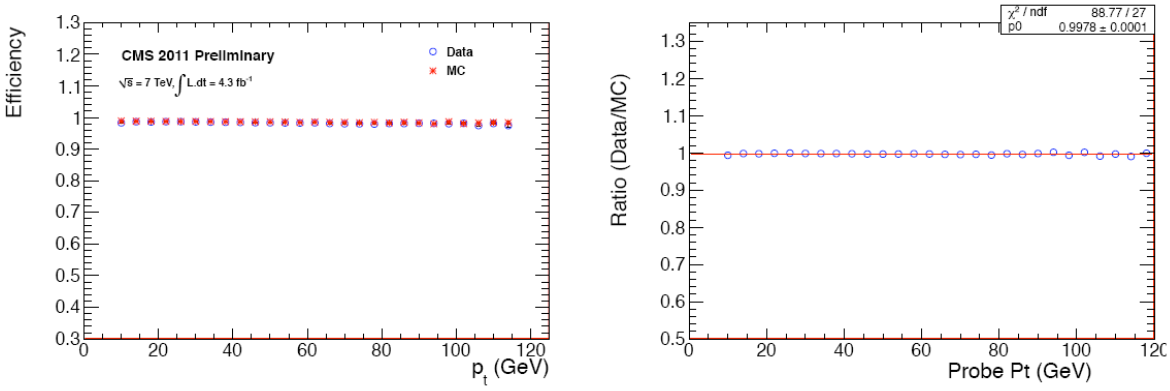

Figure 8.15: Muon identification efficiency (over probe) as a function of probe pt (left) and ratio of data and MC (right). Reference (97)

The Monte Carlo models the identification efficiencies to within a few percent throughout the whole pt range. Figures 8.15 and 8.16 show the identification efficiency and corresponding data to Monte Carlo ratio as a function of probe pt for muons and electrons, respectively.

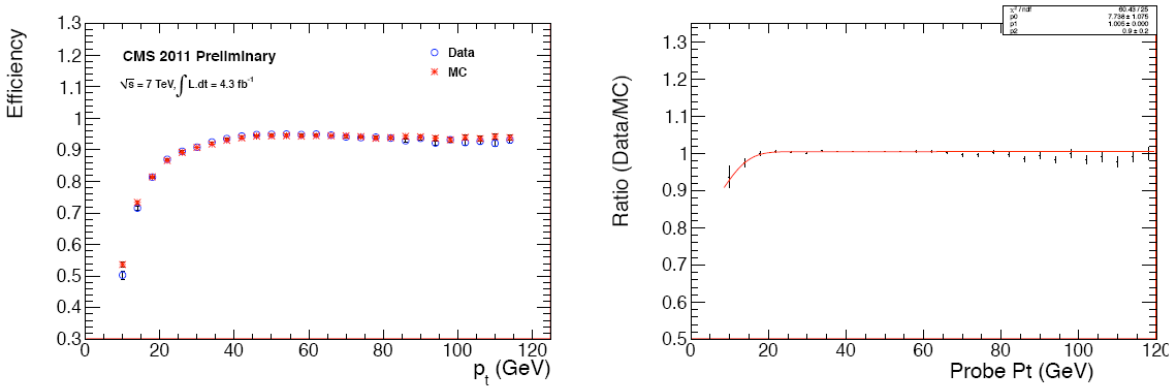

Figure 8.16: Electron identification efficiency as a function of probe pt (left) and ratio of data and MC (right). Reference (97)

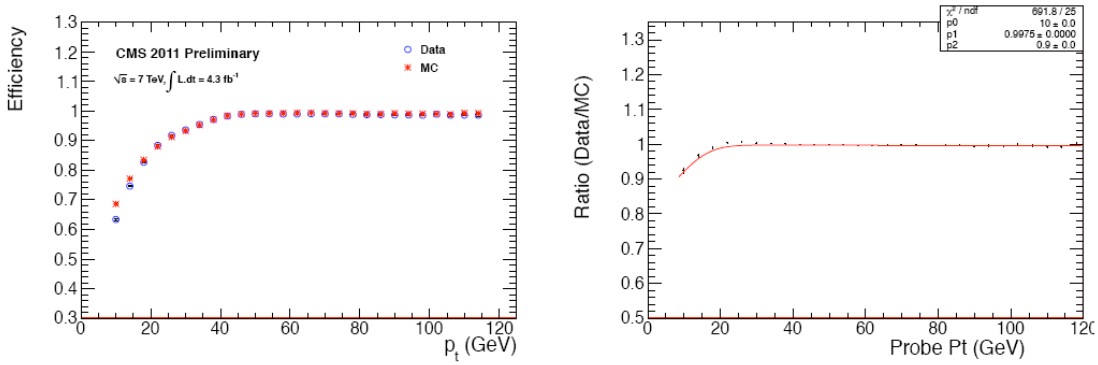

Figure 8.17: Muon isolation efficiency as a function of probe pt (left) and ratio of data and MC (right). Reference (97)

8.5.0.3 Isolation Efficiencies

During LHC run multiple interactions occur at high instantaneous luminosity, which can affect the lepton isolation but are not considered by CMS simulation. Therefore a correction factor (the ratio of MC and data isolation efficiency) must be applied to all MC events.

In Reference (97) there is a computation of the lepton isolation efficiency for CMS, and we will refer to these results, summarized below.

For the isolation efficiency, the measured efficiency in the range of $p_T < 25$ GeV/c

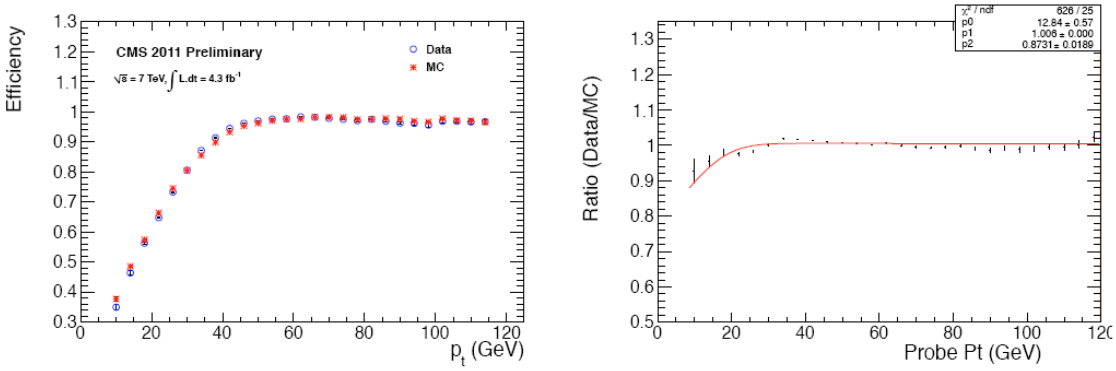

Figure 8.18: Electron isolation efficiency as a function of probe pt (left) and ratio of data and MC (right). Reference (97)

is significantly smaller than in Monte Carlo. Figures 8.17 and 8.18 show the isolation efficiency and corresponding data to Monte Carlo ratio as a function of probe $p_{\mathrm{T}}$for muons and electrons, respectively. This was modeled in Reference (97), with a fit of the ratio of data and MC isolation efficiencies to the equation which was proposed in the same sign di-lepton analysis for lepton efficiencies,

Although the isolation efficiency may depend on the number of jets(vertexes) in the event, they find that variations in the parameters with the number of jets (vertexes) is consistent with the statistical uncertainties. In this analysis the average ratio of data and MC muon isolation efficiencies is found to be 0.9974 for muons and 1.0053 for electrons, at plateau at high momenta. Systematic errors are around 7%.

One more possible concern with the ever growing luminosity is pileup. For lepton $pt > 25GeV/c$ we need not worry about ID or Isolation efficiencies as the MC agrees well with data. This can be seen from the plots provided in the Reference (97). For softer leptons care must be taken, and further studies would be needed to have the efficiency behavior under control. They will be investigated in further works.

9

Signal-Background Discrimination

9.1 Introduction

In this Chapter we will present the analysis strategy adopted to discriminate Seesaw signal from background. The event preselection requirements are discussed in Section 9.3, the selections are discussed and motivated in Section 9.4, and finally the results about event yields are given for 2011 luminosity in Section 9.5.

In this introduction the highlights of the analysis are summarized. They were described in deep detail in the previous chapters, but pinpoint them now is important to understand the subsequent analysis selections.

Seesaw type-III Model. Electroweak scale heavy neutrino fermion triplets (Seesaw type-III) signals are investigated in this analysis. We restrict ourselves to heavy Majorana fermion triplets decaying to light leptons plus gauge or Higgs bosons, which are dominant except for unnaturally small mixings. As described in Chapter 2, the seesaw mechanism could provide an explanation that accounts for neutrino mass.

The seesaws of type II and III can be produced at LHC via gauge interactions and can be observed if their mass is sufficiently small, regardless of the size of Youkawa couplings. The possibility of type III Seesaw discovering at LHC for a center-of-mass $\sqrt{s} = 14$ TeV is discussed in (24, 29). Recently a complete evaluation of the signal at $\sqrt{s} = 7$ TeV and a code allowing calculations and simulations with the model has been provided, see Reference (30).

Mixing Scenarios. The heavy lepton production cross section is independent from the mixing angle values, while the decay branching ratios depend on the mixing V_α

where $\alpha = \mathrm{e}$, μ or τ. Constraints on the mixing parameters and their products exists as reported in (30) and described in Chapter 4. Given the results reported in that Chapter, we choose the following scenarios as benchmarks to set limits on the seesaw mass:

1. $V_\mathrm{e} = V_\tau = V_\mu = 4.1 \times 10^{-4}$;
2. $V_\mu = 0.063$, and $V_\mathrm{e} = V_\tau = 0$;
3. $V_\mathrm{e} = 0.05$ and $V_\mu = V_\tau = 0$;

Signature. Given the triplet charge status Σ^+, Σ^0 and Σ^-, the most promising signal chain are:

$$pp \to \Sigma^0\Sigma^+,\ \Sigma^0 \to \ell^\mp W^\pm, \Sigma^+ \to W^+\nu \tag{9.1}$$
$$pp \to \Sigma^0\Sigma^+,\ \Sigma^0 \to \ell^\pm W^\mp, \Sigma^+ \to W^+\nu \tag{9.2}$$

These processes have the higher cross sections. Other processes with a smaller cross section, but potentially ending in the same final state, are:

$$pp \to \Sigma^0\Sigma^+,\ \Sigma^0 \to \ell^\mp W^\pm, \Sigma^+ \to \ell^+ Z \tag{9.3}$$
$$pp \to \Sigma^0\Sigma^+,\ \Sigma^0 \to \ell^\pm W^\mp, \Sigma^+ \to \ell^+ Z \tag{9.4}$$

By requiring $W^\pm$ decay to $\ell^\pm\nu$ (here ℓ is an electron or muon), and Z decay to neutrinos or jets, the final state shows a very clean signature with a positive charged triplet of leptons. We focus the search on tree positive charged leptons final state.

Signal. The model was implemented in FeynRules package and the signal samples have been generated with the MadGraph (58) event generator. The hadronization and fragmentation of quarks and gluons is then performed by PYTHIA (47). Detector simulation and reconstruction was performed using Fast Simulation CMSSW_4_2_8_patch4 release with true pile up distribution. The signal samples are listed with the cross section from Madgraph output in Table 9.1, with the cross section from CMS simulation

in Table 9.2 and with the number of events in Table 9.3, versus Σ mass point spanning from the lower limit (set by L3 at LEP (98)) to 180 GeV mass point[1].

ID	Process	Cross Sections (fb) for Σ mass (GeV)				
		100	120	130	140	180
P1	$\ell^- W^+ W^+ \nu, W^+ \to \ell^+$	182.7	65.11	43.66	30.25	9.17
P11	$\ell^+ W^- W^+ \nu, W^\pm \to \ell^\pm$	183.0	65.15	43.64	30.24	18.09
P2	$\ell^- \ell^+ Z W^+, W^+ \to \ell^+, Z \to \nu\nu$	18.35	13.53	10.28	7.68	2.63
P3	$\ell^+ \ell^+ Z W^-, W^- \to \ell^-, Z \to \nu\nu$	18.34	13.54	10.26	7.66	2.63
P4 (*)	$\ell^+ \ell^+ Z W^-, W^- \to \ell^-, Z \to jj$	44.75	33.39	25.41	18.98	6.54
P5 (*)	$\ell^- \ell^+ Z W^+, W^+ \to \ell^+, Z \to jj$	44.80	33.43	25.47	18.97	6.55
PAllJets(*)	$\Sigma^+ \Sigma^0 j \to \mathrm{P}*$	296.7	-	-	-	-
P1Jets(*)	$\ell^- W^+ W^+ \nu j, W^+ \to \ell^+$	85.93	32.70	-	-	-
P11Jets(*)	$\ell^+ W^- W^+ \nu j, W^\pm \to \ell^\pm$	86.12	32.71	-	-	-
P2Jets(*)	$\ell^- \ell^+ Z W^+ j, W^+ \to \ell^+, Z \to \nu\nu$	18.42	14.58	-	-	-
P3Jets(*)	$\ell^+ \ell^+ Z W^- j, W^- \to \ell^-, Z \to \nu\nu$	18.38	14.57	-	-	-
P4Jets(*)	$\ell^+ \ell^+ Z W^- j, W^- \to \ell^-, Z \to jj$	43.80	-	-	-	-
P5Jets(*)	$\ell^- \ell^+ Z W^+ j, W^+ \to \ell^+, Z \to jj$	44.10	-	-	-	-
P1pSmallV100(#)	$\mu^- W^+ W^+ \nu$	1173.	-	-	-	-
P1pVtau100	$\ell^- W^+ W^+ \nu, W^+ \to \ell^+$	182.6	-	-	-	-

Table 9.1: Cross sections of the signal Monte Carlo samples in output from Madgraph5. Cross section is relative to the final state, before Pythia hadronization and jet-matching, CMS simulation and reconstruction. The process PAllJets includes P1, P11, P2, P3; P4 and P5 with with a hard jet at parton-level generation added. Processes with (*) have a different jet-matching parameters: xqcut=10, QCUT=15, while the other processes settings are: xqcut=20, QCUT=30. Process with (#) has no jet-matching.

Definition of Analysis Categories. The signature for this search is **three leptons of charge ++- plus missing energy and jets**. Leptons in this search can be either electrons or muons. Selected events are subdivided into the six categories here listed:

1. $\mu^- \mathrm{e}^+ \mathrm{e}^+$,

[1]The mass dependence of the expected cross section is very steep and other signatures could be more relevant at higher mass values. Their study is not included here.

ID	Process	Cross Sections (fb) for Σ mass (GeV)				
		100	120	130	140	180
P1	$\ell^- W^+ W^+ \nu, W^+ \to \ell^+$	130.7	44.78	29.60	20.12	5.84
P11	$\ell^+ W^- W^+ \nu, W^\pm \to \ell^\pm$	130.8	44.88	29.68	20.19	5.85
P2	$\ell^- \ell^+ Z W^+, W^+ \to \ell^+, Z \to \nu\nu$	13.12	9.34	6.97	5.13	1.67
P3	$\ell^+ \ell^+ Z W^-, W^- \to \ell^-, Z \to \nu\nu$	13.12	9.35	6.95	5.13	1.67
P4 (*)	$\ell^+ \ell^+ Z W^-, W^- \to \ell^-, Z \to jj$	21.79	15.31	11.37	8.37	2.67
P5 (*)	$\ell^- \ell^+ Z W^+, W^+ \to \ell^+, Z \to jj$	21.82	15.48	11.52	8.33	2.69
Total	$\ell^- \ell^+ \ell^+ + E_{\mathrm{T}}^{\mathrm{miss}} + \mathrm{jets}$	331.35	139.14	96.09	67.27	20.39
PAllJets(*)	$\Sigma^+ \Sigma^0 j \to \mathrm{P}*$	92.07	-	-	-	-
P1Jets(*)	$\ell^- W^+ W^+ \nu j, W^+ \to \ell^+$	26.88	-	-	-	-
P11Jets(*)	$\ell^+ W^- W^+ \nu j, W^\pm \to \ell^\pm$	26.60	-	-	-	-
P2Jets(*)	$\ell^- \ell^+ Z W^+ j, W^+ \to \ell^+, Z \to \nu\nu$	5.65	-	-	-	-
P3Jets(*)	$\ell^+ \ell^+ Z W^- j, W^- \to \ell^-, Z \to \nu\nu$	5.68	-	-	-	-
P4Jets(*)	$\ell^+ \ell^+ Z W^- j, W^- \to \ell^-, Z \to jj$	13.59	-	-	-	-
P5Jets(*)	$\ell^- \ell^+ Z W^+ j, W^+ \to \ell^+, Z \to jj$	13.68	-	-	-	-
P1pSmallV100(#)	$\mu^- W^+ W^+ \nu$	1174	-	-	-	-
P1pVtau100	$\ell^- W^+ W^+ \nu, W^+ \to \ell^+$	131	-	-	-	-

Table 9.2: Cross sections of the signal Monte Carlo samples used for the analysis. Cross section is relative to the final state, after CMS simulation and reconstruction. The final state is $\ell^- \ell^+ \ell^+ E_{\mathrm{T}}^{\mathrm{miss}}$ for P1, P11, P2, P3; P4 and P5 give $\ell^- \ell^+ \ell^+ E_{\mathrm{T}}^{\mathrm{miss}}$jets final state. The process PAllJets includes P1, P11, P2, P3; P4 and P5 with with a hard jet at parton-level generation added. Processes with (*) have a different jet-matching parameters: xqcut=10, QCUT=15, while the other processes settings are: xqcut=20, QCUT=30. Process with (#) has no jet-matching.

2. $\mu^- \mathrm{e}^+ \mu^+$,

3. $\mu^- \mu^+ \mu^+$,

4. $\mathrm{e}^- \mu^+ \mu^+$,

5. $\mathrm{e}^- \mathrm{e}^+ \mu^+$,

6. $\mathrm{e}^- \mathrm{e}^+ \mathrm{e}^+$.

ID	Process	Number of Events for Σ mass (GeV)				
		100	120	130	140	180
P1	$\ell^- W^+ W^+ \nu, W^+ \to \ell^+$	71502	68778	67794	66794	63682
P11	$\ell^+ W^- W^+ \nu, W^\pm \to \ell^\pm$	71508	68890	68010	66791	63559
P2	$\ell^- \ell^+ Z W^+, W^+ \to \ell^+, Z \to \nu\nu$	71501	69023	67857	66816	63432
P3	$\ell^+ \ell^+ Z W^-, W^- \to \ell^-, Z \to \nu\nu$	71547	69017	67786	66955	63565
P4 (*)	$\ell^+ \ell^+ Z W^-, W^- \to \ell^-, Z \to jj$	48693	45864	44756	44090	40887
P5 (*)	$\ell^- \ell^+ Z W^+, W^+ \to \ell^+, Z \to jj$	48717	46304	45228	43890	41181
PAllJets(*)	$\Sigma^+ \Sigma^0 j \to \mathrm{P}*$	31025	-	-	-	-
P1Jets(*)	$\ell^- W^+ W^+ \nu j, W^+ \to \ell^+$	8988	-	-	-	-
P11Jets(*)	$\ell^+ W^- W^+ \nu j, W^\pm \to \ell^\pm$	8952	-	-	-	-
P2Jets(*)	$\ell^- \ell^+ Z W^+ j, W^+ \to \ell^+, Z \to \nu\nu$	1925	-	-	-	-
P3Jets(*)	$\ell^+ \ell^+ Z W^- j, W^- \to \ell^-, Z \to \nu\nu$	1904	-	-	-	-
P4Jets(*)	$\ell^+ \ell^+ Z W^- j, W^- \to \ell^-, Z \to jj$	4629	-	-	-	-
P5Jets(*)	$\ell^- \ell^+ Z W^+ j, W^+ \to \ell^+, Z \to jj$	4627	-	-	-	-
P1pSmallV100 (#)	$\mu^- W^+ W^+ \nu$	10000	-	-	-	-
P1pVtau100	$\ell^- W^+ W^+ \nu, W^+ \to \ell^+$	71718	-	-	-	-

Table 9.3: Number of events of the signal Monte Carlo samples used for the analysis. The process PAllJets includes P1, P11, P2, P3; P4 and P5 with with a hard jet at parton-level generation added. Processes with (*) have a different jet-matching parameters: xqcut=10, QCUT=15, while the other processes settings are: xqcut=20, QCUT=30. Process with (#) has no jet-matching.

To avoid double counting events that are found in multiple datasets, a check was performed on selected events and double counted events rejected.

Backgrounds. All standard model sources of three isolated leptons (two same sign) at CMS are vanishingly small. Nevertheless, several background sources have been analyzed, divided into physics and instrumental. As described in Chapter 8, the most relevant of the former is the irreducible background WZ, with both bosons decaying into leptons. The physics background includes also the ZZ production with one of the leptons either out of the detector acceptance or mis-reconstructed.

We analyzed physical backgrounds using the official CMS Standard Model datasets of Summer 11 production, listed in Appendix D. The details about simulation are given

in Chapter 5. The background discussion is contained in Chapter 8.

Drell Yan+γ conversion process is an important source of background and has been evaluated with a data-driven methods as described in Chapter 8.

The instrumental backgrounds are due to mis-identified leptons from jets and include Drell-Yan+jets, W+jets, WW+jets, $t\bar{t}$, etc. The contribution of two isolated leptons plus a lepton fake, or a possibly small contribution form multi-jet events where both leptons are fakes, has been evaluated using data-driven techniques (as described in Chapter 8, Section 8.4.1).

Data. The data analyzed were collected by the CMS detector (a detailed description of the detector was given in Chapter 3). The data sample analyzed corresponds to an integrated luminosity of 4697 pb^{-1} for the Di-Muon Primary Dataset, of 4606 pb^{-1} for the Di-Electron Primary Dataset, and of 4611 pb^{-1} for the Muon-Electron Primary Datset. The trigger criteria are similar to those used in previous CMS analysis and are described in Chapter 7. The data sample has been collected requiring events to pass one or several di-lepton triggers. The trigger efficiency for the events passing all the selection cuts is very high since each event has three combinations of di-lepton trigger. Di-lepton trigger efficiencies have been measured to be between 92% and 100%. and hence an overall efficiency of $99.5 \pm 0.5\%$ is assumed. See Section 7.3.1 for details.

9.2 Search Strategy

Our strategy takes advantage of the strong background suppression obtained when requiring three leptons; this allows us to relax requirements and selections for SM background reduction relative to other searches with fewer leptons or purely hadronic searches at the LHC.

In general, the event selection aims at minimizing the background contribution in the signal region, while at the same time allowing for the preservation of control regions that can be used for the estimation of some of the backgrounds by using data.

The search strategy is as described in detail in the following paragraph.

- We start out with a pre-selection of at least two same sign leptons: ee, $\mu\mu$, $e\mu$, with the following characteristics:

    1. leptons are well reconstructed as described in Section 9.3;

2. lepton $p_T > 10$ GeV; such a low p_{T} limit is necessary to maintain sensitivity to possible signals with relatively low p_T leptons generated in the cascade decays of heavy objects;

- We perform a counting experiment in this region and predict the expected yield for the standard model background contribution of true isolated tri-leptons (i.e. physical irreducible backgrounds) by Monte Carlo simulation.

- We then tighten the selection further as follows:

  1. we require the presence of a third lepton and no other leptons in the event, in addition we require at least two leptons of $p_T > 15$ GeV;
  2. we measure the yield for with an additional requirement of $E_{\mathrm{T}}^{\mathrm{miss}} > 20$ GeV (this cut was chosen a priori to reduce the total standard model expected yield in Monte Carlo);
  3. we measure the yield for an additional $HT < 100GeV$ cut and b-tag veto.

- We perform a counting experiment in the regions after each of the selection steps and predict:

  1. the expected yield for non-physical backgrounds using data driven techniques for the sum of single and double fake events,
  2. we consider a contribution from conversions of isolated photons from Wγ and Zγ. These contributions are computed using data driven technique. We find the Zγ contribution to be not negligible, as discussed in Section 8.3.4. The Wγ is negligible.

- We compute the event yield after all the cuts above;

- We compare observations with background expectations;

- We compare signal expectations;

- Finally, if no excess yield is observed we place an upper limit on cross section.

9.3 Event pre-selection

The pre-selected events must have a well reconstructed primary interaction vertex and at least two positive-charged well-reconstructed lepton candidates, as described in the following subsections. The analysis relies on the reconstruction of three types of objects: electrons, muons and jets. The events are reconstructed using a full Particle Flow approach (PF2PAT) (85, 86, 87) as described in Chapter 6 and the details of the object selection are provided below.

9.3.1 Event Cleanup and Vertex Selection

The events are cleaned up by requiring:

- Event cleaning (i.e. Scraping cut): if there are ≥ 10 tracks, require at least 25% of them to be high purity.
- Require at least one good vertex:
  1. not fake;
  2. ndof > 4;
  3. $|\rho| < 2$ cm;
  4. $|z| < 24$ cm.
- HBHE event-level noise filtering

9.3.2 Electron selection

Electron candidates are reconstructed from a collection of electromagnetic clusters with matched pixel tracks. The momentum of the electron track is fitted using a Gaussian-Sum Filter (GSF) algorithm along its trajectory with the algorithm taking into account the possible emission of Bremsstrahlung photons in the silicon tracker. Requirements on electrons are:

- $p_T > 10\,GeV$
- $|\eta| < 2.5$; we also exclude the barrel and endcap transition region ($1.4442 < |\eta_{sc}| < 1.566$).

- electron identification using the *Cut in Categories* (CiC) approach (see Chapter 6)[1]. Electrons are required to pass the *eidMediumMC* CiC selection.
- Particle Flow based relative isolation is required to be less than 0.20[2].
- Conversion rejection cuts: we reject an electron if the number of missing expected inner hits is equal to zero and the electron is flagged as conversion using the partner track conversion veto (0.02, 0.02).
- Transverse impact parameter of the electron with respect to the beamspot $<$ 0.02 cm.
- Require that all three charge measurements for an electron agree (Gsf-Ctf-ScPix charge consistency (cfr. Chapter 6).[3].
- Conversion rejection[4].

9.3.3 Muon Selection

- $p_T > 10\,\text{GeV}$;
- $|\eta| < 2.1$;
- Classified as GlobalMuon and TrackerMuon;
- Number of valid Silicon hits $\geq$11;
- Transverse impact parameter of the electron with respect to the beamspot < 0.02 ;
- $\chi^2/ndof < 10$;
- Number of Muon hits > 0;

[1]This method classifies an electron in a number of categories (barrel versus endcap, fbrem versus E/p, and transverse energy) which are optimized to select electrons from W or Z decays and reject fakes from jets or conversions.

[2]relative combined particle flow isolation calculated using tracks, Ecal and HCal energy deposit within a cone $\Delta R < 0.3$.

[3]One from the charge of the GSF track, one from the charge of the CTF track associated to the GSF track and one, the so-called supercluster charge, determined from the relative position of the supercluster with respect to the projected track from the pixel seed.

[4]$nLostHits == 0$ and ($|convDCot| > 0.02$ or $|convDist > 0.02$).

- Number of Pixel Hits > 0;
- Number of chambers with matched segments > 1;
- Particle Flow based relative isolation is required to be less than 0.15.

9.3.4 Jets

- Jets are reconstructed using the Anti-kT algorithm (cfr. Chapter 6);
- Jet energy corrections: charged hadron subtraction, L1FastJet corrections and L2L3Jet-EnergyScale corrections;
- $P_T > 30\,\text{GeV}$;
- $|\eta| < 2.4$;
- Loose jet Id (see (110) for more info) ;

9.3.5 Preselection Yield

The number of events after preselection for the simulated background are listed in Tables 9.11 and 9.10, in the 2SS column. The dominant contribution is from $Z_0 \rightarrow e^+e^-$ with one of the two electrons with the charge misidentified.

Signal samples yields are shown in Tables 9.7 and 9.6 in the same column. The signal is computed for five mass points ranging from 100 to 180 GeV.

9.4 Selections

By comparing the kinematics of signal and background events, we can use a series of cuts to reject background with minimal effect on signal acceptance.

For multi-lepton searches, the SM background (once the total number and charge of leptons is imposed) is small and can be further reduced by minimal requirements on either hadronic activity or missing energy above the typical SM values[1]

Moreover, both hadronic activity and $E_{\mathrm{T}}^{\mathrm{miss}}$are good discriminating observables for physics beyond the SM.

[1] These variables are well described by the simulation, as shown in Fig. 9.1 from Reference (96) for events with two isolated and one lepton with isolation selection removed.

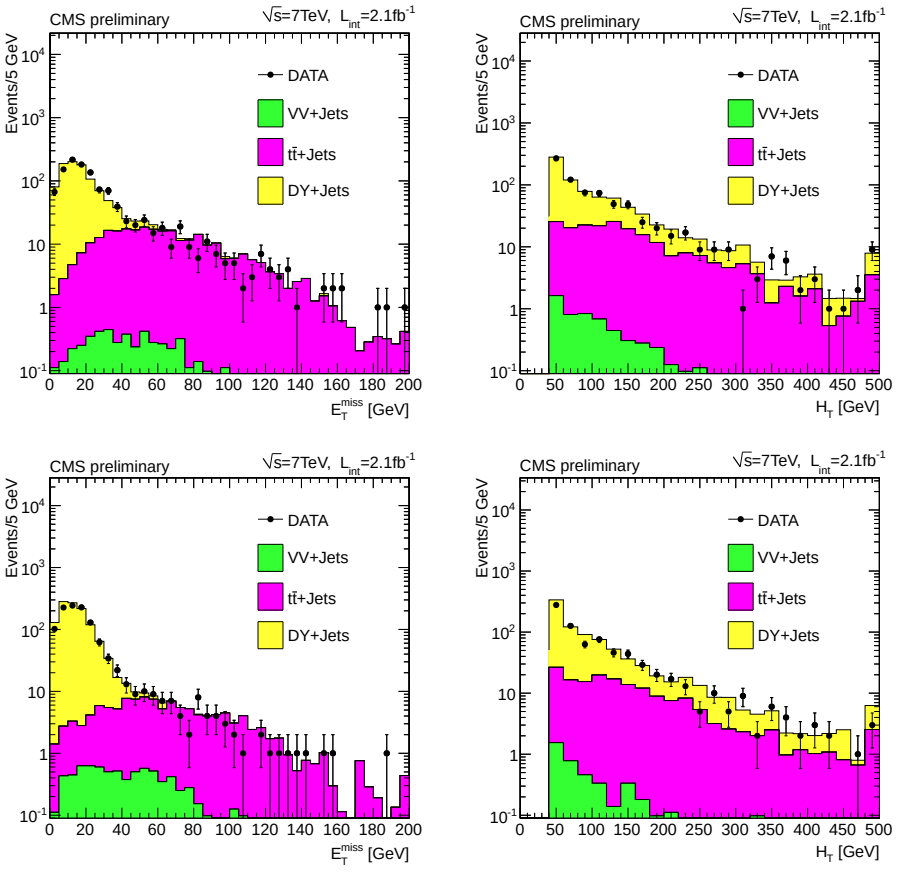

Figure 9.1: $E_{\mathrm{T}}^{\mathrm{miss}}$(left)and H_{T}(right) distributions for $\ell\ell-\mu$ (top), $\ell\ell-e$ (bottom), where two leptons $\ell\ell$ are isolated but the third lepton is required to be non-isolated. VV, TT and DY refers to the diboson, top-quark and Drell-Yan SM production, respectively. Reference (96).

In order to retain search sensitivity for our signal region both $E_{\mathrm{T}}^{\mathrm{miss}}$ and H_{T} selections have been used.

The distribution of various kinematic variables form the signal sample (for one specific mass point) have been compared to the distribution of the overall predicted backgrounds after each of the cuts, in order to optimize the event selection and obtain the best sensitivity for signal extraction or for setting a limits.

The selections applied in this analysis are summarized here, and discussed and motivated in the following sections. The selection requires:

- Exactly three isolated leptons as defined above, with charges ++-, at least two leptons with $p_T > 15$ GeV/c.
- $E_{\mathrm{T}}^{\mathrm{miss}}$>20 GeV.
- H_{T}< 100 GeV, where $H_{\mathrm{T}}$is summed over the selected jets only.
- reject events with a b-tag;
- $M(\ell\ell) > 4\,GeV$.
- Z Veto: $M(\ell\ell)$ <82 GeV or $M(\ell\ell)$ >102 GeV.
- Z asymmetric conversion veto: $M(\ell\ell\ell)$ <82 GeV or $M(\ell\ell\ell)$ >102 GeV for categories: $e^-e^+e^+$ and $\mu^-e^+\mu^+$.

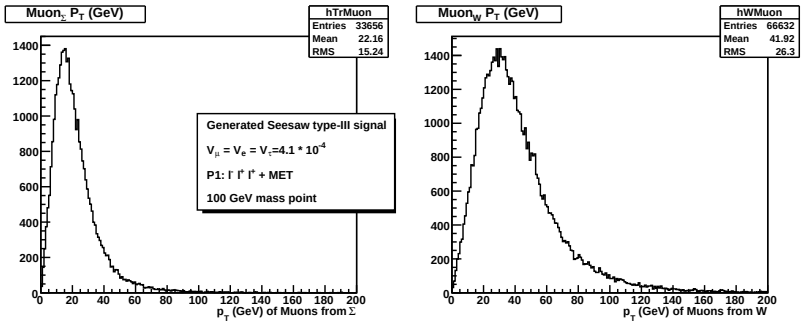

Figure 9.2: Transverse momentum distribution for muons from Σ^0 (left) and W (right) $\mu^-\mu^+\mu^+$ events for different background and signal samples.

9.4.1 Momentum Requirements

As it can be seen on Fig. 9.2 the lepton p_T distribution depends on the parent particle. In particular leptons coming from Σ^0 decay have a softer spectrum with respect to the W-generated one, especially for mass points close to 100 GeV. Consequently, to ensure a reasonable selection efficiency, the selected candidate events are required to have:

- at least two isolated muons (electrons) with $p_T > 15$ GeV/c;
- a third isolated lepton with $p_T > 10$ GeV/c;
- no other leptons in the event, to reject background from ZZ leptonic decays;

9.4.2 Missing Transverse Energy

The missing transverse energy ($E_{\mathrm{T}}^{\mathrm{miss}}$) is defined as the magnitude of the vectorial sum of the transverse energy of all Particle Flow(PF) candidates. The low backgrounds in the multilepton selections allows us to selectively impose the E_{miss}^{T} requirement. We exploit the background reduction ability of E_{miss}^{T} plotting $E_{\mathrm{T}}^{\mathrm{miss}}$distribution after the selection cuts.

Events with $E_{\mathrm{T}}^{\mathrm{miss}}$> 20 GeV are said to satisfy the requirement.

9.4.3 Hadron Activity

The presence of hadronic activity in an event is characterized by the variable H_{T}, defined as the scalar sum of the transverse jet energies for all jets with kinematic cuts of the analysis ($p_T > 30$ GeV). Jets used for the H_{T}determination must be well separated from any identified leptons, hence jets are required to have no lepton in a cone $\Delta R < 0.3$ around the jet axis. To remove residual backgrounds from events with leptonic W decay and an additional lepton, we state the H_{T}requirement: H_{T}<100 GeV/c.

9.4.4 Z veto

Another criterion for background reduction is the requirement of Z veto, as discussed in Chapter 8. The first and the fourth categories in Section 9.1 have no contributions from Z decay, while the others can be produced by WZ events and they have one or

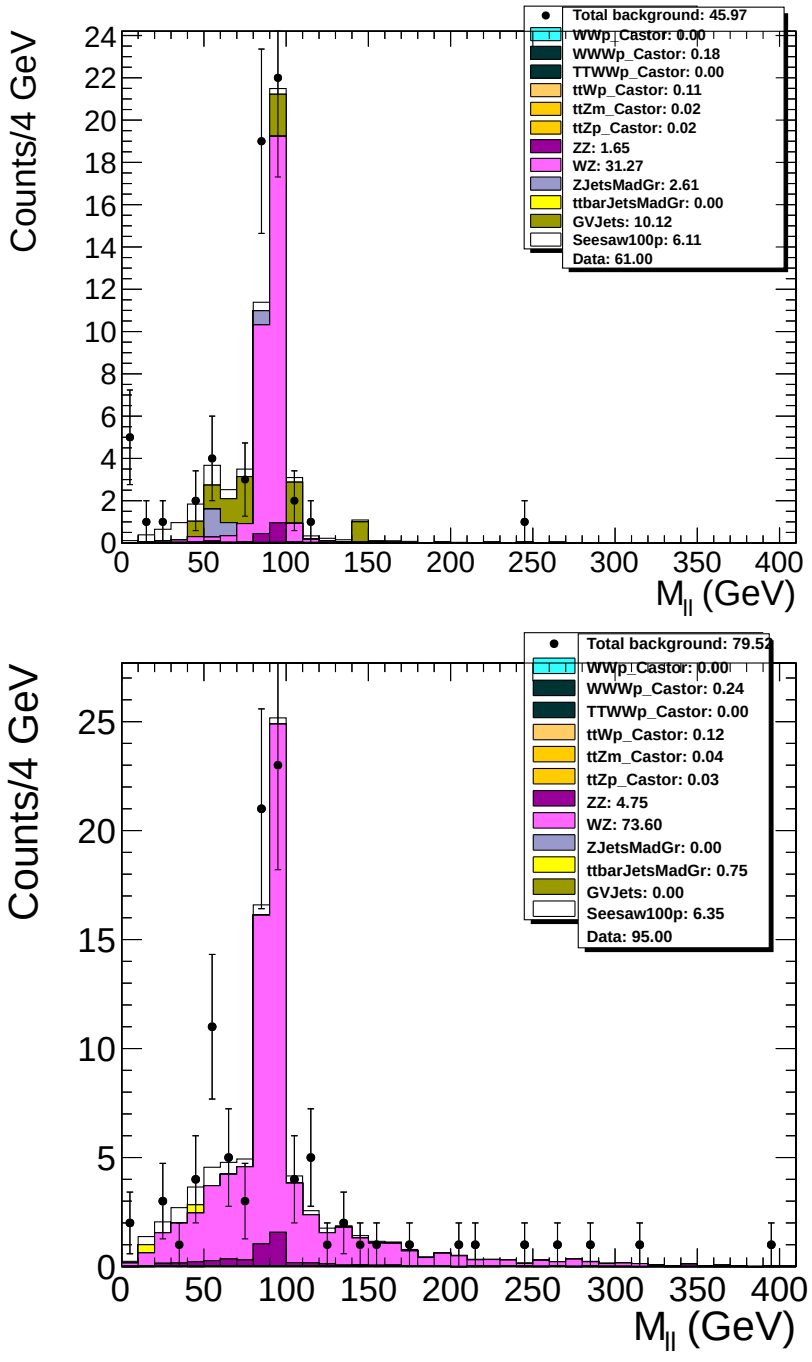

Figure 9.3: Invariant mass for $\mu^-e^+\mu^+$ (top) and $\mu^-\mu^+\mu^+$ (bottom) events for different background and signal samples.

two possible combinatorial contributions to the Z→ $\ell^+\ell^-$ invariant mass. As shown in Fig. 9.3 a clear Z peak is evident in the simulated events. To reduce the WZ background an Z veto has been added to the selection requirements for categories 2,3,5,6 (as described in 9.1).

We veto events for which a third lepton is found that passes all the lepton requirements and makes an opposite sign same flavor Z candidate with one of the two same sign leptons we require. Events with at least one $\mu^+\mu^-$ (e^-e^+) mass combination in the range $82 > m_{\mu^+\mu^-} > 102$ ($82 > m_{e^-e^+} > 102$) are rejected.

To reject low mass Drell–Yan production and the $J/\Psi(1S)$ we required opposite sign same flavor lepton pairs to have $M(2\ell) > 4\ GeV/c^2$ for all combinations.

As described in detail in Chapter 8, Section 8.3.4, a possible source of background is from the final state radiation in $Z \rightarrow 2l(l = e, \mu)$ events undergoing a $\gamma \rightarrow 2l$ conversion. Therefore, the Z veto requirement is also applied to the invariant mass $M(3l)$ of three leptons for category $e^-e^+e^+$ and $\mu^-e^+\mu^+$: in these cases the asymmetric gamma conversion background is significant. For categories: $\mu^-\mu^+\mu^+$ and $e^-e^+\mu^+$ the background is much more smaller and thus we estimated the background with data-driven techniques to ensure minimal loss of signal efficiency. The remaining categories, $\mu^-e^+e^+$ and $e^-\mu^+\mu^+$ have no contribution from this kind of background.

9.5 Event Yields

After all the selections, we are able to discriminate signal from background. As an example, we show some kinematics distributions at pre-selection (2 same sign leptons) in Figure 9.8 and after all selections in Figure 9.9 for channel $\mu^-e^+e^+$. Signal sample at 100 GeV point mass is plot. Clearly, this channel is almost free from standard model background, and the signal is evident after selections.

To see the step-by-step background rejection capabilities of our selections, we show some plots of lepton distributions for channel $e^-e^+\mu^+$, at preselection (Figure 9.4), after the requirements on lepton multiplicity and p_{T}(Figure 9.4.4), after the requirement on H_{T} and the b-tag veto (Figure 9.6), and adding the Z-veto after all the selections (Figure 9.7).

The expected event yields for the signal in each category as function of the cuts and for each Σ mass point are shown in Table 9.6 for $\mu^-\ell^+\ell^+$ categories, and in Table 9.7

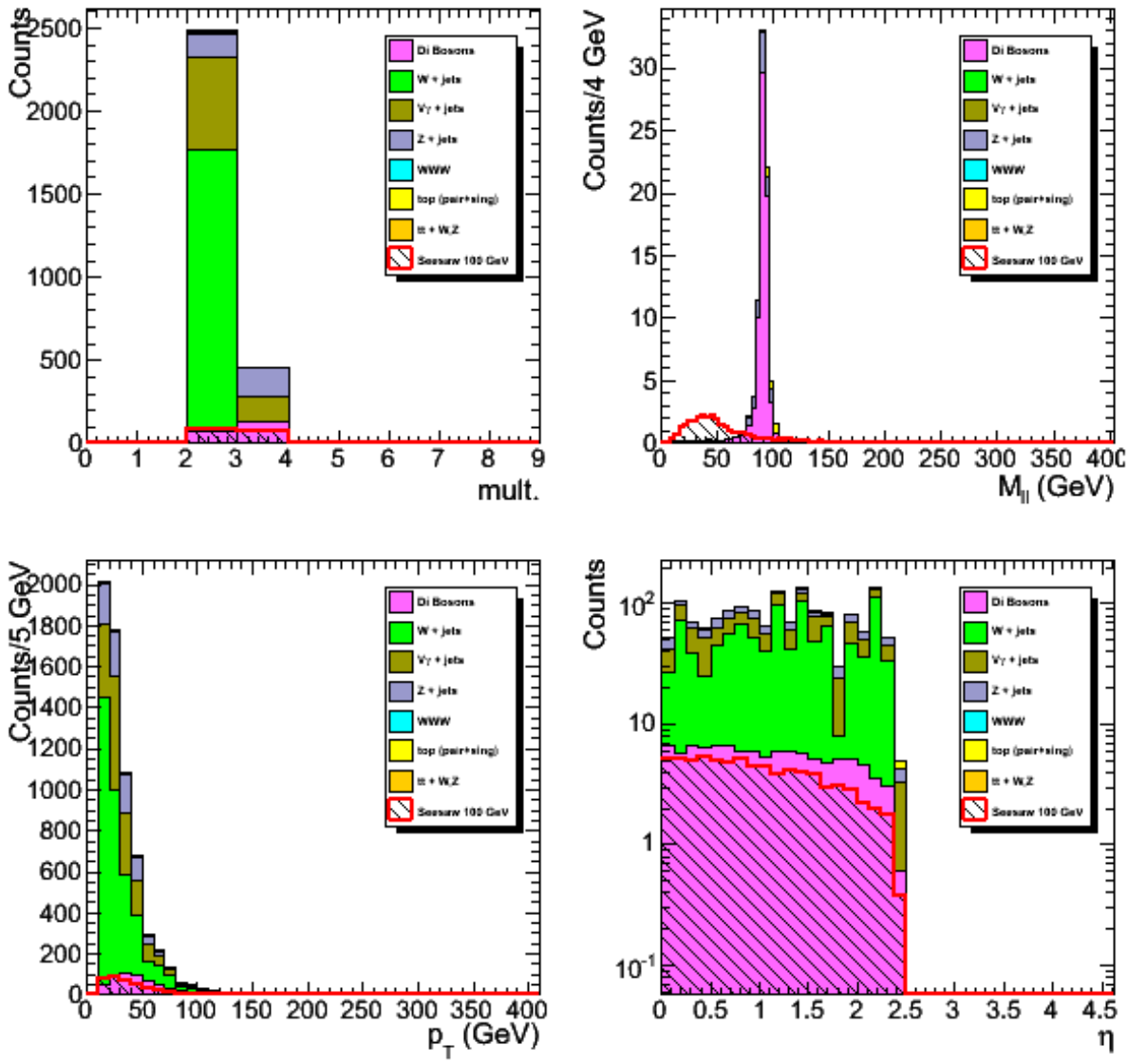

Figure 9.4: $e^-e^+\mu^+$ lepton kinematics distributions at pre-selection.

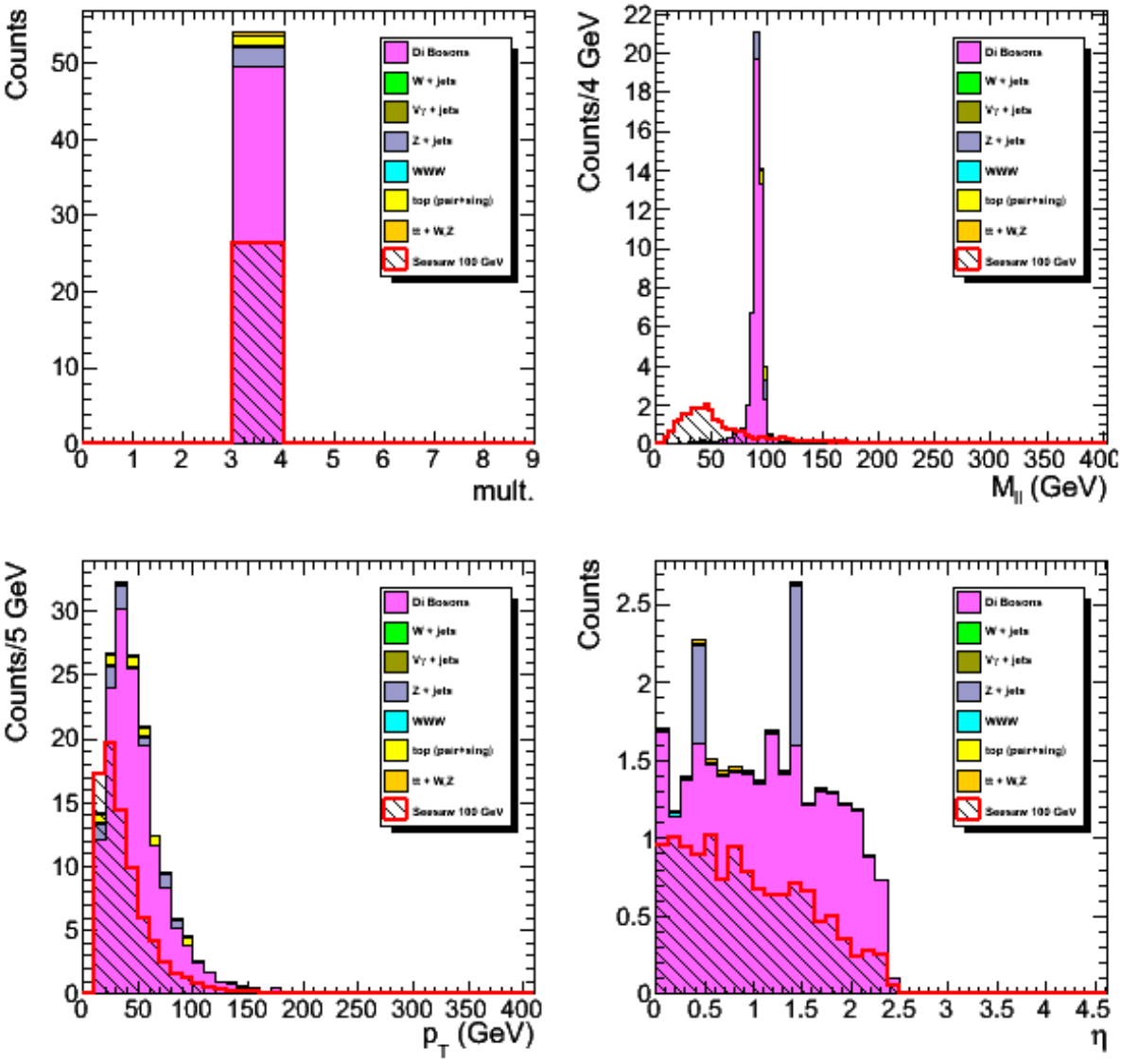

Figure 9.5: $e^-e^+\mu^+$ lepton kinematics distributions after lepton selections.

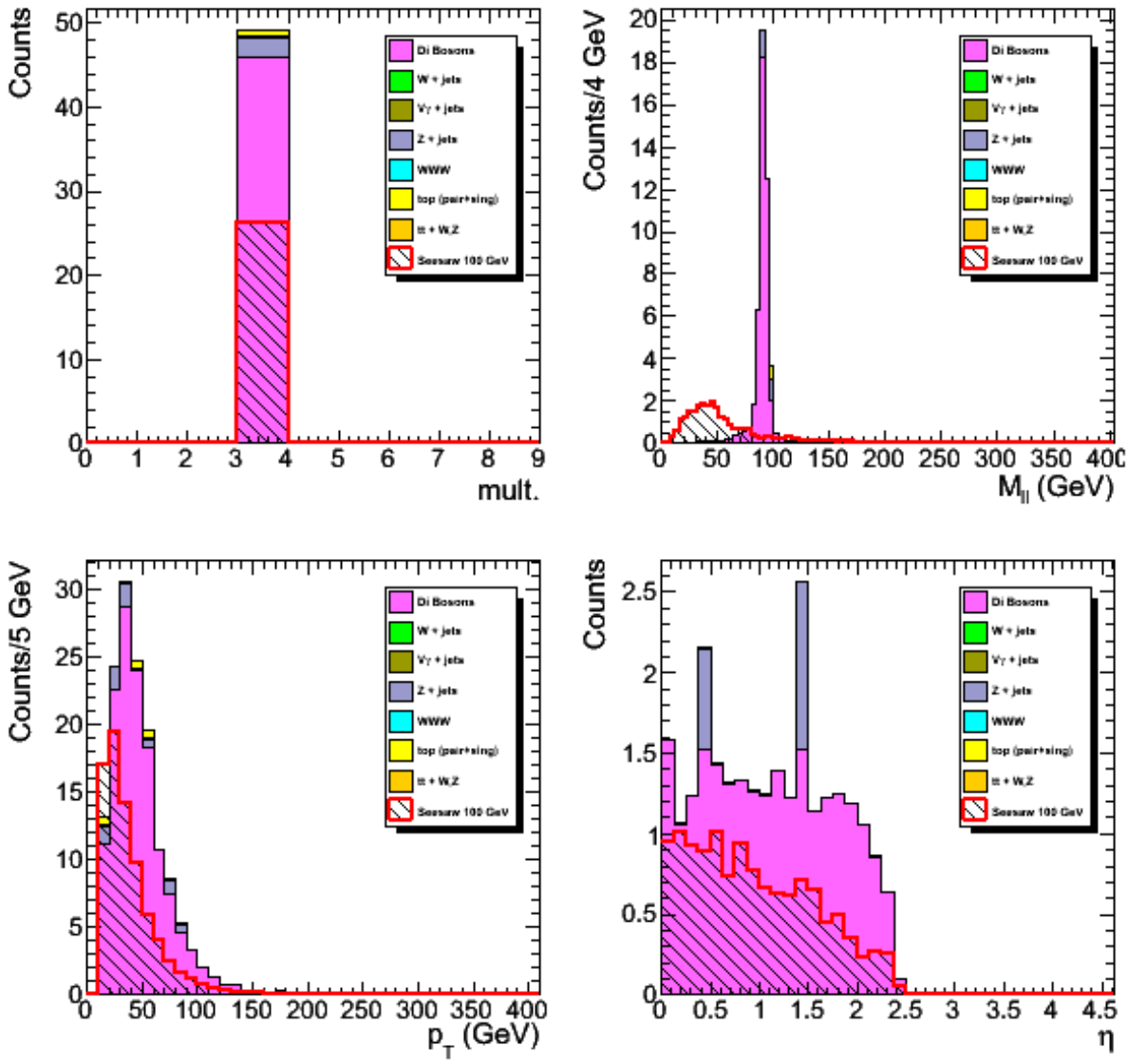

Figure 9.6: $e^-e^+\mu^+$ lepton kinematics distributions after leptons and jet selections.

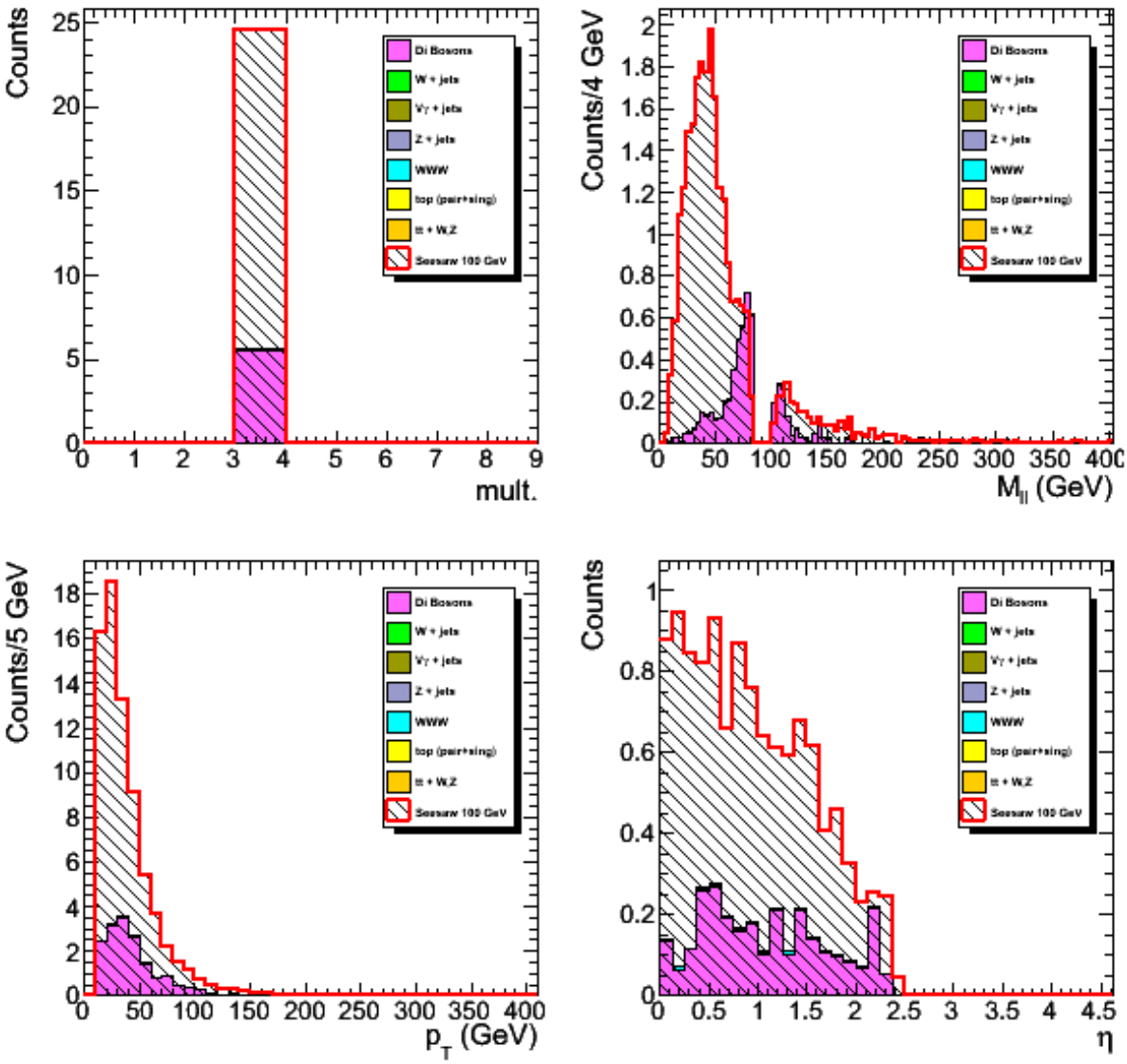

Figure 9.7: $e^-e^+\mu^+$ lepton kinematics distributions after all selections.

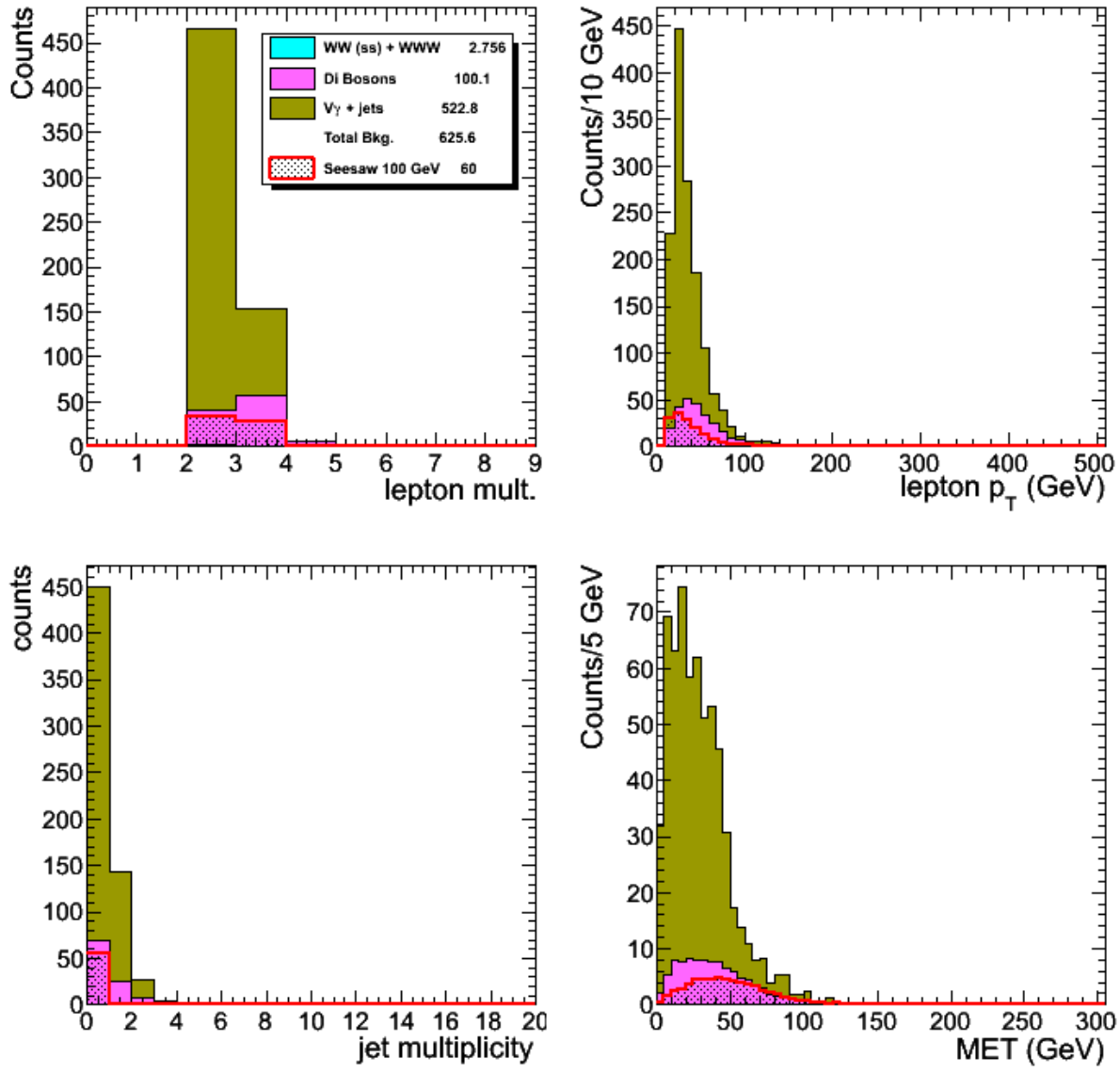

Figure 9.8: $\mu^- e^+ e^+$ kinematics distribution before all selections

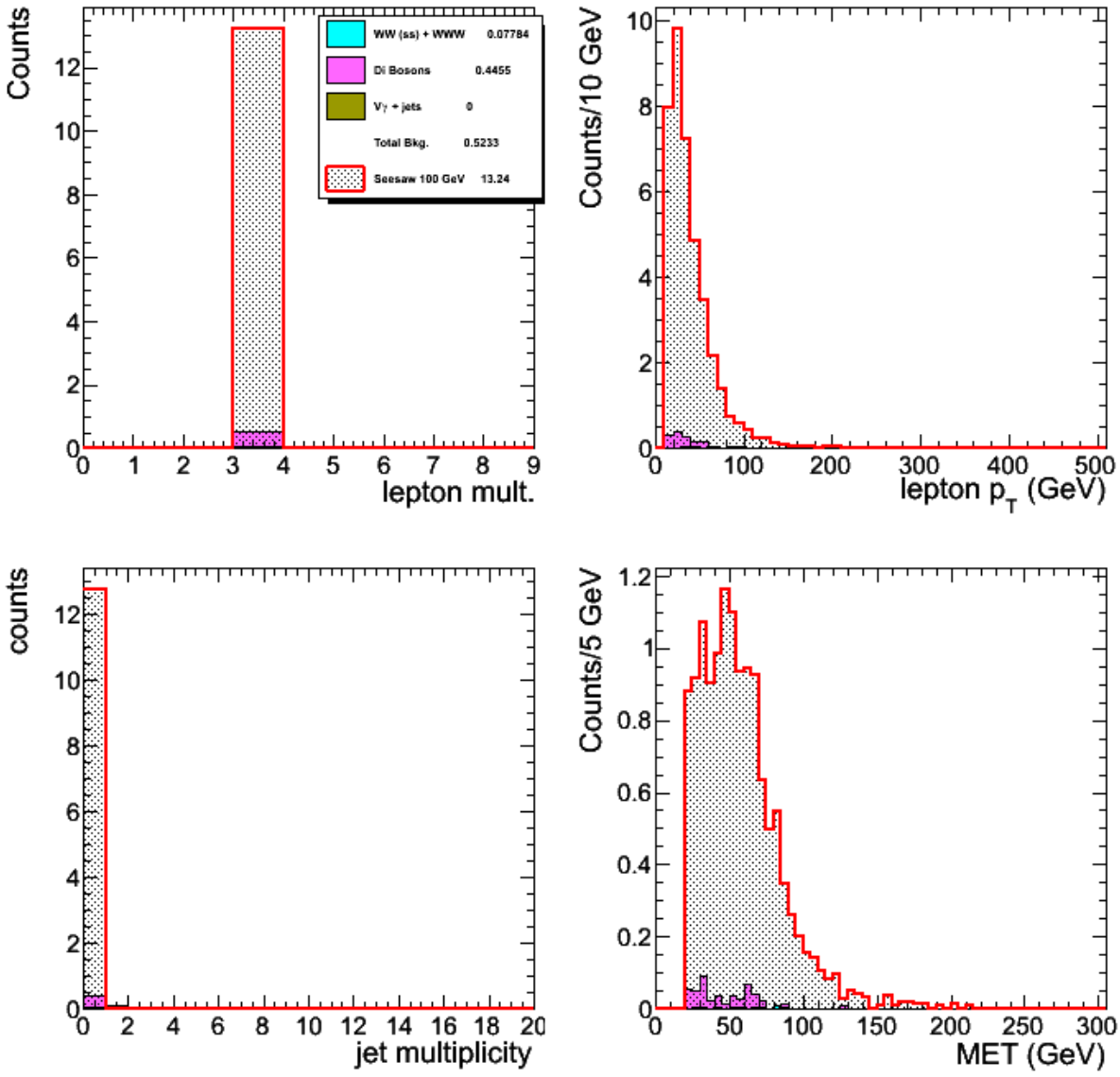

Figure 9.9: $\mu^- e^+ e^+$ kinematics distribution after all selections

for $e^-\ell^+\ell^+$ categories. The contribution to the signal yield of each relevant process fort he final state we analyzed is reported in Table 9.8 and Table 9.9. Similar expected events yields for backgrounds (exclusively from Monte-Carlo) are shown in Table 9.10 for $\mu^-\ell^+\ell^+$ channels, Table 9.11 for $e^-\ell^+\ell^+$ channels.

As mentioned before, we used Monte-Carlo samples for estimating backgrounds with three prompt, same sign leptons. Data driven methods were used to estimate asymmetric gamma conversions as described in Chapter 8, Section 8.3.4 (Dalitz in the Tables). For non-prompt fake lepton backgrounds, we used the data driven methods described in Chapter 8, Section 8.4.1. The background yields divided for each of these sources are listed in Table 9.4. The final estimates of observed and expected event yields are shown in Table 9.5.

	VV	VVV	Vγ	Fakes	Dalitz
$\mu^-e^+e^+$	0.36 ± 0.04	0.08 ±0.04	-	0.24±0.41	-
$\mu^-e^+\mu^+$	4.49±0.63	0.16±0.08	6.90±2.63	4.83 ±1.59	-
$\mu^-\mu^+\mu^+$	5.51±0.77	0.08 ±0.04	-	6.05±1.99	2.95± 0.84
$e^-\mu^+\mu^+$	0.35±0.05	0.06±0.03	-	0.76±0.54	-
$e^-e^+\mu^+$	5.42±0.78	0.18±0.09	-	4.73±1.54	-
$e^-e^+e^+$	2.97±0.44	0.05±0.03	3.45±1.86	2.49±0.95	5.31±0.97

Table 9.4: Summary table of expected and observed events for all channels, after all the Seesaw selections. The expected yield is composed of the physical backgrounds from MC (di and tri-bosons, were V is the bosons Z or W in the table, and Vγ), the contribution due to Dalitz estimation, an the contribution due to fake leptons.

	MC Backgrounds	Data-Driven Backgrounds	Total	Data
$\mu^-e^+e^+$	0.44 ± 0.06 (13.6%)	0.24 ±0.41 (170.8%)	0.68±0.41	1
$\mu^-e^+\mu^+$	11.55±2.70 (23.4%5)	4.83±1.59 (32.9%)	16.38±3.14	21
$\mu^-\mu^+\mu^+$	5.59±0.77 (13.8%)	9 ±2.16 (24.%)	14.59±2.29	14
$e^-\mu^+\mu^+$	0.41±0.06 (14.6%)	0.76±0.54 (71.1%)	1.17±0.54	0
$e^-e^+\mu^+$	5.60±0.78 (13.9%)	6.42±1.61 (25.1%)	12.02±1.79	11
$e^-e^+e^+$	6.47±1.91 (29.5%)	2.49±0.95 (38.2%)	8.96±2.13	6

Table 9.5: Summary table of expected events for all channels, for backgrounds from MonteCarlo and data-driven, after all the Seesaw selections. Percentage errors are reported in parenthesis.

$\mu^-e^+e^+$					
M_Σ (GeV)	2SS	E_T^{miss}>20 GeV	3 leptons	$H_T \leq$ 100 b-veto	Z veto
100	59.10	52.85	13.36	13.24	13.24±3.64
120	33.12	29.79	8.63	8.24	8.24±2.87
130	24.77	22.44	6.68	6.24	6.24±2.50
140	18.48	16.92	4.10	4.59	4.59±2.14
180	6.73	6.32	1.93	1.72	1.72±1.31
$\mu^-e^+\mu^+$					
M_Σ (GeV)	2SS	E_T^{miss}>20 GeV	3 leptons	$H_T \leq$ 100 b-veto	Z veto
100	150.56	132.43	33.34	32.98	24.76±4.98
120	79.84	71.75	20.22	19.25	14.03±3.75
130	60.18	54.43	15.60	14.55	10.08±3.18
140	44.86	40.98	11.87	11.01	7.75±2.78
180	15.79	14.81	4.47	3.97	3.19±1.79
$\mu^-\mu^+\mu^+$					
M_Σ (GeV)	2SS	E_T^{miss}>20 GeV	3 leptons b-veto	$H_T \leq$ 100	Z veto
100	95.03	83.05	20.40	20.20	17.59±4.19
120	48.90	43.86	12.21	11.61	9.56±3.09
130	35.99	32.59	9.27	8.66	6.16±2.48
140	26.72	24.47	6.95	6.40	4.21±2.05
180	9.26	8.71	2.60	2.31	1.61±1.27

Table 9.6: Summary table of expected events from signal in the $\mu^-\ell^+\ell^+$ channel, for the five mass points and after each selection step. are also given. Reported errors are statistical

$e^-\mu^+\mu^+$					
M_Σ (GeV)	2SS	E_T^{miss}>20 GeV	3 leptons	$H_T \leq$ 100 b-veto	Z veto
100	93.28	81.52	16.10	15.93	15.93±3.99
120	48.00	43.05	9.91	9.43	9.43±3.07
130	35.33	31.99	7.57	7.09	7.09±2.66
140	26.23	24.02	5.76	5.33	5.33±2.31
180	9.09	8.55	2.16	1.92	1.92±1.39
$e^-e^+\mu^+$					
M_Σ (GeV)	2SS	E_T^{miss}>20 GeV	3 leptons	$H_T \leq$ 100 b-veto	Z veto
100	150.56	132.43	26.36	26.13	24.55±4.95
120	79.84	71.75	16.84	16.01	14.39±3.79
130	60.18	54.43	13.13	12.32	10.31±3.21
140	44.86	40.98	10.02	9.22	7.33±2.71
180	15.79	14.81	3.82	3.40	2.84±1.68
$e^-e^+e^+$					
M_Σ (GeV)	2SS	E_T^{miss}>20 GeV	3 leptons	$H_T \leq$ 100 b-veto	Z veto
100	59.94	52.80	10.33	10.22	7.14±2.67
120	33.09	29.76	6.92	6.60	4.18±2.05
130	24.74	22.42	5.40	5.07	2.93±1.71
140	18.47	16.91	4.10	3.80	2.09±1.45
180	6.72	6.32	1.62	1.43	0.96±0.98

Table 9.7: Summary table of expected events from signal in the $e^-\ell^+\ell^+$ channels, for the five mass points and after each selection step. Reported errors are statistical.

$\mu^-e^+e^+$							
M_Σ (GeV)	P1	P11	P2	P3	P4	P5	Total
100	6.25	6.05	0.33	0.25	0.17	0.20	13.24±3.64
120	3.16	3.13	0.54	0.51	0.44	0.47	8.24±2.87
130	2.25	2.16	0.51	0.46	0.42	0.45	6.24±2.50
140	1.62	1.53	0.41	0.40	0.32	0.31	4.59±2.14
180	0.57	0.57	0.17	0.17	0.11	0.12	1.72±1.31
$\mu^-e^+\mu^+$							
M_Σ (GeV)	P1	P11	P2	P3	P4	P5	Total
100	11.54	11.52	0.57	0.47	0.33	0.33	24.76±4.98
120	5.48	5.18	0.95	0.90	0.70	0.81	14.03±3.75
130	3.72	3.53	0.81	0.79	0.61	0.61	10.08±3.18
140	2.66	2.64	0.69	0.65	0.53	0.58	7.75±2.78
180	1.03	1.04	0.32	0.31	0.24	0.25	3.19±1.79
$\mu^-\mu^+\mu^+$							
M_Σ (GeV)	P1	P11	P2	P3	P4	P5	Total
100	8.63	7.62	0.39	0.40	0.25	0.29	17.59±4.19
120	3.69	3.42	0.68	0.61	0.52	0.62	9.56±3.09
130	2.19	2.13	0.49	0.50	0.44	0.41	6.16±2.48
140	1.46	1.40	0.37	0.37	0.28	0.32	4.21±2.05
180	0.54	0.51	0.17	0.16	0.11	0.12	1.61±1.27

Table 9.8: Summary table of expected events from signal in the $\mu^-\ell^+\ell^+$ channel, for the five mass points and after all selections. Contribution from the different channels is reported.

$e^-\mu^+\mu^+$							
M_Σ (GeV)	P1	P11	P2	P3	P4	P5	Total
100	7.56	7.24	0.35	0.33	0.24	0.20	15.93±3.99
120	3.63	3.42	0.66	0.63	0.55	0.55	9.43±3.07
130	2.55	2.39	0.57	0.56	0.49	0.53	7.09±2.66
140	1.98	1.70	0.47	0.45	0.35	0.38	5.33±2.31
180	0.64	0.61	0.20	0.20	0.13	0.14	1.92±1.39
$e^-e^+\mu^+$							
M_Σ (GeV)	P1	P11	P2	P3	P4	P5	Total
100	11.54	11.25	0.54	0.53	0.34	0.34	24.55±4.95
120	5.45	5.31	0.99	0.94	0.81	0.88	14.39±3.79
130	3.65	3.62	0.87	0.77	0.68	0.72	10.31±3.21
140	2.53	2.48	0.66	0.62	0.52	0.53	7.33±2.71
180	0.99	0.89	0.28	0.27	0.19	0.22	2.84±1.68
$e^-e^+e^+$							
M_Σ (GeV)	P1	P11	P2	P3	P4	P5	Total
100	3.64	2.97	0.17	0.13	0.11	0.12	7.14±2.67
120	1.56	1.60	0.29	0.28	0.22	0.24	4.18±2.05
130	1.07	1.06	0.23	0.22	0.17	0.18	2.93±1.71
140	0.75	0.69	0.19	0.18	0.13	0.14	2.09±1.45
180	0.32	0.31	0.10	0.10	0.07	0.07	0.96±0.98

Table 9.9: Summary table of expected events from signal in the $e^-\ell^+\ell^+$ channels, for the five mass points and after all selections. Contribution from the different channels is reported.

$\mu^-e^+e^+$					
MC Sample	2SS	E_T^{miss}>20 GeV	3 leptons	$H_T \leq$ 100 ,b-veto	Z veto
Vγ+jets	522.78	306.61	0	0	0
WZ	76.29	65.17	0.40	0.29	0.29±0.04
ZZ	15.65	5.01	0.07	0.07	0.07
WWW	2.02	1.89	1.57	0.08	0.08±0.04
$\mu^-e^+\mu^+$					
MC Sample	2SS	E_T^{miss}>20 GeV	3 leptons	$H_T \leq$ 100 ,b-veto	Z veto
Vγ+jets	718.57	454.52	26.37	21.96	6.90±2.63
WZ	172.45	149.67	48.34	44.60	4.08±0.63
ZZ	36.49	12.51	2.91	2.57	0.41
WWW	4.74	4.49	0.41	0.20	0.16±0.08
$\mu^-\mu^+\mu^+$					
MC Sample	2SS	E_T^{miss}>20 GeV	3 leptons	$H_T \leq$ 100 ,b-veto	Z veto
Vγ+jets	0	0	0	0	0
WZ	102.72	89.49	58.33	54.34	4.95±0.77
ZZ	22.18	8.50	4.34	4.00	0.56
WWW	2.60	2.44	0.25	0.11	0.08±0.04

Table 9.10: Summary table of expected events from MC background in the $\mu^-\ell^+\ell^+$ channels, after each selection step.The error is computed using error propagation from the bin statistical errors assuming that all the bins are uncorrelated.

$e^-\mu^+\mu^+$					
MC Sample	2SS	E_T^{miss}>20 GeV	3 leptons	$H_T\leq$ 100 ,b-veto	Z veto
Vγ+jets	0	0	0	0	0
WZ	100.83	87.85	0.39	0.32	0.32±0.05
ZZ	21.77	8.34	0.03	0.03	0.03
WWW	2.55	2.39	0.18	0.06	0.06±0.03
$e^-e^+\mu^+$					
MC Sample	2SS	E_T^{miss}>20 GeV	3 leptons	$H_T\leq$ 100 ,b-veto	Z veto
Vγ+jets	718.57	454.52	0	0	0
WZ	172.45	149.67	46.51	43.21	5.00±0.78
ZZ	36.49	12.51	3.03	2.74	0.42
WWW	4.74	4.49	0.43	0.20	0.18±0.09
$e^-e^+e^+$					
MC Sample	2SS	E_T^{miss}>20 GeV	3 leptons	$H_T\leq$ 100 ,b-veto	Z veto
Vγ+jets	532.58	312.36	17.85	15.78	3.45±1.86
WZ	76.21	65.11	38.68	35.70	2.81±0.44
ZZ	15.95	5.11	2.12	1.84	0.16
WWW	2.06	1.92	0.17	0.07	0.05±0.03

Table 9.11: Summary table of expected events from MC background in the $e^-\ell^+\ell^+$ channels, after each selection step. The error is computed using error propagation from the bin statistical errors assuming that all the bins are uncorrelated.

10

Systematic Uncertainties

10.1 Uncertainties Description

Systematic uncertainties affect expected events passing all selections calculated from simulation. Systematic uncertainties can be due to imperfect knowledge of either detector effects (energy scales and resolution, pile-up,etc.) or uncertainties on process production at generator level. Moreover, uncertainties arise from the absolute normalization of the total number of expected events.

Systematic uncertainties can be grouped into three categories. In the first group, we combine the theoretical uncertainties in the parton distribution functions (PDFs) and from NLO effects, together with uncertainties that affect the product energy scales and resolution of final-state objects, as determined from simulation.

The second group includes the systematic uncertainties affecting the data versus simulation correction factors for the efficiencies of the trigger, reconstruction, and identification requirements. In particular for our analysis these include lepton trigger, reconstruction and identification efficiencies[1].

The third category comprises uncertainties on the background yield, either simulated and data-driven, and uncertainty on the total integrated luminosity.

We will describe all those sources of uncertainty in the following sections.

[1]The lepton efficiencies could be determined by the tag-and-probe method (111) in the same way for data and simulation, and the uncertainty on the ratio of efficiencies is taken as a systematic uncertainty.

10.1.1 Simulation Uncertainties

1. PDF uncertainties on the efficiency were determined according to the method described in (109). The PDFs are computed via the fit of multiple results from different experimental measurements. The CTEQ collaboration Reference (117) provides 40 eigenvectors, obtained from a Hessian method, corresponding to positive or negative variations of 20 uncorrelated parameters that affect the PDF value. The cross section is then computed for each eigenvector and the resulting errors are summed quadratically via the formula:

$$\Delta\sigma = \frac{1}{2}\sqrt{\sum_{i=1} 40[\sigma_i^+ - \sigma_i^-]^2} \qquad (10.1)$$

   where σ_i^+ (σ_i^-) is the cross section for positive (resp. negative) variation of the i^{th} parameter. The resulting PDF's uncertainty can then be compared to the estimate.

   Basically we followed the procedure of the PDF collaboration: we computed the cross section for 40 different PDF variations and then sum up the error quadratically. We run 40 simulations for the production pp $\rightarrow \Sigma^+\Sigma^0$, Σ, mixing scenario: $V_e = V_\mu = V_\tau$, and the CTEQ6 (117) PDF set was used.

   We found an error of 14 fb (on a cross section of 4330 fb) for 100 GeV mass point, which correspond to 0.32%. For the other mass points (120, 130, 140, 180 GeV) it oscillates between 0.35% and 0.3%. We compared the values we have obtained with PDF uncertainties that were found in previous analysis (Ref. (104), less than 1%) and the results were consistent. We assumed 0.4% uncertainty.

2. Additional contributions to the uncertainty are due to electron and muon momentum scale and resolution[1].

3. Uncertainty on the jet selection is discussed for example in Reference (103), were they quote a ±5% systematics due to the JES (jet energy scale) uncertainty for all regions. We have cross-checked the value, computing the JES uncertainties

[1] The standard procedure is to vary the lepton momentum and energy scales of few percentage (e.g. 1% applied to muon and 2% to electron) kinematic variables and propagated through the selection to assess the systematic effect - usually the result amounts at few percent of uncertainty.

by varying the JES according to the recommended recipes in the Monte-Carlo samples we have considered. The JES uncertainties are summarized in Table 10.1 for the backgrounds. We have taken the overall value of 5%. They are considered negligible for the signal, since jet energy is not relevant for the final state.

4. From Reference (106) $E_{\mathrm{T}}^{\mathrm{miss}}$resolution and scale systematics have been evaluated. We will assume an Uncertainty of 0.6% for the overall $E_{\mathrm{T}}^{\mathrm{miss}}$uncertainties. The effect of this uncertainty on the event yield could be considered negligible.

5. Uncertainty due to pile-up is discussed for example in Reference (103), were systematics on the efficiency due to pile-up has been considered negligible. We have cross checked this analysis results, estimating the systematic effect of pileup uncertainty (the recommended ±8% minimum bias uncertainty as in Reference (107)), on the final selection yield. Estimated pile-up effect are reported in Table 10.1. We will consider these effects negligible on final yields.

10.1.2 Simulation versus Data Efficiency Differences

The uncertainty on event selection efficiency differences in simulation compared to data includes the following:

1. The uncertainties on trigger efficiencies are low since each event category has a trigger efficiency which is almost saturated to values near 100%. A conservative overall value of 1% for muons ans electrons has been assumed.

2. The systematics uncertainty due to charge mis-ID has been evaluated in (106), and checked for our same-sign di-lepton preselected sample in Chapter 8, both for electrons and for muons. We found very small effect, so it can be negligible.

3. Uncertainty on the lepton selection efficiency (which depends on the lepton flavor and p_T). We will take the take this systematics values from Reference (100), where the integral value of the corrections is reported[1]. We list the uncertainties in Table 10.2. Further details about lepton identification and isolation criteria are discussed in Section 8.5.0.2 and 8.5.0.3 of Chapter 8.

[1]In this analysis, the single lepton efficiency evaluated with simulation has been cross checked with data by means of tag and probe methods on $Z_0 \rightarrow e^+e^-$ and $Z_0 \rightarrow \mu^+\mu^-$ events.

Sample	Pileup	Normalization
WZ	1.9%	17%
ZZ	1.2%	7.5%
$V\gamma$	1.5%	13%
WWW	0.5%	50%

Table 10.1: Systematic uncertainties for backgrounds that are taken from Monte-Carlo.

4. The uncertainties on the remaining selections (primary vertex, event cleaning, etc.) are negligible compared to the ones mentioned above as the corresponding efficiencies are essentially 100%.

10.1.3 Background

1. Uncertainties on the background estimates contribute to the overall systematic uncertainty. As discussed in Chapter 9 the main physical backgrounds relevant for our analysis are the di-bosons backgrounds and Vγ. We will pinpoint here their uncertainties.

   Usually the uncertainties on the background estimates are dominated by the uncertainties on the NLO k-factor corrections for the simulated background components, in the case the cross section is the one computed by the Monte Carlo Ref. (112). In our analysis, we will use the measured cross section for the dominant irreducible background (WZ), so no uncertainties on NLO k-factors need to be quoted.

   Uncertainties on the ZZ and Vγ have been computed, and the values have been reported in previous studies: 7.5% for ZZ in Reference (113), 13% for (114). Same values are reported in Reference (107). For the rare backgrounds, we assume a normalization uncertainty of 50%. Table 10.1 contains the overall normalization uncertainty for each background sample considered in the analysis. It should be remarked that the effect of these uncertainties on the final event yield is very small, in particular for background like WW and Vγ that are non influential respect to WZ background. The backgrounds and the systematics on final event yields are reported in Table 9.5 of Chapter 9.

Uncertainties on the yield from data-driven background estimation uncertainties have been calculated, and the values have been reported in Table 9.5 of Chapter 9 too.

2. As regards the absolute normalization of backgrounds events, we will assume a systematic uncertainty for the luminosity of 4.5% which is correlated among signal and background from simulation (116).

10.2 Summary

The sources of the relevant systematic uncertainty are listed in Table 10.3. Uncertainties in the efficiency of the trigger, lepton reconstruction, lepton ID and isolation and the lepton p_T scale are taken from (107), (100). Additional uncertainties are being incorporated from (106). Other have been measured for the Seesaw analysis.

The effect of the systematic uncertainty on the signal and background final yields are reported in Table 10.2. Signal systematics are taken from Reference (100). Background systematics have been discussed in this Chapter and in Chapter 8.

Table 10.2: Relative systematic uncertainties on the signal and background acceptance. The uncertainties are assumed constant for all signal mass points.

Systematic Uncertainties	Channel					
	$\mu^-e^+e^+$	$\mu^-e^+\mu^+$	$\mu^-\mu^+\mu^+$	$e^-\mu^+\mu^+$	$e^-e^+\mu^+$	$e^-e^+e^+$
on signal	5.6%	4.2%	3.6 %	4.2 %	5.6 %	6.7 %
on background MC	13.6%	23.4%	13.8%	14.6%	13.9 %	29.5 %
on background dd	170.8 %	32.9 %	24.0%	71.1 %	25.1 %	38.2 %

Table 10.3: Summary of the input systematic uncertainties for the Seesaw analysis. Reference (107) and (106). Only those background which contributed to the final yield are listed.

Simulation	Systematic uncertainty
Electron energy scale	2%
Muon p_T scale	1%
$E_{\mathrm{T}}^{\mathrm{miss}}$Resolution and scale	0.6%
JES	5%
Pileup	
PDF	
Drell-Yan EW corrections	7 %
Drell-Yan QCD correction	5 %
NLO effect	2.5%
Simulation versus Data	Systematic uncertainty
Di-lepton trigger	1%
Electron reconstruction	0.9%
Electron ID and isolation	1.%
Muon reconstruction	0.7%
Muon ID and isolation	0.7%
Background Estimation	Systematic uncertainty
ZZ	7.5%
$Z\gamma$	13%
Fakes	50%
Dalitz	100%
WZ cross section	17%
Luminosity	4.5%

11 Exclusion Limits

11.1 Event Yield Interpretation

As discussed in Chapter 9, all of the data events that pass the selections are sorted into the six exclusive channels as described in Section 9.1, and results about event yield are summarized in Table 9.5.

In each channel we can compare data with the number of expected Standard Model background events, either from MonteCarlo and from data-driven prediction. Several observation can be made here.

- The number of events observed in all the categories is consistent with the number of predicted background events. Therefore: **no hints of new physics from Seesaw model is present in 2011 LHC data**.

- There are no events observed in category $e^-\mu^+\mu^+$ and only 1 event in category μ^-e^+e+, consistent with the background expectation. Since no excess is found in these categories an upper limit to the **an upper limit to the Seesaw cross section could be set**. This is a remarkable result since no limit have been computed on Seesaw type-III cross section by know.

- In channels $\mu^-e^+\mu^+$ and $e^-e^+e^+$ there is a small excess of events in the background prediction over data, but it is within statistical and systematic errors on background prediction.

Given the event yields and the systematic uncertainties described in Chapter 10, we calculated exclusion limits on the production cross section of the Seesaw fermionic triplet $\sigma(pp \to \Sigma^+\Sigma^0 \to \ell^-\ell^+\ell^+ + E_{\mathrm{T}}^{\mathrm{miss}} + \mathrm{jets})$.

Exclusion limits between combined channels are calculated at the 95% C.L. by employing the CL95 technique in the `RooStats` implementation (81), using Bayesian statistics and a flat prior for the signal production cross section. A brief description of the statistical method is contained in Section 11.2.

Conclusions are drawn in Section 11.3.

11.2 Statistical Procedure

This section describes the method we used for setting statistical limits with multiple channels[1].

For Seesaw analysis we used the CMS Higgs Combined Limit Analysis Toolkit to set limits (References (118), (97), (105)). We will briefly describe it in the following. We used the MarkovChainMC tool of the Higgs Combined Limit Analysis Toolkit, which is a RooStats based package put out by the Higgs PAG in CMS collaboration. This tool calculates the Bayesian limit using Monte Carlo integration (moreover, we used CLs approach as well for a cross-check of results). For the observed limit, we run 100 chains, with a burn-in of 100 steps [2]. For the expected limit and uncertainty band, we run 50 toy Monte Carlos. Log-normal nuisance parameters were used for the systematic uncertainties on both signal and background. We cross-checked the results using a CLs approach tool, results of both methods are reported in the plots.

We will a brief review of the RooStats statistical algorithm. This framework is used to compute likelihoods. The key inputs to the fitter for channel i are:

- The irreducible background events from Monte Carlo in channel i: $b_i^{B-Irr} = \sigma_i^{B-Irr} \times L$ for a L luminosity
- The number of expected background events in the i-th channel predicted by the data-driven method, b_i^{DD} [3].

[1] It is important to note that channels that do not expect any signal do not have an effect on the limit setting. The reason for this is that terms associated with signal free channels analytically factor out of the likelihood when calculating a Bayesian upper limit. Effectively, the signal model in question tells which channels are important, and weighs them according to which channels expect the most signal.

[2] Depending on the mass point, this value was decreased for convergence issues.

[3] The reason for splitting the background prediction into irreducible Monte Carlo and data driven

- σ_S, which represents the specific signal process cross section, and depends on the decay chain and on the combinatorial contribution to the final state.
- ϵ_i^S combined efficiency for the signal
- ϵ_i^{B-Irr} combined efficiency for the background

The statistical model for the number of events in channel i is a Poisson distribution with expected value λ_i and truncated Gaussian constraints for all of the nuisance parameters.

λ_i is the sum of the signal and the expected backgrounds given by:

$$\lambda_i = L \times (\sigma_i^S \times \epsilon_i^S + \sigma_i^{B-Irr} \times \epsilon_i^B) + b_i^{DD} \tag{11.1}$$

where the first term corresponds to the expected signal, the second term corresponds to the expected background from Monte-Carlo simulations, and the third term is the expected background from the data-driven method.

Given the number of observed events N_i on the ith category a Poisson likelihood function (i.e. the probability of observing the N_i events) can be written as:

$$\mathcal{L}\left(N_i\right) = \frac{\lambda_i^{N_i}}{N_i!} \cdot e^{-\lambda_i} \ , \tag{11.2}$$

We then combine the Poissonian distributions Eq.11.1 for each channel into a likelihood function:

$$\mathcal{L}(N_1, N_2 ... | N^S) = \prod_i f(N_i, \lambda_i(N^S)) \tag{11.3}$$

which is the joint conditional probability of observing $N_1, N_2, N_3, ...$ events in channel 1, channel 2, etc.

The posterior distribution for σ^S is given by the integral over the nuisance parameters, with proper prior functions. The fit is performed in order to maximize the likelihood function. The nuisance parameters are allowed to vary during the fit according to their log-normal distributions.

components is because in the background numbers predicted using the data-driven method the luminosity, lepton identification efficiencies, lepton isolation efficiencies, and lepton trigger efficiencies are included. While, in the background numbers derived from simulation all the above parameters have to be accounted for.

We set our exclusion upper limit on cross section (σ) times branching fraction times acceptance at 95% C.L.

To determine the number of signal events required to exclude the model at 95% confidence, we use the Bayesian 95% upper limit using the N_{signal} prior $[0, \infty]$. Therefore, we solve the following integral equation for N_{95}:

$$0.95 = \frac{\int_{-\inf}^{N_{95}} \pi(N^S)\mathcal{L}(N^S)dN^S}{\int_{-\inf}^{+\inf} \pi(N^S)\mathcal{L}(N^S)dN^S} \tag{11.4}$$

where $\pi(N^S)$ is a flat prior probability, equal to 1 for $N^S \geq 0$ and equal to 0 when $N^S \leq 0$. (Reference (105)).

11.3 Results

As pointed out in the introduction of this Chapter, no significant excess of events with respect to the SM expectations have been found in the channels analyzed in this study, described in Chapter 9. The 95% confidence level limits on cross section for the combination of all the six analyzed channels was computed.

The limits on cross section versus Seesaw fermion mass are shown in Figures 11.1, 11.2 The red horizontal line correspond to exactly the 95% CL. Therefore, **we can conclude that Seesaw mass are excluded below 180-185(at NLO) GeV for equal mixing scenario. If the Seesaw triplet couples with one leptonic flavor only, the limit on the mass is 200 GeV.**

The limit on Seesaw cross section is shown in in Figures 11.3: were the theoretical cross section is reported in blue line. **The limit on cross section is 20 fb for the equal mixings scenario**.

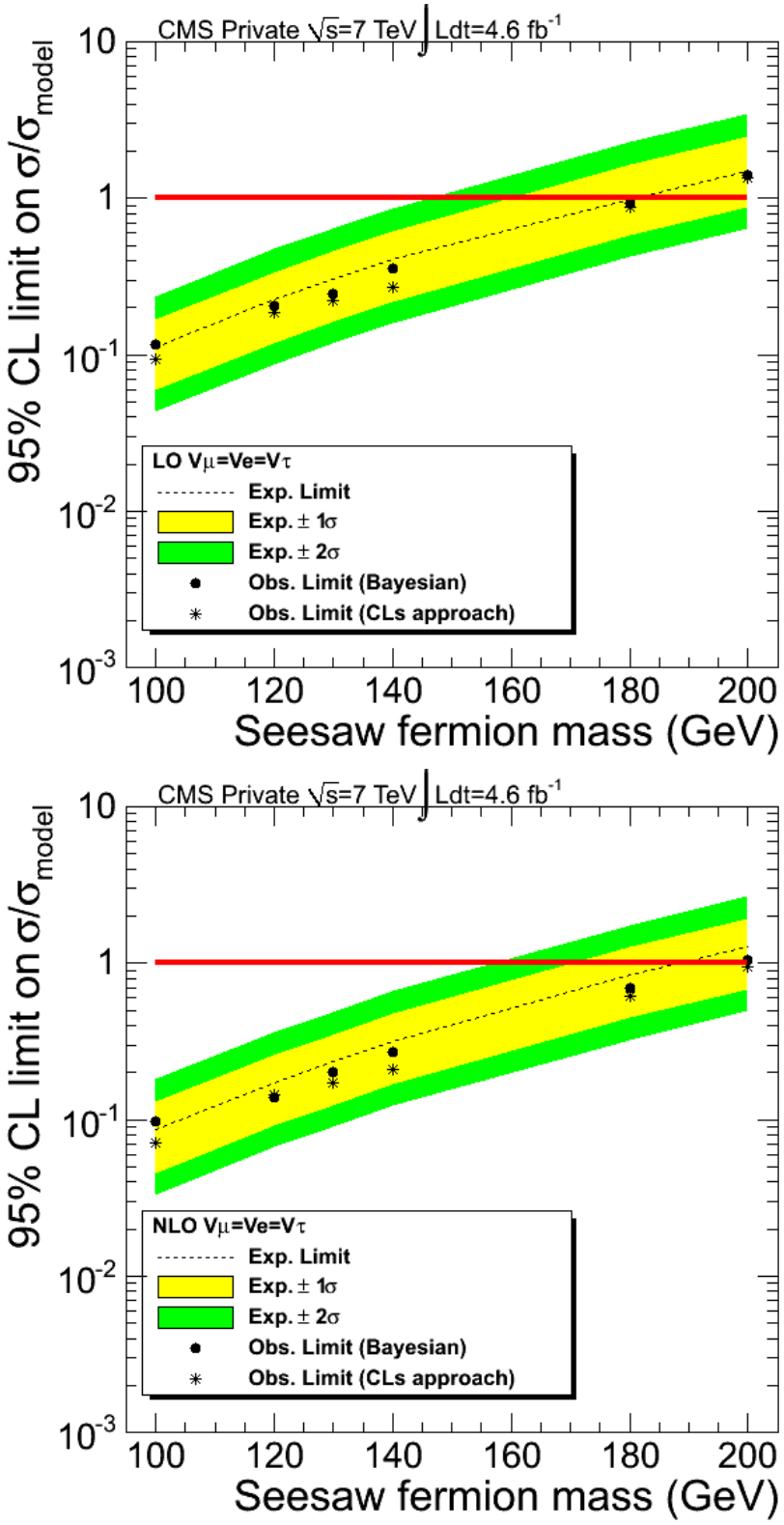

Figure 11.1: The 95% CL upper limit on the Seesaw fermion mass is shown, for $V_\mu = V_e = V_\tau$ mixing scenario. LO (leading order) prediction is shown on top, NLO (next-to-leading-order) on bottom plot.

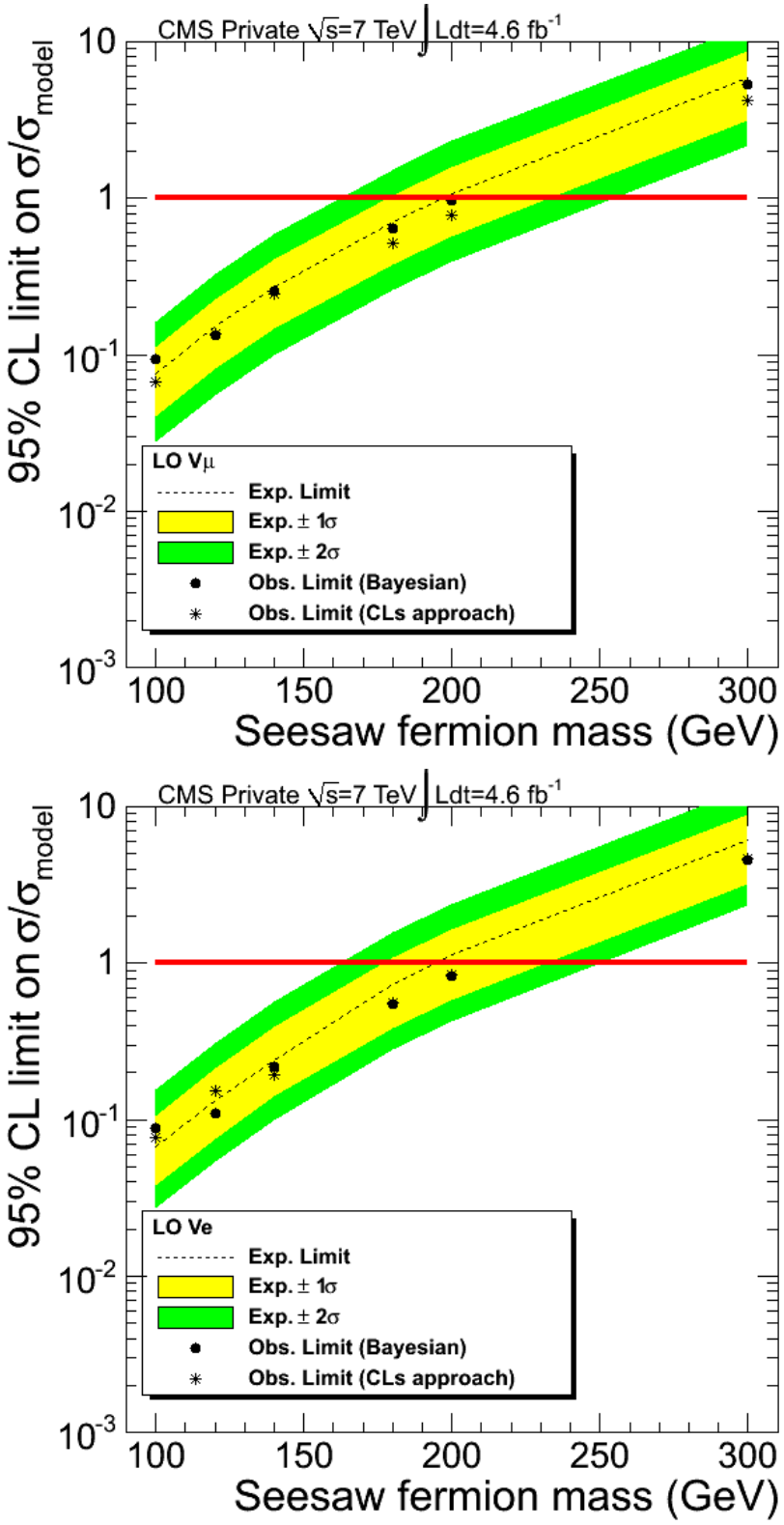

Figure 11.2: The 95% CL upper limit on the Seesaw fermion mass is shown, for $V_\mu \neq 0$, $V_e = V_\tau = 0$ mixing scenario(top), and for $V_\mu = V_\tau = 0$, and $V_e \neq 0$ mixing scenario (bottom).

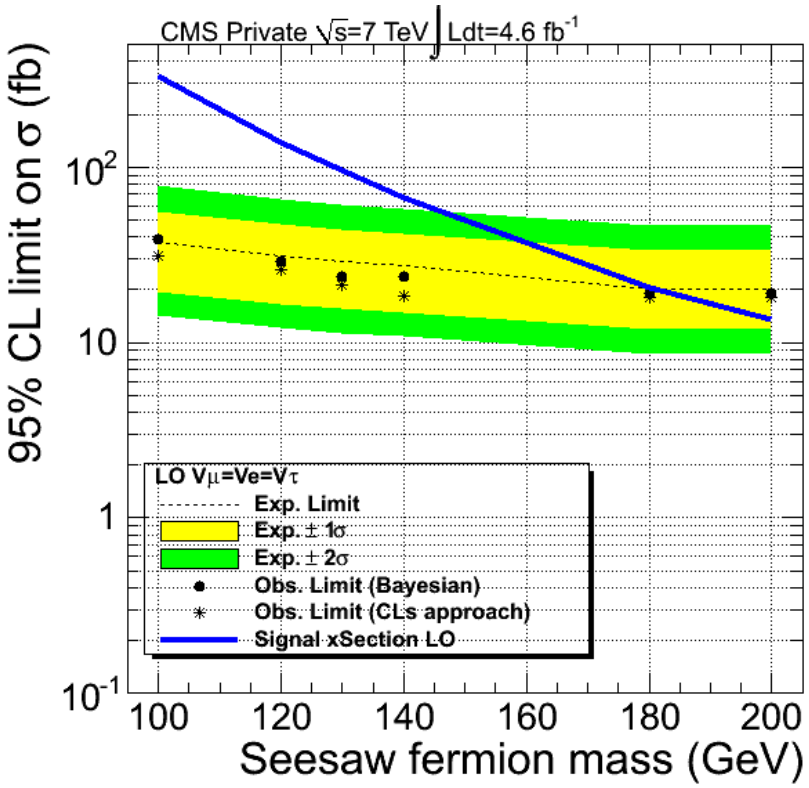

Figure 11.3: The 95% CL upper limit on the Seesaw σ is shown, for $V_\mu = V_e = V_\tau$ mixing scenario.

12 Conclusions

12.1 2011 Data Analysis Conclusions

We have searched for evidence of Seesaw type III signal from pp collisions at 7 TeV using the CMS detector data at LHC. In the Minimal Seesaw type III, the lightest fermion triplet would be produced in pp collision and decay into Standard Model gauge bosons and leptons, plus neutrinos which are stable and will escape the detector resulting in a missing energy signature.

In this thesis we searched for three lepton production from Seesaw decays. This channel have the largest production cross section among all states at LHC. The signature in the detector would be three standard leptons (electrons and muons), jets, and missing energy. We neglected the analysis of signatures with tau lepton production.

The Standard Model background for the Seesaw signature is dominated by WZ irreducible background (taken from MonteCarlo Summer11 official CMS production) while other backgrounds dominated by fake lepton events have been computed with data-driven techniques.

The Seesaw signal Monte Carlo samples were generated with madgraph5 and passed through CMS detector simulation and objects reconstruction. Event pre-selection criteria were chosen according to the Physical Analysis Group recommendation and according to the kinematic distribution of decay products determined from Monte Carlo studies. Event selection requirement were optimized in order to reject background with a minimal loss of signal acceptance.

We searched for Seesaw signature in $4.6 fb^{-1}$ of integrated luminosity data collected during CMS 2011 RunA and RunB period. We found no evidence for Seesaw fermion triplet pair production.

We set a lower limit at 95% confidence level on the Seesaw-type III fermion mass of 180-200 GeV, depending on the Seesaw mixing with leptons scenarios.

12.2 Further Development with 2012 Data

The LHC will continue to operate at $3.5TeV$ per beam, half of its planned capability, until the end of 2012 (draft schedule is in Figure 12.1). It will then be shut down for a year for upgrades to allow full energy operation ($7TeV$ per beam), with reopening planned for 2014. The key 2012 expectations are:

- possibly move to higher beam energy: $3.5TeV \rightarrow 4TeV$ (will be decided at the beginning of 2012);
- possible peak performance with $50ns$ beams:
  - 3.5 TeV: higher bunch intensity, smaller β^* (0.8-0.9 m);
  - peak luminosity increase: 20 to 30 %;
  - 4 TeV: higher bunch intensity, smaller β^* (0.7 0.8 m);
  - peak luminosity increase: 60 to 75 %;
- **luminosity of about** $10fb^{-1}$ **should be within in reach**.

Therefore, more data will be collected in CMS run from April 2012 to the end of the year, and a further development of this analysis can be done using the same technique and increased statistics. Assuming the limit on $\Sigma\Sigma$ pair production cross section depends primarily on statistics, we can expect an improvement in the cross section limit.

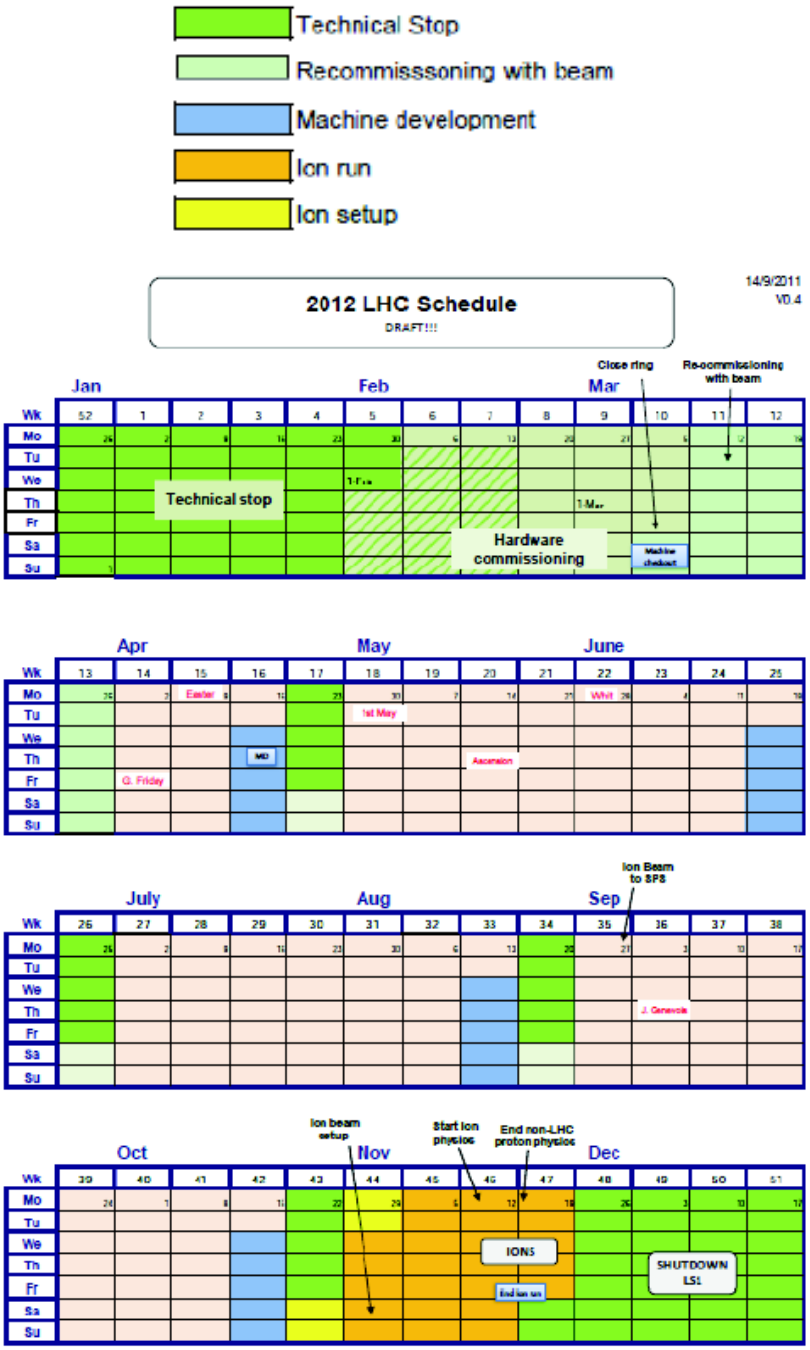

Figure 12.1: 2012 LHC schedule.

References

[1] *http://cms.web.cern.ch/news/summary-2011-p-p-running*. 5

[2] S. Willenbrock, **Hadron Colliders, the Standard Model, and Beyond**, *arXiv:hep-ph/0212032v1*, 2002. 7

[3] S. Willenbrock, **Proceedings of the Advanced Study Institute on Techniques and Concepts of High Energy Physics, St. Croix, U. S. Virgin Islands**, *arXiv:hep-ph/0211067*, 2006. 7, 12

[4] C. Amsler *et al.* [Particle Data Group], **Review of particle physics**, *Phys. Lett. B* **667** *(2008) 1*, 2008. 51

[5] S. Weinberg, **Baryon And Lepton Nonconserving Processes**, *Phys. Rev. Lett.* **43** *(1979) 1566*, 1979. 17

[6] S. Weinberg, **Baryon And Lepton Nonconserving Processes**, *Phys. Rev. Lett.* **43**, *1566*, 1979. 12

[7] S. Weinberg, **Conceptual Foundations Of The Unified Theory Of Weak And Electromagnetic Interactions**, *Rev. Mod. Phys.* **52**, *515*,(1980), *Science* **210**, *1212*, (1980). 15

[8] F. Maltoni, J. M. Niczyporuk and S. Willenbrock, **The scale of fermion mass generation**, *Phys. Rev. D* **65**, *033004 (2002) [arXiv:hep-ph/0106281]*, 2002. 15

[9] H. Georgi and S. L. Glashow, **Unity Of All Elementary Particle Forces**, *Phys. Rev. Lett.* **32**, *438*, (1974). 16

[10] K. Hagiwara *et al.* [Particle Data Group Collaboration], **Review Of Particle Physics**, *Phys. Rev. D* **66**, *010001*, (2002). 207

[11] A. F. Falk **The CKM matrix and the heavy quark expansion**, **in** *Flavor Physics for the Millennium, TASI 2000, ed. J. Rosner (World Scientific,Singapore, 2001), p. 379 [arXiv:hep-ph/0007339]*, 2001.

[12] W. Buchmüller and D. Wyler, **Effective Lagrangian Analysis Of New Interactions And Flavor Conservation**, *Nucl. Phys. B* **268**, *621 (1986)*, 1986.

[13] B. Kayser, **On the Quantum Mechanics of Neutrino Oscillation**, *Phys. Rev.* ***D24,*** *110 (1981)*, 1981. 13

[14] I. d. M. Varzielas, **Family symmetries and the origin of fermion masses and mixings**, *arXiv:0801.2775 [hep-ph]*, 2008. 13

[15] W.-M. e. a. Yao, **Review of Particle Physics**, *Journal of Physics G* ***33,*** *1+ (2011)*, 2001. 13, 30, 54, 71

[16] M. Maltoni, T. Schwetz, M. A. Tortola and J. W. F. Valle, **Status of global fits to neutrino oscillations**, *New J. Phys.* ***6,*** *122 (2004), hep-ph/0405172*, 2004. 10, 11

[17] A. Y. Smirnov, **Neutrino masses and oscillations**, *(0700), hep-ph/9611465*, 2007. 11

[18] P. Minkowski, *Phys. Lett. B 67 421*, (1977); M. Gell-Mann, P. Ramond and R. Slansky, **Supergravity**, *edited by P. van Nieuwenhuizen and D. Freedman, (North-Holland, 1979), p. 315*, 1979; T. Yanagida, **Proceedings of the Workshop on the Unified Theory and the Baryon Number in the Universe**, *edited by O. Sawada and A. Sugamoto (KEK Report No. 79-18, Tsukuba, 1979), p. 95*, 1979; R.N. Mohapatra and G. Senjanović, *Phys. Rev. Lett.* **44** *(1980) 912*, 1980. 17

[19] M. Magg and C. Wetterich, *Phys. Lett. B94 (1980) 61*, 1980; J. Schechter and J. W. F. Valle, *Phys. Rev. D 22 (1980) 2227*, 1980; C. Wetterich, *Nucl. Phys. B187 (1981) 343*, 1981; G. Lazarides, Q. Shafi and C. Wetterich, *Nucl Phys. B181 (1981) 287*, 1981; R.N. Mohapatra and G. Senjanović, *Phys.Rev. D23 (1981) 165*, 1981. 17

[20] R. Foot, H. Lew, X.-G. He and G.C. Joshi, *Z. Phys. C44 (1989) 441*, 1989. 17

[21] J. Kersten and A. Y. Smirnov, **Right-Handed Neutrinos at LHC and the Mechanism of Neutrino Mass Generation**, *Phys. Rev. D* **76** *(2007) 073005* `[arXiv:0705.3221 [hep-ph]]`, 2007.

[22] F. del Aguila, J. A. Aguilar-Saavedra and R. Pittau, **Neutrino physics at large colliders**, *J. Phys. Conf. Ser.* **53**, *506 (2006) [arXiv:hep-ph/0606198], 2006* 68

[23] F. del Aguila, J. A. Aguilar-Saavedra and R. Pittau, **Heavy neutrino signals at large hadron colliders**, *JHEP* **0710** *(2007) 047* `[hep-ph/0703261]`, 2007. 51, 68

[24] F. del Aguila and J. A. Aguilar-Saavedra, **Distinguishing seesaw models at LHC with multi-lepton signals**, *Nucl. Phys. B* **813**, *22 (2009)[arXiv:0808.2468 [hep-ph]]*, 2009. ix, 17, 21, 51, 54, 55, 56, 60, 66, 68, 73, 74, 75, 81, 149

[25] F. del Aguila, J. de Blas and M. Perez-Victoria, **Effects of new leptons in Electroweak Precision Data**, *Phys. Rev. D* **78** *(2008) 013010,[arXiv:0803.4008 [hep-ph]]*, 2008. 19, 23, 59, 68

[26] F. del Aguila, J. A. Aguilar-Saavedra, J. de Blas and M. Perez-Victoria, **Electroweak constraints on seesaw messengers and their implications for LHC**, *arXiv:0806.1023 [hep-ph]*, 2008. 21, 68

[27] A. Y. Smirnov, **Recent developments in neutrino phenomenology**, *(0200), hep-ph/0702061*, 2002. 11

[28] A. Abada, C. Biggio, F. Bonnet, M. B. Gavela and T. Hambye, $\mu \to e\gamma$ **and** $\tau \to l\gamma$ **decays in the fermion triplet seesaw model**, *Phys. Rev. D* **78** *(2008) 033007 [arXiv:0803.0481 [hep-ph]]*, 2008. 23, 24, 52, 59, 213

[29] R. Franceschini, T. Hambye and A. Strumia, **Type-III see-saw at LHC**, *Phys. Rev. D* **78** *(2008) 033002 [arXiv:0805.1613 [hep-ph]]*, 2008 51, 54, 57, 63, 81, 149

[30] C. Biggio and F. Bonnet, **Implementation of the type III seesaw model in FeynRules/MadGraph and prospects for discovery with early LHC data**, *arXiv:1107.3463 [hep-ph]*, 2011. 23, 24, 52, 73, 81, 149, 150

[31] Gregor Herten, **The First Year of the Large Hadron Collider: A Brief Review**. *arXiv:1104.4205v1*, 2011. 35

[32] D. Froidevaux and V. A. Mitsou, **Experimental prospects at the Large Hadron Collider**, *J. Phys. Conf. Ser.* **171**, *012021 (2009) [arXiv:0905.0258 [hep-ex]]*, 2009. 33, 34

[33] Godbole, Rohini M., **Story of a journey: Rutherford to the Large Hadron Collider and onwards**, *[arXiv:1007.0946[hep-ex]]*, 2010. 28, 29, 31, 32, 34

[34] K. Moenig, **View point: First bounds on the Higgs boson from hadron colliders**, *Physics 3, 14 (2010); http://physics.aps.org/*, 2010. 30

[35] T. J. Orimoto [CMS Collaboration], **First CMS Results with LHC Beam**, *arXiv:0905.4814 [hep-ex]*, 2009. 42

[36] G. L. Bayatian *et al.* [CMS Collaboration], **CMS Technical Design Report**, **CERN-LHCC-2006-001**, **CERN-LHCC-2006-021**, **CMS-TDR-008-2**, *J. Phys. G* **34**, *995 (2007)*, 2007. 42

[37] *http://lhc.web.cern.ch/lhc/LHC-DesignReport.html*

[38] *https://twiki.cern.ch/twiki/bin/view/CMS/MadgraphGridpackPreparation* 82

[39] *https://twiki.cern.ch/twiki/bin/view/CMS/WorkBookGeneration.* 80, 226

[40] *https://twiki.cern.ch/twiki/bin/view/CMS/SWGuidePythia6Interface.* 85

[41] *https://twiki.cern.ch/twiki/bin/view/CMS/MadGraphCMSPage.*

[42] *http://cp3wks05.fynu.ucl.ac.be/twiki/bin/view/Library/MadGraphSamples* 219

[43] *https://twiki.cern.ch/twiki/bin/view/CMS/SWGuideEventGeneration.*

[44] *https://twiki.cern.ch/twiki/bin/view/CMS/SWGuideLHEInterface.* 80

[45] *https://twiki.cern.ch/twiki/bin/view/CMS/SWGuideMadGraphInterface.* 85

[46] *https://twiki.cern.ch/twiki/bin/view/CMS/SWGuidePythia6Interface.* 80

[47] T. Sjostrand, S. Mrenna and P. Skands, **PYTHIA 6.4 physics and manual**, *JHEP* **0605** *(2006) 026* [hep-ph/0603175], 2006. 73, 80, 85, 150, 231

[48] The CMS Collaboration, **Search for Pair Production of Second Generation Scalar Leptoquarks in pp Collisions at ps = 7 TeV**, *CMS PAS EXO-10-007*, 2007.

[49] G. Brooijmans et al., **New Physics at the LHC: A Les Houches Report. Physics at Tev Colliders 2007 – New Physics Working Group**, *Part 8 "A search for top partners at the LHC using same-sign dilepton final states; arXiv:0802.3715v1 [hep-ph]*, 2008.

[50] R. Contino and G. Servant, *arXiv:0801.1679 [hep-ph]*,2008.

[51] *http://ceballos.web.cern.ch/ceballos/hwwlnln/samples_cms-sw35x.txt*

[52] The CMS Collaboration, **Search for a Heavy Bottom-like quark in pp Collisions at ps = 7 TeV**, *CMS PAS EXO-10-018*, 2010. 124

[53] The CMS Collaboration, **Measurements of InclusiveW and Z Cross Sections in pp Collisions at ps = 7 TeV**, *CMS PAS EWK-10-002*, 2010.

[54] The CMS Collaboration, **Performance of CMS muon identification in pp collisions at ps = 7 TeV**, *CMS PAS MUO-2010-002 (2010)*, 2010. **Performance of muon reconstruction, identification, and trigger in 2010 data**, *CMS PAS MUO-2010-004 (2010)*, 2010. 93

[55] The CMS Collaboration, **Performance of tau reconstruction algorithms in 2010 data collected with CMS**, *CMS PAS TAU-11-001 (2011)*, 2011.

[56] *https://twiki.cern.ch/twiki/bin/view/CMSPublic/SWGuidePFTauID.*

[57] Murayama et al., **HELAS libraries**, *KEK-91-11*, 1992.

[58] J. Alwall *et al.*, *JHEP* **0709** *(2007) 028, [arXiv:0706.2334 [hep-ph]]*, 2007; J. Alwall, M. Herquet, F. Maltoni, O. Mattelaer, T. Stelzer, *JHEP* **1106** *(2011) 128, [arXiv:1106.0522 [hep-ph]]*, 2011. *http://madgraph.hep.uiuc.edu/*, *http://madgraph.roma2.infn.it/*, *http://madgraph.phys.ucl.ac.be/*. 80, 83, 150, 231

[59] *http://lepp.cornell.edu/public/theory/BRIDGE/index.html.*

[60] Torbjörn Sjöstrand, **A model for initial state parton showers**, *Physics Letters B, 157(4):321325*, 1985. 79

[61] *https://twiki.cern.ch/twiki/bin/view/Main/PowhegBOX.* 231

[62] *http://geant4.cern.ch/*. 87

[63] *http://feynrules.irmp.ucl.ac.be/*. 80

[64] *https://cms-cpt-software.web.cern.ch/cmscpt-software/General/* 80

[65] *http://feynrules.irmp.ucl.ac.be/wiki/TypeIIISeeSaw* 81

[66] N. D. Christensen and C. Duhr, **FeynRules - Feynman rules made easy**, *Comput. Phys. Commun.* **180** *(2009) 1614 [arXiv:0806.4194 [hep-ph]]*, 2009.

[67] R. N. Mohapatra, *Phys. Rev. Lett.* **56** *(1986) 561-563*, 1986; R. N. Mohapatra, J. W. F. Valle, *Phys. Rev.* **D34** *(1986) 1642*, 1986.

[68] B. Bajc, G. Senjanovic, *JHEP* **0708** *(2007) 014, [hep-ph/0612029]*, 2007; B. Bajc, M. Nemevsek, G. Senjanovic, *Phys. Rev.* **D76** *(2007) 055011, [hep-ph/0703080]*, 2007; A. Arhrib, B. Bajc, D. K. Ghosh, T. Han, G. -Y. Huang, I. Puljak, G. Senjanovic, *Phys. Rev.* **D82** *(2010) 053004, [arXiv:0904.2390 [hep-ph]]*, 2010. 51, 81

[69] P. Meade and M. Reece, **BRIDGE: Branching ratio inquiry / decay generated events**, *arXiv:hep-ph/0703031*, 2007.

[70] A. Abada, C. Biggio, F. Bonnet, M. B. Gavela and T. Hambye, **Low energy effects of neutrino masses**, *JHEP* **0712** *(2007) 061 [arXiv:0707.4058 [hep-ph]]*, 2007. 17, 51, 59

[71] J. Conway et al., **PGS4: Pretty Good Simulation of high energy collisions**, *http://www.physics.ucdavis.edu/ conway/research/software/-pgs/pgs4-general.htm*, 2006. 73

[72] L. Basso, A. Belyaev, S. Moretti and C. H. Shepherd-Themistocleous, **Phenomenology of the minimal B-L extension of the Standard model: Z' and neutrinos**, *Phys. Rev. D* **80** *(2009) 055030 [arXiv:0812.4313 [hep-ph]]*, 2009; L. Basso, **Phenomenology of the minimal B-L extension of the Standard Model at the LHC**, *arXiv:1106.4462 [hep-ph]*, 2011. 73

[73] S. Chatrchyan *et al.* [CMS Collaboration], **Search for a Heavy Bottom-like Quark in pp Collisions at $\sqrt{s} = 7$ TeV**, *[arXiv:1102.4746 [hep-ex]]*, 2011. 231

[74] N. D. Christensen, P. de Aquino, C. Degrande, C. Duhr, B. Fuks, M. Herquet, F. Maltoni, S. Schumann, **A Comprehensive approach to new physics simulations**, *Eur. Phys. J.* **C71** *(2011) 1541 [arXiv:0906.2474 [hep-ph]]*, 2011.

[75] S. Chatrchyan *et al.* [CMS Collaboration], **Measurement of the Top-antitop Production Cross Section in pp Collisions at sqrt(s)=7 TeV using the Kinematic Properties of Events with Leptons and Jets**, *[arXiv:1106.0902 [hep-ex]]*, 2011. 137

[76] G. Aad *et al.* [ATLAS Collaboration], **Measurement of the top quark pair production cross section in pp collisions at sqrt(s) = 7 TeV in dilepton final states with ATLAS**, *[arXiv:1108.3699 [hep-ex]]*, 2011. 137

[77] S. Chatrchyan *et al.* [CMS Collaboration], **Measurement of W+W- Production and Search for the Higgs Boson in pp Collisions at sqrt(s) = 7 TeV**, *Phys. Lett.* **B699** *(2011) 25-47 [arXiv:1102.5429 [hep-ex]]*, 2011. 136

[78] G. Aad *et al.* [ATLAS Collaboration], **Measurement of the WW cross section in sqrt(s) = 7 TeV pp collisions with ATLAS**, *[arXiv:1104.5225 [hep-ex]]*, 2011. 136

[79] [CMS Collaboration], **Measurement of the WW, WZ and ZZ cross sections at CMS**, *CMS-EWK-11-010-PAS*, 2011. 122, 136

[80] *https://twiki.cern.ch/twiki/bin/view/CMSPublic/SWGuide-FastSimPileUp#Arbitrary_distribution*, *https://indico.cern.ch/getFile.py/access?contribId=1&sessionId=5&resId=0&materialId=slides&confId=126180*, *https://twiki.cern.ch/twiki/bin/view/CMSPublic/SWGuide-FastSimulation?redirectedfrom=CMS.SWGuideFastSimulation#Recipe_for_CMSSW_3_8_X_cmsDriver*, *https://twiki.cern.ch/twiki/bin/view/CMSPublic/SWGuide-FastSimTags*, *https://twiki.cern.ch/twiki/bin/view/CMS/FastSimTag42X*. 229

[81] *http://root.cern.ch/drupal/*. 84, 184

[82] [CMS Collaboration], *EXO-10-015*,2011.

[83] [CMS Collaboration], *CMS AN -2010/034*,2010. 92

[84] R Fruhwirth, Wolfgang Waltenberger, and Pascal Vanlaer, **Adaptive Vertex Fitting**, *Technical Report CMS-NOTE-2007-008. CERN-CMS-NOTE-2007-008, CERN, Geneva*, Mar 2007. 91

[85] [CMS Collaboration], *CMS PAS PFT-10-003*, 2010. 92, 156

[86] [CMS Collaboration], **Commissioning of the Particle-flow Event Reconstruction with the first LHC collisions recorded in the CMS detector**, *CMS PAS PFT-10-001*, 2010. 95, 156

[87] [CMS Collaboration], **Particle–Flow Event Reconstruction in CMS and Performance for Jets, Taus, and $E_{\mathrm{T}}^{\mathrm{miss}}$**, *CMS PAS PFT-09-001*, 2010. 95, 156

[88] [CMS Collaboration], *CMS PAS PFT-08-001*, 2008. 93

[89] [CMS Collaboration], *CMS PAS TAU-11-001*, 2011. 93, 94

[90] [CMS Collaboration], *CERN-LHCC-2004-035/G-083, CMS NOTE / 2004-031*, December 2004. **CMS Computing TDR**, *CERN-LHCC-2005-023, CMS TDR 7*, 20 June 2005. 97, 98

[91] *https://twiki.cern.ch/twiki/bin/viewauth/CMS/RecoSkimming*; *http://cmssw.cvs.cern.ch/cgi-bin/cmssw.cgi/CMSSW/Configuration/Skimming/python/-PDWG_HWWSkim_cff.py*. 106

[92] *https://indico.cern.ch/conferenceDisplay.py?confId=156711*, *https://espace.cern.ch/cms-quarkonia/tnp/default.aspx*. 101, 102, 103

[93] *https://twiki.cern.ch/twiki/bin/view/CMS/TriggerTables* 99

[94] *https://cmswbm.web.cern.ch/cmswbm/cmsdb/servlet/-L1Summary*, *https://cmswbm.web.cern.ch/cmswbm/cmsdb/servlet/-TriggerMode*, *https://cmswbm.web.cern.ch/cmswbm/cmsdb/servlet/-HLTSummary*, *https://cmswbm.web.cern.ch/cmswbm/cmsdb/servlet/-RunSummary*. 99

[95] *https://twiki.cern.ch/twiki/bin/viewauth/CMS/StandardModelCrossSections*. 231

[96] CMS Collaboration, **Multileptonic SUSY searches with Jets and E_T^{miss} pp Collisions at 7 TeV**, *CMS PAS SUS-11-013*, 2011. 124, 127, 128, 135, 137, 158, 159

[97] S. Arora, K. Chan, J.P. Chou, E. Contreras-Campana, R.C. Gray, A. Lath, K. Mei, S. Panwalkar, S. Somalwar, S. Thomas, M. Walker, E. Williams, **Background and efficiency determination methods for multilepton analyses**, *CMS AN -2011/281*, 2011. x, 103, 104, 127, 128, 129, 130, 145, 146, 147, 184

[98] L3 Collaboration, **Search for heavy neutral and charged leptons in e+e- annihilation at LEP**, *Phys. Lett., B517 pag.75,doi=10.1016/j.physletb.2003.10.071* , 2001. 151

[99] CMS Collaboration, **Determination of Jet Energy Calibration and Transverse Momentum Resolution in CMS**, *Submitted to JINST, arXiv 1107.4277* , 2011. 95

[100] CMS Collaboration, **Measurement of the WW, WZ and ZZ cross sections at CMS**, *CMS Physics Analysis Summary, CMS-PAS-EWK-11-010, http://cdsweb.cern.ch/record/1279362*, 2011. 179, 181

[101] CMS Collaboration, **Measurement of the Inclusive W and Z Production Cross Sections in pp Collisions at $\sqrt{s} = 7$ TeV**, *arXiv 1107.4789 hep-ex*, 2011 .

[102] D. Barge, C. Campagnari, P. Kalavase, D. Kovalskyi, V. Krutelyov, J. Ribnik W. Andrews, D. Evans, F. Golf, J. Mülmenstädt, S. Padhi, Y. Tu, F. Würthwein, A. Yagil, J. Yoo, L. Bauerdick, I. Bloch, K. Burkett, I. Fisk, Y. Gao, O. Gutsche, B. Hooberman, **Fake Rates for dilepton Analyses**, *CMS AN -2010/257*, 2010. 139, 143

[103] D. Barge, C. Campagnari, P. Kalavase, D. Kovalskyi, V. Krutelyov, J. Ribnik W. Andrews, D. Evans, F. Golf, J. Mülmenstädt, S. Padhi, Y. Tu, F. Würthwein, A. Yagil, J. Yoo, L. Bauerdick, I. Bloch, K. Burkett, I. Fisk, Y. Gao, O. Gutsche, B. Hooberman **Inclusive search for New Physics with Same-Sign Dileptons using early LHC data**, *CMS AN -2010/247*, 2010. 132, 139, 143, 178, 179

[104] D. Barge et al., *AN-CMS2010/258 http://arxiv.org/abs/1010.5994*, 2010. 178

[105] J. Conway, *http://www-cdf.fnal.gov/physics/statistics/code/bayes.f* , 2010. 184, 186

[106] Aytul Adiguzel, Vuko Brigljevic, Tulika Bose, Claude Charlot, Cory Fantasia, Nicola De Filippis, Senka Duric, Jeff Klukas, Jelena Luetic, Yurii Maravin, Arabella Martelli, Srecko Morovic, and Salvatore A. Tupputi, **Measurement of the WZ cross section at the CMS Experiment**, *AN-11-259*, 2011. 179, 181, 182, 233

[107] Aytul Adiguzel, Vuko Brigljevic, Tulika Bose, Cory Fantasia, Matthew Herndon, Jeff Klukas, Christos Leonidopoulos, Yurii Maravin, and Srecko Morovic, **Search for exotic WZ resonances at CMS**, *CMS AN AN-11-333*, 2011. 179, 180, 181, 182

[108] CMS Collaboration, **Pileup Reweighting Utilities**, *"CMS TWiki (PileupMCReweightingUtilities)", url = https://twiki.cern.ch/twiki/bin/view/CMS/PileupMCReweightingUtilities*, 2011. 144

[109] **Campbell, John M. and Huston, J.W. and Stirling, W.J., Hard Interactions of Quarks and Gluons: A Primer for LHC Physics**, *Rept.Prog.Phys, vol 70, doi: 10.1088/0034-4885/70/1/R02, arXiv:hep-ph/0611148*, 2006. 178

[110] *https://twiki.cern.ch/twiki/bin/viewauth/CMS/TopLikeBSMSpring2011*, 2011. 158

[111] **Measuring Electron Efficiencies at CMS with Early Data**, *CMS Physics Analysis Summary, EGM-07-001* ,2007 . 177

[112] Campbell, John M. and Ellis, R. K., **MCFM for the Tevatron and the LHC**, *Nucl. Phys. Proc. Suppl.,205-206,10-15, arXiv:1007.3492*, 2010. 180

[113] John Campbell, Keith Ellis, Ciaran Williams, **Vector boson pair production at the LHC**, *JHEP, 07, 018, arXiv: hep-ph/1105.0020v1*, 2011. 180

[114] Chatrchyan, Serguei and others, **Measurement of W-gamma and Z-gamma production in pp collisions at sqrt(s) = 7 TeV**, *Physics Letters B, vol.701, n.5, pag.535 - 555, doi:10.1016/j.physletb.2011.06.034*, 2011. 180

[115] CMS Collaboration, **Measurement of the WW, WZ, and ZZ cross sections at CMS**, *CMS Physics Analysis Summary, EWK-11-010*, 2011.

[116] CMS Collaboration, **Luminosity Estimation for 2010 Data - Update**, *CMS Physics Analysis Summary, CMS-PAS-EWK-11-001*, 2011. 181

[117] J. Pumplin, D. R. Stump, J. Huston, H. L. Lai, P. M. Nadolsky and W. K. Tung, **New generation of parton distributions with uncertainties from global QCD analysis**, *JHEP* **0207** *(2002) 012 [arXiv:hep-ph/0201195]*, 2002. 178

[118] **CMS Higgs Combined Limit Analysis Toolkit**, *https://twiki.cern.ch/twiki/bin/view/CMS/SWGuideHiggsAnalysisCombinedLimit*, . 184

[119] *http://feynrules.phys.ucl.ac.be/wiki/TypeIIISeeSaw*, 2011.
81

Declaration

I herewith declare that I have produced this paper without the prohibited assistance of third parties and without making use of aids other than those specified; notions taken over directly or indirectly from other sources have been identified as such. This paper has not previously been presented in identical or similar form to any other Italian or foreign examination board.

The thesis work was conducted from 2009 to 2011 under the supervision of Paolo Checchia and Gianni Zumerle.

Padua, January 31^{th} 2012

A

Standard Model Review

A.1 Particle Content

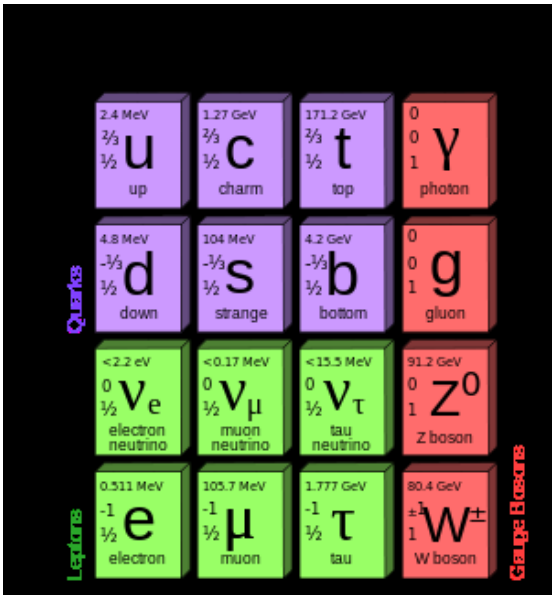

Figure A.1: Particle content of the Standard Model - Particle content of the Standard Model, with associated mass, charge and spin.

The Standard Model particle content arises by construction from:

- observed evidences from which the *fields* are postulated;
- the particular choice of the underlying gauge theory: the gauge symmetries.

Once the fields and the gauge symmetries ($SU(3)_C \times SU(2)_L \times U(1)_Y$) are specified the rest follows automatically, and the Standard Model is the most general theory that can be constructed.

Table A.1: The fields of the standard model and their gauge quantum numbers: the index $i = 1, 2, 3$ on each field refers to the generation, and the subscript L, R refers to the chirality of the field ($\psi_{L,R} \equiv \frac{1}{2}(1 \mp \gamma_5)\psi$). The left-chiral and right-chiral fields corresponding to a given particle have different $SU(2) \times U(1)$ quantum numbers, which leads to parity violation in the weak interaction.

	fields			$SU(3)$	$SU(2)$	$U(1)_Y$
$Q_L^i =$	$\begin{pmatrix} u_L \\ d_L \end{pmatrix}$	$\begin{pmatrix} c_L \\ s_L \end{pmatrix}$	$\begin{pmatrix} t_L \\ b_L \end{pmatrix}$	3	2	$\frac{1}{6}$
$u_R^i =$	u_R	c_R	t_R	3	1	$\frac{2}{3}$
$d_R^i =$	d_R	s_R	b_R	3	1	$-\frac{1}{3}$
$L_L^i =$	$\begin{pmatrix} \nu_{eL} \\ e_L \end{pmatrix}$	$\begin{pmatrix} \nu_{\mu L} \\ \mu_L \end{pmatrix}$	$\begin{pmatrix} \nu_{\tau L} \\ \tau_L \end{pmatrix}$	1	2	$-\frac{1}{2}$
$e_R^i =$	e_R	μ_R	τ_R	1	1	-1
$\phi =$	$\begin{pmatrix} \phi^+ \\ \phi^0 \end{pmatrix}$			1	2	$\frac{1}{2}$

Particle content is shown in graphically in Figure A.1, and is described in detail in Table A.1 where particles are listed along with their $SU(3)_C \times SU(2)_L \times U(1)_Y$ quantum numbers. There are three generations of quarks and leptons and one Higgs field, ϕ.

A.2 Symmetry

The symmetry that describes all Standard Model interactions is: $SU(3)_C \times SU(2)_L \times U(1)_Y$.

- $SU(3)_C$ is a non-Abelian symmetry that describes the *strong* interactions between particles that carry a property called *color* ("C" in the subscript). The symmetry generator is a color triplet. The carriers of the strong interaction are the massless fields called gluons. There are eight different color combinations of gluons generated by the $SU(3)_C$ symmetry. The only other particles that carry color are quarks.

- $SU(2)_L$ is another non-Abelian symmetry that describes the *weak* interaction,

which acts on particles having weak isospin, t, which is a quantum number associated with an $SU(2)$ doublet. The subscript "L" indicates that this symmetry only acts on the *left-handed* doublets, or the doublets whose eigenvalue is -1 when acted by chirality operator $\gamma 5$.

- $U(1)_Y$ is an Abelian symmetry, which is similar to the $U(1)$ symmetry of electromagnetism, but instead of electric charge it is acting on particles carrying a quantum number called hyper-charge, Y.

A.3 The Lagrangian

To describe the particles and their interactions, the Standard Model uses the Lagrangian density which is a classical mechanics invention. By using local gauge symmetries, one can construct a theory of interactions between particles and describe the properties of these interactions. With the Lagrangian density the equations of motion are derived, and the Lagrangian density and the resulting equation of motion are required to be invariant under the transformations of the symmetry.

The complete Lagrangian of the standard model is the sum of the gauge, matter, Higgs, and Yukawa interactions, and so it could be written in the following pieces:

$$\mathcal{L}_{SM} = \mathcal{L}_{Gauge} + \mathcal{L}_{Matter} + \mathcal{L}_{Yukawa} + \mathcal{L}_{Higgs} \, . \tag{A.1}$$

This is the simplest and most general Lagrangian, given the field content and gauge symmetries of the standard model. Given this Lagrangian, one can proceed to calculate any physical process of interest.

The pure gauge Lagrangian is the first piece, given by

$$\mathcal{L}_{Gauge} = \frac{1}{2g_S^2} \mathrm{Tr}\, G^{\mu\nu} G_{\mu\nu} + \frac{1}{2g^2} \mathrm{Tr}\, W^{\mu\nu} W_{\mu\nu} - \frac{1}{4} B^{\mu\nu} B_{\mu\nu} \, , \tag{A.2}$$

where $G^{\mu\nu}$, $W^{\mu\nu}$, and $B^{\mu\nu}$ are the gluon, weak, and hypercharge field-strength tensors. These terms contain the kinetic energy of the gauge fields and their self interactions.

The matter Lagrangian is the next piece, and is given by

$$\mathcal{L}_{Matter} = i\bar{Q}^i_L \not{D} Q^i_L + i\bar{u}^i_R \not{D} u^i_R + i\bar{d}^i_R \not{D} d^i_R + i\bar{L}^i_L \not{D} L^i_L + i\bar{e}^i_R \not{D} e^i_R \ . \qquad \text{A.3}$$

This piece contains the kinetic energy of the fermions and their interactions with the gauge fields, which are contained in the covariant derivatives (D). These two pieces of the Lagrangian depend only on the gauge couplings g_S, g, g'. Mass terms for the gauge bosons and the fermions are forbidden by the gauge symmetries, i.e., similar to electro-magnetic case, the mass terms are not invariant under the transformations of these symmetries.

In the case of the fermions, for example, masses are forbidden by the fact that the left-chiral and right-chiral components of a given fermion field have different $SU(2) \times U(1)_Y$ quantum numbers. [1]

Because all fermions are massless there is no difference between the three generations - they are physically indistinguishable. This manifests itself as a global flavor symmetry of the matter Lagrangian, Eq. (A.3).

The next pieces of the Lagrangian: $\mathcal{L}_{Higgs}$ and $\mathcal{L}_{Yukawa}$, are introduced for arranging in the simplest and most general way consistent with the gauge symmetry the Higgs field, responsible for generating the masses of the gauge bosons and fermions, as briefly described in the following sections.

A.4 Electroweak Symmetry Breaking

Electroweak symmetry breaking is the mechanism that has been introduced in the Standard Model for generating the masses of the gauge bosons and fermions. Electroweak symmetry breaking is achieved by introducing another field into the model, the Higgs field ϕ, with the quantum numbers shown in Table A.1. The simplest and most general Lagrangian for the Higgs field, consistent with the gauge symmetry, is given by

$$\mathcal{L}_{Higgs} = (D^\mu \phi)^\dagger D_\mu \phi + \mu^2 \phi^\dagger \phi - \lambda (\phi^\dagger \phi)^2 \ . \qquad \text{A.5}$$

[1] For example, a mass term for the up quark,

$$\mathcal{L} = -m \bar{u}_L u_R + h.c. \ , \qquad \text{A.4}$$

is forbidden by the fact that u_L is part of the $SU(2)$ doublet Q_L, so such a term violates the $SU(2)$ gauge symmetry (it also violates $U(1)_Y$).

This piece contains the kinetic energy of the Higgs field, its gauge interactions, and the Higgs potential. The coefficient of the quadratic term, μ^2, is the *only* dimensionful parameter in the standard model. The sign of this term is chosen such that the Higgs field has a nonzero vacuum-expectation value on the circle of minima in Higgs-field space given by $\langle\phi^0\rangle = \mu/\sqrt{2\lambda} \equiv v/\sqrt{2}$. The dimensionful parameter μ is replaced by the dimensionful parameter $v \approx 246$ GeV.

When the $SU(2)_L$ doublet of the scalar field obtains vacuum expectation value, it spontaneously breaks the $SU(2)_L \times U(1)_Y$ symmetry to $U(1)_{em}$, which is electromagnetic gauge symmetry. The breaking of the symmetry mixes the electro-weak gauge fields and as a result gives masses to the gauge fields that carry weak interaction, the $W^{\pm}$ and Z^0 bosons, and leaves massless the electro-magnetic gauge field, γ or the photon.

$$M_W = \frac{1}{2}gv$$
$$M_Z = \frac{1}{2}\sqrt{g^2 + g'^2}\, v \,, \tag{A.6}$$

and the fermions,

Regarding the fermions, diagonalizing the fermion mass matrices generates the Cabibbo-Kobayashi-Maskawa (CKM) matrix, including the CP-violating phase, and the mass expression is:

$$M = \Gamma\frac{v}{\sqrt{2}} \,. \tag{A.7}$$

For a more detailed description see Section A.5.

A.5 Fermion masses and mixing

The simplest and most general Lagrangian, consistent with the gauge symmetry, that describes the interaction between the Higgs field and the fermions is:

$$\mathcal{L}_{Yukawa} = -\Gamma_u^{ij}\bar{Q}_L^i\epsilon\phi^* u_R^j - \Gamma_d^{ij}\bar{Q}_L^i\phi d_R^j - \Gamma_e^{ij}\bar{L}_L^i\phi e_R^j + h.c. \tag{A.8}$$

where $\Gamma_u, \Gamma_d, \Gamma_e$ are 3×3 complex matrices in generation space (in general they need not be diagonal, so there is mixing between different generations). These matrices contain most of the parameters of the standard model. A sum on the index i, which

represents the generation, is implied in the Lagrangian. We have therefore apparently introduced $3 \times 3 \times 3 \times 2 = 54$ new parameters into the theory, but only a subset of these parameters are physically relevant because these so-called Yukawa interactions of the Higgs field with fermions violate almost all of the $[U(3)]^5$ global symmetry of the fermion gauge interactions, Eq. (A.3). The only remaining global symmetries are the subset corresponding to baryon number

$$\begin{aligned} Q_L^i &\to e^{i\theta/3} Q_L^i \\ u_R^i &\to e^{i\theta/3} u_R^i \\ d_R^i &\to e^{i\theta/3} d_R^i \end{aligned} \tag{A.9}$$

and lepton number

$$\begin{aligned} L_L^i &\to e^{i\phi} L_L^i \\ e_R^i &\to e^{i\phi} e_R^i \, . \end{aligned} \tag{A.10}$$

[1]

Replacing the Higgs field with its vacuum-expectation value, $\phi = (0, v/\sqrt{2})$, in Eq. (A.8) yields

$$\mathcal{L}_M = -M_u^{ij} \bar{u}_L^i u_R^j - M_d^{ij} \bar{d}_L^i d_R^j - M_e^{ij} \bar{e}_L^i e_R^j + h.c. \, , \tag{A.11}$$

where

$$M^{ij} = \Gamma^{ij} \frac{v}{\sqrt{2}} \tag{A.12}$$

are fermion mass matrices. The Yukawa interactions are therefore responsible for providing the charged fermions with mass; the neutrinos, however, remain massless. To make the masses of the fermions manifest, a unitary field redefinitions on the fields is performed in order to diagonalize the mass matrices in Eq. (A.11). [2]

[1] The conservation of baryon number and lepton number in the standard model is a consequence of these symmetries, which are not put in by hand, but follow automatically from the field content and gauge symmetries of the theory.

[2] The field redefinition is the following:

$$\begin{aligned} u_L^i &= A_{u_L}^{ij} u_L'^j \quad & u_R^i &= A_{u_R}^{ij} u_R'^j \\ d_L^i &= A_{d_L}^{ij} d_L'^j \quad & d_R^i &= A_{d_R}^{ij} d_R'^j \\ e_L^i &= A_{e_L}^{ij} e_L'^j \quad & e_R^i &= A_{e_R}^{ij} e_R'^j \\ \nu_L^i &= A_{\nu_L}^{ij} \nu_L'^j & & \end{aligned} \tag{A.13}$$

After the field redefinitions are performed, the physically-relevant parameters of the Standard Model that remain could be calculated. [1]

A.6 The Standard Model Assessment

The gauge-boson self interactions and the gauge interactions of the fermions (with the exception of the top quark) have been tested to very good accuracy, so we are sure that they are described by the standard model. The top-quark's gauge interactions have been tested less accurately, but thus far they agree with the standard model. Quark mixing agrees with the CKM picture to very good accuracy in the first two generations, but with less accuracy in the third generation. The relation between the W- and Z-boson masses that follows from Eq. (A.6),

$$M_W^2 = M_Z^2 \cos^2\theta_W (1 + \Delta\rho) \,, \tag{A.14}$$

where $\Delta\rho$ contains the radiative corrections, has been tested to good accuracy. The pieces of the standard model that we have no direct knowledge of involve the coupling of the Higgs boson to fermions, gauge bosons, and to itself.

The Fermilab Tevatron have contributed to our knowledge of the pieces of the standard model. The CERN Large Hadron Collider (LHC) will luckly discover the Higgs boson, as well as measure its coupling to other particles.

Once the mass matrices are diagonalized, the masses of the fermions are manifest. These transformations also diagonalize the Yukawa matrices Γ, since they are proportional to the mass matrices [see Eq. (A.12)]. The impact of these field redefinitions on the rest of the Lagrangian is the following. They have no effect on the pure gauge or Higgs parts of the Lagrangian, Eqs. (A.2) and (A.5), which are independent of the fermion fields. They do impact the matter part of the Lagrangian, Eq. (A.3). However, a subset of these field redefinitions is the global $[U(3)]^5$ symmetry of the matter Lagrangian; this subset therefore has no impact.

[1] For example for the quark sector: the ten remaining parameters correspond to the six quark masses and the four parameters of the Cabibbo-Kobayashi-Maskawa (CKM) matrix (three mixing angles and one CP-violating phase). One expects the field redefinitions that diagonalize the mass matrices to yield a CKM matrix with large mixing angles. Nevertheless the measured angles are (10)

$$\begin{aligned} \theta_{12} &\approx 13^\circ \\ \theta_{23} &\approx 2.3^\circ \\ \theta_{13} &\approx 0.23^\circ \\ \delta &\approx 60^\circ \end{aligned}$$

which, with the exception of the CP-violating phase δ, are small.

A.7 Experimental Properties of SM Particles

After having reviewed the theoretical properties of the Standard Model fields, in this section I will briefly describe the experimental properties of the Standard Model particles. Experimental properties define the characteristic of the *physical objects* that are going to be reconstructed from the detector signals, and are particularly important for the object definition and selection for the analysis, as will be described in chapter 9.

A.7.1 Electro-Weak Bosons

Photon is the carrier of the electro-magnetic interaction. It has zero rest mass, zero charge, and infinite lifetime. In this analysis we do not search for photons, however, if a photon converts into an electron-positron pair while interacting with material, it may interfere with our signal. See section 8.3.4.

The charged $W^{\pm}$ bosons are the carriers of weak interactions. They have the same mass $m_W \approx 80.4GeV$ and the same inclusive production cross-section in proton-proton collision at 7 TeV: $\sigma \approx 92nb$. W bosons are responsible for flavor-changing-charged-currents, interactions where the incoming particle has the charge and the flavor different from that of an outgoing particle. In fact, most of the decays of the Standard Model particles occur with inter mediation of the W boson. Thus the decay of the W boson determines the decays of most particles.

Decay mode	**fraction of all decays (%)**
$e^-\bar{\nu}_e$	10.75± 0.13
$\mu^-\bar{\nu}_\mu$	10.57 ± 0.15
$\tau^-\bar{\nu}_\tau$	11.25 ± 0.20
Hadronic decays	67.60 ± 0.27

Table A.2: List of important W^- decays, W^+ decays are analogous.

Z^0 is the neutral vector boson, it is the carrier of weak interactions. It has mass $m_Z \approx 91GeV$, and its inclusive production cross-section in proton-proton collisions at 7 TeV is about $\sigma \approx 28nb$. The invariant mass of Z^0 decay products sharply peaks at m_Z owning to a narrow width of Z^0 decay. The decays of the off-shell Z^0 boson,

whose decay products have invariant mass lower than m_Z, are indistinguishable from the decays of the virtual photon, γ^*. The decay processes of the Z^0 and γ^* into lepton-antilepton pairs are collectively called Drell-Yan processes and the decay products are called Drell-Yan pairs or Drell-Yan leptons. In Table A.3 Z^0 important decay modes, with their branching ratio, are listed for reference.

Decay mode	**fraction of all decays (%)**
e^-e^+	3.36 ± 0.004
$\mu^-\mu^+$	3.37 ± 0.006
$\tau^-\tau^+$	3.37 ± 0.008
Invisible decays	20.00 ± 0.06
Hadronic decays	69.9 1 ± 0.06

Table A.3: List of important Z^0 decays.

A.7.2 Leptons

The Neutrinos are neutral leptons which interact weakly and escape the detector leaving energy imbalance in the detector. This energy imbalance is called missing energy and is indicated with symbol $E_{\mathrm{T}}^{\mathrm{miss}}$.

The Electron is the lightest charged lepton; the mass is $\approx 0.5MeV$; it is a stable particle and it leaves charge trace in the tracker and quite all its energy deposit in the electro-magnetic calorimeter.

The Muon is a charged lepton heavier than electron, with mass $106MeV$, mean life time $\tau \approx 2\mu s$, and mean decay length $c\tau \approx 600m$. Thus most of the time muon decays outside of the detector. It interacts with matter weakly and electro-magnetically, although since it is 2000 times heavier than electron it leaves a lot less energy in the detector and only leaves a charge trace in the tracker and in the muon system.

The Tau is the heaviest of all known leptons, with mass $172.9 \pm 0.6 \pm 0.9$ GeV and a very short lifetime, $\tau \approx 3 \cdot 10^{-13} sec$, and a mean decay length $c\tau \approx 90\mu m$. This means that tau decays almost immediately after its production and before it is able to be registered by the detector. The detector registers only tau decay products. The

tau decay proceeds via $W^{\pm}$ see Figure A.2. However, since the tau is lighter than the $W^{\pm}$, the $W^{\pm}$ in the tau decay is virtual. Therefore some of the decay modes are not accessible, while the branching fractions of the remaining decay modes increase.

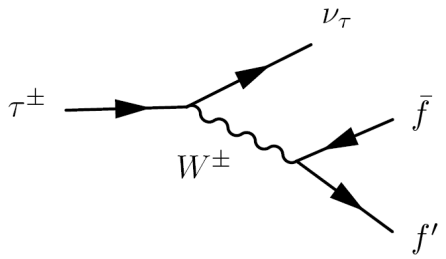

Figure A.2: Tau decay - The $W^{\pm}$ in tau decay is virtual, thus ($f^{'}$,$\bar{f}$) can only be ($e^{-}, \bar{\nu}_e$),($\mu^{-}, \bar{\nu}_\mu$), (d,$\bar{u}$), and their charge conjugates. The decay to (s,$\bar{u}$) occurs rarely and does not affect the branching fraction of other decays.

The most important decay modes are listed in table A.4. They are usually categorized into:

- Leptonic decay modes, which include the decay modes with a charged lepton, either electron or muon in the final state.
- Hadronic single-prong decay modes, which include the decay modes with a single charged hadron, usually π_0, in the final state.
- Hadronic three-prong decay modes, which include the decay modes with three charged hadrons in the final state.

A.7.3 Quarks and gluons

There are six quarks in the Standard Model, forming three generations, each generation includes an up-like quark and a down-like quark. The three lightest quarks are u, d, and s named up, down, and strange. They have masses ranging from few MeV for 'up' and 'down' quarks to 100 MeV for 'strange' quark. The light quarks have a long lifetime, but due to color confinement cannot be seen individually in the detector, and instead form hadrons, which are particles consisting of two or more quarks.

Decay mode	fraction of all decays (%)
$e^-\bar{\nu}_e\nu_\tau$	17.85 ± 0.05
$\mu^-\bar{\nu}_\mu\nu_\tau$	17.36 ± 0.05
$\pi^-\nu_\tau$	10.91 ± 0.07
$K-\nu_\tau$	0.007 ± 0.0002
$\pi^-\pi^0\nu_\tau$	25.52 ± 0.10
$\pi^-2\pi^0\nu_\tau$	9.27 ± 0.12
$\pi^-3\pi^0\nu_\tau$	1.04 ± 0.07

Table A.4: List of important tau decay modes. Only τ^- decay modes are shown. τ^+ decays are analogue.

The heavier b and c quarks deserve special attention because their weak decays contain charged leptons (electrons and muons) which sometimes may appear isolated, thus they can be confused with signal leptons. The lifetime of the charm hadrons is on the order of $\tau \approx 0.5 - 1ps$, which makes $c\tau \approx 150 - 300\mu m$. The lifetime of the bottom hadrons is on the order of $\tau \approx 1.5ps$ which means $c\tau \approx 450\mu m$. Thus the decay products of these quarks appear to originate away from the interaction point. This feature can be utilized to mark the leptons coming from the decays of the heavy flavor hadrons.

Top quark is in a league of its own. With the mass $m_\tau \approx 172GeV$, it is the heaviest elementary particle known to date. Top quarks are usually produced in pairs. The cross-section of their production in proton-proton collisions at $7TeV$ is very high: $\sigma \approx 164pb$. Top quark lifetime is very short, roughly $5 \cdot 10^{25}s$. This is about 20 times shorter than the timescale for strong interactions, and therefore it does not form hadrons, giving physicists a unique opportunity to study a "bare" quark. Top quark decay through weak interaction. The main decay mode of the top quark is $t \to W^+b$ thus the W decays (see table A.2) determine the final state of the top-quark decay Top-quark decays are the main background to many searches for new physics.

B

The Seesaw Type-III Lagrangian

B.1 The Lagrangian in the mass basis

The Lagrangian in the mass basis after the diagonalization of the mass matrices of the charged and the neutral sectors (the diagonalization procedure is described in Ref. (28)), is the following:

$$\mathcal{L} = \mathcal{L}_{Kin} + \mathcal{L}_{CC} + \mathcal{L}^{\ell}_{NC} + \mathcal{L}^{\nu}_{NC} + \mathcal{L}^{\ell}_{H} + \mathcal{L}^{\nu}_{H} + \mathcal{L}^{\ell}_{\eta} + \mathcal{L}^{\nu}_{\eta} + \mathcal{L}_{\phi^-}\,, \tag{B.1}$$

where

$$\mathcal{L}_{CC} = \frac{g}{\sqrt{2}} \left(\begin{array}{cc} \bar{l} & \overline{\Psi} \end{array} \right) \gamma^{\mu} W^{-}_{\mu} \left(P_L g^{CC}_L + P_R g^{CC}_R \sqrt{2} \right) \left(\begin{array}{c} \nu \\ \Sigma \end{array} \right) + \text{h.c.} \tag{B.2}$$

$$\mathcal{L}^{\ell}_{NC} = \frac{g}{cos\theta_W} \left(\begin{array}{cc} \bar{l} & \overline{\Psi} \end{array} \right) \gamma^{\mu} Z_{\mu} \left(P_L g^{NC}_L + P_R g^{NC}_R \right) \left(\begin{array}{c} l \\ \Psi \end{array} \right) \tag{B.3}$$

$$\mathcal{L}^{\nu}_{NC} = \frac{g}{2cos\theta_W} \left(\begin{array}{cc} \overline{\nu} & \overline{\Sigma^{0c}} \end{array} \right) \gamma^{\mu} Z_{\mu} \left(P_L g^{NC}_{\nu} \right) \left(\begin{array}{c} \nu_L \\ \Sigma^{0c} \end{array} \right) \tag{B.4}$$

$$\mathcal{L}^{\ell}_{H} = -\left(\begin{array}{cc} \bar{l} & \overline{\Psi} \end{array} \right) H \left(P_L g^{H\ell}_L + P_R g^{H\ell}_R \right) \left(\begin{array}{c} l \\ \Psi \end{array} \right) \tag{B.5}$$

$$\mathcal{L}^{\nu}_{H} = -\left(\begin{array}{cc} \overline{\nu} & \overline{\Sigma^0} \end{array} \right) \frac{H}{\sqrt{2}} \left(P_L g^{H\nu}_L + P_R g^{H\nu}_R \right) \left(\begin{array}{c} \nu \\ \Sigma^0 \end{array} \right) \tag{B.6}$$

$$\mathcal{L}^{\ell}_{\eta} = -\left(\begin{array}{cc} \bar{l} & \overline{\Psi} \end{array} \right) i\eta \left(P_L g^{\eta\ell}_L + P_R g^{\eta\ell}_R \right) \left(\begin{array}{c} l \\ \Psi \end{array} \right) \tag{B.7}$$

$$\mathcal{L}^{\nu}_{\eta} = -\left(\begin{array}{cc} \overline{\nu} & \overline{\Sigma^0} \end{array} \right) \frac{i\eta}{\sqrt{2}} \left(P_L g^{\eta\nu}_L + P_R g^{\eta\nu}_R \right) \left(\begin{array}{c} \nu \\ \Sigma^0 \end{array} \right) \tag{B.8}$$

$$\mathcal{L}_{\phi^-} = -\left(\begin{array}{cc} \bar{l} & \overline{\psi} \end{array} \right) \phi^- (P_L g^{\phi^-}_L + P_R g^{\phi^-}_R) \left(\begin{array}{c} \nu \\ \Sigma^0 \end{array} \right) + \text{h.c.} \tag{B.9}$$

we have indicated $\mathcal{U}_{PMNS}$ simply with $\mathcal{U}$. The couplings are:

$$g_L^{CC} = \begin{pmatrix} \left(1+\frac{\epsilon}{2}\right) U & -Y_\Sigma^\dagger M_\Sigma^{-1} \frac{v}{\sqrt{2}} \\ 0 & \sqrt{2}\left(1-\frac{\epsilon'}{2}\right) \end{pmatrix} \quad \text{B.10}$$

$$g_R^{CC} = \begin{pmatrix} 0 & -m_l Y_\Sigma^\dagger M_\Sigma^{-2} v \\ -M_\Sigma^{-1} Y_\Sigma^* \mathcal{U}^* \frac{v}{\sqrt{2}} & 1-\frac{\epsilon'^*}{2} \end{pmatrix} \quad \text{B.11}$$

$$g_L^{NC} = \begin{pmatrix} \frac{1}{2} - cos^2\theta_W - \epsilon & \frac{1}{2} Y_\Sigma^\dagger M_\Sigma^{-1} v \\ \frac{1}{2} M_\Sigma^{-1} Y_\Sigma v & \epsilon' - cos^2\theta_W \end{pmatrix} \quad \text{B.12}$$

$$g_R^{NC} = \begin{pmatrix} 1 - cos^2\theta_W & m_l Y_\Sigma^\dagger M_\Sigma^{-2} v \\ M_\Sigma^{-2} Y_\Sigma m_l v & -cos^2\theta_W \end{pmatrix} \quad \text{B.13}$$

$$g_\nu^{NC} = \begin{pmatrix} 1 - \mathcal{U}^\dagger \epsilon \, \mathcal{U} & \mathcal{U}^\dagger Y_\Sigma^\dagger M_\Sigma^{-1} \frac{v}{\sqrt{2}} \\ \frac{v}{\sqrt{2}} M_\Sigma^{-1} Y_\Sigma \, \mathcal{U} & \epsilon' \end{pmatrix} \quad \text{B.14}$$

$$g_L^{H\ell} = \begin{pmatrix} \frac{m_l}{v}(1-3\epsilon) & m_l Y_\Sigma^\dagger M_\Sigma^{-1} \\ Y_\Sigma (1-\epsilon) + M_\Sigma^{-2} Y_\Sigma m_l^2 & Y_\Sigma Y_\Sigma^\dagger M_\Sigma^{-1} v \end{pmatrix} \quad \text{B.15}$$

$$g_R^{H\ell} = \left(g_L^{H\ell}\right)^\dagger \quad \text{B.16}$$

$$g_L^{H\nu} = \begin{pmatrix} -\frac{\sqrt{2}}{v} \mathcal{U}^T m_\nu \, \mathcal{U} & \mathcal{U}^T m_\nu Y_\Sigma^\dagger M_\Sigma^{-1} \\ (Y_\Sigma - Y_\Sigma \frac{\epsilon}{2} - \frac{\epsilon'^T}{2} Y_\Sigma)\mathcal{U} & Y_\Sigma Y_\Sigma^\dagger M_\Sigma^{-1} \frac{v}{\sqrt{2}} \end{pmatrix} \quad \text{B.17}$$

$$= \begin{pmatrix} -\frac{\sqrt{2}}{v} m_\nu^d & m_\nu^d \mathcal{U}^\dagger Y_\Sigma^\dagger M_\Sigma^{-1} \\ (Y_\Sigma - Y_\Sigma \frac{\epsilon}{2} - \frac{\epsilon'^T}{2} Y_\Sigma)\mathcal{U} & Y_\Sigma Y_\Sigma^\dagger M_\Sigma^{-1} \frac{v}{\sqrt{2}} \end{pmatrix}$$

$$g_R^{H\nu} = \left(g_L^{H\nu}\right)^\dagger \quad \text{B.18}$$

$$g_L^{\eta\ell} = \begin{pmatrix} -\frac{m_l}{v}(1+\epsilon) & -m_l Y_\Sigma^\dagger M_\Sigma^{-1} \\ Y_\Sigma(1-\epsilon) - M_\Sigma^{-2} Y_\Sigma m_l^2 & v Y_\Sigma Y_\Sigma^\dagger M_\Sigma^{-1} \end{pmatrix} \quad \text{B.19}$$

$$g_R^{\eta\ell} = -\left(g_L^{\eta\ell}\right)^\dagger \quad \text{B.20}$$

$$g_L^{\eta\nu} = g_L^{H\nu} \quad \text{B.21}$$

$$g_R^{\eta\nu} = -\left(g_L^{\eta\nu}\right)^\dagger \quad \text{B.22}$$

$$g_L^{\phi^-} = \begin{pmatrix} \sqrt{2}\frac{m_l}{v}(1-\frac{\epsilon}{2})\mathcal{U} & m_l Y_\Sigma^\dagger M_\Sigma^{-1} \\ \sqrt{2} m_l^2 M_\Sigma^{-2} Y_\Sigma \mathcal{U} & 0 \end{pmatrix} \quad \text{B.23}$$

$$g_R^{\phi^-} = \begin{pmatrix} -\sqrt{2}\mathcal{U}\frac{m_\nu^{d*}}{v} & \left[(Y_\Sigma^\dagger - \epsilon Y_\Sigma^\dagger - Y_\Sigma^\dagger \frac{\epsilon'^*}{2}) - 2 m_\nu^* Y_\Sigma^\dagger M_\Sigma^{-1}\right] \\ -\sqrt{2} Y_\Sigma^* (1-\frac{\epsilon^*}{2})\mathcal{U}^* & 2[-\frac{M_\Sigma}{v}\epsilon'^T + \epsilon' \frac{M_\Sigma}{v}] \end{pmatrix}. \quad \text{B.24}$$

Here $\mathcal{U}$ is the lowest order leptonic mixing matrix which is unitary, m_l is a diagonal matrix whose elements are the masses of the charged leptons, $v \equiv \sqrt{2}\langle\phi^0\rangle = 246$ GeV,

$\epsilon = \frac{v^2}{2} Y_\Sigma^\dagger M_\Sigma^{-2} Y_\Sigma$, $\epsilon' = \frac{v^2}{2} M_\Sigma^{-1} Y_\Sigma Y_\Sigma^\dagger M_\Sigma^{-1}$and $\delta = \frac{m_l^2}{M_\Sigma^2}$. The above expressions are all valid at $\mathcal{O}\left(\epsilon, \epsilon', \delta, \sqrt{\epsilon\delta}, \sqrt{\epsilon'\delta}\right)$.

B.2 The explicit Lagrangian in the minimal model

$$g_L^{CC} = \begin{pmatrix} \left(1 + \frac{V^T \wedge V}{2}\right) \mathcal{U} & -V^T \\ 0 & \sqrt{2}\left(1 - \frac{V \cdot V^T}{2}\right) \end{pmatrix} =$$

$$= \left(\begin{array}{ccc|c} \mathcal{U}_{e1} + \frac{V_e V_\alpha}{2}\mathcal{U}_{\alpha 1} & \mathcal{U}_{e2} + \frac{V_e V_\alpha}{2}\mathcal{U}_{\alpha 2} & \mathcal{U}_{e3} + \frac{V_e V_\alpha}{2}\mathcal{U}_{\alpha 3} & -V_e \\ \mathcal{U}_{\mu 1} + \frac{V_\mu V_\alpha}{2}\mathcal{U}_{\alpha 1} & \mathcal{U}_{\mu 2} + \frac{V_\mu V_\alpha}{2}\mathcal{U}_{\alpha 2} & \mathcal{U}_{\mu 3} + \frac{V_\mu V_\alpha}{2}\mathcal{U}_{\alpha 3} & -V_\mu \\ \mathcal{U}_{\tau 1} + \frac{V_\tau V_\alpha}{2}\mathcal{U}_{\alpha 1} & \mathcal{U}_{\tau 2} + \frac{V_\tau V_\alpha}{2}\mathcal{U}_{\alpha 2} & \mathcal{U}_{\tau 3} + \frac{V_\tau V_\alpha}{2}\mathcal{U}_{\alpha 3} & -V_\tau \\ 0 & 0 & 0 & \sqrt{2}(1 - \frac{V_e^2 + V_\mu^2 + V_\tau^2}{2}) \end{array}\right)$$

$$g_R^{CC} = \begin{pmatrix} 0 & -\sqrt{2} m_l V^T M_\Sigma^{-1} \\ -V\,\mathcal{U} & 1 - \frac{V \cdot V^T}{2} \end{pmatrix} =$$

$$= \begin{pmatrix} 0 & 0 & 0 & -\sqrt{2} M_\Sigma^{-1} m_e V_e \\ 0 & 0 & 0 & -\sqrt{2} M_\Sigma^{-1} m_\mu V_\mu \\ 0 & 0 & 0 & -\sqrt{2} M_\Sigma^{-1} m_\tau V_\tau \\ -V_\alpha \mathcal{U}_{\alpha 1} & -V_\alpha \mathcal{U}_{\alpha 2} & -V_\alpha \mathcal{U}_{\alpha 3} & 1 - \frac{V_e^2 + V_\mu^2 + V_\tau^2}{2} \end{pmatrix}$$

$$g_L^{NC} = \begin{pmatrix} \frac{1}{2} - cos^2\theta_W - V^T \wedge V & \frac{1}{\sqrt{2}} V^T \\ \frac{1}{\sqrt{2}} V & V \cdot V^T - cos^2\theta_W \end{pmatrix} =$$

$$= \begin{pmatrix} \frac{1}{2} - cos^2\theta_W - V_e^2 & V_e V_\mu & V_e V_\tau & \frac{V_e}{\sqrt{2}} \\ V_e V_\mu & \frac{1}{2} - cos^2\theta_W - V_\mu^2 & V_\mu V_\tau & \frac{V_\mu}{\sqrt{2}} \\ V_e V_\tau & V_\mu V_\tau & \frac{1}{2} - cos^2\theta_W - V_\tau^2 & \frac{V_\tau}{\sqrt{2}} \\ \frac{V_e}{\sqrt{2}} & \frac{V_\mu}{\sqrt{2}} & \frac{V_\tau}{\sqrt{2}} & V_e^2 + V_\mu^2 + V_\tau^2 - cos^2\theta_W \end{pmatrix}$$

$$g_R^{NC} = \begin{pmatrix} 1 - cos^2\theta_W & \sqrt{2} m_l V^T M_\Sigma^{-1} \\ \sqrt{2} M_\Sigma^{-1} V m_l & -cos^2\theta_W \end{pmatrix} =$$

$$= \begin{pmatrix} 1-cos^2\theta_W & 0 & 0 & \sqrt{2}M_\Sigma^{-1}m_eV_e \\ 0 & 1-cos^2\theta_W & 0 & \sqrt{2}M_\Sigma^{-1}m_\mu V_\mu \\ 0 & 0 & 1-cos^2\theta_W & \sqrt{2}M_\Sigma^{-1}m_\tau V_\tau \\ \sqrt{2}M_\Sigma^{-1}m_eV_e & \sqrt{2}M_\Sigma^{-1}m_\mu V_\mu & \sqrt{2}M_\Sigma^{-1}m_\tau V_\tau & -cos^2\theta_W \end{pmatrix}$$

$$g_\nu^{NC} = \begin{pmatrix} 1-\mathcal{U}^T V^T \wedge V\mathcal{U} & \mathcal{U}^T V^T \\ V\mathcal{U} & V\cdot V^T \end{pmatrix} =$$

$$= \left(\begin{array}{cc|c} 1-\mathcal{U}_{\alpha1}V_\alpha V_\beta\mathcal{U}_{\beta1} & -\mathcal{U}_{\alpha1}V_\alpha V_\beta\mathcal{U}_{\beta2} & \\ -\mathcal{U}_{\alpha2}V_\alpha V_\beta\mathcal{U}_{\beta1} & 1-\mathcal{U}_{\alpha2}V_\alpha V_\beta\mathcal{U}_{\beta2} & \\ -\mathcal{U}_{\alpha3}V_\alpha V_\beta\mathcal{U}_{\beta1} & -\mathcal{U}_{\alpha3}V_\alpha V_\beta\mathcal{U}_{\beta2} & \\ V_\alpha\mathcal{U}_{\alpha1} & V_\alpha\mathcal{U}_{\alpha2} & \end{array}\right.$$
$$\left.\begin{array}{c|c} -\mathcal{U}_{\alpha1}V_\alpha V_\beta\mathcal{U}_{\beta3} & V_\alpha\mathcal{U}_{\alpha1} \\ -\mathcal{U}_{\alpha2}V_\alpha V_\beta\mathcal{U}_{\beta3} & V_\alpha\mathcal{U}_{\alpha2} \\ 1-\mathcal{U}_{\alpha3}V_\alpha V_\beta\mathcal{U}_{\beta3} & V_\alpha\mathcal{U}_{\alpha3} \\ V_\alpha\mathcal{U}_{\alpha3} & V_e^2+V_\mu^2+V_\tau^2 \end{array}\right)$$

$$g_L^{H\ell} = \begin{pmatrix} \frac{m_l}{v}\left(1-3V^T\wedge V\right) & \sqrt{2}\frac{m_l}{v}V^T \\ \sqrt{2}\frac{M_\Sigma}{v}V\cdot(1-V^T\wedge V)+\sqrt{2}M_\Sigma^{-1}V\frac{m_l^2}{v} & 2\frac{M_\Sigma}{v}V\cdot V^T \end{pmatrix} =$$

$$= \left(\begin{array}{cc|c} \frac{m_e}{v}(1-3V_e^2) & -3\frac{m_e}{v}V_eV_\mu & \\ -3\frac{m_\mu}{v}V_\mu V_e & \frac{m_\mu}{v}(1-3V_\mu^2) & \\ -3\frac{m_\tau}{v}V_\tau V_e & -3\frac{m_\tau}{v}V_\tau V_\mu & \\ \sqrt{2}\frac{M_\Sigma}{v}V_e(1-V_e^2-V_\mu^2-V_\tau^2)+\sqrt{2}M_\Sigma^{-1}\frac{m_e^2}{v}V_e & \sqrt{2}\frac{M_\Sigma}{v}V_\mu(1-V_e^2-V_\mu^2-V_\tau^2)+\sqrt{2}M_\Sigma^{-1}\frac{m_\mu^2}{v}V_\mu & \end{array}\right.$$
$$\left.\begin{array}{c|c} -3\frac{m_e}{v}V_eV_\tau & \sqrt{2}\frac{m_e}{v}V_e \\ -3\frac{m_\mu}{v}V_\mu V_\tau & \sqrt{2}\frac{m_\mu}{v}V_\mu \\ \frac{m_\tau}{v}(1-3V_\tau^2) & \sqrt{2}\frac{m_\tau}{v}V_\tau \\ \sqrt{2}\frac{M_\Sigma}{v}V_\tau(1-V_e^2-V_\mu^2-V_\tau^2)+\sqrt{2}M_\Sigma^{-1}\frac{m_\tau^2}{v}V_\tau & 2\frac{M_\Sigma}{v}(V_e^2+V_\mu^2+V_\tau^2) \end{array}\right)$$

$$g_L^{H\nu} = \begin{pmatrix} \frac{\sqrt{2}}{v}m_\nu^d & \frac{\sqrt{2}}{v}m_\nu^d\mathcal{U}^TV^T \\ \frac{\sqrt{2}}{v}\left(1-\epsilon'\right)M_\Sigma V\mathcal{U} & \frac{\sqrt{2}}{v}M_\Sigma\epsilon' \end{pmatrix} =$$

$$= \frac{\sqrt{2}}{v}\begin{pmatrix} m_{\nu1} & 0 & 0 & m_{\nu1}\mathcal{U}_{\alpha1}V_\alpha \\ 0 & m_{\nu2} & 0 & m_{\nu2}\mathcal{U}_{\alpha2}V_\alpha \\ 0 & 0 & m_{\nu3} & m_{\nu3}\mathcal{U}_{\alpha3}V_\alpha \\ \left(1-\epsilon'\right)M_\Sigma V_\alpha\mathcal{U}_{\alpha1} & \left(1-\epsilon'\right)M_\Sigma V_\alpha\mathcal{U}_{\alpha2} & \left(1-\epsilon'\right)M_\Sigma V_\alpha\mathcal{U}_{\alpha3} & M_\Sigma\epsilon' \end{pmatrix}$$

$$g_L^{\eta\ell} = \begin{pmatrix} -\frac{m_l}{v}(1+V^T\wedge V) & -\frac{m_l}{v}\sqrt{2}V^T \\ \frac{M_\Sigma}{v}\sqrt{2}V(1-V^T\wedge V-\frac{m_l^2}{M_\Sigma^2}) & \frac{2M_\Sigma}{v}V\cdot V^T \end{pmatrix} =$$

$$= \left(\begin{array}{cc|c} -\frac{m_e}{v}(1+V_e^2) & -\frac{m_e}{v}V_eV_\mu & -\frac{m_e}{v}V_eV_\tau \\ -\frac{m_\mu}{v}V_\mu V_e & -\frac{m_\mu}{v}(1+V_\mu^2) & -\frac{m_\mu}{v}V_\mu V_\tau \\ -\frac{m_\tau}{v}V_\tau V_e & -\frac{m_\tau}{v}V_\tau V_\mu & -\frac{m_\tau}{v}(1+V_\tau^2) \\ \hline \sqrt{2}\frac{M_\Sigma}{v}V_e(1-V_e^2-V_\mu^2-V_\tau^2) - \sqrt{2}M_\Sigma^{-1}\frac{m_e^2}{v}V_e & \sqrt{2}\frac{M_\Sigma}{v}V_\mu(1-V_e^2-V_\mu^2-V_\tau^2) - \sqrt{2}M_\Sigma^{-1}\frac{m_\mu^2}{v}V_\mu & \sqrt{2}\frac{M_\Sigma}{v}V_\tau(1-V_e^2-V_\mu^2-V_\tau^2) - \sqrt{2}M_\Sigma^{-1}\frac{m_\tau^2}{v}V_\tau \end{array} \right| \left| \begin{array}{c} -\sqrt{2}\frac{m_e}{v}V_e \\ -\sqrt{2}\frac{m_\mu}{v}V_\mu \\ -\sqrt{2}\frac{m_\tau}{v}V_\tau \\ \hline 2\frac{M_\Sigma}{v}(V_e^2+V_\mu^2+V_\tau^2) \end{array} \right)$$

$$g_L^\phi = \left(\begin{array}{cc} \sqrt{2}\frac{m_l}{v}(1-\frac{V^T\wedge V}{2})\mathcal{U} & \frac{\sqrt{2}}{v}m_l V^T \\ 2M_\Sigma^{-1}V\frac{m_l^2}{v}\mathcal{U} & 0 \end{array} \right) =$$

$$= \left(\begin{array}{cccc} \frac{\sqrt{2}}{v}(m_e(\delta_{e\alpha}-\frac{V_eV_\alpha}{2})\mathcal{U}_{\alpha 1}) & \frac{\sqrt{2}}{v}(m_e(\delta_{e\alpha}-\frac{V_eV_\alpha}{2})\mathcal{U}_{\alpha 2}) & \frac{\sqrt{2}}{v}(m_e(\delta_{e\alpha}-\frac{V_eV_\alpha}{2})\mathcal{U}_{\alpha 3}) & \frac{\sqrt{2}}{v}m_eV_e \\ \frac{\sqrt{2}}{v}(m_\mu(\delta_{\mu\alpha}-\frac{V_\mu V_\alpha}{2})\mathcal{U}_{\alpha 1}) & \frac{\sqrt{2}}{v}(m_\mu(\delta_{\mu\alpha}-\frac{V_\mu V_\alpha}{2})\mathcal{U}_{\alpha 2}) & \frac{\sqrt{2}}{v}(m_\mu(\delta_{\mu\alpha}-\frac{V_\mu V_\alpha}{2})\mathcal{U}_{\alpha 3}) & \frac{\sqrt{2}}{v}m_\mu V_\mu \\ \frac{\sqrt{2}}{v}(m_\tau(\delta_{\tau\alpha}-\frac{V_\tau V_\alpha}{2})\mathcal{U}_{\alpha 1}) & \frac{\sqrt{2}}{v}(m_\tau(\delta_{\tau\alpha}-\frac{V_\tau V_\alpha}{2})\mathcal{U}_{\alpha 2}) & \frac{\sqrt{2}}{v}(m_\tau(\delta_{\tau\alpha}-\frac{V_\tau V_\alpha}{2})\mathcal{U}_{\alpha 3}) & \frac{\sqrt{2}}{v}m_\tau V_\tau \\ 2M_\Sigma^{-1}V_\alpha\frac{m_\alpha^2}{v}\mathcal{U}_{\alpha 1} & 2M_\Sigma^{-1}V_\alpha\frac{m_\alpha^2}{v}\mathcal{U}_{\alpha 2} & 2M_\Sigma^{-1}V_\alpha\frac{m_\alpha^2}{v}\mathcal{U}_{\alpha 3} & 0 \end{array} \right)$$

$$g_R^\phi = \left(\begin{array}{cc} -\sqrt{2}\mathcal{U}\frac{m_\nu^d}{v} & (V^T-(V^T\wedge V)\cdot V^T - V^T\cdot\frac{V.V^T}{2})\sqrt{2}\frac{M_\Sigma}{v} - 2\sqrt{2}\mathcal{U}\frac{m_\nu^d}{v}\mathcal{U}^TV^T \\ -2\frac{M_\Sigma}{v}V(1-\frac{(V^T\wedge V)}{2})\mathcal{U} & 0 \end{array} \right) =$$

$$= \left(\begin{array}{ccc} -\frac{\sqrt{2}}{v}m_{\nu_1}\mathcal{U}_{e1} & -\frac{\sqrt{2}}{v}m_{\nu_2}\mathcal{U}_{e2} & -\frac{\sqrt{2}}{v}m_{\nu_3}\mathcal{U}_{e3} \\ -\frac{\sqrt{2}}{v}m_{\nu_1}\mathcal{U}_{\mu 1} & -\frac{\sqrt{2}}{v}m_{\nu_2}\mathcal{U}_{\mu 2} & -\frac{\sqrt{2}}{v}m_{\nu_3}\mathcal{U}_{\mu 3} \\ -\frac{\sqrt{2}}{v}m_{\nu_1}\mathcal{U}_{\tau 1} & -\frac{\sqrt{2}}{v}m_{\nu_2}\mathcal{U}_{\tau 2} & -\frac{\sqrt{2}}{v}m_{\nu_3}\mathcal{U}_{\tau 3} \\ \hline \frac{M_\Sigma}{v}V_\alpha(V_e^2+V_\mu^2+V_\tau^2-2)\mathcal{U}_{\alpha 1} & \frac{M_\Sigma}{v}V_\alpha(V_e^2+V_\mu^2+V_\tau^2-2)\mathcal{U}_{\alpha 2} & \frac{M_\Sigma}{v}V_\alpha(V_e^2+V_\mu^2+V_\tau^2-2)\mathcal{U}_{\alpha 3} \end{array} \right| \left| \begin{array}{c} \sqrt{2}\frac{M_\Sigma}{v}V_e(1-\frac{3}{2}(V_e^2+V_\mu^2+V_\tau^2)) - 2\sqrt{2}\frac{m_{\nu_i}}{v}\mathcal{U}_{ei}\mathcal{U}_{\alpha i}V_\alpha \\ \sqrt{2}\frac{M_\Sigma}{v}V_\mu(1-\frac{3}{2}(V_e^2+V_\mu^2+V_\tau^2)) - 2\sqrt{2}\frac{m_{\nu_i}}{v}\mathcal{U}_{\mu i}\mathcal{U}_{\alpha i}V_\alpha \\ \sqrt{2}\frac{M_\Sigma}{v}V_\tau(1-\frac{3}{2}(V_e^2+V_\mu^2+V_\tau^2)) - 2\sqrt{2}\frac{m_{\nu_i}}{v}\mathcal{U}_{\tau i}\mathcal{U}_{\alpha i}V_\alpha \\ \hline 0 \end{array} \right)$$

In the above expressions repeated flavor indexes are summed. As we will discuss later, we will take neutrino masses equal to zero, except in the case of small mixing angles [1].

[1] In this case, indeed, for consistency we will turn neutrino masses, as well as electron and muon masses, on. However, this will not basically affect the result.

C

Simulation Programs Details

C.1 Madgraph

C.1.1 Model Assumptions

- In seesaw type III model we add 3 fermion triplets. Since only the lightest one could be detected in LHC, we build a model including the lightest triplet only. It is easier to develop, and it doesn't have drawbacks. The Yukawa coupling (Y) will reduce to be a vector, instead of a matrix.
- We are not interested in the phase, so $Y^t = Y$.
- As input parameter we will use the quantity $U = YMv$ instead of the Yukawa coupling.
- Neutrino masses are zero.

C.1.2 Run Card

Examples of Madgraph configuration cards could be taken from (42). The run card used for the signal generation is the following:

```
   #*********************************************************************
# MadGraph/MadEvent *
# http://madgraph.hep.uiuc.edu *
# *
# run_card.dat *
# *
# This file is used to set the parameters of the run.  *
# *
```

```
# Some notation/conventions:  *
# *
# Lines starting with a '# ' are info or comments *
# *
# mind the format:  value = variable !  comment *
#*********************************************************************
#
#*******************
# Running parameters
#*******************
#
#*********************************************************************
# Tag name for the run (one word) *
#*********************************************************************
'seesaw' = run_tag !  name of the run
#*********************************************************************
# Run to generate the grid pack *
#*********************************************************************
.false.  = gridpack !True = setting up the grid pack
#*********************************************************************
# Number of events and rnd seed *
# Warning:  Do not generate more than 100K event in a single run *
#*********************************************************************
100000 = nevents !  Number of unweighted events requested
0 = iseed !  rnd seed (0=assigned automatically=default))
#*********************************************************************
# Collider type and energy *
#*********************************************************************
1 = lpp1 !  beam 1 type (0=NO PDF)
1 = lpp2 !  beam 2 type (0=NO PDF)
3500 = ebeam1 !  beam 1 energy in GeV
3500 = ebeam2 !  beam 2 energy in GeV
#*********************************************************************
# Beam polarization from -100 (left-handed) to 100 (right-handed) *
#*********************************************************************
0 = polbeam1 !  beam polarization for beam 1
```

```
0 = polbeam2 !  beam polarization for beam 2
#*********************************************************************
# PDF CHOICE: this automatically fixes also alpha_s and its evol.  *
#*********************************************************************
'cteq6l1' = pdlabel !  PDF set
#*********************************************************************
# Renormalization and factorization scales *
#*********************************************************************
F = fixed_ren_scale !  if .true.  use fixed ren scale
F = fixed_fac_scale !  if .true.  use fixed fac scale
91.1880 = scale !  fixed ren scale
91.1880 = dsqrt_q2fact1 !  fixed fact scale for pdf1
91.1880 = dsqrt_q2fact2 !  fixed fact scale for pdf2
1 = scalefact !  scale factor for event-by-event scales
#*********************************************************************
# Matching - Warning!  ickkw > 1 is still beta
#*********************************************************************
1 = ickkw !  0 no matching, 1 MLM, 2 CKKW matching
1 = highestmult !  for ickkw=2, highest mult group
1 = ktscheme !  for ickkw=1, 1 Durham kT, 2 Pythia pTE
1 = alpsfact !  scale factor for QCD emission vx
F = chcluster !  cluster only according to channel diag
T = pdfwgt !  for ickkw=1, perform pdf reweighting
#*********************************************************************
# Automatic ptj and mjj cuts if xqcut > 0
# (turn off for VBF and single top processes)
#*********************************************************
T = auto_ptj_mjj
#*********************************************************
#
#*********************************
# BW cutoff (M+/-bwcutoff*Gamma)
#*********************************
10000 = bwcutoff
#*********************************************************
# Apply pt/E/eta/dr/mij cuts on decay products or not
```

```
# (note that etmiss/ptll/ptheavy/sorted cuts always apply)
#*********************************************************
T = cut_decays
#*************************************************************
# Number of helicities to sum per event (0 = all helicities)
# 0 gives more stable result, but longer run time (needed for
# long decay chains e.g.).
# Use >=2 if most helicities contribute, e.g.  pure QCD.
#*************************************************************
0 = nhel
#*******************
# Standard Cuts
#*******************
# #*********************************************************************
# Minimum and maximum pt's *
#*********************************************************************
20 = ptj !  minimum pt for the jets
20 = ptb !  minimum pt for the b
0 = pta !  minimum pt for the photons
0 = ptl !  minimum pt for the charged leptons
0 = misset !  minimum missing Et (sum of neutrino's momenta)
0 = ptheavy !  minimum pt for one heavy final state
1.0 = ptonium !  minimum pt for the quarkonium states
1d5 = ptjmax !  maximum pt for the jets
1d5 = ptbmax !  maximum pt for the b
1d5 = ptamax !  maximum pt for the photons
1d5 = ptlmax !  maximum pt for the charged leptons
1d5 = missetmax !  maximum missing Et (sum of neutrino's momenta)
#*********************************************************************
# Minimum and maximum E's (in the lab frame) *
#*********************************************************************
0 = ej !  minimum E for the jets
0 = eb !  minimum E for the b
0 = ea !  minimum E for the photons
0 = el !  minimum E for the charged leptons
1d5 = ejmax !  maximum E for the jets
```

```
1d5 = ebmax !  maximum E for the b
1d5 = eamax !  maximum E for the photons
1d5 = elmax !  maximum E for the charged leptons
#*********************************************************************
# Maximum and minimum rapidity *
#*********************************************************************
5 = etaj !  max rap for the jets
5 = etab !  max rap for the b
2d5 = etaa !  max rap for the photons
2d5 = etal !  max rap for the charged leptons
0.6 = etaonium !  max rap for the quarkonium states
0d0 = etajmin !  min rap for the jets
0d0 = etabmin !  min rap for the b
0d0 = etaamin !  min rap for the photons
0d0 = etalmin !  main rap for the charged leptons
#*********************************************************************
# Minimum and maximum DeltaR distance *
#*********************************************************************
0.001 = drjj !  min distance between jets
0.001 = drbb !  min distance between b's
0 = drll !  min distance between leptons
0 = draa !  min distance between gammas
0.001 = drbj !  min distance between b and jet
0 = draj !  min distance between gamma and jet
0 = drjl !  min distance between jet and lepton
0 = drab !  min distance between gamma and b
0 = drbl !  min distance between b and lepton
0 = dral !  min distance between gamma and lepton
1d2 = drjjmax !  max distance between jets
1d2 = drbbmax !  max distance between b's
1d2 = drllmax !  max distance between leptons
1d2 = draamax !  max distance between gammas
1d2 = drbjmax !  max distance between b and jet
1d2 = drajmax !  max distance between gamma and jet
1d2 = drjlmax !  max distance between jet and lepton
1d2 = drabmax !  max distance between gamma and b
```

```
1d2 = drblmax !  max distance between b and lepton
1d2 = dralmax !  maxdistance between gamma and lepton
#*********************************************************************
# Minimum and maximum invariant mass for pairs *
#*********************************************************************
0 = mmjj !  min invariant mass of a jet pair
0 = mmbb !  min invariant mass of a b pair
0 = mmaa !  min invariant mass of gamma gamma pair
0 = mmll !  min invariant mass of l+l- (same flavour) lepton pair
1d5 = mmjjmax !  max invariant mass of a jet pair
1d5 = mmbbmax !  max invariant mass of a b pair
1d5 = mmaamax !  max invariant mass of gamma gamma pair
1d5 = mmllmax !  max invariant mass of l+l- (same flavour) lepton pair
#*********************************************************************
# Minimum and maximum invariant mass for all letpons *
#*********************************************************************
0 = mmnl !  min invariant mass for all letpons (l+- and vl)
1d5 = mmnlmax !  max invariant mass for all letpons (l+- and vl)
#*********************************************************************
# Minimum and maximum pt for 4-momenta sum of leptons *
#*********************************************************************
0 = ptllmin !  Minimum pt for 4-momenta sum of leptons(l and vl)
1d5 = ptllmax !  Maximum pt for 4-momenta sum of leptons(l and vl)
#*********************************************************************
# Inclusive cuts *
#*********************************************************************
0 = xptj !  minimum pt for at least one jet
0 = xptb !  minimum pt for at least one b
0 = xpta !  minimum pt for at least one photon
0 = xptl !  minimum pt for at least one charged lepton
#*********************************************************************
# Control the pt's of the jets sorted by pt *
#*********************************************************************
0 = ptj1min !  minimum pt for the leading jet in pt
0 = ptj2min !  minimum pt for the second jet in pt
0 = ptj3min !  minimum pt for the third jet in pt
```

```
0 = ptj4min !  minimum pt for the fourth jet in pt
1d5 = ptj1max !  maximum pt for the leading jet in pt
1d5 = ptj2max !  maximum pt for the second jet in pt
1d5 = ptj3max !  maximum pt for the third jet in pt
1d5 = ptj4max !  maximum pt for the fourth jet in pt
0 = cutuse !  reject event if fails any (0) / all (1) jet pt cuts
#*********************************************************************
# Control the Ht(k)=Sum of k leading jets *
#*********************************************************************
0 = htjmin !  minimum jet HT=Sum(jet pt)
1d5 = htjmax !  maximum jet HT=Sum(jet pt)
0 = ihtmin !inclusive Ht for all partons (including b)
1d5 = ihtmax !inclusive Ht for all partons (including b)
0 = ht2min !  minimum Ht for the two leading jets
0 = ht3min !  minimum Ht for the three leading jets
0 = ht4min !  minimum Ht for the four leading jets
1d5 = ht2max !  maximum Ht for the two leading jets
1d5 = ht3max !  maximum Ht for the three leading jets
1d5 = ht4max !  maximum Ht for the four leading jets
#*********************************************************************
# WBF cuts *
#*********************************************************************
0 = xetamin !  minimum rapidity for two jets in the WBF case
0 = deltaeta !  minimum rapidity for two jets in the WBF case
#*********************************************************************
# maximal pdg code for quark to be considered as a light jet *
# (otherwise b cuts are applied) *
#*********************************************************************
5 = maxjetflavor
#*********************************************************************
# Jet measure cuts *
#*********************************************************************
20 = xqcut !  minimum kt jet measure between partons
#*********************************************************************
```

C.1.3 Run Card Parameters Notes

Notes about crucial run card parameters are given below.

maxjetflavor defines which cuts to apply on jet types. For example if maxjetflavor=5 this means that the b quarks will be constrained by the cuts for jets, (ptj, etaj). On the contrary the usual cuts for b's are applied (ptb, etab, etc).

xqcut is the minimal distance between the ISR in the matrix-element calculation. It is typically closed to the cutoff used for the matching. The good value for xqcut is always a compromise between the fact that we want a reasonable matching efficiency, and in the same time not too high cause in this case there could be dead zones in the PS region of the phase-space.

Some typical choices of xqcut/qcut for processes with massive particles are in Table C.1.

Process	xqcut	Qcut
V, VV, VVV +jets	10	15
ttbar	20	30

Table C.1: Typical qcut values

.

C.2 Pythia6-CMSSW Interface

C.2.1 Configuration Setting

Configuration file example for processing a MadGraph sample with Pythia6 in CMSSW could be seen for example in CMSSW directory:
`Configuration/Generator/python/MadGraph_matching_cfi.py`. Reference: (39).

Here I'll give some details of interest about the configuration file I've used to run Madgraph signal LHE files in Pythia-CMSSW.

1. LHESource (rather than EmptySource) feed with parton-level MadGraph sample (.lhe file);

2. `generator = cms.EDFilter("Pythia6HadronizerFilter")`: it means that we use Pythia6-based module that is dedicated to processing externally generated partons;

3. The module configured specifically for processing MadGraph events is:

```
processParameters = cms.vstring('MSEL=0 !  User defined processes',
'PMAS(5,1)=4.4 !  b quark mass',
'PMAS(6,1)=172.4 !  t quark mass',
'MSTJ(1)=1 !  Fragmentation/hadronization on or off',
'MSTP(61)=1 !  Parton showering on or off'),
```

4. Dedicated Madgraph parton-shower matching algorithm, to decide on the event internal validity, or to veto events of incorrect topology:

```
jetMatching = cms.untracked.PSet(
scheme = cms.string("Madgraph"),
mode = cms.string("auto"), # soup, or "inclusive" / "exclusive"
MEMAIN_etaclmax = cms.double(5.0),
MEMAIN_qcut = cms.double(30.0),
MEMAIN_minjets = cms.int32(0),
MEMAIN_maxjets = cms.int32(15),
MEMAIN_showerkt = cms.double(0),
MEMAIN_nqmatch = cms.int32(5),
MEMAIN_excres = cms.string(""),
outTree_flag = cms.int32(0)
)
```

   Note: the use of matching procedure is optional; Pythia6HadronizerFilter may operate without it. However, if parton-shower matching is used, in case an event is vetoed the EDFilter will return a false code, and the HepMCProduct will be empty.

5. Those event will be filtered out of the output, because event generation step is included in the "production filtering sequence":

```
ProductionFilterSequence = cms.Sequence(generator)
```

Configuration fragment could be processed through cmsDriver.py, for example for Summer 11 datasets production I've used the following: `cmsDriver.py`

```
Configuration/GenProduction/python/SeesawToLeptons_M_120_7TeV_pythia6_cff.py
-s GEN --conditions START311_V2::All --beamspot Realistic7TeV2011Collision
--datatier GEN-SIM --eventcontent RAWSIM --filein file:...lhe -n 10000 --no_exec
```

and `cmsDriver.py`

```
Configuration/GenProduction/python/SeesawToLeptons_M_120_7TeV_pythia6_cff.py
-s GEN,SIM,DIGI,L1,DIGI2RAW,HLT --conditions START311_V2::All --beamspot
Realistic7TeV2011Collision --datatier GEN-SIM-RAW --eventcontent RAWSIM --filein
file:...lhe -n 30 --no_exec
```

The even loop is driven by a special purpose LHESource (rather than EmptySource)

```
source = cms.Source("LHESource",
fileNames = cms.untracked.vstring(
'file:....lhe')
)
```

which is feed with the parton-level MadGraph sample.

C.2.2 Fast Simulation

We used Fast Simulation to run simulation-reconstruction chain of the signal datasets analyzed in the thesis.

The code used is:

```
   CMSSW_4_2_8_patch4
FastSimulation/PileUpProducer tag:  V04-05-12
```

The cmsDriver command used is:

```
   cmsDriver.py SeesawTo3lept_30qcut_7TeV_pythia6_cff.py --filein=file:....lhe
--filetype=LHE -s GEN,FASTSIM,HLT:GRun --pileup=E7TeV_Fall2011_Reprocess_inTimeOnly
--geometry DB --conditions=auto:startup --eventcontent=AODSIM --datatier
GEN-SIM-DIGI-RECO -n 100000 --no_exec
```

The pileup distribution superimposed to events have been taken from *real* 2011 data pileup distributions.

References about CMSSW Fast Simulation could be see in Reference (80).

D

Backgrounds Samples

Reference: (95)

D.1 Datasets

The signal and background samples used in this analysis have been obtained using detailed Monte Carlo simulations. In most cases, the samples are taken from the official CMS `Summer 11` production cycle with digitization and reconstruction done with `CMSSW_4_2_X`. Background processes for `Summer 11` production have been generated using Madgraph (58), Pythia (47), and POWHEG (61) generators.

The 2011 Monte Carlo samples used in this analysis for the backgrounds include all the luminosity-dependent trigger configurations as used in the data. Therefore, implementation of the trigger matching was introduced. We require the HLT objects to match the leptons selected for our analysis, and reproduce the HLT requirements by applying the corresponding p_T thresholds.

Private Madgraph5 generations have been performed for the samples not present in the official production (i.e. $t\bar{t}W$, $t\bar{t}WW$, $t\bar{t}Z$, WW same sign), and the request for official simulation and reconstruction processing was submit to the CMS generators team. They have been approved, processed and included in Summer 11 dataset.

Whenever the cross section for the different background under study has not been measured, we have used `MadGraph/MadEvent` to obtain the cross-sections for LHC running at 7 TeV and compared our results with previous results obtained by the CMS collaboration (73).

The full list of background samples we considered or studied, including their dataset

names and cross sections, are presented in Table D.1 and D.2. Detail about the generator and the number of events of the main backgrounds are listed in Table D.3.

Table D.1: Samples, Dataset names, leading order (LO) and next-to-leading order (NLO) cross sections for the physical background samples considered in this analysis. Datasets marked with * are taken from the Spring11 production, while all others are from Summer11. Cross sections marked with † are next-to-next-to-leading order.

Sample	Dataset Name	σ_{LO} (pb)	σ_{NLO} (pb)
$TTbarJetMadGr$	TTJets_TuneZ2_7TeV-madgraph-tauola		157.5
$V\gamma+$ jets	GVJets_7TeV-madgraph	173	
WZ	WZ_TuneZ2_7TeV_pythia6_tauola	18.3 (#)	
$WZ3L$	WZTo3LNu_7TeV-pythia6	0.34	0.594
ZZ	ZZ_TuneZ2_7TeV_pythia6_tauola	4.3	5.9
$ZZTo4mu$	ZZTo4mu_7TeV-powheg-pythia6	0.0154	
$ZZTo2e2mu$	ZZTo2e2mu_7TeV-powheg-pythia6	0.0308	
$ZZTo4e$	ZZTo4e_7TeV-powheg-pythia6	0.0154	
$ZZTo4L$	ZZTo4L_TuneZ2_7TeV-pythia6-tauola*	0.065	0.082
$WWWm\_Castor$	WWWTo2Lminus2Nu_Qcut-20_Castor_7TeV-madgraph	0.003402	
$WWWp\_Castor$	WWWTo2Lplus2Nu_Qcut-20_Castor_7TeV-madgraph	0.007903	
$TTWWm\_Castor$	TTWWTo2Lminus2Nu_Qcut-20_Castor_7TeV-madgraph	0.00004719	
$TTWWp\_Castor$	TTWWTo2Lplus2Nu_Qcut-20_Castor_7TeV-madgraph	0.0000476	
WWm_Castor	WWminusTo2L2Nu_Castor_7TeV-madgraph	0.001559	
WWp_Castor	WWplusTo2L2Nu_Castor_7TeV-madgraph	0.004216	
$TTZm\_Castor$	TTZTo2Lminus2Nu_Castor_7TeV-madgraph	0.001946	
$TTZp\_Castor$	TTZTo2Lplus2Nu_Castor_7TeV-madgraph	0.002024	
$TTWm\_Castor$	TTWTo2Lminus2Nu_Castor_7TeV-madgraph	0.002705	
$TTWp\_Castor$	TTWTo2Lplus2Nu_Castor_7TeV-madgraph	0.006841	

Table D.2: Samples, Dataset names, leading order (LO) and next-to-leading order (NLO) cross sections for the non-physical background samples considered in this analysis. Datasets marked with * are taken from the Spring11 production, while all others are from Summer11. Cross sections marked with † are next-to-next-to-leading order. (#)For WZ sample we used the measured cross section instead of the MC one. The value is taken from Reference (106), and is equal to: 17.0 ± 2.4(stat.)± 1.1(syst.)± 1.0(lumi).

Sample	Dataset Name	σ_{LO} (pb)	σ_{NLO} (pb)
$QCD - MuEnrichedPt15$	QCD_Pt-20_MuEnrichedPt-15_TuneZ2_7TeV-pythia6	84679.3	
$QCD - EMEnriched$	QCD_Pt-20to30_EMEnriched_TuneZ2_7TeV-pythia6	2502.66	
Zee	DYToEE_M-20_TuneZ2_7TeV-pythia6	1667	
$Zmumu$	DYToMuMu_M-20_TuneZ2_7TeV-pythia6	1667	
$Ztautau$	DYToTauTau_M-20_TuneZ2_7TeV-pythia6-tauola	1667	
$Wenu$	WtoENu_TuneD6T_7TeV-pythia6	10438	
$Wmunu$	WtoMuNu_TuneD6T_7TeV-pythia6	10438	
$Wtaunu$	WtoTauNu_TuneD6T_7TeV-pythia6-tauola	10438	
WW	WW_TuneZ2_7TeV_pythia6_tauola	42.9	
$WW2L$	WWTo2L2Nu_TuneZ2_7TeV_pythia6_tauola		
$SingleTop\_t$	T_TuneZ2_t-channel_7TeV-powheg-tauola		41.92
$SingleAntiTop\_t$	Tbar_TuneZ2_t-channel_7TeV-powheg-tauola		22.65
$SingleTop\_tW$	T_TuneZ2_tW-channel-DR_7TeV-powheg-tauola		7.87
$SingleAntiTop\_tW$	Tbar_TuneZ2_tW-channel-DR_7TeV-powheg-tauola		7.87
$SingleTop\_s$	T_TuneZ2_s-channel_7TeV-powheg-tauola		3.19
$SingleAntiTop\_s$	Tbar_TuneZ2_s-channel_7TeV-powheg-tauola		1.44
$ZJetsMadGr$	DYJetsToLL_TuneD6T_M-50_7TeV-madgraph-tauola	2289	3048
$ZJetsMadgr\_10-50$	DYJetsToLL_TuneD6T_M-10To50_7TeV-madgraph-tauola * 310		
$WJetsMadGr$ jets	WJetsToLNu_TuneZ2_7TeV-madgraph-tauola	24640*3	31314*3†
$DYToCC$	DYToCC_M_50_TuneZ2_7TeV_pythia6		1809.6
$DYToBB$	DYToBB_M_50_TuneZ2_7TeV_pythia6		2272.65
$Zbb + 0$ jets	ZBB0JetsToLNu_TuneZ2_7TeV-alpgen-tauola*	1.7	2.9
$Zbb + 1$ jets	ZBB1JetsToLNu_TuneZ2_7TeV-alpgen-tauola*	0.962	1.645
$Zbb + 2$ jets	ZBB2JetsToLNu_TuneZ2_7TeV-alpgen-tauola*	0.364	0.622
$Zbb + 3$ jets	ZBB3JetsToLNu_TuneZ2_7TeV-alpgen-tauola*	0.16	0.273
$Zcc + 0$ jets	ZCC0JetsToLNu_TuneZ2_7TeV-alpgen-tauola*	1.71	2.92
$Zcc + 1$ jets	ZCC1JetsToLNu_TuneZ2_7TeV-alpgen-tauola*	0.953	1.629
$Zcc + 2$ jets	ZCC2JetsToLNu_TuneZ2_7TeV-alpgen-tauola*	0.366	0.626
$Zcc + 3$ jets	ZCC3JetsToLNu_TuneZ2_7TeV-alpgen-tauola*	0.164	0.28

Process	MC Generator	σ (pb)	Number of events
Background Samples:			
$t\bar{t}$	MADGRAPH	164.4 (NNLO)	3,701,947
$W(\rightarrow)\ell\nu$+jets	MADGRAPH	31314 (NNLO)	77,105,816
Drell Yan - $Z/\gamma^*(\rightarrow \ell\ell)$+jets	MADGRAPH	3048 (NNLO)	36,277,961
WW	MADGRAPH	3.78	1,197,558
WZ	MADGRAPH	0.72	1,221,134
ZZ	MADGRAPH	0.04	1,185,188
$W\gamma \rightarrow e\nu\gamma$	MADGRAPH	114.7	524,503
$W\gamma \rightarrow \mu\nu\gamma$	MADGRAPH	114.6	521,774
$W^{\pm}W^{\pm}$	MADGRAPH	0.006	99,307
WWW	MADGRAPH	0.01	60,469
$t\bar{t}W$	MADGRAPH	0.01	99,199
$t\bar{t}Z$	MADGRAPH	0.004	73,521

Table D.3: Details of the background Monte Carlo samples used for the analysis.